Design Synthesis Exercise

Final Report

Mukhamejan Baimoldayev
Tomas Bakker
Mykolas Grinevicius
Tristan Hamers
Kaloyan Kirilov
Sihyeong Lim
Christiaan Nouws
Jelle Poland
Tobias Pütz
Julian Schmidt

January 29, 2019

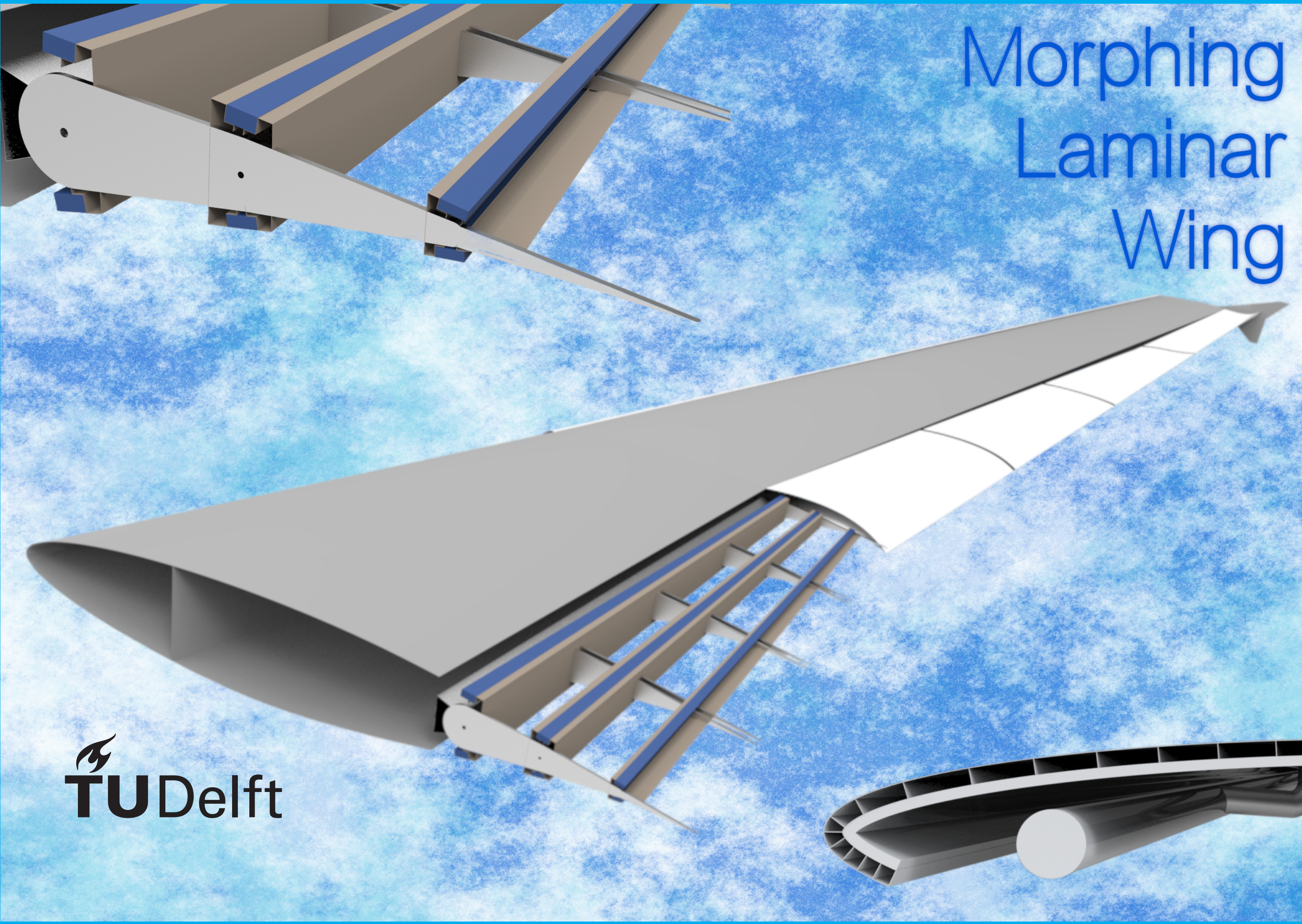

TU Delft

Preface

This is the final report in a series of four reports for the Design Synthesis Exercise (DSE) at the faculty of Aerospace Engineering of Delft University of Technology. The DSE is the final exercise of the Bachelor programme, in which ten students work on a design project for ten weeks. This project is about the design process of a smart autonomous wing.

In the first report, the project plan, the organisation of the team and the planning of the project was established. The preliminary design phase was covered in the baseline report. The third report, the midterm report, contained the conceptual design. In this final report a overview of the whole process so far and the detailed analysis is presented.

We would like to thank our tutor Dr.ir. Roeland de Breuker and coaches Ir. Jos Sinke and Ir. Reno Elmendorp for continuous support and advice during tough times. Moreover, we thank Dr. Jurij Sodja for his insights and help with load alleviation problems. Group 2 is grateful for having had an opportunity to dive into the topic of smart autonomous wing and give our perspective to it.

Mukhamejan Baimoldayev
Tomas Bakker
Mykolas Grinevicius
Tristan Hamers
Kaloyan Kirilov
Sihyeong Lim
Christiaan Nouws
Jelle Poland
Tobias Pütz
Julian Schmidt

Executive Overview

Over the course of the last century, the aircraft-industry has continuously been developing and optimising the performance of their products. The rate of improvement has been decreasing, and it seems like an asymptote is being approached in the development of the current technologies. The demand for new innovative solutions is growing and these solutions shall allow the performance increase to bypass this stagnation. One of the solutions investigated is to develop an aircraft wing which has the capability to fly at optimal shape by autonomously optimising its own wing-shape during all phases of the mission. This could potentially lead to a severe increase in aerodynamic performance and controllability while actively minimising structural loads.

This is the final report of a series which describe the design process of such an autonomous wing, an overview of the final design phase is presented in this executive overview. The main mission objectives are captured in the mission need statement (MNS) and project objective statement (POS) which are presented below.

Mission Need Statement: *"Provide an aircraft wing which is able to autonomously optimise its wing configuration during flight ."*

Project Objective Statement: *"Design an aircraft wing that uses autonomous control for continuous optimisation of its wing configuration to outperform an A320 like aircraft wing while still complying with the desired flight control behaviour with ten people in ten weeks."*

Preliminary Design

In order to end up with a design that is able to satisfy the MNS and the POS, several concepts were developed. The concept development was based upon the functional analysis and the requirements analysis. The functional analysis was split up into five high level blocks: Interface functions, Aerodynamics & Performance, Structural load bearing, Sense & Control and other operational functions &constrains. The requirements analysis consists out of the stakeholder requirements and the customer requirements. The stakeholder requirements are provided by the customer, an example of a driving requirements is that the wing shall result in a drag reduction of 7.5% over the entire flight with respect to the Airbus A320 legacy wing.

Concept development and selection

The first concept coming out of the concept development is a morphing trailing edge (MTE), which consists out of eight sections covering the entire span and each of these sections is made from three flaps. Main advantages are its load alleviation potential and the reduction of viscous drag to the elimination of gaps. The second concept is a movable top skin, which allows for changing the thickness of the airfoil during flight. The main advantage is the potential to increase the flows laminar region which shall decreasing the drag. The third concept is Hybrid laminar flow control (HLFC) which sucks the airflow through holes in the leading edge of the wing. The main advantage of the HLFC is its potential for significant drag reduction. The main disadvantage is that in order to keep the holes from being contaminated a Krueger flap needs to be installed on the leading edge.

A trade-off was preformed using these concepts where, the high-level trade off criteria consists of: performance, system cost, RAMS characteristics, compatibility, sustainability, complexity and technology readiness level. Each criteria was based on the requirements and from all criteria the performance got the highest weight factor of 0.5. The high-level trade off criteria performance is further split up into: system mass, drag reduction, contribution to load alleviation and the effect on laminar flow region. From which the drag reduction got the highest weight factor of 0.5, due to its effect on multiple driving requirements. Finally the sensitivity analysis showed that either the MTE or the HLFC depending on the weights of the criteria would win the trade-off.

For the final design chose the decision was made to incorporate both the MTE and the HLFC concept. This decision was made in of increasing the likely hood of fulfilling the requirements. What helped for the decision is that the MTE affects the trailing edge and the HLFC the leading edge thus not much interference is expected. The final design that is further analysed and worked out in more detail in this report, its initial render is shown in Figure 1.

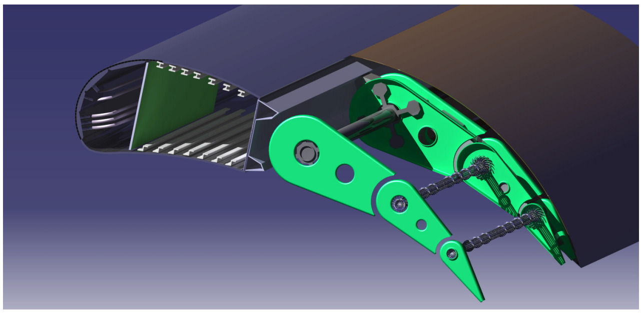

Figure 1: Render of the final configuration (not to scale)

Morphing laminar wing description

In order to make a detailed design of the morphing laminar wing (MLW), the MTE and HLFC should first be better understood. The MTE architecture is made out of four main components: electrical system, control & monitoring system, actuation system and the structural elements. The electrical system controls the electrical power for the MTE and obtains it from the primary power unit of the aircraft. The control & monitoring system has to provide the required deflections for load alleviation and for optimal aerodynamic performance with shape optimisation. The control unit prioritises the pilots input, than the load alleviation and finally the drag optimisation. The software diagram is shown in Figure 2.

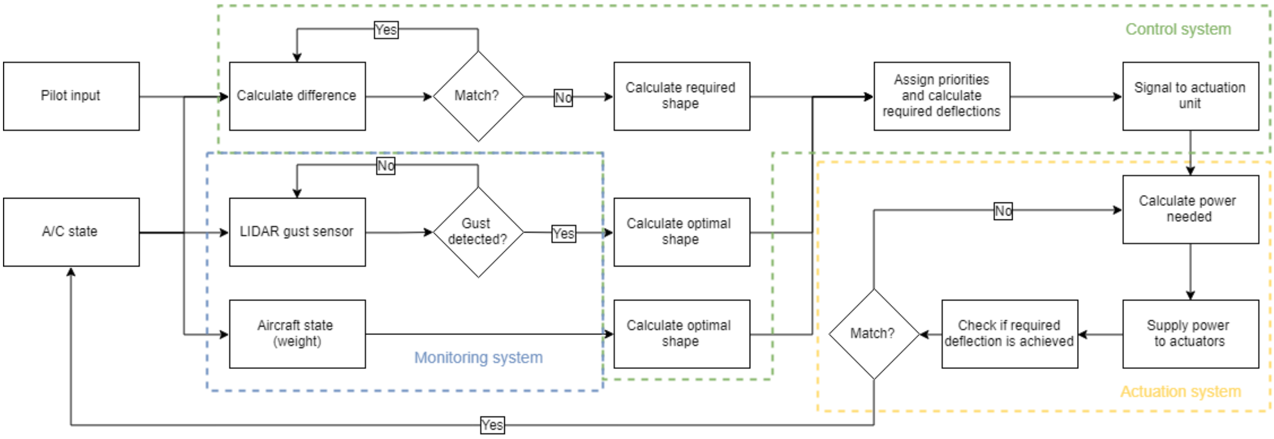

Figure 2: Software diagram MTE

The actuation system uses rotary electro-mechanical actuators to deflect all 24 different flaps. Each flap segment has roughly the same structure, consisting of two chord wise ribs which itself consist of three sections. A skin is placed on top of these ribs consisting of thee main components: elastomer coating, u-shaped reinforcement and hinge line reinforcement. Polydimethylsilioxane is used in span-wise direction as connection between the different flap segments, which allows for high strain connection and results in a smooth trailing edge flap system.

HLFC

The HLFC focuses on decreasing the wing friction drag. HLFC consists out of a suction system and airfoil modifications to laminar airfoils. For swept wings without suction systems laminar airfoils are not able to enhance the laminar flow [1]. The HLFC system shall be applied on the top part of the wing at the leading edge where it does not interfere with the fuel tanks. The HLFC is split up into four main parts: suction surface, pressurisation system, control & monitoring system and the anti-contamination system.

The suction surface panels are made of titanium and placed on the outboard section where there is potential to create laminar flow. The pressurisation system contains of several pipes, valves, cabins and a suction device which uses bleed air from the engine high pressure compressor to start. The control & monitoring system uses pressure sensors to determine the stagnation point and from there the valve openings shall be adjusted to create the required pressure. The HLFC computer shall autonomously monitor the flow data and mechanically adjust to in order to minimise the drag. For anti-contamination a Krueger flap is designed to shield the suction panels from contaminants. However in some situation the Krueger flap is not able to prevent contamination, this issues was resolved by equipping the HLFC with a heated air flow reversal mode. The hot air de-ices and unclogs the perforations and removes humidity in the system. This anti-contamination mode is switched on during on-ground operations, take-off/landing and climb/descent.

The HLFC suction system its there to provide the required suction velocity distribution. The air flows through the perforations due to it they being differential pressure chambers which are called flutes. The mass flow rate through these flutes are estimated using Goldstein method and Sutherland's formula for air [1] [2]. After the flutes, the air flows through an orifice to a bigger pressure chamber called a manifold. With this step a pressure drop is expected and estimated using Borda-Carnot Relations. The air then flows into main pipes through "tee pipe" connectors, where the pressure loss is calculated using the geometry. By understanding how the airflow runs and by being able to calculate the pressure at each sections of the HLFC one can design the suction system. A software tool was created for this purposes, that uses an object oriented approach to simplify testing and to minimise mistakes. This tool uses several inputs and as output gives the pressures, mass flows and geometrical properties of suction system. By comparing the end pressure to the ambient pressure during cruise, it was found that the pressure ratio of the pump should be 2.3 and the total mass flow equals 0.52 kg/s. The Krueger flap was already mentioned as a necessary modification in order to ensure that the HLFC suction system is not covered by a slat. The Krueger flap is due to time constraints not designed into detail but its effect on the lift coefficient C_L, mass and cost with respect to the legacy slat is estimated. A bull-nose type of Krueger flap is chosen which decreases $C_{L_{max}}$ by 0.05 only and those do not affect the C_L to angle of attack curve slope either [3]. The respective mass of the bull-nose Krueger flap compared to the legacy three-position slat differs less than 3%, calculated using estimations from NASA based on existing aircraft [4]. The cost of the new flap increases by 0.8% calculated using the same relations. Due to these difference in C_L, mass and cost being below 5% changing the flap is not expected to be detrimental to the project goal. The Krueger flap chord was chosen to be 12% of the wing chord and the smallest gap in extracted position to be 2.2%, for these decision the NASA HLFC test flap design was used [3].

Aerodynamic Analysis

For performing reverse engineering procedures to find the aerodynamic performance of the MLW, XFLR5 based on the XFOIL engine is used as a tool. Since as every tool it has its limitations and downsides it shall be analysed and corrected for using MATLAB scripts and DATCOM like approaches. For bench-marking, concept and final analysis 3D VLM simulations are developed since the phenomena at interest (laminarity, viscosity, streamline interaction with bodies like fuselage) can not be evaluated using 2D strip method with compressibility corrections.

The panel method within XFLR5 is used to perform a 2D analysis, determining different distributions and transition points. These calculations are only accurate for incompressible flow and shall be corrected for using the Karman-Tsien compressibility correction rule [5].

The VLM method makes a number of different assumptions: incompressible and inviscid flow, all airfoils having small thicknesses and small angle approximations. Which are expected to not cause significant deviations since it shall be mainly used for trade-off comparison of the same wing planform. However for calculating high AoA during take-off and landing for example, VLM can not be used.

The analysis of the MTE and the HLFC aerodynamic effects is separated, this due to the difficulty of modelling flow separation. The MTE its effect shall be calculated using a pseudo optimisation algorithm which is required to be automated to a high degree, without automation an estimated 810 hours of manual work would have to be performed. XFLR5 shall import XML files for aircraft geometry, their respective airfoil selection and the freestream analysis configuration file linked to the name of the aircraft. Combining this with an algorithm that modifies the airfoil geometry files to create the three-hinged MTE deflection, shall result in the desired level of automation. This automation process becomes a tedious software architecture problem combining different tools and programming languages.

The software starts with a MTE airfoil generator which is used to rotate the original airfoil files around the three hinge lines and stores them as new airfoils. Secondly a XML 3D aircraft configuration generator is run which uses these

---

[1] `https://www.cfd-online.com/Wiki/Sutherland's_law`

airfoils to create multiple aircraft configurations with different deflections and includes the constant fuselage, horizontal & vertical stabiliser geometry. Thirdly a XML MTE analysis generator creates all the free stream information. Once these three generators have been executed, the results are combined and fed into XFLR5. XFLR5 uses 2D panel analysis and 3D VLM analysis where the output is stored and read by MATLAB. MATLAB than calculates the expected C_L for that particular mass and freestream condition. A compressibility correction is than used and as output the most efficient MTE configuration (max C_L/C_D) is given.

Airfoil selection

The MLW requires an optimal airfoil selection and the benchmark aircraft its airfoil is found using reverse engineering. The benchmark shall serves as the basis for the optimisation of the A320 wing. For the MLW an optimum selection of airfoils is required to get the most extended region of laminar flow over the wing. For this selection airfoils with good transonic behaviour with acceptable low-speed characteristics are chosen, e.g. NASA supercritical airfoils [6]. All 23 airfoils are tested for M = 0.8, assuming that cruise conditions are the driving factor with regards to the performance aspect, at three different locations: root, half span and tip. In finding the two different airfoil selections its important to note that for the benchmark the time period of airfoil design as well as their intended application was taken into account. For the benchmark the SC(2)-0414, SC(2)-0612 and SC(2)-0710 are chosen for the three wing sections from root to tip respectively.

While determining the optimal airfoil selection for the MLW, the natural laminar flow characteristics are taken into account for better performance once combined with the HLFC. From the analysis the Grumman K-1, RAE 2822 and Boeing HSNLF airfoils can be found as optimal for the root, centre and tip section in respective order. In Figure 3 the C_L/C_D graph is presented.

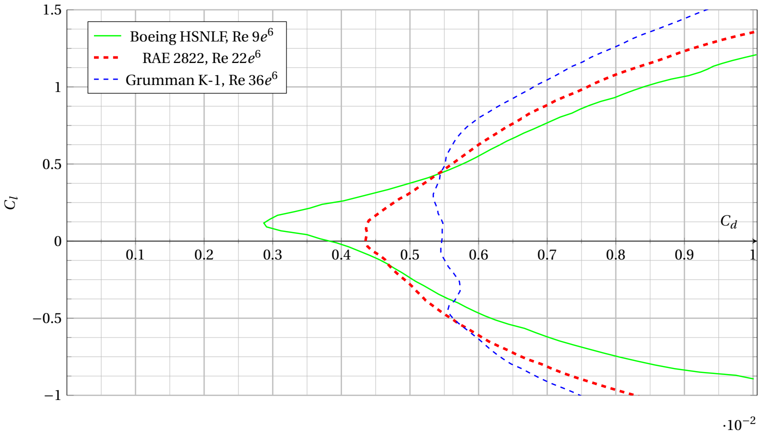

Figure 3: C_l/C_d graph of Boeing HSNLF, RAE 2822 and Grumman K-1 airfoils

For the XFLR5 model, to analyse the performance a model of the entire aircraft was made. NACA airfoils were used for the horizontal and vertical stabilisers as suggested by Torenbeek [7]. Besides fuselage, wing, horizontal and vertical stabiliser the effect of rest of the aircraft is taken into account with coefficients. These coefficients change between modelling of the benchmark and the MLW. With this model and the set of airfoils, for both models the lift distribution can be optimised to an elliptical shape by fine tuning the exact span wise usage of the airfoil set. Elliptical lift distributions is associated with minimum induced drag and is therefore aimed for. For both models a total of nine airfoil sections are identified, where linear interpolation is used to determine the airfoil shape between the selected airfoils.

In order to asses the drag performance, the flight profile of the A320 needs to be investigated. The optimum design range that is used as the foundation for the mission profile is specified as 4,774 km [8]. The flight profile is determined based on the aerodynamic layout of the benchmark aircraft. The MLW however has the ability to alter its aerodynamic layout during flight, making that potentially another flight profile proves to be more optimal. Due to time constraints only one alternative was tested, which was restricted by the maximum cruise altitude specified in the A320 Flight Crew Operation Manual [9].

HLFC Aerodynamics

In order to quantify the HLFC aerodynamic performance friction coefficient estimations based on flat plate theory are used to predict natural transition with the data from XFLR5 aerodynamic analysis and estimate transition delay due to suction by means of investigating previous suction system tests. Several assumptions were made in order to be able to make these estimations, the results gave that the aircraft drag decreased due to the suction system was shown to equal to 3.5 %. Validation from comparison to flight experiments for a B757 gave a 0.2 % deviation in total aircraft drag reduction [10].

This 3.5 % drag decrease is used for analysing the drag performance, it affects the high climb/descent and cruise phases of flight. For the drag performance analysis the optimal MTE settings for the benchmark mission profile was analysed and the MLW shows a drag decrease of 11.37 % compared to the legacy A320. For the alternate flight profile the MLW shows a 8.8 % drag decrease, therefore the original mission profile is kept. By building a discretised version of the Brequet Range model, which uses the optimised C_L/C_D values the fuel savings were estimated to be 1142 kg.

Load Alleviation

The MLW is equipped with a MTE that is capable of alleviating these loads. There are two types of load alleviation possible: manoeuvre load alleviation (MLA) and gust load alleviation (GLA).

The MLA system shall alleviate the loads during manoeuvres, with the sizing cases being a 2.5g pull-up manoeuvre and a -1g push-down manoeuvre. The regulations do not allow for lowering of the load factor, however the lift-distribution may be altered. By moving the centre of pressure inboard one can lower the bending stress induced on the wing. Additional torque load and for the inboard section extra shear stress is induced. The difference in stress these changes cause shall be calculated and checked by the structures model, where several loops were made to determine the optimal MLA shape.

The GLA system uses the MTE flaps to lower the lift factor and keep it as close to one as possible. The GLA induced extra torque load as well, however it lowers the bending moment and the shear load. Once again, the difference in stress cause by these changes shall be checked by the structures model.

During flight the MLA system works as an open loop controller and is activated once the aircraft senses a change in load factor. This change shall be checked with a database containing the appropriate deflections for different load factors. The GLA system works with an closed loop controller that uses a Doppler LIDAR sensor. The sensor is placed in the nose of the aircraft and is capable of detecting gusts [11]. With the approaching gust fed into the controller, it is capable of calculating the required deflections. For both systems, once the deflections are known they are fed to the actuators which shall deflect the flaps in order to alleviate the loads

GLA and MLA Models

In order to build models that can quantify the load alleviation capabilities and feed additional loads into the structures model, Several assumptions were made like: gusts do not hit during manoeuvres and quasi-steady flow conditions.

The MLA model, for the 2.5g sizing loading case, deflects the most outboards flaps located at the last hinge line upwards by 11°. Since the load factor has to remain the same the inboard flaps shall have to deflect downwards in order to so the three most inboard segments have deflect by 10.5°. The effect on the torque load, due to these deflections is calculated using an equation from Theodorsen [12].

The GLA model requires a gust model in order to quantify its capabilities. This gust model was build following the regulations (CS.25), where the gust model that is specified remains a function of the factor H ranging from 30 to 350 ft. H is half of the distance of the gust and has thus an effect on its width but also on the strength of the gust. In order to quantify the response to the gust a SIMULINK model was build which requires several transfer functions. Equations describing the increase in lift due to gust and the increase in lift due to flap deflection were taken from Bisplinghoff and Theodorsen [13] [12]. With the physical limitations of the system: maximum flap deflection (β) and maximum flap deflection rate ($\dot{\beta}$), the equations written in the Laplace domain as transfer function and the gust model the GLA capabilities can be calculated. This was done for different gusts and the result showed that the sizing gust is when H equals 350 ft. For this sizing gust a load factor due to the gust of 1.9 was found which could be alleviated by the GLA system to a load factor of 1.3. Different than during manoeuvres not only the flaps induce additional torque load, but the gust themselves as well. The resulting lift distributions due to GLA and MLA are presented in Figure 4.

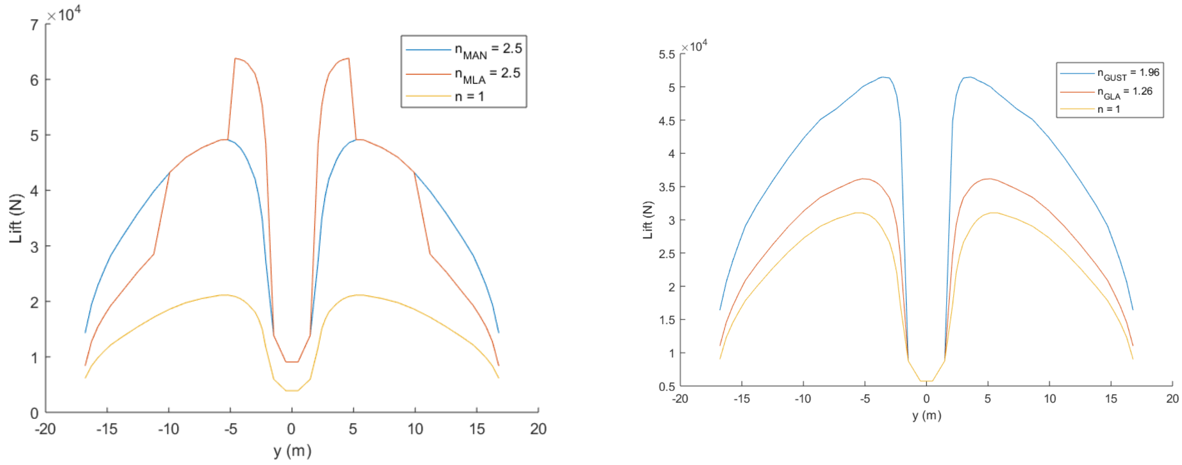

Figure 4: On the left: The lift distribution for 1g, 2.5g manoeuvre and 2.5g manoeuvre with MLA
On the right: The lift distributions for n =1, n = 1.96 due to a gust and n = 1.26 due to gust with GLA

MLW mass Analysis

In order to ensure structural integrity of the system, a structural model was set up. The model was tuned with corrections in order to replicate the benchmark A320 mass estimations as close as possible. In order to build the model several assumptions and limitations were use like limiting the analyses to normal stress, shear stress and internal torque. First the equations of motions were derived for the moment, shear stress and torque acting on the wingbox due to the external lift force and mass of the wingbox itself. Second a structural idealisation was made where each stringer and spar cap are represented by booms. For the stringer area an estimation equal to $328mm^2$ was found using stringer mass and dimensional information from the benchmark A320 [9]. Thirdly the stresses were calculated, starting with the normal stress (σ_n) due to the applied moment. The shear stress (τ) was calculated independently by calculating the shear flow first for both the shear force and torque. Afterwards the two were added together by superimposing in order to find τ. With that the Von Mises stress (σ_v) is calculated using Equation 1.

$$\sigma_v = \sqrt{\sigma_n^2 + \tau^2} \tag{1}$$

These calculations are performed for 24 different spanwise locations and for each cross section at 32 different locations. The resulting σ_v is than checked against the failure criteria. Which is defined by the yield stress of the material divided by 1.5, which for aluminium 6062 that is used for the entire wingbox, results in a failure criteria equal to $200Mpa$. The wingbox structures is than altered by changing the thickness and adding stringers were necessary until the ratio of the σ_v divided by the yield criteria is below one but the absolute difference is smaller than 5%.

From this analysis for the benchmark a discrepancy between the benchmark A320 wing structural mass and the calculated wing structural mass of 24.6% was found. Which is accounted for using a correction factor, the offset was expected due to the simplifications and limitations of the analysis used. The results of the analysis are displayed in Table 1 The loading case as experienced during manoeuvre is revealed to be critical and is thus leading in sizing of the structural parameters of the wingbox. With the MLA implemented a decrease of 18.3% structural mass with respect to Benchmark A320 was found.

Type	**Mass A320 [kg]**	**Mass MLA [kg]**	**Mass GLA [kg]**
- spars	1161.4	948.9	653.8
- stringers	418.8	342.1	234.5
- rib	6224.7	5085.3	3504.4
- skin	1240.9	1013.8	698.6
Total	9045.8	7390.1	5092
% A320	**100**	**81.7**	**56.3**

Table 1: Structural mass comparison of Benchmark A320 to MLW

Several verification & validation procedures where followed, using analytical checks and a finite element model (FEM) build using ABAQUS. A sensitivity analysis of the effect of GLA with changing load factor and of MLA for different locations of the centre of pressure was performed. For MLA it showed that the described deflections used for the 2.5g loading case, resulted in the least required wing structural mass, namely 7390 kg.

MTE Mass estimation

For estimating the mass of the structural components of the MTE, a finite element model (FEM) was build using ABAQUS. Where each of the components were checked to ensure the maximum stresses were below the critical σ_v.

The stringers of the MTE are sized according to the required deflections they have to undergo to cope with the bending moment of the wing. They are tapered, follow the dihedrial and sweep of the wing but are assumed to have a constant thickness along the span. Since with the minimum thickness of $1mm$ the stress on the stringers still showed large deviations compared to the σ_v, several holes were placed to save structural mass. The rib was modelled as a single integral part, which required all actuators to be locked. The rib closes to the root at the highest lift loading was analysed and the other ribs were assumed to size proportionally in mass to the TE chord. The skin reinforcement, was sized using the maximum flap deflections of 15 °. Finally the gap material was sized using the maximum deflection difference equal to 11 ° used for MLA. With the eight TE section, seven junctions using a Polydimethylsilioxan as gap material are required. The Polydimethylsilioxan is a rubber like material and has not been used in the aerospace industry so far, therefore a safety factor of two was used. The skin-coating, skin hinge-line re-information, skin-reinforcement, active ribs, stringers and gap material lead to a total mass of $188.1kg$.

In order to size the actuation system, the hinge moments calculated in the load alleviation chapter were used. The hinge moments for the first and second hinge line are lowered by using a gearbox system, which increases the mass of the wing and decreases the maximum deflection rates. However this is not considered as a problem since only the last hinge line is required to have a maximum deflection rate of 30 $°/s$. The estimated mass of the actuation system is estimated to be 824 kg.

HLFC Mass estimation

The mass estimation for the HLFC system is done by splitting it into three parts: (1) Suction surface, ducts and valves; (2) Control & Monitoring system; (3) Pump system & Power supply. Part (1) was calculated by taken into account each components and their respective mass, which resulted in a combined mass of $141kg$. The other two segments were sized using a reference design study on a B757 HLFC system [14]. In order to be able to use the output of this paper, the pump power of the HLFC was calculated to be $37.2kW$. Adding the components of all three parts a total HLFC mass of $287kg$ was found.

Wing Stability Analysis

Since, aeroelasticity as a phenomenon is the main source of instability of an aircraft, it is crucial to consider aeroelastic characteristics in aircraft structure design. To achieve this, a wing is modelled as 24 lumped mass-spring system. Each discretised section has three Degrees of Freedom (DOF) meaning that it is elastically restrained by linear springs in pitch (α), heave (h) and the rotation of morphing trailing edge (β). For the spring stiffness in three DOFs, the local stiffness parameters K_h and K_α are calculated using the material and structural properties, while K_β is approximated by scaling with respect to the experimental model developed by [15]. For illustration purposes a 2D wing section with deflected MTE is shown in Figure 5.

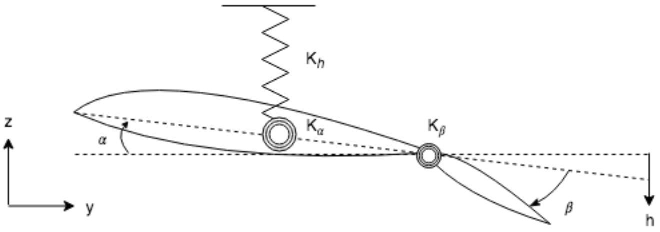

Figure 5: 2D wing section with deflected MTE

The governing equations of the wing model are aeroelastic equations of motion for the pitch-plunge aileron model with quasi-steady aerodynamics developed by Theodorsen [16]. The state matrix is derived, and this coupled aeroelastic model is used for the following analysis. In the modal analysis, self-excitation vibration of a wing is analysed to ensure that each DOF does not have the ability to be excited by a forcing resonance at the same frequency. The natural frequencies for the first four modes show that indeed all three natural frequencies are different.

According to the aeroelastic stability requirement of CS25.629, if there is any aeroelastic instabilities, the freestream velocity in flight where these instabilities occur should be higher than the defined V-n range by 15% [17]. The divergence and flutter were analysed. The flutter speed is identified to be $952 m/s$. And, the divergence does not occur until the divergence speed of $2201 m/s$. Since both are more than the required 15 % over the dive speed the MLW is considered aeroelestically stable. The numerical model is validated to an experimental aeroelastic model developed by Duke University aeroelastic group, with a discrepancy in flutter speed of 1.9% [15].

Financial Analysis

To determine the volume of the market for the MLW and to establish a competitive cost price, a market analysis is performed. This analysis is based on two business cases, the first is the retrofitting of the MLW to existing A320 aircraft and the second one is selling a new A320 aircraft with the MLW implemented right away. For the market analysis: the customers, market volume, market trends, competition & barriers, SWOT analysis and the foreseen market share are investigated.

The customers are divided into two categories: the airlines that own an A320 and are interested in retrofitting the A320 with MLW and those that are interested in buying a A320 with the MLW implemented. The market volume of selling new A320 aircraft is determined to be 3,434 billion USD up until 2037. Where for retrofitting the A320 taking the ROI, average aircraft age, development time and economy into account the market value is found to be 52.6 billion USD. Two trends are found in the single-aisle market, increase of range and increase of payload from which the first one is the most promising. Airbus and Boeing, where the latter is the biggest competitor and almost only competitor. The barriers for entering the market are small considering Airbus is well known and has its own different manufacturing lines. From the SWOT analysis two main conclusions can be drawn, many of the strengths of the MLW overlap with the current trends within the single-aisle aircraft market and the main disadvantage of the MLW is the increase in runway length which will limit the number of airports the A320 can land. The market share for the A320 is 54 % taking the runway length, development and production time into account a market value of 996.97 billion USD is expected up until 2037.

The production cost of both systems is determined by analysing both manufacturing cost and material cost. For the manufacturing cost the estimation technique from [18] is used. With this technique, it is possible to make an estimation for both the recurring and non-recurring cost of producing an aircraft structure. This is done by looking at the type and mass of the materials used. Next to the manufacturing cost, the material cost were analysed. The results from this analysis is shown for the HLFC and MTE in Table 2. With the values it was found that the A320 with MLW cost increase equalled to 1.9 %.

	Recurring [USD]	Non-recurring [USD]	Total Cost [USD]
Total Production Cost HLFC	566,000	93,000	**659,000**
Total Production Cost MTE	5,573,000	619,000	**6,574,000**

Table 2: Overview of recurring and non-recurring manufacturing cost for the HLFC and MTE

Using the fuel savings, increases in payload and the added production cost the time it takes to earn the cost of investment back (PBP) is 13 years. Also taken into account the development phase cost the ROI is estimated to be 8.6% in 2037.

Budget Breakdown and Resource Allocation

To ensure that the final wing design satisfies its specified requirements, a technique called Technical Performance Measurement (TPM) is applied. First the following TPM parameters were identified: mass, drag, payload and cost. These parameters come from an analysis of the customer requirements. Each parameter was individually analysed and all showed that the requirements were not violated, as an example the payload increase is 11.35 % which is above the minimal set 7.5 %. A cost breakdown structure of the total system was made were the analysis is mainly focused on the production cost. The importance of having such a breakdown structure of the complete system cost will allow to solve any cost budget related issues that arise during the later stages of the project more efficiently and strategically. The TPM parameters are used to setup the contingency allowance, which shows a decrease in percentage as the maturity increases.

Risk Analysis

The risks that the design is subjected to are ranked in both impact on the system and likelihood of occurrence. The risks are split up in two main categories: organisational risk and technical risk, the former was implemented during the project and the latter is further elaborated upon in this risk analysis. The risk events have been split up into: general risk, design & production risk and operational risk. An example of one of the general risks, is the risk to fail in increasing the flow laminarity. The risk mitigation technique consist out of revising and improving the HLFC to ensure the risk of not increasing in flow laminarity is minimised. The design & production risks are mainly governed by the implementation of the MTE and HLFC system. A example of an operational risk, is the risk of the MTE gust sensing system failing. As a risk mitigation technique a secondary gust sensing mechanism could be implemented, which would be able to take over the function if the primary system fails. With all risks before and after the implementation of the risk mitigation techniques two risk maps are drawn. The risk map with risk mitigation implemented shows that the risk of the HLFC and Krueger flap system not fitting in the leading edge and the Krueger flap under-performing for take-off/landing, as the highest and qualified as: “critical & likely".

RAMS

The reliability, availability, maintainability and safety of the MLW is analysed qualitatively. Reliability can be measure by the rate of non-occurrence of failure. For the reliability of the MLW it has to be concluded that due to both the MTE and HLFC systems are being novel technologies, the reliability shall be less compared to the legacy A320. The availability is defined as the ability for a system to stay in functioning state, which due to the similar reasons is expected to be less compared to the legacy A320. The maintainability is defined as the ease at which a system can be repaired, the conclusion is drawn that in terms of time and cost the MLW maintenance is increased. Safety is the ability of a system to not fail during its life cycle, mostly due to the increase in the number of actuators the MLW is less safe.

Sustainable Development Strategy

The sustainable development strategy is based on life cycle thinking and aims to reduce the negative impact upon the environment combining: social, environmental and economic factors. The life cycle phases are split up into: production phase, operations phase and end-of-life. During the production phase in order to satisfy the customer requirements, the wing is produced lead free using no toxic material and 95% of the mass is made up of non-recyclable materials. During the operations phase the MWL uses less fuel and the emission of greenhouse gasses is therefore reduced. For the end-of-life phase to be sustainable the process developed by Airbus together with other companies called the 'Process for Advanced Management of End-of-Life Aircraft' (PAMELA) shall be used [19].

The sustainability of the MLW compared to the benchmark was assessed using a tool called: CES EduPack Eco Audit. The tool is capable of calculating the CO_2 - footprint, bases on the different system components and their properties. A total of 16% decrease in CO_2 - footprint is found which is estimated to double at end-of-life when the fuel savings would also be incorporated.

Requirement Compliance Summary

A requirement compliance matrix shows all requirements, with their ID, specification, verification method and whether or not it is verified. Seven requirements have not been verified from which six required tests in order to verify those. The one that does not states: "The wing shall perform symmetric and asymmetric required maneuvers". Which was unfeasible to verify for the scope of this report taken the resource and time constraints into account.

Project Development Logic

Before describing the project development logic it should be noted that the assumption was made that additional resource would be available including a large engineering team, access to CFD/FEM software, testing facilities and budget for test aircraft setup. The first step towards developing this project further would be an additional design phase. During this phase more in depth analysis could be performed using complex tools, which would include virtual testing and computer aided design drawings to build models for wind tunnel tests. The wind tunnel tests shall provide validation data to ensure all analysis is done accurately and provide means for further optimisation of the MLW system. Afterwards, a prototype MLW A320 aircraft shall be subjected to varies in flight tests, to further validate the performance. With these data the HLFC and MTE system can be further fine-tuned for optimal performance. Lastly the production phase is entered, where the MLW is split up into three stages: component acquisition or production, wing assembly and aircraft integration. For effective project management a gantt chart describing the project development logic is made.

During standing aircraft have the highest incidence rates when looking at the time spend on ground, these operations shall therefore be focused on. Since at first the MLW is retrofitted to the legacy A320, several operations like: Check-in, Boarding, Cleaning, Catering and Cargo loading remain unchanged. However the MLW shall change the ground support and maintenance operations. For the de-icing process for example, the HLFC shall maintain operational since its anti-contamination system needs to keep working to protect the system. Another example is the visual inspection of the trailing edge, where now the entire span has to be checked and with the elastomer in place different failure models shall have to be checked for.

Conclusions and Recommendations

A new and innovative design has been created which shows great potential in both aerodynamic performance increase as well as load alleviation capabilities. The design is a MLW which utilises a combination of HLFC and a MTE. Analysis of the design loads shows that even after alleviating the manoeuvre loads, manoeuvres are still the critical design case with GLA implemented. The MLA shows a decrease in structural mass of 18.3 %. And the dynamic analysis showed that the design satisfies dynamic stability since it does not experience flutter or divergence within the MLW operation profile.

While not exceeding the A320 MTOW, the increase in mass due to implementing the HLFC and MTE structures minus the decrease in mass due to the fuel savings and structural mass savings from load alleviation equals a total payload increase of 2270 kg. Furthermore, the reduction in wing mass and fuel burn leads to a decrease in CO_2-footprint of 16 %. The payback time of retrofitting an MLW was shown to be seven years.

For the recommendations, several improvements could be made. Mostly regarding reducing the number of assumptions by increasing complexity. Which could be attainable with sufficient resources and and time available.

Contents

List of Abbreviations

List of Abbreviations	
ADIRU	Air Data Inertial Reference Unit
ADS-B	Automatic Dependent Surveillance—Broadcast
AoA	Angle of Attack
BIT	Built-in Tests
CDS	Cockpit Display System
CEO	Current Engine Option
CFD	Computational Fluid Dynamics
DOF	Degrees of Freedom
DSE	Design Synthesis Exercise
EMA	Electromechanical Actuator
FBD	Free-Body Diagram
FBS	Functional Breakdown Structure
FEM	Finite-Element Method
GLA	Gust Load Alleviation
GUI	Graphical User Interface
HLFC	Hybrid Laminar Flow Control
HMS(CMS)	Health Management System
IMA	Integrated Modular Avionics
IP	Intellectual Property
LCC	Life Cycle Cost
LRU	Line Replacement Unit
MDOF	Multiple Degree-Of-Freedom
MLA	Manoeuvre Load Alleviation
MLW	Morphing Laminar Wing
MTE	Morphing Trailing Edge
MTOW	Maximum Take-Off Weight
MTS	Movable Top Skin
OEM	Original Equipment Manufacturer
PAMELA	Process for Advanced Management of End-of-Life Aircraft
PBP	Payback Period
POF	Phases of Flight
R&D	Research & Development
RAMS	Reliability, Availability, Maintainability, Safety
RoI	Return on Investment
RPK	Revenue Passenger Kilometres
SMA	Shape Memory Alloy
SWOT	Strength, Weakness, Opportunity, Threats
TLR	Top-Level Requirement
TPM	Technical Performance Measurement
USD	U.S. Dollar
VC	Variable Chamber
VLM	Vortex Lattice Method

1

Introduction and Project Objectives

After over a hundred years of continuous development, most aeronautics engineers agree that the conventional wing-and-tube aircraft configuration is approaching the capacity limits of its performance. However, due to increasing fuel costs and market competition, the aviation industry is challenged to continue pushing the aircraft design to even higher performance levels. In order to achieve that, the engineers need to take a more global view on how the aircraft can be improved with the modern technological advancements. This Design Synthesis Exercise aims to contribute to that mission by pursuing the following Project Objective Statement:

Design an aircraft wing that uses autonomous control for continuous optimisation of its wing configuration to outperform an Airbus A320-like aircraft wing while still complying with the desired aircraft dynamic behaviour with ten people in ten weeks.

This objective will be achieved by implementing design features that enable the wing to autonomously optimise its configuration in-flight for minimum drag as well as create means for gust and manoeuvre load alleviation. In addition, flow laminarity over the wing will be increased in further attempt to decrease the total aircraft drag. These performance enhancing features will be exploited in improving airline operating profits due to the reduced fuel consumption, lowered carbon footprint and additional payload capacity.

This report contains the analysis, that an engineering team of ten students conducted in ten weeks to achieve the best possible wing design. The document starts with a preliminary design chapter (chapter 2), which describes the first stages of the project and in particular the procedures behind determining the system level requirements and choosing the most promising concept. This is followed by an extensive description of the chosen concept in chapter 3, where the design is explained in a terms of wing's sub-component architectural properties. The report then takes a turn into a detailed engineering analysis of the concept in terms of aerodynamics (chapter 4), load alleviation capabilities (chapter 5), mass analysis (chapter 6) and wing stability analysis (chapter 7). After that, the analysis takes a product-based shape starting with financial analysis in chapter 8 and budget breakdown in chapter 9. Furthermore, technical risk analysis and sustainable development strategy studies are provided in chapter 10 and chapter 11. The report proceeds with a requirement compliance summary in chapter 12 and a logic of further project development (chapter 13). Conclusions and recommendations are given in chapter 14 and finally the project management and system engineering applications is presented in Appendix A.

2

Preliminary Design

In this chapter, the process up to the detailed design phase will be described. Firstly, the preliminary design starts with the functional analysis of the wing, given in section 2.1, and is followed by a system-level requirement analysis in section 2.2. After that, concept development for the wing is presented in section 2.3, describing three main architectures that were created. These concepts are then traded-off (section 2.4) and the final concept, that enters further analysis stage, is defined (section 2.5).

2.1. Functional Analysis

Before the development of concepts could be started, it was necessary to know the functions the wing has to perform and the requirements the design has to fulfil. To fulfil that purpose, a functional analysis and a requirement analysis have been performed. The starting point for the functional analysis was the design assignment provided by the customer. The functions that were identified were combined in a Functional Breakdown Structure (FBS), shown in Figure 2.1 up to Figure 2.4. There are five blocks of functions : interface functions, aerodynamics and performance, structural load bearing, sensing and control and other operational functions.

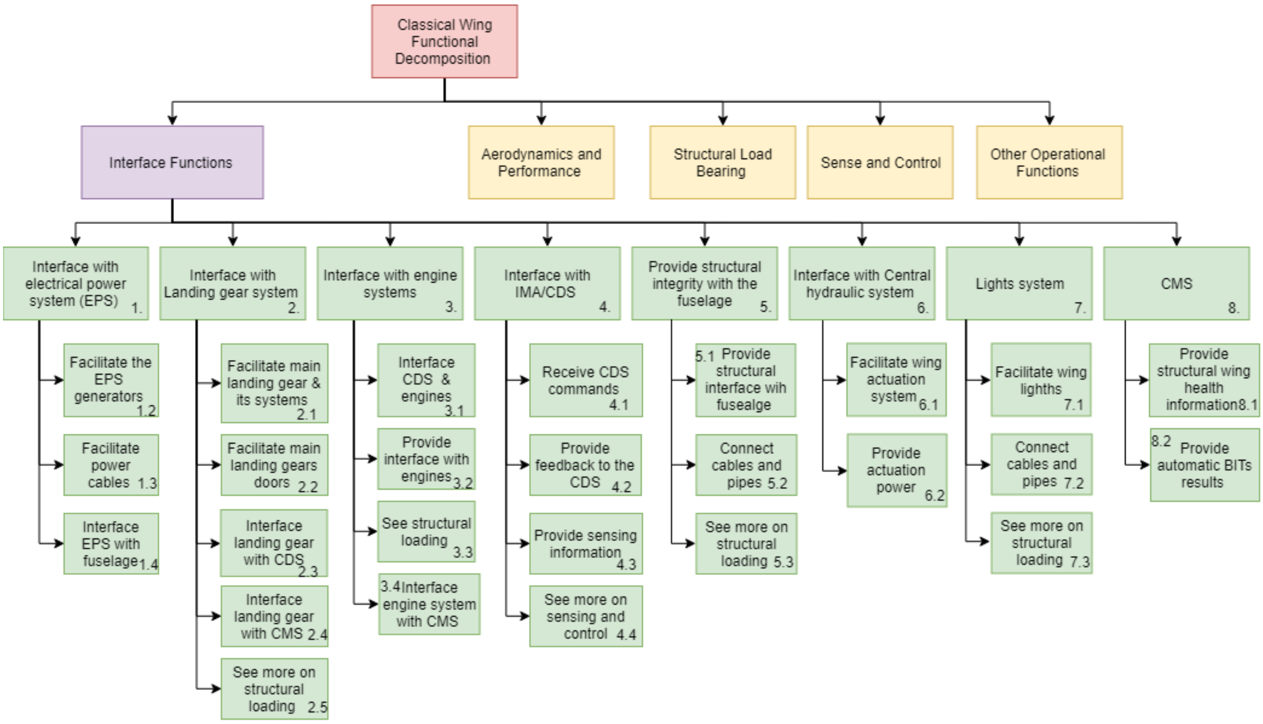

Figure 2.1: Functional breakdown diagram - Interface Functions

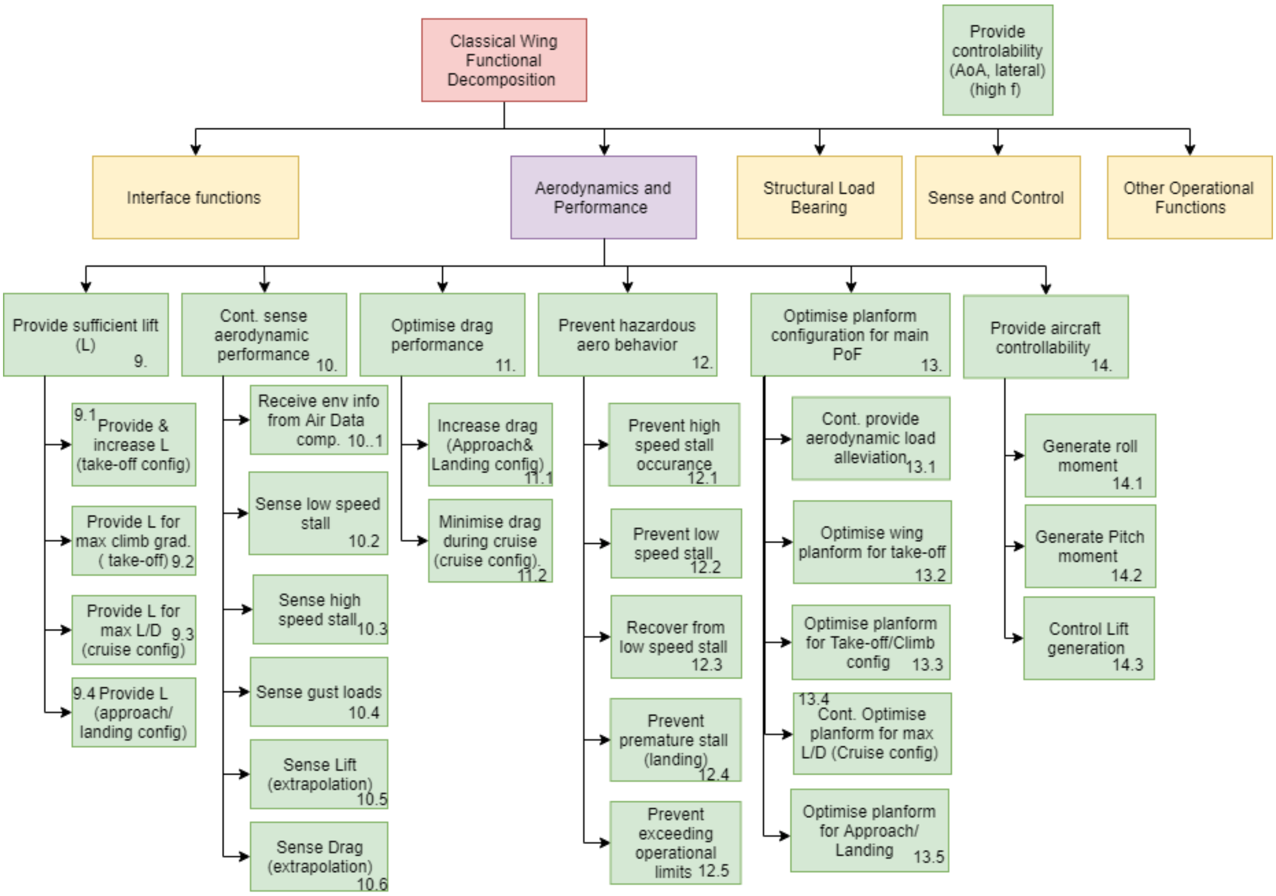

Figure 2.2: Functional breakdown diagram - Aerodynamics and Performance

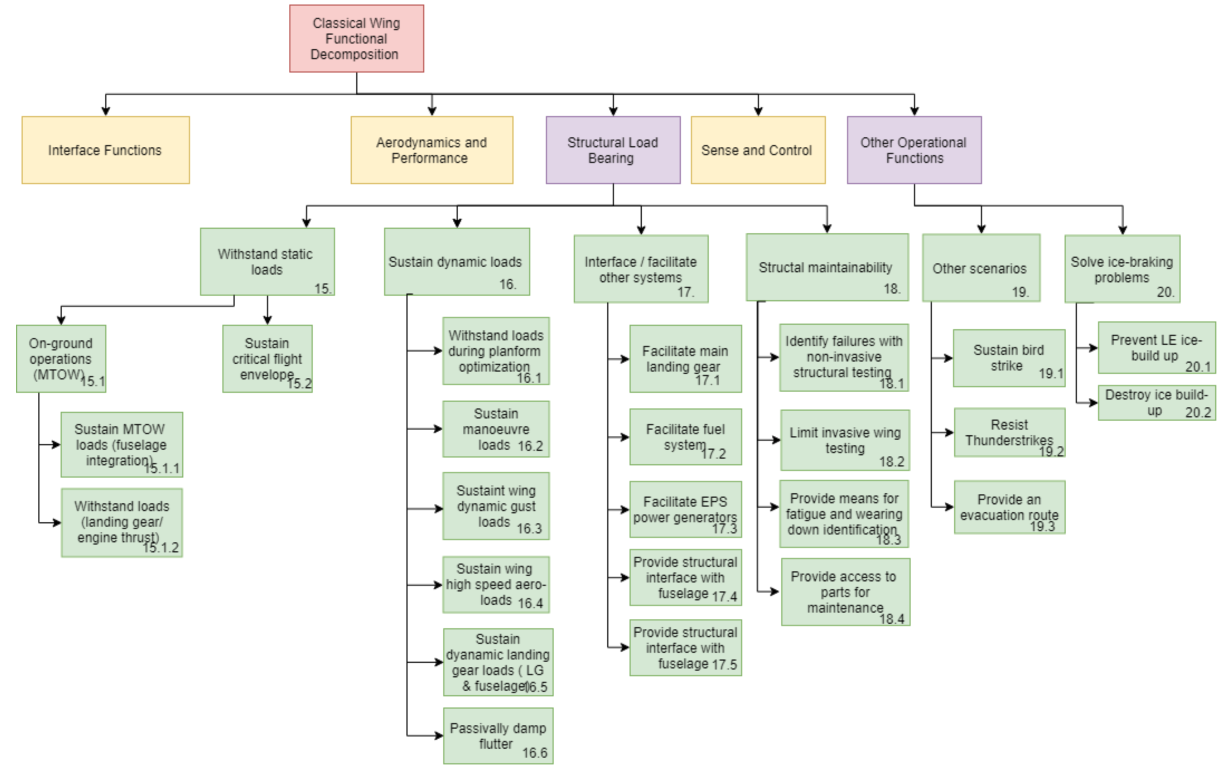

Figure 2.3: Functional breakdown diagram - Structural load bearing and other operational functions and constraints

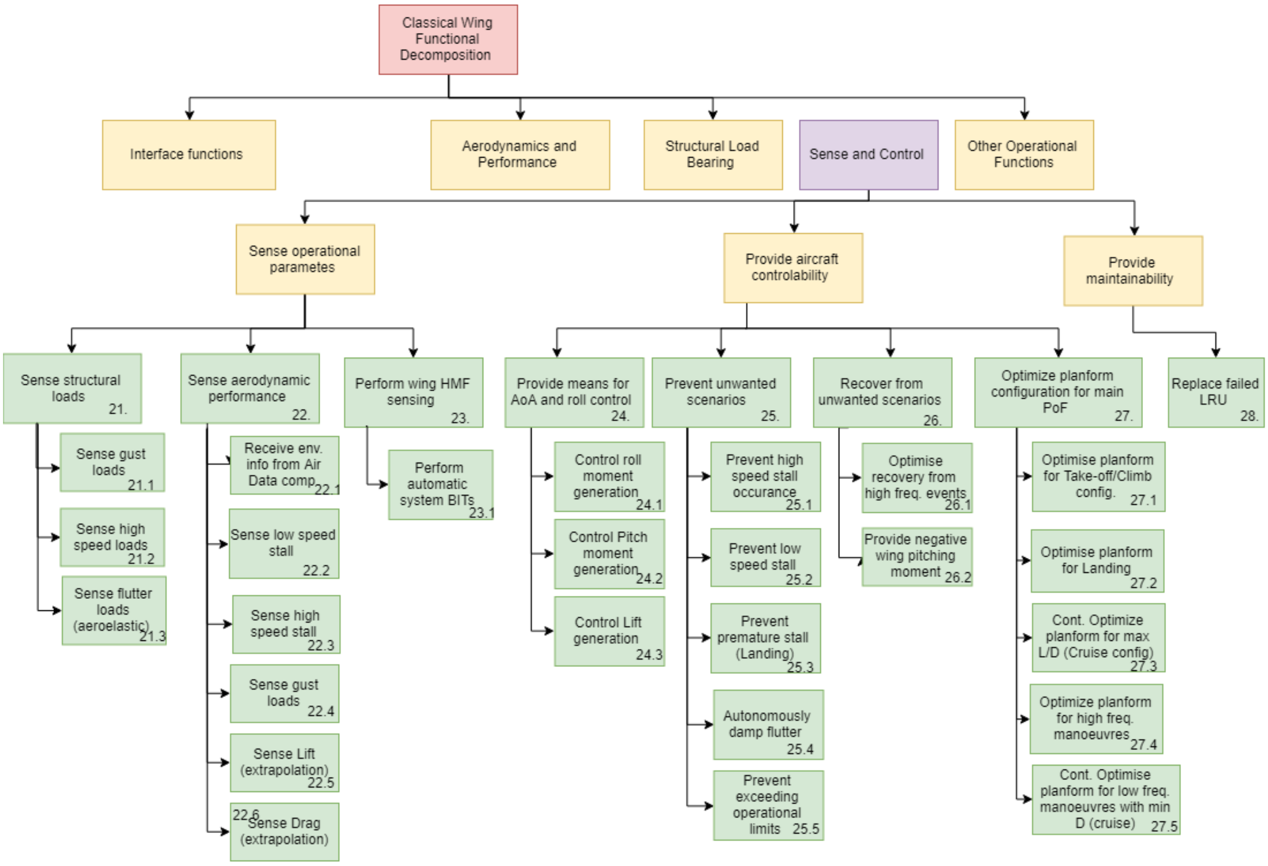

Figure 2.4: Functional breakdown diagram - Sensing and Control

2.2. Analysis of Requirements

The main objectives that this project aims to achieve come from the stakeholders - they indicate what needs they have but not how they should be achieved. This makes up the stakeholder requirements, described in the section below. Also, once the wing functions are established, the system-level requirements can be generated and are also provided in this section.

2.2.1. Stakeholder Requirements

Stakeholder requirements, provided by the customer and identified during stakeholder analysis is presented below.

MLW-CuSh-001 The wing shall autonomously change its planform during flight

MLW-CuSh-002 The wing shall autonomously optimise its aerodynamic drag performance during flight

MLW-CuSh-003 The wing shall provide means for flight dynamic controls

MLW-CuSh-004 The wing shall provide automatic manoeuvre load alleviation

MLW-CuSh-005 The wing shall provide automatic gust load alleviation

MLW-CuSh-006 The wing shall result in drag reduction of 7.5% throughout the entire flight with respect to Airbus A320 legacy wing

MLW-CuSh-007 The wing shall result in payload increase of 7.5% with respect to A320ceo

MLW-CuSh-008 Application of new actuators and sensors shall have the same reliability as compared to existing actuators and sensors

MLW-CuSh-009 Any smart materials used in production of the wing shall be lead free

MLW-CuSh-010 The wing shall have means to measure laminarity of the flow around itself

MLW-CuSh-011 The wing shall have larger laminar flow region than A320 wings

MLW-CuSh-012 The mass of the wing shall not exceed the mass of the A320 wings

MLW-CuSh-013 The cost of the wing shall not exceed 103% of the A320 wing cost

MLW-CuSh-014 The lifetime cost of the aircraft shall not exceed lifetime cost of the benchmark A320

MLW-PiSh-001 The wing shall have the same control capabilities as the wing of an A320ceo

MLW-ReSh-001 The wing shall comply with certification specifications of Subpart C, CS25

MLW-HuSh-001 The wing shall contain no more than 5% mass non-recyclable materials

MLW-HuSh-002 The wing shall be made of only non-toxic materials

2.2.2. System Level Requirements

With the functions that the wing has to perform defined, the requirements that the wing has to fulfil could be investigated and determined. Some requirements followed directly from the design assignment provided by the customer. Other requirements were defined as a result of the functional analysis. The following list of requirements was obtained.

Table 2.1: System Level Requirements

ID	Requirement Specification	Rationale	Traceability	Verification method
MLW-Sys-000	The wing shall reduce drag with 7.5% throughout the entire flight with respect to Airbus A320 legacy wing.	Customer requirement	MLW-CuSh-006	Analysis: a complete chapter 4 is dedicated to verification of this requirement

MLW-Sys-001	The wing shall provide sufficient lift during each flight phase, as defined in "A320 Flight Envelop" document.	Providing Lift is the main function of the wing	Mission Need Statement, MLW-CuSh-007, Function 3.3.2b	Analysis: chapter 4
MLW-Sys-003	The wing shall continuously sense approaching gusts at least 300ms before they hit the leading edge of the wing		MLW-CuSh-005, Function 3.5.3b	Design Review: section 5.1 demonstrates design of a sensor layout which enables to sense upcoming gusts
MLW-Sys-004	(GLA) The wing shall autonomously alleviate loads due to gusts, described by model in subsection 5.3.1, and gust induced load factors shall not exceed 1.3		MLW-CuSh-005	Analysis: chapter 5
MLW-Sys-005	(MLA) The wing shall autonomously update lift distribution during symmetric manoeuvres to decrease bending moment at the root by at least 14.5%		MLW-CuSh-004	Analysis: chapter 5 and chapter 6
MLW-Sys-008	The wing shall generate sufficient roll moment to perform 45° in 1.4s			Analysis
MLW-Sys-009	The wing shall autonomously optimise its shape during flight for minimal drag		MLW-CuSh-001, MLW-CuSh-002	Design Review: chapter 3
MLW-Sys-010	The wing shall perform asymmetric required manoeuvres.		Functional	Analysis: chapter 3
MLW-Sys-011	The wing shall withstand limit loads, as defined in chapter 6, without permanent deformation	Structural requirements, as provided by CS25, Subpart C are given in terms of: • *limit load* — maximum load, expected during the operational cycle • *ultimate load* — limit load multiplied by Factor of Safety (FS=1.5)	MLW-ReSh-001	Analysis: chapter 6
MLW-Sys-012	The wing shall withstand limit loads without local stresses exceeding yield stress as defined in chapter 6 to be 200MPa,		MLW-ReSh-001	Analysis: chapter 6

MLW-Sys-013	The Wing shall withstand ultimate loads without failure for 3 seconds, as defined in "Operational loads" document		MLW-ReSh-001	Test: this is certification requirement, which will be verified through a test set
MLW-Sys-014	The Wing shall withstand birdstrike of 4lb bird at a sea level V_c or $0.85V_c$ at 2438 m.		CS25.631	Test: this is certification requirement, which will be verified through a test set
MLW-Sys-015	The wing shall function with the Hybrid Laminar Flow Control system (HLFC) inoperative	Risk OP05 (chapter 10) mitigation: Wing shall be reliable enough to function without HLFC system at all		Demonstration: chapter 4
MLW-Sys-016	The wing shall be free from these aeroelastic instabilities: flutter and divergence - below the 1.15% of the maximum flight envelope velocity.	Based on the aeroelastic stability requirements of CS 25.629	MLW-ReSh-001	Analysis: section 7.4
MLW-Sys-017	The wing shall result in payload increase of 7.5% with respect to A320		MLW-CuSh-007	Analysis: section 6.4
MLW-Sys-018	The cost of the wing shall not exceed 103% of the A320 wing cost		MLW-CuSh-013	Analysis: section 8.2
MLW-Sys-019	The mass of the wing shall exceed the mass of the A320 benchmark wing		MLW-CuSh-012	Analysis: section 6.4
MLW-Sys-020	The wing shall perform required symmetric manoeuvres		Functionality	Analysis: chapter 4
MLW-Sys-021	The LCC of the wing shall not exceed A320 benchmark wing LCC		MLW-CuSh-014	Analysis: section 11.1

Requirements MLW-CuSh-006,-007,-004 and -005 were identified as driving requirements, since they directly lead to more efficient flight and increased operating revenue. The potential killer requirements, which could lead to not being able to create a feasible design, were identified to be MLW-CuSh-013 and the combination of MLW-CuSh-007 and -012.

2.3. Concept Development

With the functions and requirements known, the next step in the design, the concept development, could be started. In a brainstorming session, many ideas were generated that could possibly aid in creating a design that would meet the requirements. After the brainstorm, a feasibility check on the generated ideas was performed. Ideas that were determined to be unfeasible, for example because of time constraints or immature technologies, were disposed. With the ideas that remained, eight different design concepts were generated. Once again, a feasibility analysis was performed which resulted in the selection of three promising design concepts. These three concepts have been analysed in greater detail. An overview of this analysis will be presented next.

2.3.1. Concept 1: Morphing Trailing Edge

The Morphing Trailing Edge (MTE) concept features morphing flap sections covering the complete wingspan. The system consists of eight sections that can move independently. To eliminate gaps, an elastomer is applied between the section boundaries. Furthermore, every flap consists of three hinge-lines, which allow for precise altering of the airfoil shape. This creates a possibility to have better control of the aircraft dynamics as well as an option to create load alleviation capability. A visualisation of the MTE design is presented in Figure 2.5.

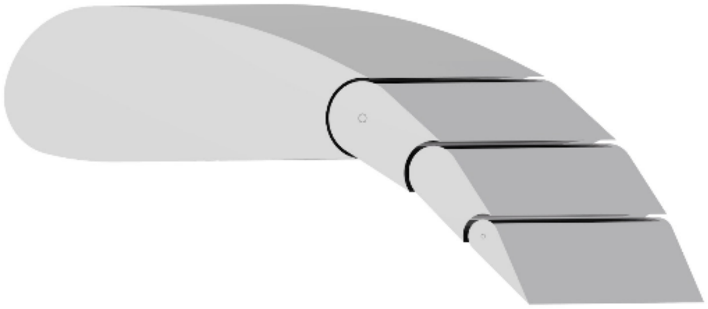

Figure 2.5: MTE design concept

Flap actuation is done by means of electromechanical actuators (EMA's). The MTE system is estimated to have a total mass of 1200 kg, which is an increase of 240 kg compared to the benchmark aircraft. In terms of drag, analysis showed that the MTE design offers a drag decrease of 7.9% compared to the benchmark. This accounts for both the decrease in viscous drag due to not having gaps or flap track fairings and the drag decrease obtained from in-flight wing shape optimisation, which is possible due to the flaps covering the whole wingspan. The total production cost for the MTE design was estimated at 6.574 million US Dollar (USD), compared to 5.555 million USD for the benchmark. The main advantages of the MTE design are:

- Extensive control of airfoil shape
- High potential for loads alleviation
- Reduction of viscous drag due to elimination of gaps, flap track fairings

and the main disadvantage is:

- System complexity due to the number of actuators

2.3.2. Concept 2: Movable Top Skin

The second concept is a wing design with a Movable Top Skin (MTS). Moving the top skin allows to change the thickness of the airfoil, which has an effect on the location of the transition point. Drag can be reduced by changing this location. In order to move the top skin, a Shape Memory Alloy (SMA) actuation system was selected. The MTS design is estimated to add a mass of 982 kg to the wing mass and increase the wing production cost by 3.214 million USD. Analysis of aerodynamic performance showed that the MTS design would result in a drag reduction of only 0.17%. Figure 2.6 shows a visualisation of the MTS design.

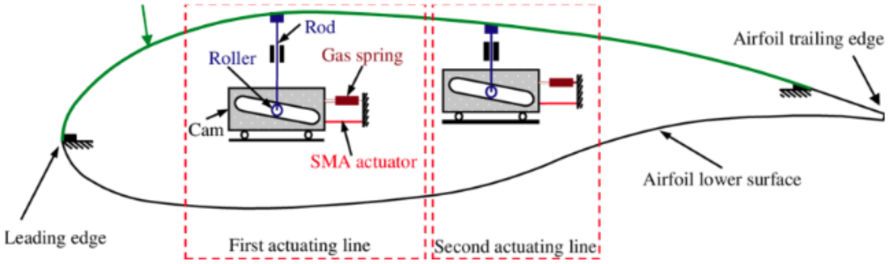

Figure 2.6: MTS design concept

The main advantage of the MTS design is:

- Potential for increase in flow laminarity

and the main disadvantages are:

- High added cost and mass
- Bad fatigue characteristics of SMA actuators
- Analysis shows only a slight drag reduction

2.3.3. Concept 3: Hybrid Laminar Flow Control

The third concept employs a Hybrid Laminar Flow Control (HLFC) system. The goal of the HLFC system is to decrease skin friction drag by postponing transition from laminar to turbulent boundary region. This is achieved by combining (hence, called “hybrid”) laminar flow airfoils, resulting in prolonged favourable pressure gradient, with a suction system on the leading edge of the wing. The lower portion of the boundary layer is sucked in to postpone transition. This suction is driven by a pump and the required pressure is generated through a set of pipes and chambers. The leading edge of the wing, where the suction takes place, is made of a perforated titanium skin. To protect the holes from contamination and to account for the fact that the HLFC system is incompatible with a regular slat, a variable chamber Krueger flap is designed for the leading edge. A CATIA render showing the pipes of the HLFC system is presented in Figure 2.7.

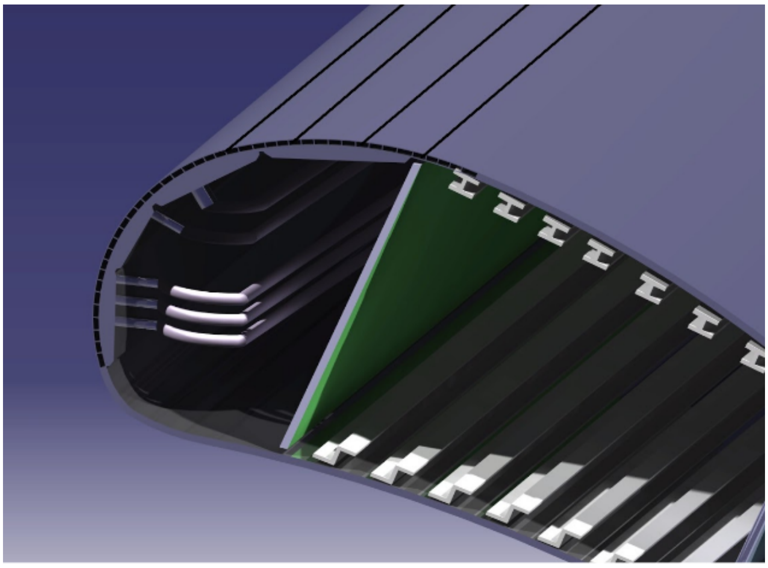

Figure 2.7: CATIA render of HLFC system

The tool that was developed for aerodynamic analysis is not able to account for the effect of the HLFC system. Therefore, the HLFC system was analysed independently, as described in subsection 4.4.1, and showed a possible total aircraft drag reduction of 3.5%. This resulted in a HLFC system that requires $12m^2$ of suction surface per wing, which means suction should be applied on the outboard part of the wing up to a meter before the wing tip. This system would add an estimated 285 kg to the wing mass and 0.66 million USD production cost.

The main advantages of the HLFC design are:

- Capabilities for significant drag reduction
- Laminar flow region increase

and the main disadvantages are:

- Incompatible with conventional A320 slat design
- Sensitive to leading edge contamination
- Added complexity leads to increased maintenance requirements

2.4. Trade-off

After the concept analysis was completed, a trade-off was performed to see which of the concepts would be suited best to meet the requirements. However, before the trade-off could be done, it was essential to define relevant trade-off criteria and their weight indicating their importance. Most trade-off criteria are based on the stakeholder requirements defined earlier. An overview of the selected trade-off criteria can be found in Table 2.2.

High-level trade-off criterion	**Lower level trade-off criterion**	**Source**
Performance	System mass	MLW-CuSH-012
	Drag reduction	MLW-CuSH-001, MLW-CuSH-002, MLW-CuSH-006
	Contribution to loads alleviation	MLW-CuSH-004, MLW-CuSH-005
	Effect on laminar flow region	MLW-CuSH-011
System Cost	System Cost	MLW-CuSH-013
RAMS characteristics	Reliability	MLW-CuSh-008
	Availability	
	Maintainability	
	Safety	
Compatibility	Compatibility	Constr.-004
Sustainability	Sustainability	MLW-CuSH-009, MLW-HuSH-001, MLW-HuSW-002
Complexity	Complexity	
Technology readiness level	Technology readiness level	Constr.-002

Table 2.2: Overview of trade-off criteria, combined with the relevant requirements (if applicable)

The next step was trade-off execution. Criteria for which numerical values were available were given a score based on these numerical values. The best performing concept obtained a score of five points; four remaining points were divided over the other two concepts, scaled with their numerical performance values. This scaling is the reason that some criteria have scorings with a decimal place. For the criteria for which quantification was not possible within the project resources, guidelines were set up to allow for fair scoring.

First, the lower level trade-offs were performed, the result of which is presented in Table 2.4 and Table 2.5. The total score of the lower level trade-off was used as score for the respective criterion in the high-level trade-off. The high-level trade-off is shown in Table 2.6. To aid in visual interpretation of the trade-off, a colouring scheme is used, shown in Table 2.3.

Colour [score range]	[1.0-1.9]	[2.0-2.9]	[3.0-3.9]	[4.0-5.0]

Table 2.3: Colour indication for scores

System Criterion	System mass [0.3]	Drag reduction [0.5]	Contribution to loads alleviation [0.1]	Effect on laminar flow region [0.1]	**Total score**
MTE	5	3.9	5	3	3.7
MTS	1.4	0.1	3	4	1.1
HLFC	2.6	5	3	5	2.7

Table 2.4: Performance trade-off

System Criterion	Reliability [0.25]	Availability [0.25]	Maintainability [0.25]	Safety [0.25]	**Total score**
MTE	2	3	2	2	2.3
MTS	3	2	3	3	2.8
HLFC	4	2	3	4	3.3

Table 2.5: RAMS trade-off

System Criterion	Performance [0.5]	System cost [0.1]	RAMS [0.2]	Compatibility [0.05]	Sustainability [0.05]	Complexity [0.05]	TRL [0.25]	**Total score**
MTE	3.7	3.0	2.3	5	3	2	3	3.2
MTS	1.1	1.0	2.8	2	3	3	2	1.7
HLFC	2.7	5.0	3.3	3	4	4	3	3.2

Table 2.6: High-level trade-off

Finally, a sensitivity analysis on changing the weight of a criterion was performed. This was done by varying a criterion weight from zero to one and changing the weight of the other criteria such that, whilst keeping their weights relative to each other the same, all the criteria weights still add up to one. This sensitivity analysis showed that, if the weight of one criterion is changed, either the MTE design or the HLFC design would always win the trade-off.

2.5. Trade-off Outcome

The trade-off resulted in the MTE design and the HLFC design receiving the same total score. This left two choices: either select one of the designs or combine both designs into one. The advantage of selecting only one design is that it would allow more resources to be spent on that design, enabling a more detailed analysis. The risk of this approach, however, is that analysis would show that the design would not be able to meet the requirements.

The decision was made to move forward with both the MTE design and the HLFC design. Since one design affects the leading edge and the other the trailing edge, little interference between the systems is expected. A CATIA render of the final design configuration is shown in Figure 2.8 and Figure 2.9. It was decided to name this new concept as Morphing Laminar Wing (MLW), due to its capability to morph as well as increase the laminarity of flow over the wing. In the final design phase, the detailed design, the MLW was analysed and worked out in more detail. The remainder of this report is dedicated to the approach and results of the detailed design phase.

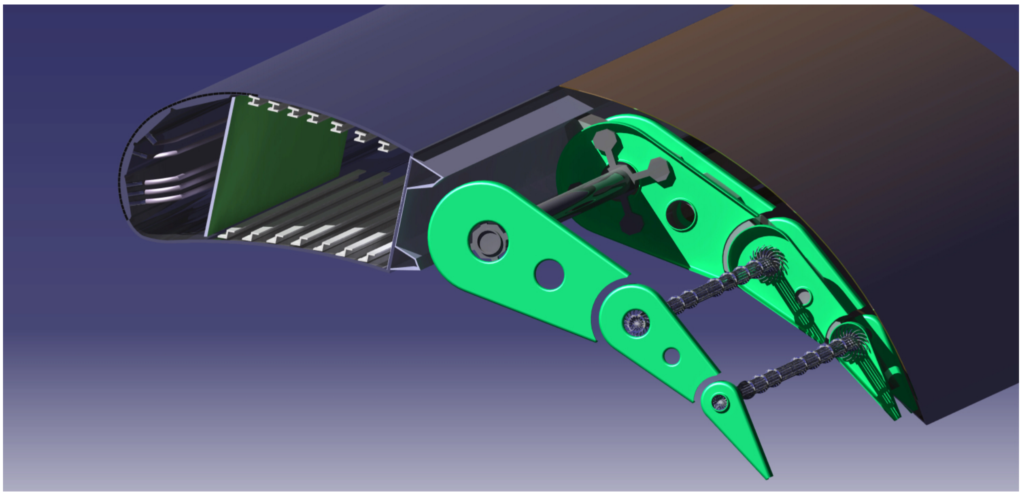

Figure 2.8: CATIA render of the Morphing Laminar Wing section (not to scale)

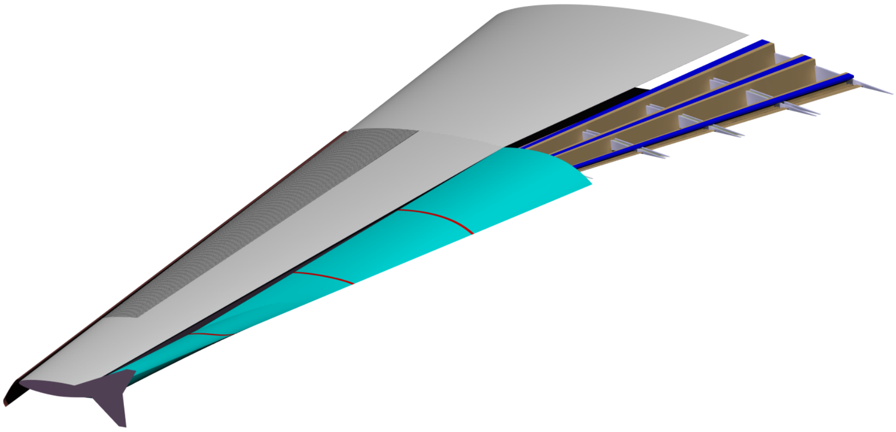

Figure 2.9: KEYSHOT render of the complete, scaled MLW model from CATIA. HLFC can be seen to be placed under the darker sheet material on the outboard section of the wing. MTE covers the entire trailing edge and the inboard TE skin has been cut out to show internal components

3

Morphing Laminar Wing Description

The final configuration which moves into the detailed design phase can be described as a retrofit A320 wing to which both a HLFC system as well as the MTE are implemented, allowing for continuous aerodynamic performance optimisation and high load alleviation potential. In this chapter the working principles and architecture of the MLW are explained by first explaining its main subsystems, which are the MTE (section 3.1 to section 3.3) and HLFC (section 3.4 to section 3.8), followed by the overall wing description (section 3.9).

3.1. MTE General Introduction

Performance increase of aviation technologies has been experiencing stagnation over the last decades due to limitations in optimisation of wing planform and airfoil selection. Implementing a continuous morphing trailing edge to conventional airfoils allows for optimisation in airfoil shape over the entire flight envelope, bypassing limitations generated by having to select a single airfoil shape for the entirety of the mission. From the morphing capabilities two main advantages of the system can be extracted: shape optimisation for drag reduction in all flight stages and active load alleviation as a result of variation in deflection setting for the different flap sections across the span. This technology, as inspired by [20], is implemented on the MLW and a render is shown in Figure 3.1.

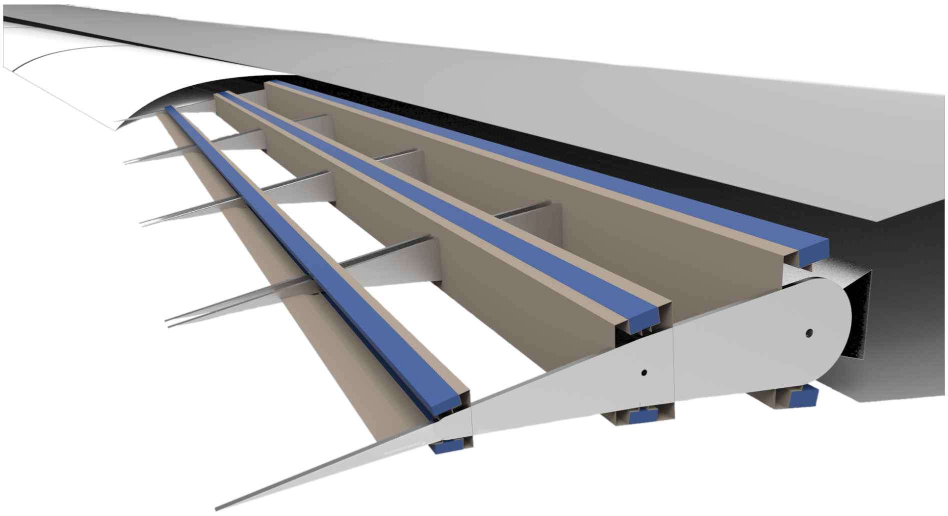

Figure 3.1: Render of the MTE

3.1.1. Extent of Implementation

The MTE replaces all control surfaces located on the trailing edge of benchmark A320 and completely takes over the functionality of these systems, this allows the MTE to be attached to the rear spar of the wingbox. From this attachment three equally spaced sections, utilising individual hinge line actuation, are placed along the chord, allowing for great variation in local airfoil shape. Spanwise, the MTE employs two main systems: inboard and outboard flap systems, both consisting of four equally spaced flap segments connected by a high strain material allowing for difference in deflection between two flap segments while preserving continuity over the span. The inboard flap system has as main function generation of high lift during take-off and landing while the outboard section provides control for manoeuvres and optimisation of airfoil shape during cruise. Both flap systems are used for active load alleviation for both manoeuvres and gust. The extend of implementation of MTE can be visualised in Figure 3.2. For a more detailed view, the flap locations are summarised in Table 3.1. The y-location is the spanwise distance from the aircraft fuselage and includes the connection material between different flaps. The location of the hinge-line is expressed as a percentage of the local chord length.

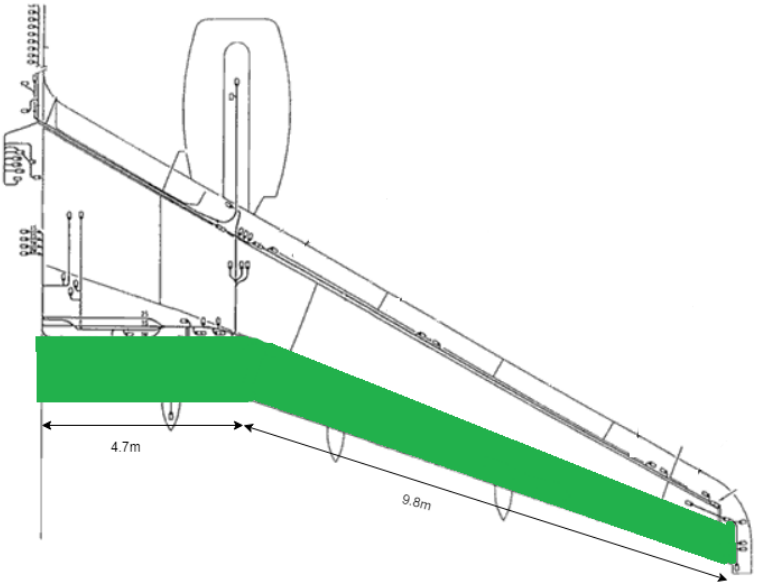

Figure 3.2: Implementation MTE on wing both inboard and outboard system. Wing drawing from [9]

Section	y-location [m]	Segment 1 [x/c]	Segment 2 [x/c]	Segment 3 [x/c]
Inboard				
1	0-1.75	0.64-0.76	0.76-0.88	0.88-1.00
2	1.75-2.35	0.66-0.77	0.77-0.88	0.88-1.00
3	2.35-3.52	0.68-0.79	0.79-0.89	0.89-1.00
4	3.52-4.70	0.74-0.83	0.83-0.91	0.91-1.00
Outboard				
1	4.70-7.15	0.74-0.83	0.83-0.91	0.91-1.00
2	7.15-9.60	0.73-0.82	0.82-0.91	0.91-1.00
3	9.6-12.05	0.73-0.83	0.83-0.91	0.91-1.00
4	12.05-14.50	0.71-0.81	0.81-0.90	0.90-1.00

Table 3.1: Geometrical layout for the MTE

3.2. MTE Architecture

The MTE hardware breakdown diagram is displayed in Figure 3.3. Each component of the system is explained in more detail below.

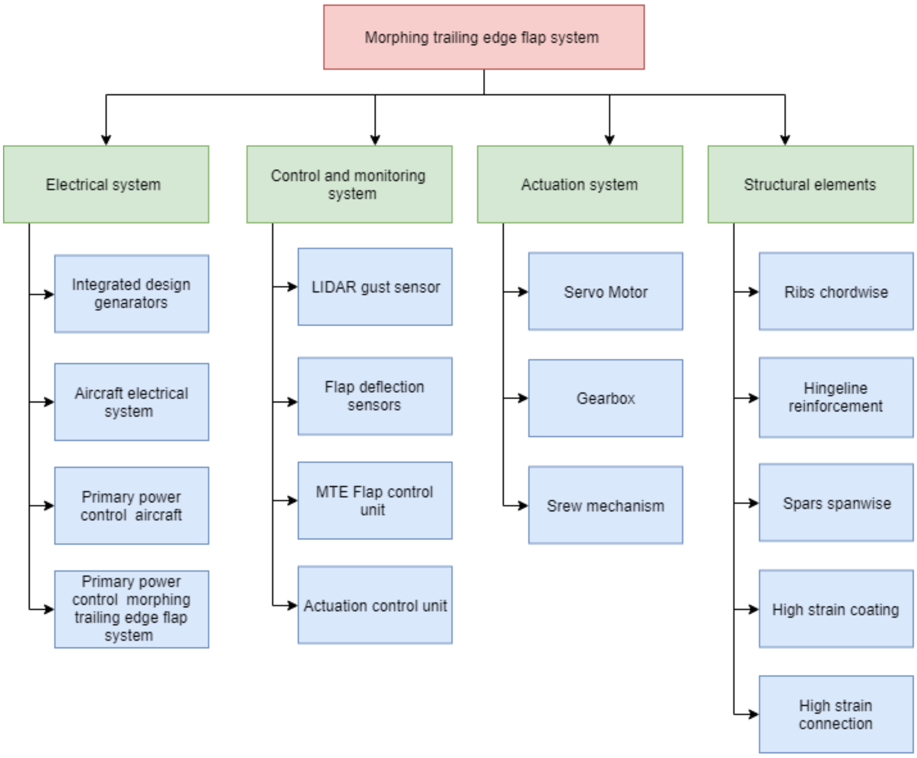

Figure 3.3: Hardware breakdown MTE

3.2.1. Electrical System

The electrical system controls and distributes all electrical power as required by the different components of MTE. The main power source is the aircraft electrical system which generates electricity from integrated design generators. This electrical power is distributed by the primary power control unit of the aircraft to the primary power control system of the MTE. From there, all electrical power is distributed among the control systems, sensing systems and actuation systems.

3.2.2. Control and Monitoring System

In order for the MTE to perform optimal, a control and monitoring system is implemented which controls deflection settings of all flap segments over all flight stages. The MTE is used for two main purposes, which are shape optimisation for optimal aerodynamic performance and load alleviation for both gust and manoeuvre. Both functions require different deflection settings, these deflections are determined by the MTE control unit which uses the sensing systems to gather information. These deflections are given as an output to the actuator control unit which steers all actuation systems. The actual deflection settings are then fed back to the MTE control unit.

Figure 3.4 presents the working mechanism of the MTE control system in the form of a software diagram. The control system prioritises the required deflection settings for the different functions of the MTE. The pilot input is given the highest priority, this input captures all manoeuvres for which the Manoeuvre Load Alleviation (MLA) system is activated. Secondly, the Gust Load Alleviation (GLA) control system takes priority alleviating any gust loads as experienced in flight. Finally, the MTE is deflected for optimal aerodynamic performance for the current flight condition. The MTE control unit then feeds the deflection settings with the highest priority to the actuation control unit, deflecting the sections of the MTE such that the required shape is obtained. The deflection settings are constantly monitored and fed back to the MTE control unit.

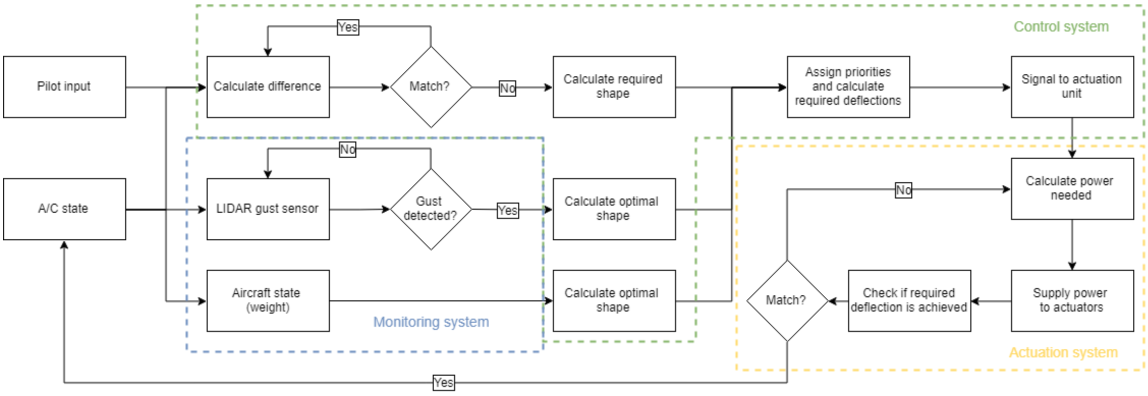

Figure 3.4: Software diagram MTE

3.2.3. Actuation System

The MTE requires an extensive actuation system allowing for variation in deflection settings along both the span and chord. Eight flap segments, consisting out of three separate hinge lines all require individual actuation. Each individual hinge line is fitted with a rotary electromechanical actuation system. This system consists of a servo motor, gearbox and screw mechanism converting deflection requirements as input to physical deflection of the individual flaps.

3.2.4. Structural Parameters

For both the inboard and outboard flap systems each flap segment is build up in similar manner. Two chord wise ribs are placed on the start and end of each flap segment. These ribs are composed of three parts, each section starting at the respective hinge-actuation line which acts as the connection between the different parts of the ribs. The material used to create the ribs is 6062-aluminium alloy, which has been widely applied in the aerospace industry[1]. The chord-wise ribs act as a connection point for the span-wise skin. This skin must accommodate for the high strain as it is experienced by the morphing system, with emphasis on the hinge lines. In response to this constraint, the skin is made of three main components: A high-strain material coating, u-shaped stiffener reinforcements and hing-line reinforcements. The elastomer coating is created from a high-strain polydimethylsilioxane elastomer. This material has high strain capabilities over a wide temperature range as well as over large number of cycles.[21]. In order to reinforce the hinge-line locations, a high-stain elastomer foam (Hyperflex-02) is attached to the skin. This material acts as a soft elastomer through a wide temperature range showing no significant stiffening effect, making it useful as the majority of strain experience will occur at low temperature. Connecting the foam reinforcements, 6062-aluminium u-shaped profiles are placed on the skin in order to maintain structural integrity. Finally, two 6062-aluminium span-wise stringers are placed in each section to improve the structural characteristics. This general layout is inspired by previously designed trailing edge morphing design SARISTU ATED as described in [21].

In order to preserve continuity of the MTE over the span, the coating material, polydimethylsilioxane, is also used as connection of the different flap segments. This is a high strain connection and thus allows for variation in deflection settings for the different flap segments. The results of the structural setup of the MTE is a continuous, smooth trailing edge flap system that allows large variation in airfoil shape along the span.

---

[1] `https://continentalsteel.com/blog/aerospace-aluminum-guide/`

3.3. MTE Subsystem Requirements

Table 3.2: Subsystem Level Requirements

ID	Requirement Specification	Rationale	Traceability	Verification
MTE-000	The MTE its last hinge-line shall be able to keep the load factor below 1.3 for all design gusts as specified by CS.25.341		MLW-Sys-011	Analysis, Section section 5.3
MTE-001	The MTE shall be able to deflect 15 deg upwards and downwards around all 3 - hinges		MLW-Sys-001	Design Review, Section subsection 5.3.3
MTE-002	The MTE shall be able to rotate with 30 deg/s around all 3 - hinges during cruise flight		MLW-Sys-010	Design Review, section subsection 5.3.3
MTE-003	The MLW shall be able to do MLA by deflecting the inboard sections opposite to the outboard sections		MLW-Sys-011	Design Review, sections section 5.3 and section 5.4
MTE-004	The MLW shall be able to perform GLA, so that load factors due to gusts stay below 1.3		MLW-Sys-004	Analysis: in section section 5.3
MTE-005	The MTE shall detect gusts 50m ahead of the fuselage nose		MLW-Sys-003	Design Review, sections section 5.1
MTE-006	The MTE shall be able to detect a change in load factor	Required for MLA, as an activation of it's system		Design Review, Section section 5.1

3.4. HLFC General Overview

After dedicating a part of this chapter to MTE description, the same is done for HLFC in the following sections.

3.4.1. Concept Introduction

For the most part of aviation history, designers thrived to maximise the extent of laminar flow because, as depicted in Figure 3.5, friction drag can account for more than half of the total aircraft drag. The wing skin friction alone creates approximately 18% of the total drag for a typical transport aircraft, which makes it an interesting focus point for further design improvements [22]. One of the driving requirements for this project also regards drag decrease and laminar flow region increase. It was chosen to capture both of these requirements with one system, the HLFC system. This system postpones the transition region of the boundary layer along the wing, which would significantly reduce the skin friction component of the drag.

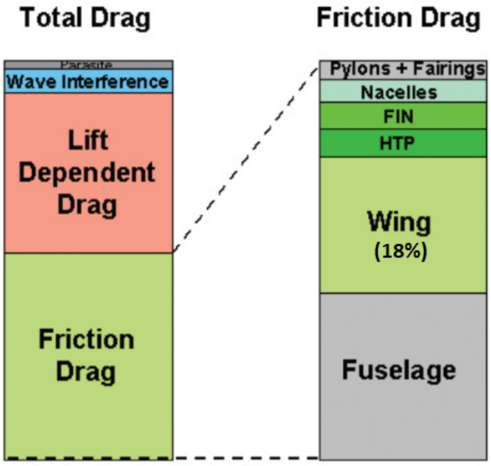

Figure 3.5: Typical drag breakdown of a transport aircraft [22]

HLFC has two components to it, a suction system and airfoil modifications, to ensure a laminar flow propagation aft of the suction region. Airfoil modifications into so-called laminar airfoils has been a long going research topic. However, standalone laminar airfoil use for transition delay suffers from several significant disadvantages. The most important one is that due to crossflow and attachment line transition triggering mechanisms, which are dominant on the leading edge of backward swept wings, transition can occur at the leading edge, no matter what airfoil is used. That would result in laminar airfoils being incapable in enhancing laminar flow, if the wing is swept [1]. That is why the suction subsystem is necessary. The basic idea of the HLFC suction concept is to eliminate a small portion of the slowest part of the boundary layer, which is attached to the skin of the wing, and extend the area of orderly flow behaviour also known as laminarity. The pump driven suction is achieved through a set of pipes and chambers, which create a required pressure difference to a micro perforated skin material to suck out the airflow. A render of the HLFC system is shown in Figure 3.6.

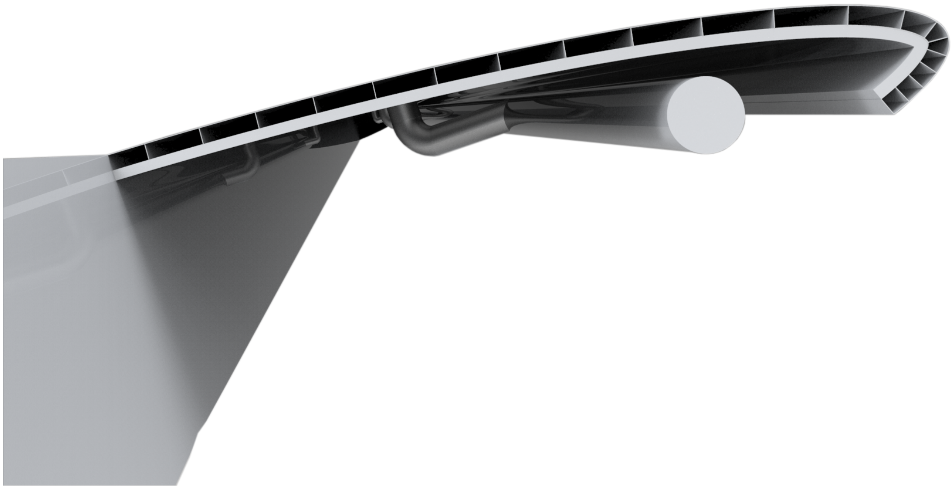

Figure 3.6: Render of the HLFC system

In the industry, the HLFC technology is seen as a promising technology for fuel-burn reduction. Recently, this technology has been commercially implemented on the vertical stabiliser of the Boeing B787-900 and is showing considerable performance improvements [23]. Boeing has carried out suction tests on the B757 wing and concluded that local drag could be reduced by 29% and the total aircraft drag by 6% [10]. These examples directly prove the potential of the HLFC system, which will be further elaborated in this report.

3.4.2. Extent of Implementation

Initially, some design decisions were made regarding how much of the wing surface should be equipped with boundary layer suction capacity. After a discussion with TU Delft aerodynamics experts, it was determined that transition is extremely difficult to reverse, once it has occurred on the wing. That inclines the fact that the suction has to start from the leading edge onward in order to be able to control the extent of laminar flow. After analysing literature and previous HLFC experiments, such as those of Boeing 757 [10] or *AFLoNext*[2], it was decided that the best position to end the suction region is at the front spar. That is because it allows the wingbox integrity to remain unaffected, while the laminarity can still be achieved up to and even beyond 65% [10]. Moreover, using a brief $XFoil$ transition analysis, it was determined that suction on the top surface of the wing is much more needed than on the bottom surface, since laminarity on the bottom surface of the wing in cruise can be achieved extensively without suction (up to 50%). As a result, it was decided that suction will be applied to the top surface only. Limiting the system to one side only is necessary due to the presence of leading edge high lift devices, which have to share space with the suction system. Since suction is to be applied on the top side of the wing, A320 slats are no longer compatible with the system, thus have to be redesigned into Krueger flaps. Further analysis of Krueger flap design and implementation is provided in section 3.8. The last conceptual design choice needed is the spanwise extend of HLFC suction. To decide this, it is important to realise that the engine nacelle and fuselage cause interference to the flow over the wing top surface, which make the laminarity practically unachievable. That is the exact reason why NASA conducted flight experiments with a Boeing 757 HLFC that had suction installed on a panel that started outboard of the engine nacelle [3]. Due to this interference effects it is established that laminarity of the flow can only be effectively manipulated outboard of the A320 aircraft engine, thus HLFC suction will only be applied in this region on both wings. A summary of this and the previous design decisions is provided in Figure 3.7.

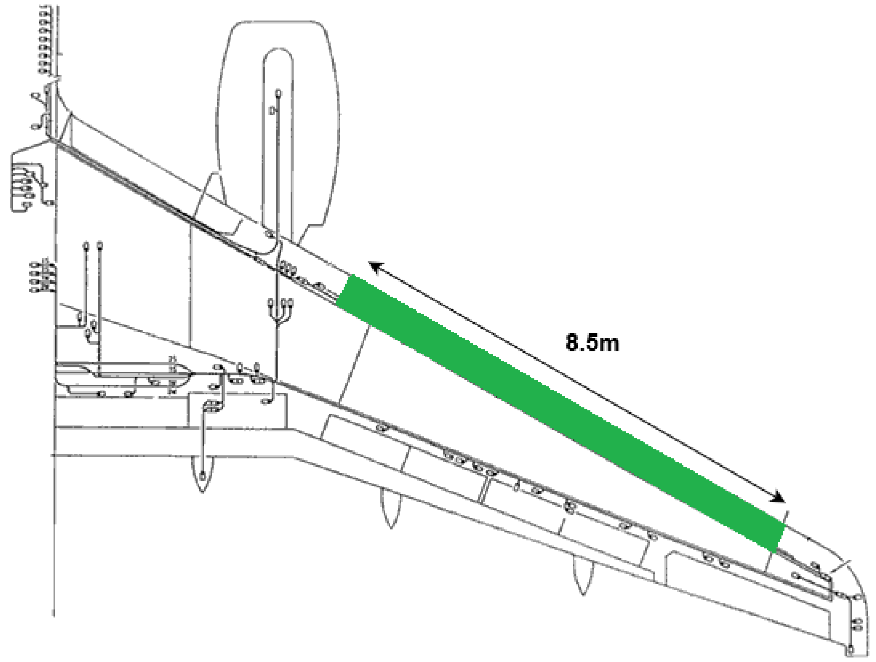

Figure 3.7: HLFC suction system extent and location on the right wing. The left wing has the same suction layout. Wing drawing from [9]

3.5. HLFC Architecture

The HLFC suction system hardware can be split into four main sub-groups: suction surface, pressurisation system, control & monitoring and anti-contamination system. The extended breakdown of these groups is given in Figure 3.8 and will be further elaborated in the upcoming sections.

---

[2] `http://www.aflonext.eu/hybrid-laminar-flow-control-24`

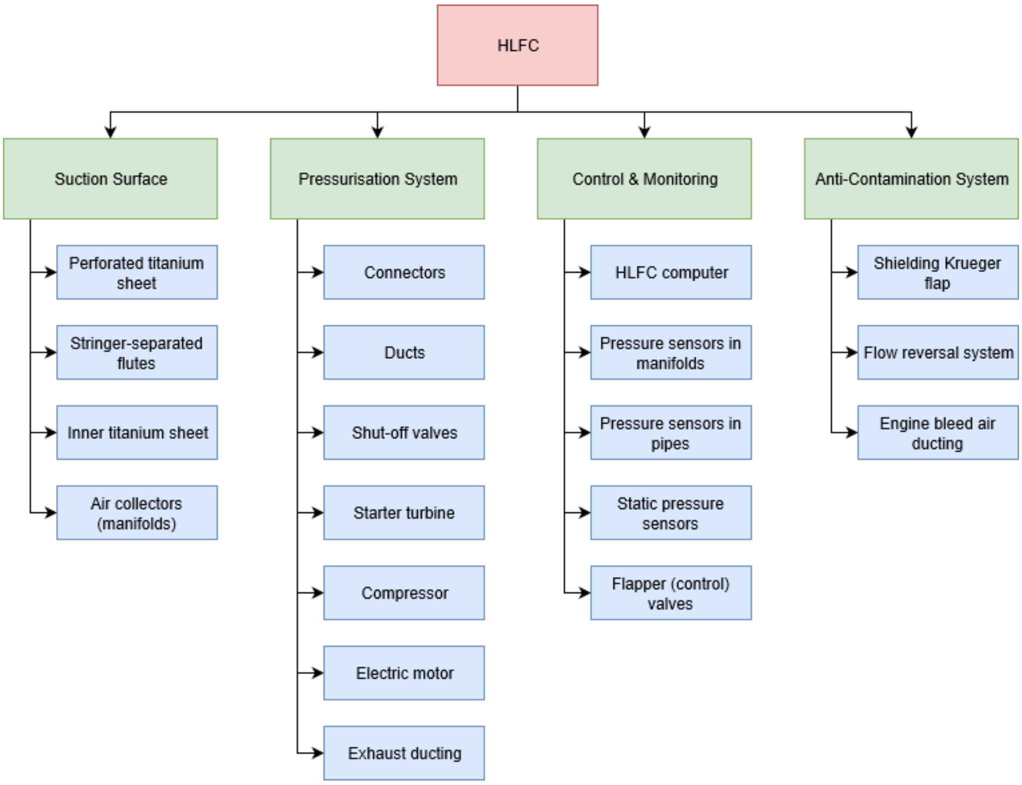

Figure 3.8: Hardware component breakdown tree for the HLFC suction system

3.5.1. Suction Surface

The section where suction is applied on the leading edge of the wing will be replaced by a micro-perforated metal upper skin reinforced by spanwise running stringers, which create differential pressure chambers, called flutes. From flutes, air is sucked through an inner sheet into a bigger accumulation chamber called manifold, from where it goes into a suction system. Titanium sheets were the only ones shown to be reliable enough to provide material for all these components due to its durability and corrosion resistance [24].

3.5.2. Pressurisation System

The description of the suction system is provided in Figure 3.9. Air from manifolds is sucked into a duct through connectors. Connectors and the pipes are separated by a flapper (control) valve, to maintain operative pressures inside of manifolds. The pressure difference for airflow is provided by the suction device, consisting of starter turbine, compressor and electric motor. To start the suction system, bleed air is taken from the engine high pressure compressor. It then runs through the starter turbine and starts the compressor. Once the system is running, the electric motor will take over the provision of power, as this is more efficient [14]. Furthermore, the suction device and a duct are separated by the main (shutoff) valve, which is closed when the system is not operating. Lastly, the sucked out flow goes through to the exhaust pipe.

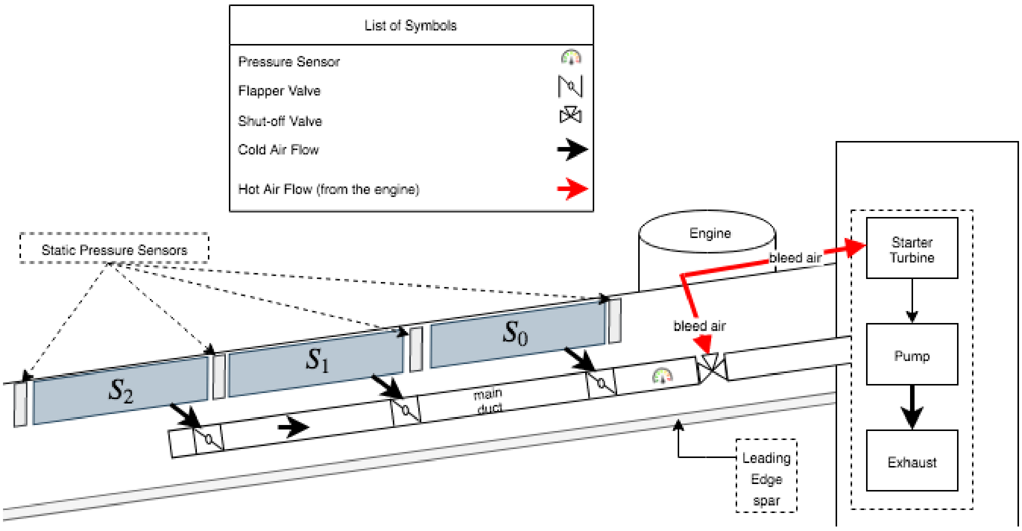

Figure 3.9: Diagram depicting the pressurisation system components and the flow of air from entering the ducts to exhaust. Moreover, it indicates the locations of the pressure sensors

3.5.3. Control & Monitoring

A monitoring and control system provides the HLFC computer with system pressure sensor data as well as flight conditions and transfers that information into inputs for valves and the pressure generation mechanism. The communication flow diagram, provided in Figure 3.10, depicts the sensing data flow into the computer as well as the hardware that receives the flow of control inputs. The static pressure sensors, which are divided over the leading edge of the wing, will determine the location of the stagnation point on the wing and thus the highest suction point. This highest suction point will be the foundation to determine suction pressure in the other leading edge locations, section 3.7 contains a detailed explanation of this process. To achieve this suction pressure distribution adjustments are made in the opening angle of the control valves. Internal pressure sensors in ducts and manifolds will monitor whether or not required pressures are achieved.

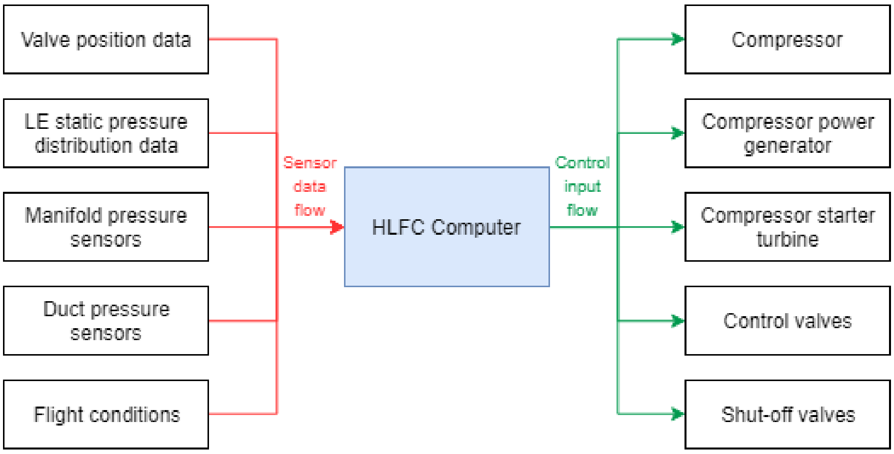

Figure 3.10: Communication flow diagram, depicting the flow of sensory data and the flow of HLFC computer-generated control inputs to the system components

The HLFC computer is the centre and the most important part of this subsystem. The objective of the HLFC computer is to enable the correct suction pressure distribution over the leading edge of the wing. Moreover, the HLFC computer is responsible for the correct dynamic adjustment of the system, which is defined in subsection 3.5.5. A thorough explanation of what happens inside the HLFC computer can be best described by means of a software diagram given in Figure 3.11.

The HLFC system does not have any external (pilot) inputs, thus it is completely autonomous. The general idea of the control system is to obtain the current boundary layer transition state from sensor data, compare it to the required state and generate the mechanical input to the hardware to obtain the required state. After generating both states, there is a check done, to determine whether the aircraft is in the HLFC operational conditions or not. If the aircraft is on the ground, in take-off, in landing or in low altitude cruise or descent (cloud layer), the anti-contamination mode is enabled and therefore protects the system from icing or other contaminants. Once the conditions are right, the HLFC goes into the operational suction mode. During this mode, continuous error determination and resolution is performed to maintain the correct state.

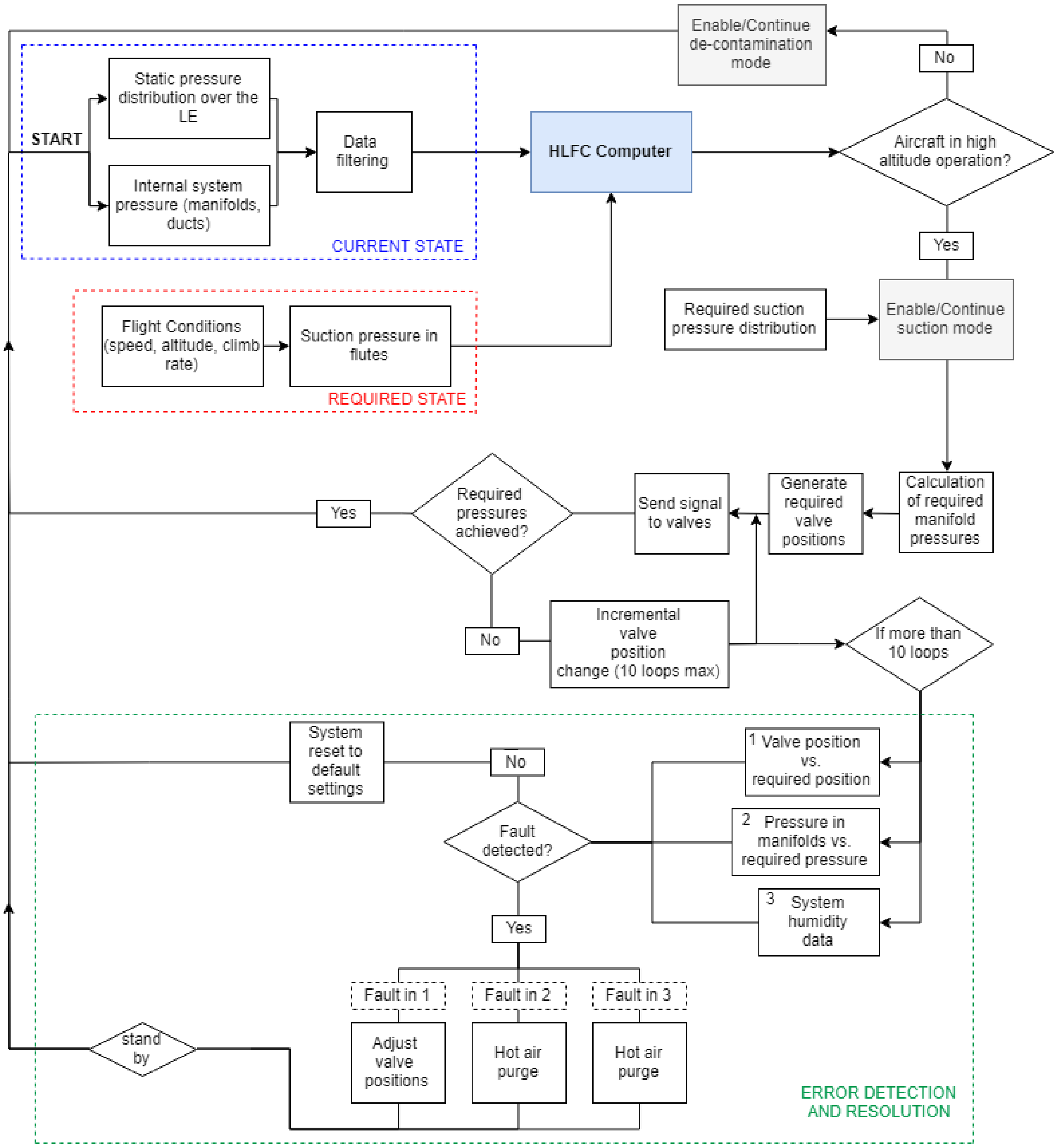

Figure 3.11: HLFC software diagram, depicting the system behind the HLFC computer and the operation of two modes - suction and de-contamination

3.5.4. Anti-contamination System

The leading edge of the wing in low altitude operations is subject to different types and amounts of contamination. Whether it is ice formation arising from flying through a cloud or particle impacts from the runway, the leading edge needs to be protected. This need is achieved by designing Krueger flap, which is able to shield the leading edge from contaminants. A detailed description of the Krueger flap regarding its application and impact with respect to the original A320 is given in section 3.8.

In some situations the Krueger flap is still unable to prevent contamination on the suction surface. As a result, the leading edge needs to be able to decontaminate itself for proper performance of the HLFC system. To solve this problem it was decided to equip the HLFC with a heated air flow reversal mode, which would purge hot air out through the perforated skin with an aim of de-icing and unclogging the perforations as well as removing excess humidity in the system. This mode will be achieved with the bleed air of the engines, which means that no additional power usage is required. Bleed air is already available on A320 engines CFM56, where hot air is taken from the high pressure compressor to feed the pneumatic system and cool down the high pressure compressor itself[3]. It is thus decided to have a link between the suction system and the pneumatic system, which is meant to provide hot pressurised air for air-conditioning, hydraulic reservoir pressurisation, water pressurisation and engine startup. A pressure regulating and shut-off valves will be used in between the pneumatic system and HLFC decontamination system. Moreover, the HLFC decontamination mode would be activated during the on-ground operations as well as take-off, landing, climb and descent, until the suction takes over. This system is summarised in the block diagram in Figure 3.12.

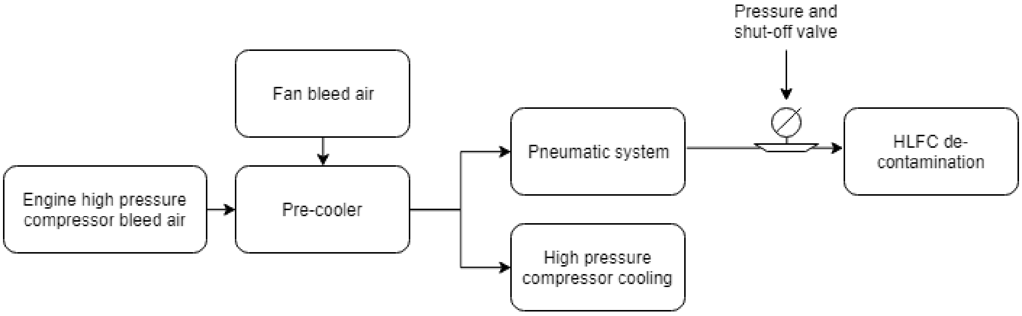

Figure 3.12: The decontamination mode of HLFC definition regarding bleed air extraction from the engines

3.5.5. System Dynamic Behaviour

Besides the normal steady operation of the system, HLFC also needs to be adjustable to the environment. It has to be able to change the suction distribution in flutes depending on where the stagnation point is as well as adjust to the different true air-speeds that the wing sees.

During different stages of flight, HLFC has to adjust to the phase of the mission, since its functionality is to be maintained during cruise and most of the climb and descent phases. With changing stage of flight, the angle of attack varies and thus the stagnation point location on the leading edge of the wing also changes. This means that in order to damp out the attachment line and cross-flow transition triggers, which are dominant at the vicinity of stagnation point, the suction distribution has to shift accordingly. This shift is defined in Figure 3.13a, more information about suction distribution is presented in section 3.7. In the climb stage, once the cloud layer is escaped, the angle of attack is higher, thus stagnation point of the flow is at the lowest point. As the angle of attack decreases, the stagnation point moves up as defined in Figure 3.13b.

Due to spanwise twist of the wing as well as airfoil shape change, the stagnation (attachment) line is not straight, which means that knowing the angle of attack of the wing is not sufficient for the system to perform optimally. Instead, the system itself has to determine where the stagnation line is, such that the suction distribution shift is applied correctly. This can be done by measuring the static pressure along the leading edge, the location with the highest static pressure will then resemble the stagnation location and thus the highest suction zone. Knowing where the peak of suction is located will allow for the suction distribution to be known. These measurements will be done by means of static pressure taps, located in between the separate suction sections, as seen in Figure 3.9. Having more than one array of sensors will allow for more accuracy on the spanwise stagnation point location. Once the stagnation line is determined from the static pressure sensor data, the suction pressure will be changed accordingly by applying the most pressure on the flute that coincides with the stagnation line.

---

[3] `https://hursts.org.uk/airbus-technical/notes.pdf`

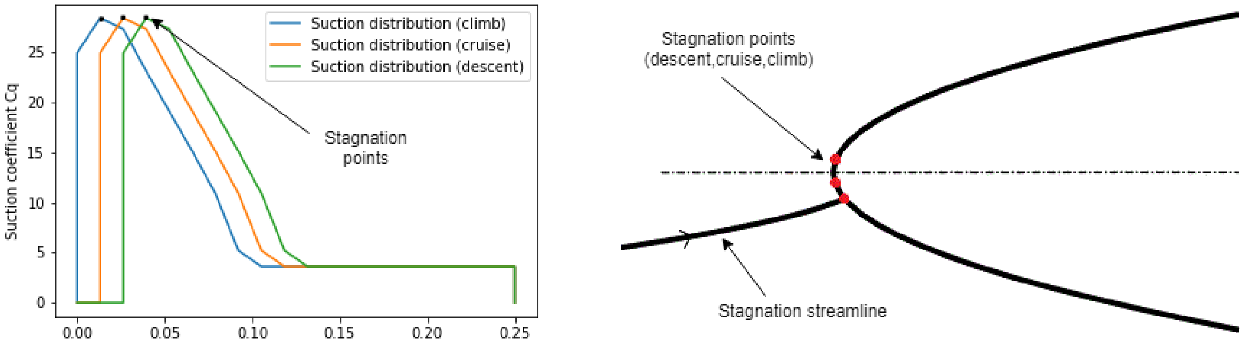

(a) Change of suction distribution with changing stage of the mission.

(b) The changing position of stagnation point with changing angle of attack. The uppermost point defines descent stagnation point, lowermost - climb.

Figure 3.13: Change in suction distribution and stagnation point with change in angle of attack

The HLFC suction system also has to be able to deal with changing airspeed. However, this is rather easy to adjust to, because the suction system is meant to maintain the same suction coefficient C_q distribution at all times. Since C_q is defined as in Equation 3.1, maintaining it constant with changing velocity is achieved by altering the mass flow rate through the system [3]. In turn, that is achievable by altering the pump power setting and the control valve positions in the piping system.

$$C_q = \frac{\dot{m}}{\rho_\infty V_\infty S_{sp}} \tag{3.1}$$

3.6. HLFC Subsystem Level Requirements

Table 3.3: Subsystem Level Requirements

ID	Requirement Specification	Rationale	Traceability	Verification
HLFC-000	The HLFC system shall decrease skin friction drag by 17.5%		MLW-Sys-000	Analysis: subsection 4.4.1
HLFC-001	The HLFC system shall provide C_q specified in figure Figure 3.14	In section section 3.7, it is explained how C_q is used as a starting point of the design		Analysis: in section section 3.7
HLFC-002	HLFC shall withstand bird impact of a 4lb bird at V_c on a Sea Level, or $0.85 V_c$ on 2438 m		MLW-Sys-014	Test: tests shall be performed on an outer surface of the suction panel

HLFC-003	HLFC Pump shall provide pressure ratio $\Pi = 3$, at $\dot{m} = 0.52\frac{kg}{s}$	Analysis has shown, that this pump is sufficient to provide required suction		Design Review: Performance sheet of a commercial of the shelf component.
HLFC-004	HLFC Leading edge shall sense pressure and identify location of stagnation point	To find stagnation point and adjust pressure in flutes and move max C_q to the stagnation point.		Design Review, section section 3.5
HLFC-005	HLFC piping subsystem shall have a connection to the engine for de-icing and purging of the outer surface	To protect system against contamination		Design Review, section section 3.5

3.7. HLFC Suction System Design

The purpose of suction system is to provide required suction velocity distribution to achieve the best possible delay in laminar-turbulent flow transition. This requirement is given in terms of suction coefficients, presented in figure Figure 3.14, which is provided by aerodynamic analysis. Due to lack of resources, a detailed investigation of required suction coefficient distribution was substituted with values borrowed from the Boeing 757 experiment [3]. Moreover, the number of flutes chosen for the design corresponds to number of flutes in the Boeing 757 HLFC as well.

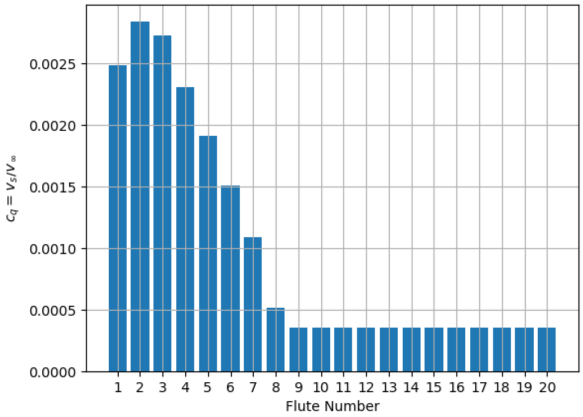

Figure 3.14: C_q distribution above each flute

3.7.1. Air Flow Path

Air enters flutes through pores on the outer surfaces because of differences between flutes pressures and outer pressure, and leaves through the orifice on a lower surface. A principal draft of one individual flute is shown on a figure Figure 3.15a. Pressure drop across the surface can be estimated using Goldstein method, equation Equation 3.2[2].

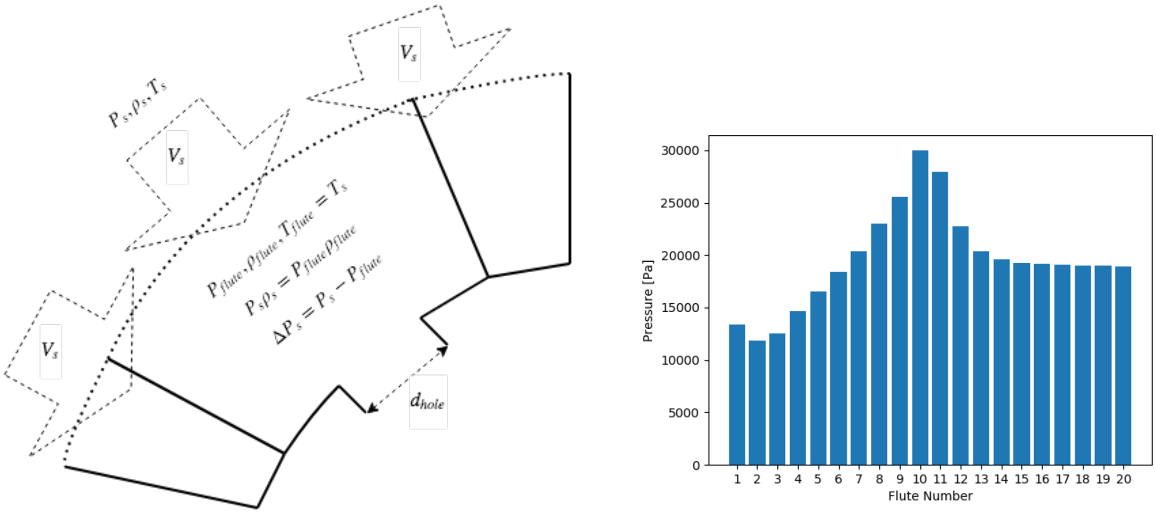

(a) Generic flute scheme

(b) Required flutes pressures

Figure 3.15: Flutes pressure design parameters

$$\Delta P_s = A\frac{\mu_s}{\mu_0}V_s + B\frac{\rho_s}{\rho_0}V_s^2 \tag{3.2}$$

Constants A and B are experimentally derived functions of material properties, aerodynamics properties and porosity of the surface. For the purposes of our design, it is assumed that $A = 14000\frac{N\cdot s}{m^2}$ and $B = 27000\frac{N\cdot s}{m^3}$ [2]. For better estimation more aerodynamic analysis has to be done. Density, temperature and pressure distributions are known from aerodynamic analysis of the airfoil. Dynamic viscosity can be estimated using Sutherland's formula for air[4] Equation 3.3. It is assumed that temperature inside of the flute is the same as on the surface of an airfoil.

$$\frac{\mu_s}{\mu_0} = \left(\frac{T_s}{T_0}\right)^{1.5}\frac{T_0 + 110}{T_s + 110} \tag{3.3}$$

Once required velocities are known (see Figure 3.14), it is possible to estimate required pressures inside of the flutes to deliver required suction distribution Figure 3.15b

Mass flow rate can be estimated from velocity distribution and porosity of the flute Equation 3.4. Porosity is defined as a ratio of summed holes areas by outer surface area: Porosity $= \frac{\pi}{4}\left(\frac{d_p}{A}\right)^2$, where d_p is a pore diameter, and A is a centre-to-centre distance between pores [14]. In our design, d_p is chosen to be 50 μm, and A is 500 μm.

$$\dot{m}_{\text{flute}} = \rho_s V_s \text{Area}_{\text{flute}} \cdot \text{Porosity} \tag{3.4}$$

Once inside of a flute, air flows though an orifice on an inner surface to a bigger pressure chamber common for 20 flutes, called *manifold*. A pressure drop between a flute and the manifold is estimated using Borda-Carnot relation Equation 3.5 [25].

$$\Delta P = \frac{\rho}{2}V^2\left(\frac{S_s}{\alpha S_h} - 1\right)^2 = P_{\text{flute}} - P_{\text{manifold}} \tag{3.5}$$
$$\text{where } \alpha = 0.6 + 0.4\left(\frac{S_h}{S_s}\right)^2$$

Since the overall outline of the flutes pressure graph does not change very much throughout the flight, it is necessary to adjust hole diameters to meet flutes pressure requirements. Design target pressure inside of the manifold is chosen to be 10,000 Pa, therefore Equation 3.5 allows to solve for hole diameters. With Equation 3.6 it is possible to

---

[4] `https://www.cfd-online.com/Wiki/Sutherland's_law`

calculate total mass flow rate into the manifold, density inside of the manifold is calculated with Equation 3.7, and temperature follows from Equation 3.8.

$$\dot{m}_{\text{total}} = \sum_{\text{flutes}} \dot{m}_{\text{flute}} \tag{3.6}$$

$$P_m \rho_m = \frac{\sum_{\text{flutes}} P_{\text{flute}} \rho_{\text{flute}} \dot{m}_{\text{flute}}}{\dot{m}_{\text{total}}} \tag{3.7}$$

$$T_m = \frac{\sum_{\text{flutes}} T_{\text{flute}} \dot{m}_{\text{flute}}}{\dot{m}_{\text{total}}} \tag{3.8}$$

From manifolds, air flows into a main pipe through the connectors. Pressure in the connector is estimated through semi-empirical method, which includes dimensionless loss coefficient K_L assumed to be 0.5, Equation 3.9 [26].

$$P_{\text{connector}} = P_{\text{manifold}} - (1 + K_L) \frac{\rho_{\text{connector}} V^2_{\text{connector}}}{2} \tag{3.9}$$

Connectors are attached to the main duct and together they comprise a so-called tee pipe component, which is shown in Figure 3.16. These tee-components make additional contributions into pressure loss, which can be calculated using Equation 3.10 and Equation 3.11, where $\psi = \frac{A_C}{A_B}$ and duct cross section area is uniform ($A_A = A_C$) [27].

$$K_{11} = \frac{2\psi}{\psi + \frac{1}{2}\cos\theta}(1 - q^2 - (1-q)^2 \psi \cos\theta) + q^2 - 1 \qquad \text{where } q = \frac{\dot{m}_A}{\dot{m}_C} \tag{3.10}$$

$$K_{12} = \frac{2\psi}{\psi + \frac{1}{2}\cos\theta}(1 - (1-q)^2 - q^2 \psi \cos\theta) + q^2 \psi^2 - 1 \qquad \text{where } q = \frac{\dot{m}_B}{\dot{m}_C} \tag{3.11}$$

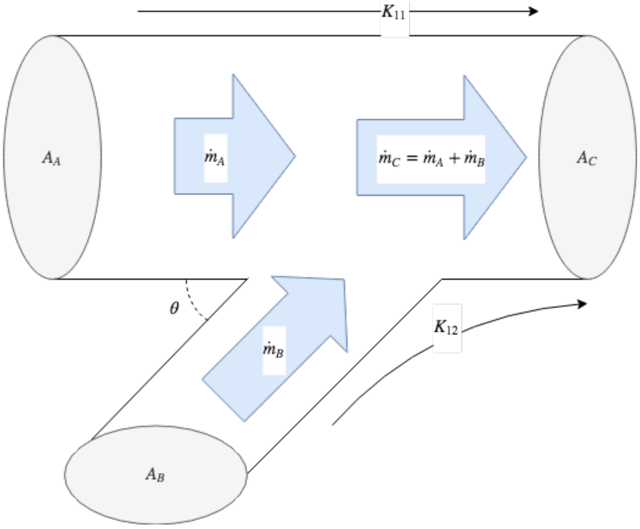

Figure 3.16: Tee pipe component

Through the main duct, air is sucked out of the system into an exhaust by a pump.

3.7.2. Software Tool and Verification & Validation

In order to automate design of the suction system, a software tool was created. Inputs of the program included: airfoil selection, aerodynamic parameters (C_p distribution), suction distribution, standard atmospheric conditions, and geometry of the flutes (flute thicknesses). Outputs included pressures at each point, pressure losses, mass flow rates, and geometrical properties of the suction panels (θ angle, hole diameters).

In order to avoid mistakes and simplify testing, an object oriented approach was used. Everything available, including input parameters and formulas presented in previous subsection were included as a set of attributes into classes presented in a class diagram Figure 3.17.

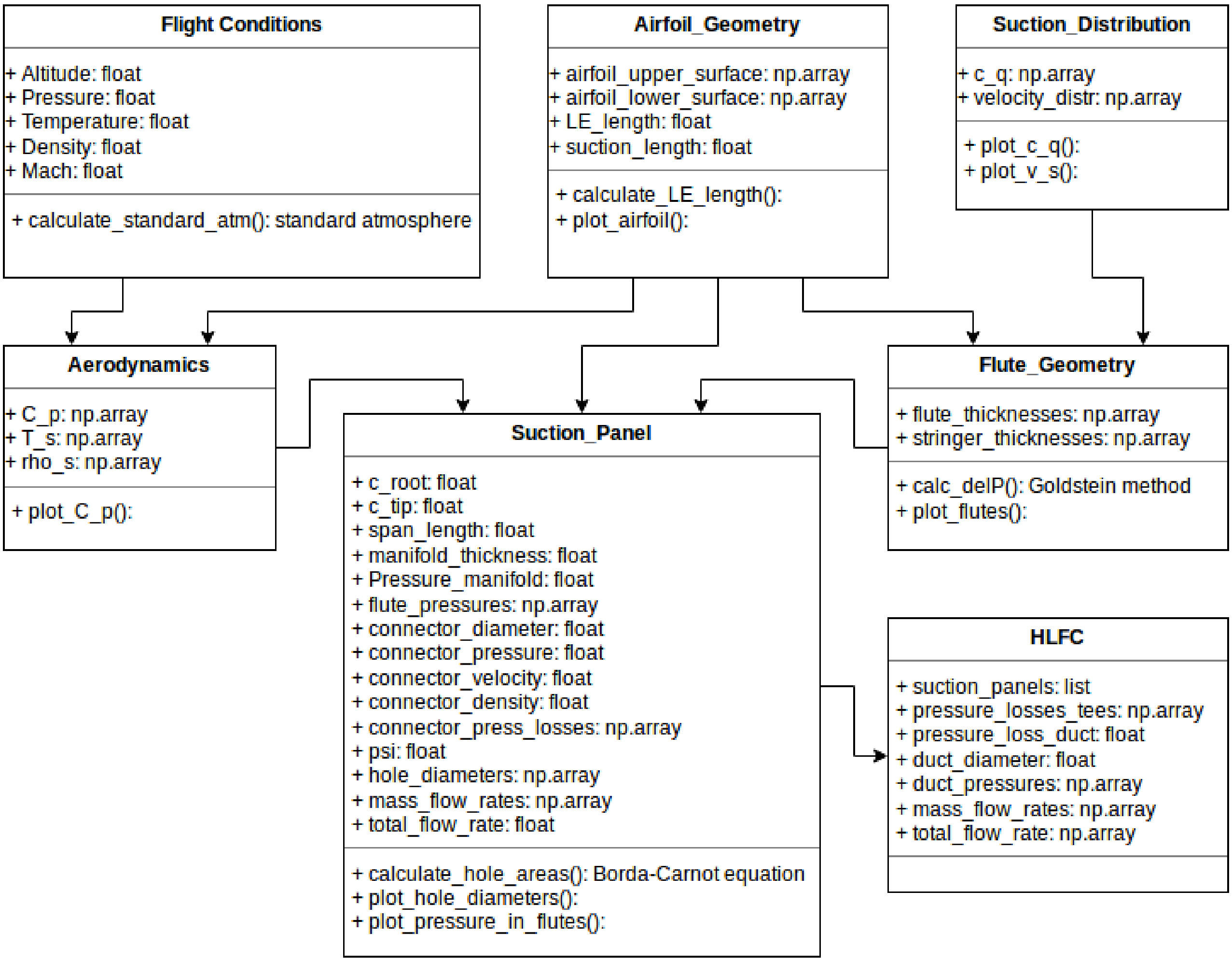

Figure 3.17: HLFC software tool class diagram

Plots and verification tests were written for each class. Each result was meticulously tested for sanity. During sanity checks, it was discovered that total mass flow rate exceeds mass flow rate of Boeing 757 HLFC by a factor of 13 [28]. Hence, code was examined for bugs, and it was discovered that pressures in flutes were calculated incorrectly. After bug fix, mass flow rate of the HLFC system has the same order of magnitude as its predecessors. The Software tool was checked against different types of airfoils for variety of flight conditions.

In order to validate software design tool, it is necessary to build a prototype and measure all pressure losses, as well as efficiency of a suction system. A cheaper alternative would be to make a full size Computational FLuid Dynamics (CFD) analysis of the flow inside piping system.

3.7.3. Design Results

Flute thicknesses and hole diameters were chosen is such a way, as to maintain suction coefficient c_q distribution. Pressure in manifolds was chosen to be 10,000 Pa. Angle θ between connectors and main duct was chosen to be 45°. The connector diameter is 8 cm.

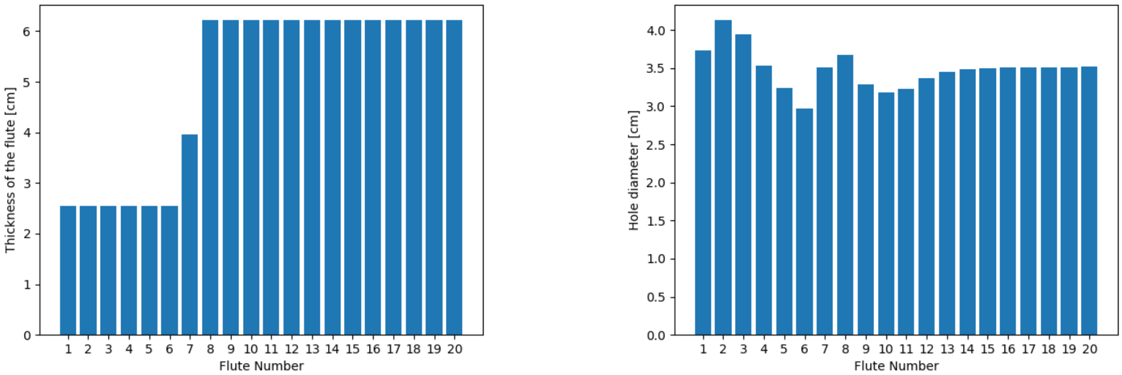

(a) Relative Flute thicknesses

(b) Hole diameters on the inner surface between flutes and a manifold

Figure 3.18: Flutes thickness and hole diameter design parameters

	panel 0	**panel 1**	**panel 2**
Span $[m]$	2.59	2.59	2.14
Connector Pressure $[Pa]$	9871.63	9909.82	9960.15
Mass Flow Rate $[\frac{kg}{s}]$	0.11	0.09	0.06
Total Mass Flow rate $[\frac{kg}{s}]$			0.26

Table 3.4: Suction panels design parameters

Duct diameter was set to be 0.1 meter. Duct pressure, is estimated to be 9,865 Pa. Since Ambient pressure during cruise is $P_\infty = 22700Pa$, therefore pressure ratio which needs to be provided by a pump is $\Pi \approx 2.3$. Total mass flow rate is estimated to be $\dot{m} = 0.26\frac{kg}{s} \times 2 = 0.52\frac{kg}{s}$. Therefore, requirement HLFC-003 for suction pump was discovered and documented in table Table 3.3.

3.8. High Lift Device Replacement

Application of HLFC subsystem on the wing requires adjustments to be made for the LE high lift device technology. This need is addressed in this section.

3.8.1. Design Considerations

Current A320 aircraft use slats as the high lift devices on the leading edge of the wing. However, slats are incompatible with the boundary layer suction system, which is to be applied on the upper leading edge of the wing. In the retracted position, the slats would cover up the perforated suction surface, thus eliminating the system effect. As a result, the slats need to be converted into devices that are stored on the bottom side of the wing instead. This can be achieved by the use of a Krueger flap system.

Due to time constraints of the project, the Krueger flap was not designed in detail, nor treated as of primary importance to the completion of the concept. Instead, it was decided to ensure that the new leading edge device will provide sufficient lift increase in take-off and landing phases as well as to ensure it fits in the leading edge of the wing together with the suction system. Moreover, the Krueger flaps were analysed in terms of cost and mass with respect to slats in order to ensure that this design change is not outweighing the advantages arising from the HLFC system.

In order to mimic the high-lift performance of the slats, Krueger flaps have to both increase the wing camber and provide a gap between the flap and the wing for flow energising. A simplistic drawing of the concept is shown in figure Figure 3.19. Note that besides enhancing the performance, the Krueger flap has to extend upwards and downwards from the leading edge, which is essential for providing the anti-contamination function to the HLFC system in low altitude flight phases.

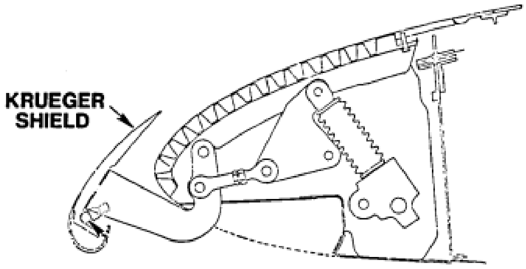

Figure 3.19: Krueger flap that acts as a high lift device as well as a contamination shield for the suction system [29]

There are two types of Krueger flaps that would be applicable to shield the system and provide high-lift, these are folding bull-nose flaps and variable camber (VC) Krueger flaps. Folding bull-nose flaps are built of two airfoil parts and is capable of folding front part of the flap, which allows to save space for the suction system and its ducting inside the leading edge compartment when the flap is retracted. The VC Krueger, on the other hand, also has a folding nose, but besides this it allows for camber changes within the flap providing a better overall aerodynamic performance even than the conventional slotted slat [4]. However, the VC Krueger support mechanism requires a four-bar linkage as well as additional mechanisms for manipulating the flap shape, which makes it a substantially more complex and expensive system than the folding bull-nose Krueger flaps. As a result, it is chosen to develop the bull-nose type of flap, ensuring its compatibility and that it performs sufficiently in take-off and landing.

3.8.2. Krueger Flap Analysis

To prove the feasibility of replacing the slats with the Krueger flap it is of the most importance to first check whether Krueger flaps can provide the high-lift characteristics that are expected from it in the take-off and landing phases. An important conclusion was drawn in the Boeing 757 HLFC test, where a portion of the wing leading edge was replaced by boundary layer suction on the top surface and subsequently leading edge slats were replaced by Krueger flaps. The low speed wind tunnel tests yielded a C_{Lmax} decrease of only 0.05 [3]. Moreover, as seen in Figure 3.20, the $C_l - \alpha$ curve slope of the new configuration was unaffected as well, the C_Lmax value is only slightly smaller with Krueger flaps but the slope of the curve is the same. These two insights prove the applicability of Krueger flaps as a leading edge high-lift device replacement in terms of aerodynamic performance.

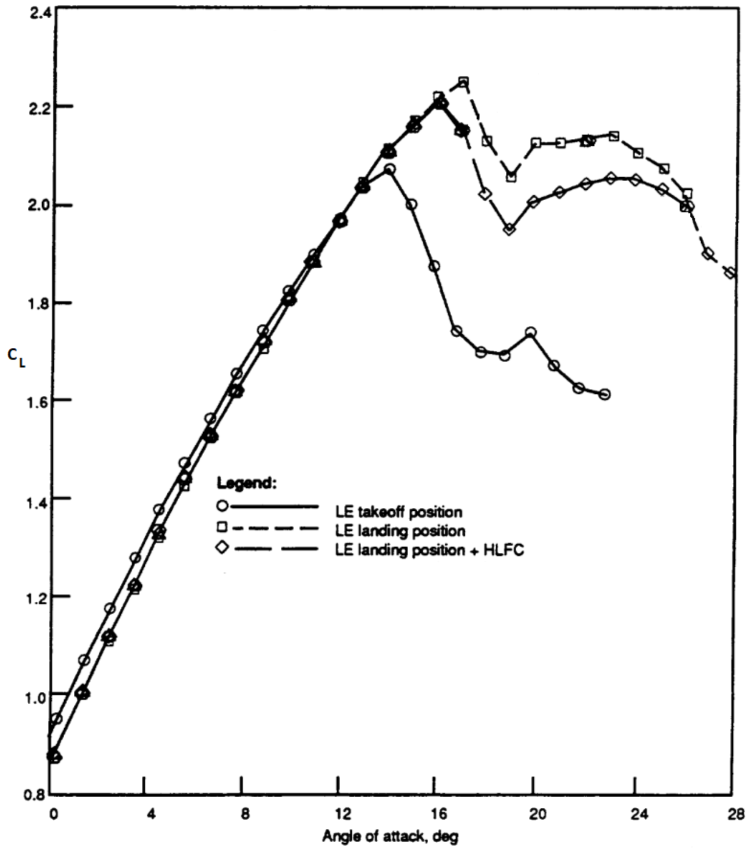

Figure 3.20: NASA B757 HLFC low-speed wind tunnel test results regarding the C_L values for the baseline configuration with slats and the results for the Krueger flap design [3]

The other aspects that require investigation are the mass and cost of this replacement. The goal here is not to determine accurate absolute values, but instead to determine the difference between mass and cost of a slotted slat and a bull-nose Krueger flap. That is because the mass and cost saving potential of changing the leading edge devices is expected to be small enough to neglect it compared to other characteristics of the developed concept. Regarding the mass, the estimations are done by means of equations that were generated by NASA from previous aircraft applications. This analysis breaks up the total mass of leading edge devices into three groups - fixed structure, moving panels and actuation [4]. The comparison between bull-nose Krueger and the three-position slat is depicted in Table 3.5. Note that the defined method of mass estimations only looks at fixed and VC Krueger flaps, but not the bull-nose flap which is chosen for the concept. Since the level of degrees-of-freedom for the chosen flap is in between the fixed and VC Krueger flaps, it was decided to average the estimations. As for the slat calculation, the method differentiates slat mechanisms with and without slave track mechanisms. The latter is chosen for the comparison, as it most closely resembles the benchmark A320 slat [30]. As seen in the table, the bull-nose Krueger flap actually is expected to be slightly lighter than the slat system, but the difference is minimal. This allows to draw a conclusion that the Krueger flap is not expected to be detrimental to the project goal of increasing payload mass for the aircraft. The calculated mass savings of using a Krueger flap will not be pursued in the analysis either, due to the lack of maturity of the calculations.

On the other hand, the cost of this design change is expected to increase slightly compared to the benchmark slat, as depicted in Table 3.5. The estimation methods were once again applied on a basis of historical aircraft where the manufacturing cost was determined as a function of system mass and number of parts [4]. The expected cost increase is considered to have a negligible effect, since the difference is only as small as 0.8% of the total wing production cost. However, these differences will be taken into account in further cost analysis in section 8.2.

	Bull-nose Krueger Flap	**Three-position Slat**
Fixed Structure $[kg/m^2]$	11.0	10.3
Moving Panels $[kg/m^2]$	8.8	11.7
Actuation $[kg/m^2]$	7.9	6.3
Total $[kg/m^2]$	27.7	28.3
Total Mass [kg]	**855**	**874**
Part Count	2425	2042
Manufacturing Cost [USD]	**0.77 M**	**0.69 M**

Table 3.5: Preliminary mass and cost estimations for the bull-nose Krueger flap and the three-position slat, as used on A320 aircraft.

3.8.3. Krueger Flap Design

After concluding that a Krueger flap is a suitable slat replacement, it is necessary to know what design characteristics are the most important in achieving the performance that is comparable to that of a slat. Important conclusions from a NASA study indicate that the largest effect on the $C_L - \alpha$ curve comes from the Krueger flap nose length and overall length (see Figure 3.21). From the results of the study it was concluded that the Krueger flap nose length should be at least 15% of the flap chord. Moreover, the flap chord itself was chosen to be 12% of the wing chord and the smallest gap between the flap and the wing in extracted position of 2.2%, as defined in a NASA HLFC test flap design [3].

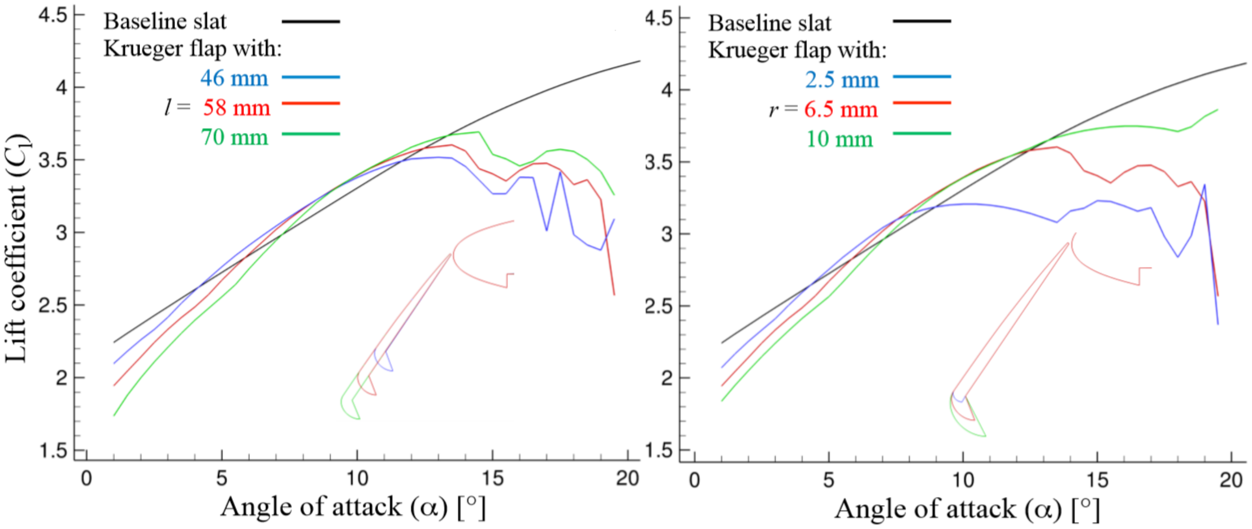

Figure 3.21: Krueger flap design options and its effect on the lift that can be achieved [31]

3.9. HLFC and MTE Integration

In this section the HLFC and MTE subsystems are treated in a more integrated way, as two subsystems of one system - the Morphing Laminar Wing, a render of which is shown in Figure 3.22. This can be addressed in a unified architecture and mission profile description.

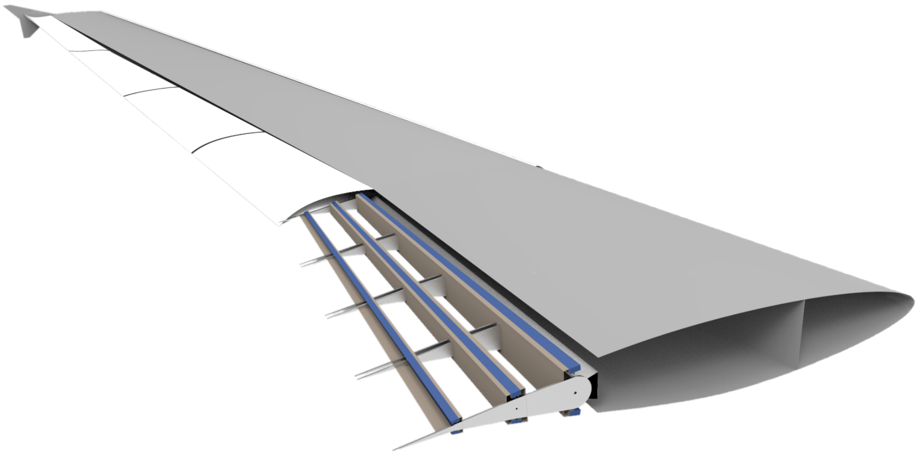

Figure 3.22: Render of the MLW

3.9.1. Global MLW Architecture

The MLW can be looked at from a more global perspective, where two systems, HLFC and MTE, work together with the remainder of wing components to achieve a better overall aircraft performance. The complete list of components and subsystems that comprise a wing can be seen in Figure 3.25. Due to a rather uncoupled nature of the two added wing features, it is difficult to make a clear link at this stage of project development regarding the hardware components that could be integrated. On the other hand, looking at the software diagram of the MLW in Figure 3.24, it can be seen that these two systems are expected to merge in the sense of signal processing of related sensors. Moreover, the required state for both the MTE and HLFC arise from the same logic. If a pilot input is present, it will affect both systems and their respective behaviour in updating the state. This leads to the conclusion that these features cannot be seen as completely independent of each other.

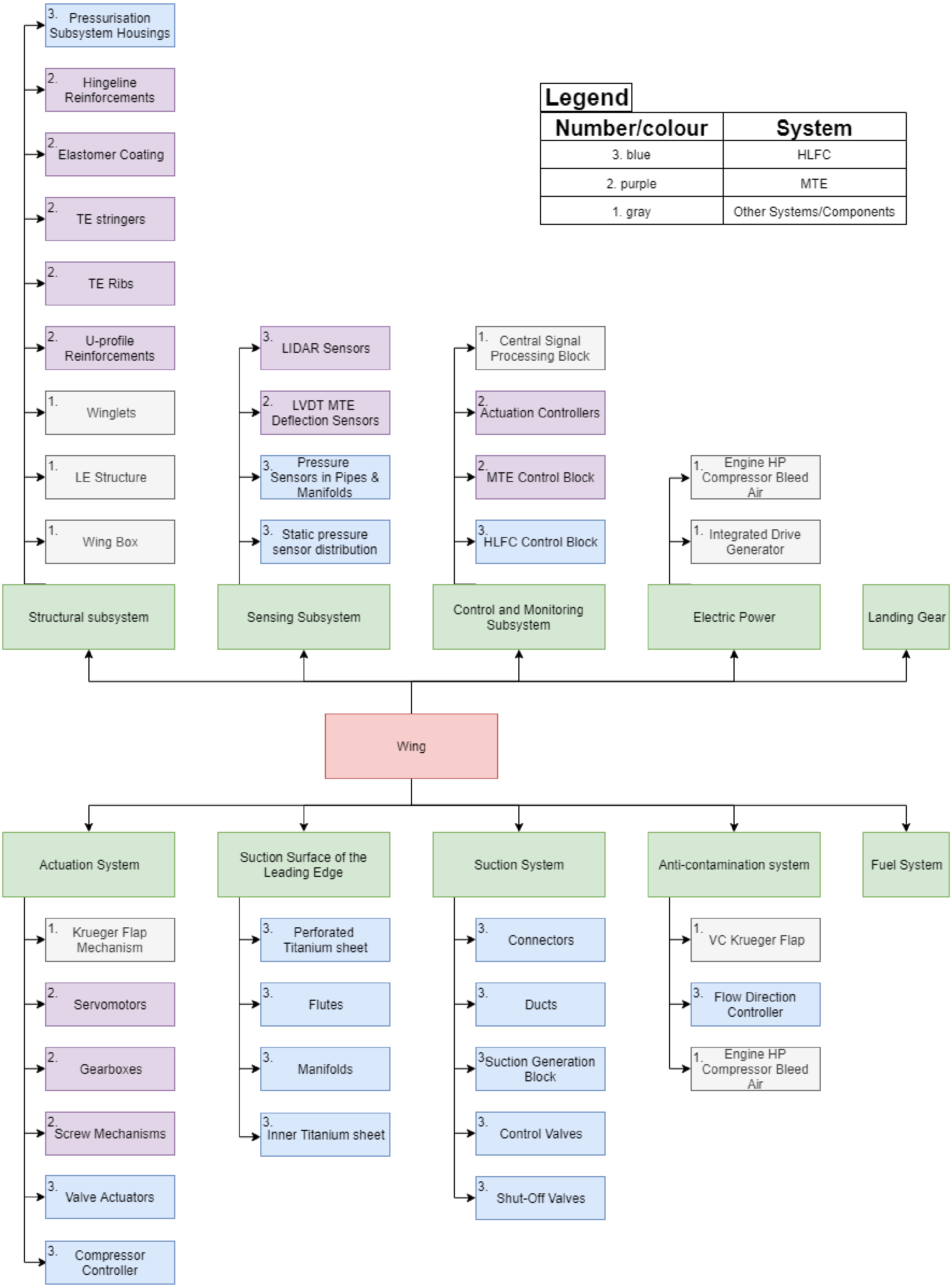

Figure 3.23: Hardware breakdown of the Morphing Laminar Wing

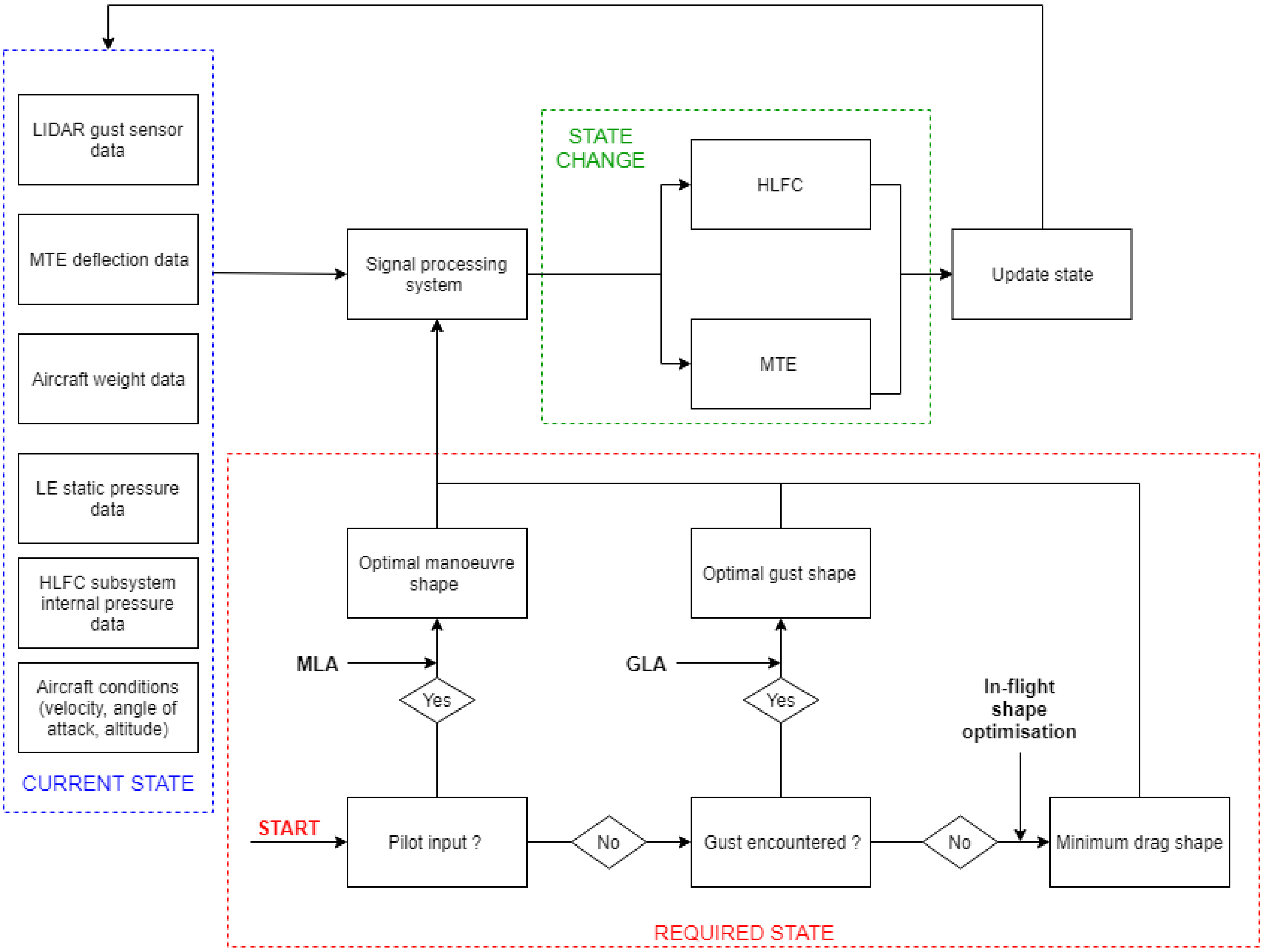

Figure 3.24: The software diagram of the Morphing Laminar Wing

3.9.2. MLW Mission Description

The description of the MLW design concludes with an explanation of the functions that the HLFC system and MTE perform throughout a typical flight of an A320 aircraft. This description is depicted in Figure 3.25, where the mission is broken down into 8 stages: ground stage (1-2), take-off (2-3), initial climb (3-4), secondary climb (4-5), cruise (5-6), descent (6-7), approach (7-8) and landing (8-9). The HLFC operation sequence is defined as follows:

- (1-3.1). HLFC is in the anti-contamination mode until the top cloud layer is escaped and no more significant icing areas are foreseen. Anti-contamination mode blows hot air from the engine high pressure compressor through the perforated skin, which removes any dirt or ice formations on the leading edge. This ensures that the system can function effectively in the succeeding flight stages
- (3.1-6.1). HLFC is operating in the laminarising suction mode. The suction is interrupted by short decontamination periods if the pressure sensors inside the system detect abnormalities, which would be caused by additional icing on the leading edge
- (6.1-9). HLFC enters the anti-contamination mode once again when the cloud layer is reached

The sequence for MTE can be broken down in a similar fashion:

- (1-3). MTE is in a take-off configuration, where all three segments of the trailing edge are deflected 10° with respect to each other
- (3-7). MTE is in the performance enhancing mode, where it is able to alleviate gust and manoeuvre loads as well as optimise the shape of the wing in flight for least drag operation

- (7-9). MTE segments are gradually deflected to 15° with respect to each other to create the C_{Lmax} wing shape and land the aircraft. Once the aircraft touches down, spoilers on the inboard part of the wing are enabled to aid slowing down

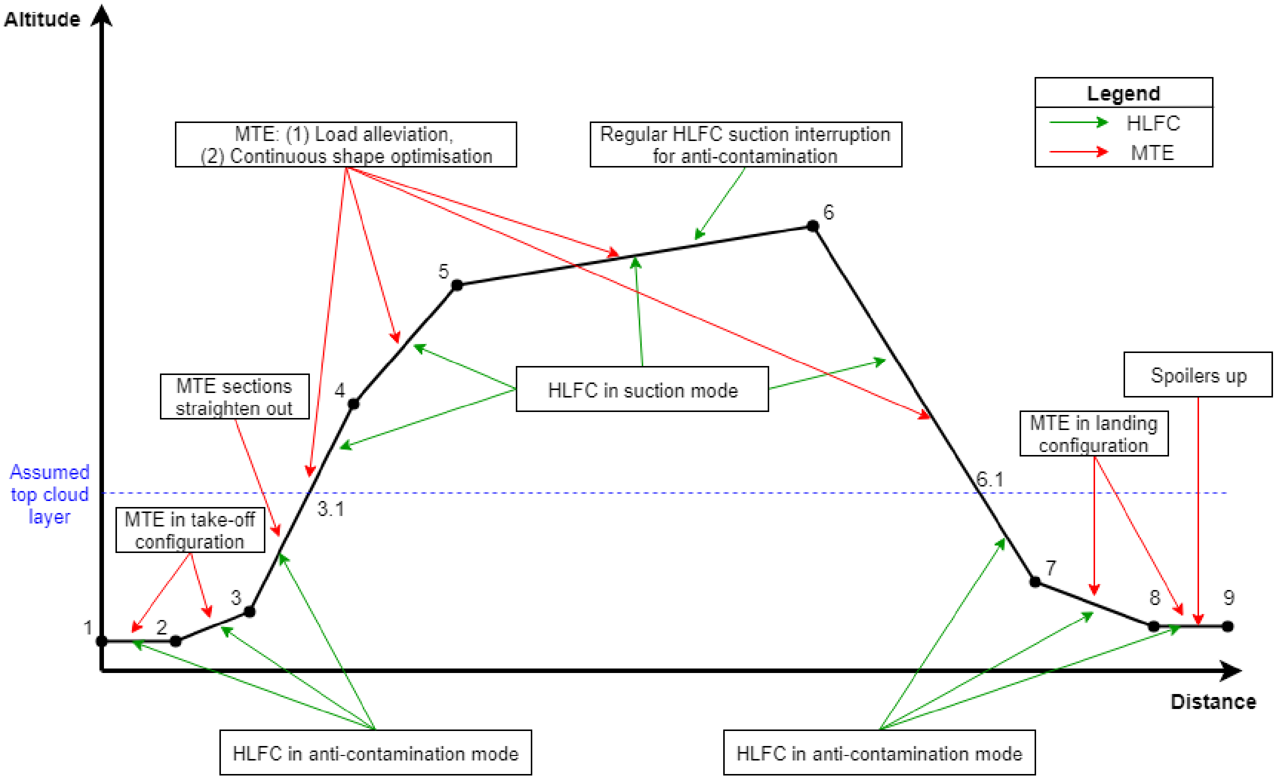

Figure 3.25: Description of the Morphing Laminar Wing activity throughout the mission profile

4

Aerodynamic Analysis

In the following chapter the approach towards the aerodynamic design and analysis of the MLW is discussed. In section 4.1 the methodology is discussed with regards to the workflow and software tools that are applied. In section 4.2 the set-up and modification of the aerodynamic model is discussed. Subsequently to that, the performance of the aircraft is analysed in section 4.3. The embedding of the MTE and HLFC in the aerodynamic model is discussed in section 4.4. In section 4.5 the performance analysis of the benchmark model and the MLW is discussed. Finally the compliance of the aircraft with regards to its take-off and landing performance requirements, the stall characteristics and stability is discussed in section 4.6.

4.1. Methodology

The aerodynamic performance of a commercial aircraft is a critical Intellectual Property (IP) of every Original Equipment Manufacturer (OEM) and this information is not publicly available. In literature, multiple reverse engineering studies were carried out [32] [33]. However, these analyses are based either on experimental data or detailed CFD/numerical simulation of the whole aircraft with internal iterative loops for Multi-Disciplinary Optimisation (MDO) methods. It is unlikely that similar level of fidelity will be achieved within the time and skill constraints of a typical Design Synthesis Exercise (DSE) project. Therefore the need for a simplified consistent aerodynamic & performance analysis methodology occurs, which can be applied on all possible design configurations and the benchmark A320ceo. This methodology does not aim for high accuracy, but rather on verifying the design decisions and their relative effects on the overall aircraft performance.

4.1.1. Tools

A preliminary aerodynamic & performance analysis can be performed using methods with different complexity, accuracy and level of fidelity. Some examples could be simple statistical/analytical DATCOM methods, low fidelity computational fluid dynamic (CFD) simulation tools like XFLR5, AVL or a high fidelity CFD analysis that works for instance with Euler codes. Phenomena like transition from laminar to turbulent flow and 3D downwash angles are part of the design options that should be evaluated. Therefore, the most straight forward approach of using analytically DATCOM methods cannot be used for concepts design and analysis. On the other hand, due to the complexity of the CFD analysis, the team skills and the high Reynolds numbers, achieving and validating even a scaled-down CFD analysis is unfeasible. Therefore, the most suitable approach is to use a fluid-dynamic numerical simulation tool. The tool choice for these simulations is XFLR5 which is based on the XFOIL engine. XFLR5 is a tool capable of simulating both 2D panel analysis and 3D wings using vortex lattice method (VLM) or lifting line theory. Both XFLR5 and it's methods have its own advantages, downsides and limits. Which shall be analysed and corrected with simple MATLAB scripts and DATCOM like approaches. The overall XFLR5 methodology together with the methods and their limitations are briefly explained in subsection 4.1.2.

4.1.2. Aerodynamics theoretical background and limitations

Due to the type of chosen architecture and the focus on aerodynamic performance, the wing-body design is subjected to improvements considering physical phenomenons like laminarity, viscosity and streamline interaction with bodies like the fuselage. These phenomenons are computationally and time demanding for detailed analysis and eliminate the possibility to use a simple 2D strip method with compressibility correction. Therefore, for both benchmarking, concept and final analysis 3D Vortex Lattice Method (VLM) simulations are developed and executed on top of the chosen airfoils simulated with 2D panel method. An overview of the steps and their sequence can be seen in the activity diagram shown in Figure 4.1.

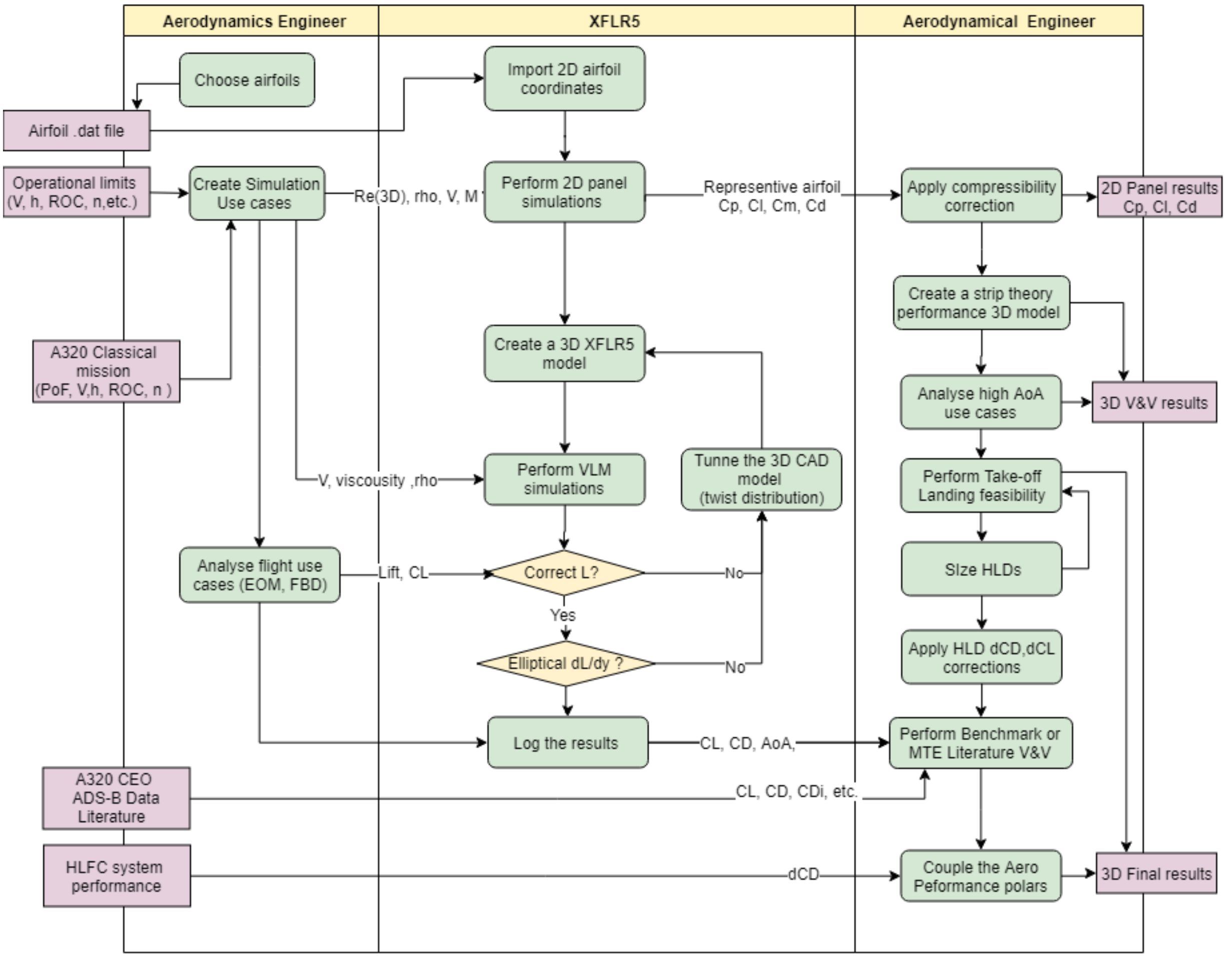

Figure 4.1: Overview of the aerodynamics and performance analysis

4.1.3. Airfoil Panel Method - 2D Batch Analysis

The panel method of XFLR5 is a method for approximating the 2D aerodynamic parameters by calculating vorticity of the panels between the points of the airfoil. The tool achieves that by solving the Kutta conditions, from which it estimates the local tangential velocity and the local pressure. An important characteristic for these airfoil simulations are the number of points describing the airfoil, where the range is limited to a maximum of 300 points. The number of points define the number of panels and consequently the mesh for the simulation. Working with an insufficient number of points can lead to significant deviation on areas with high thickness gradient, as found experimentally when running different test cases of the analysis in XFLR5. Therefore, the maximum of 300 points is used for all airfoils. The method takes into account the Reynolds number (Re), Mach number and the turbulence level of the wind tunnel (N_{crit}). Based on this information it simulates and outputs both viscous and inviscous data like 2D C_P distribution, airfoil C_l,C_d, C_m and transition positions, etc. all depending on the angle of attack (AoA). XFLR5 has a well performing 2D panel analysis, however it is only accurate at low Re numbers, incompressible flow and infinite wings.

4.1.4. Compressibility Corrections for Airfoil Panel Method

XFLR5 and the panel method do not converge well for high AoA and mach numbers (M>0.3), which as previously stated is a need for simulation of Take-off, Landing and Cruise verification. To analyse the airfoils in these flow conditions, first the 2D panel method will be applied at incompressible Mach numbers. This still accounts for the real viscous effects with Re derived from V_{TAS} and the local μ_{kin} for the real geometry. Then by applying a compressibility correction on top of the Cp distribution and lift/drag polars, both the effects of viscosity and compressibility are accounted for in the 2D simulations. In literature multiple corrections have been studied and derived [5], however due to the transonic Mach number and inaccuracy of Prandtl-Glauert rule the more sophisticated Karman-Tsien rule shown in Equation 4.1 is used. Note that the airfoil will not account the M_∞ due to the sweep angle ($\Lambda_{0.25c}$), but a cosine of the free stream velocity.

$$Cp = \frac{Cp_0}{\sqrt{1-(M_\infty cos(\Lambda_{0.25c}))^2} + [M_\infty^2/(1+\sqrt{1-M_\infty^2})]Cp_0/2} \tag{4.1}$$

4.1.5. 3D Vortex Lattice Method

The VLM is a numerical method for estimating the 3D aerodynamic performance of a wing-body model, and accounts for the effects of sweep more accurately. The VLM discretises the MLW to a finite mesh of span wise strips and chord wise panels between the strips. Every lattice panel has assigned a horseshoe vortex at $\frac{1}{4}$c. The intensity of the panel vortex is evaluated by satisfying the boundary conditions at the $\frac{3}{4}$c with the Biot-Savart law, Kutta conditions and satisfaction of the tangency criteria for the control points.

Like every numerical method, the VLM has its assumptions and limitations. The first one is the assumption that the free stream flow is incompressible and inviscid. Since this is not true for a typical commercial aircraft, a significant deviation from the real values is expected. The assumption will cause errors for twist tuning and lift distribution. However, the analysis in this report will be mainly used for trade-off comparison of the same wing planform and therefore the error is not expected to cause significant comparable deviations.

The second assumption is that all airfoils in the VLM 3D wing have small thicknesses. The airfoils used in the simulations are between 10.8% and 15.2% of the chord and therefore negligible deviations are expected for small AoA. The effects for high AoA however will be considerable both due to errors from 2D analysis and the VLM. Lastly, the VLM uses small angle approximation for AoA and β. This approximation is used in the performance parameters like the C_L downwash angles. Also taking into account deviations for the 2D lift and drag polars at high AoA, it can be concluded that XFLR5 and any other tool using VLM cannot be used for phases of flight (PoF) like take-off, landing or steep climb.

4.1.6. Aerodynamics and Performance Software Architecture

As it will be explained more in detail a decoupling of the aerodynamic effects of HLFC and MTE will be performed. This allows for a decreasing complexity and implementing a pseudo optimisation algorithm with multiple configurations for the MTE system. The MTE design allows an improvement of the cruise performance of the aircraft by deflections of the MTE depending on the freestream conditions and the mass of the aircraft. To analyse this improvement a need for a fast, iterative way of creating, modifying and analysing various 3-hinged MTE configurations on the aircraft model is necessary. However, in XFLR5 this is a tedious process taking around 15 minutes per wing section configuration per freestream conditions. Having nine airfoil sections on the MLW and the desire to analyse for nine different freestream conditions of 40 configurations will cause a manual work load of about 810 hours. From this it is clear that a high degree of automation of the process is necessary.

Unfortunately, XFLR5 does not posses any 3D iterative capabilities or even the function of creating multi-hinged MTE flaps. However, XFLR5 can import XML files for aircraft geometry, a corresponding airfoil selection and the freestream analysis configuration file linked to the name of the aircraft. This together with an algorithm modifying the airfoil geometry files for creating the 3-hinged MTE deflection is assumed to be a sufficient level of automation. The estimations show a process automation of about 98%-99% of the manual work, not accounting the time for Research & Development (R&D) activities - about 2-3%.

Given the amount of pre-processing tasks this analysis becomes a complex software architecture problem on its own involving multiple tools and programming languages (C++, FORTRAN, MATLAB). A software diagram showing the four automation algorithms and all other smaller design scripts is presented in Figure 4.2. In the diagram the three MATLAB generators and their main functions are displayed. First by executing the MTE Airfoil Generator, the MATLAB script reads the original airfoil coordinates from a folder and performs their rotation around the three hinge lines. This generates new airfoils as .dat files for the different MTE deflections. Then the XML 3D Aircraft Configuration Generator reads all .dat files and generates multiple aircraft configurations. These are created for different airfoil deflections and use the exact geometry of the fuselage as well as horizontal and vertical stabiliser, which is assumed to have constant deflection angle. Lastly the XML Analysis Generator creates the final input file for setting up the freestream conditions and extra drag coefficients like for example the engines and nacelles.

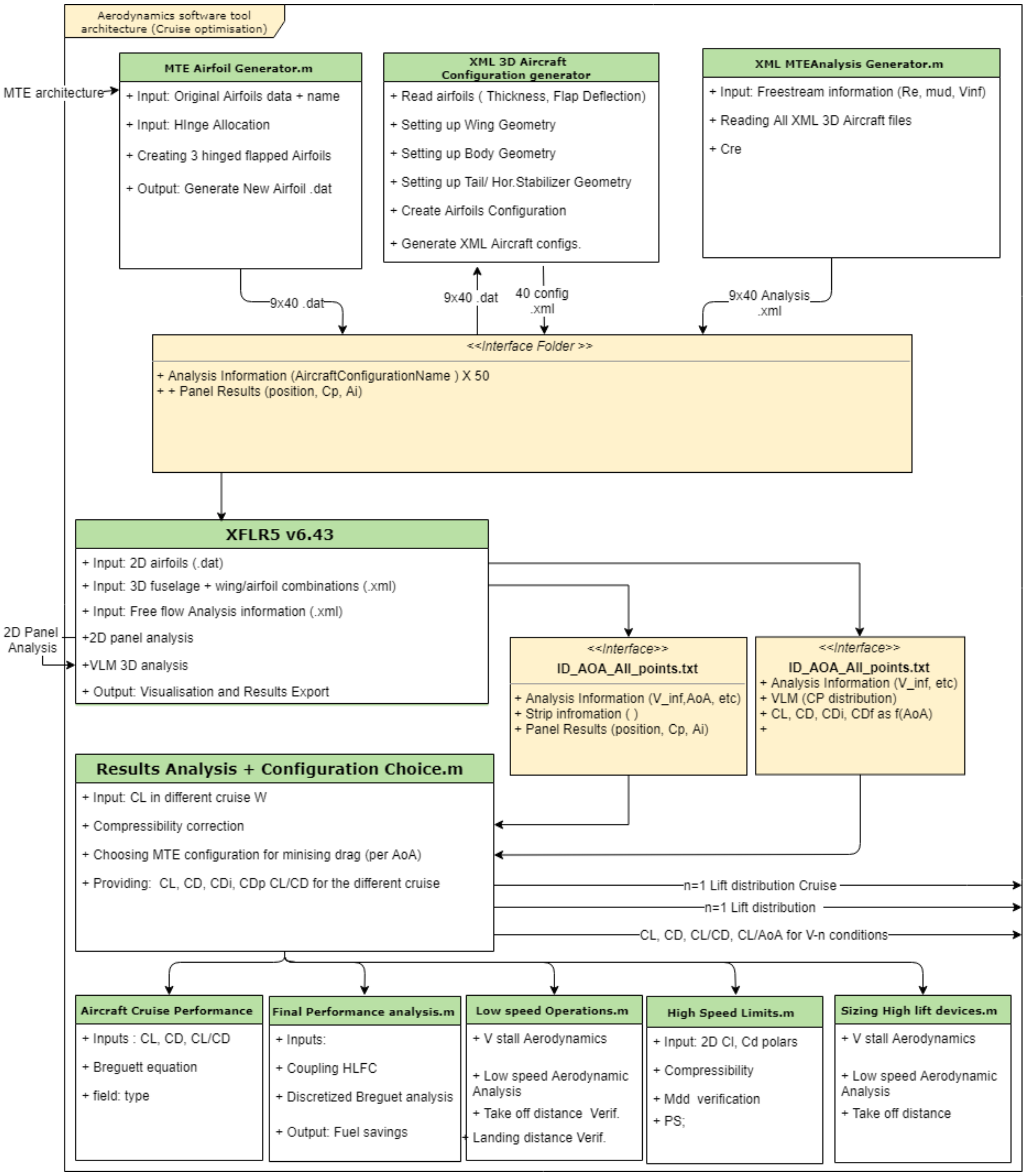

Figure 4.2: Software architecture for pseudo-optimisation design

Once generated, all these input files are imported into the XFLR5 tool and go through XFOIL 2D panel analysis for the expected 3D Re. Then the aircraft VLM analyses are imported and executed one by one for a specific range of

AoA. Lastly output files are automatically generated by XFLR5 for every freestream condition and for every aircraft configuration (MTE setting). These text files are read together by another MATLAB script, which calculates the expected C_L for the particular mass and freestream and outputs the most efficient MTE configuration (max CL/CD). These configurations are coupled later on with the HLFC and are used in the typical preliminary aircraft sizing and verification & validation procedures, discretised Breguett Range equation, load estimations for critical cases (V-n), etc.

The current limitations and consequently further recommendations are related to performing direct interface between the MATLAB code, XFLR5 2D panel analysis and 3D VLM. Activities like importing every freestream analysis file per aircraft configuration and starting its execution in XFLR5 are still manual. This limits the scalability of the tool to an approximate three-digit number of iterations. Automation of this process requires the development of an interface between the source code of the XFLR5 Graphical User Interface (GUI) and MATLAB, which is not possible due to limited resources. On a side note such an interface would be a benefit for the whole aerospace community by providing an end-to-end tool for fast and iterative numerical aerodynamic analysis with sufficient accuracy and GUI.

4.2. Aerodynamic Model

In the following section the aerodynamic model and the characteristics of both the benchmark aircraft as well as the new configuration are discussed. This addresses the selection of airfoils, the set-up and tuning of the aircraft model and the determination of the aerodynamic loads acting on the structure.

4.2.1. Airfoil Selection

A set of airfoils is chosen for the reversely engineered design of the benchmark aircraft, which serves as the basis for the optimisation of the MLW that includes a new set of airfoils. As one of the primary means to achieve a reduction in drag is an extended region of laminar flow over the wing, an investigation into the the most optimum selection of airfoils is required. In Table 4.1 characteristics of the various airfoils that were analysed can be found.

A well known family of airfoils that was developed for the purpose of combining a good transonic behaviour with acceptable low-speed characteristics are the NASA supercritical airfoils [6]. These airfoils are characterised by a large leading edge radius, a minimal curvature on the upper surface as well as a significant camber at the trailing edge. Possible candidates within that family are the SC(2)-0410 airfoil and the SC(2)-0612 airfoil which could be applied at the tip and the centre section of the wing respectively. Another profile that is similar in its characteristic is the Whitcomb airfoil, that originates from the same time period where NASA's supercritical airfoils were developed. Next to its supercritical airfoils, NASA developed the HSNLF(1)-0213 airfoil [34] which has the objective to maximise laminar flow on the upper and lower surface at transonic speeds.

Airfoils by Boeing include the Boeing J airfoil and the Boeing BACXX airfoil, which was developed in the context of NASA's Energy Efficient Transport Program [35] in 1976. Another Boeing airfoil that is highly interesting with respect to the use on the MLW is the Boeing HSNLF airfoil [36]. It combines the characteristics of a supercritical airfoil with the the geometrical features of a laminar flow airfoil such as a small leading edge radius and the point of maximum thickness at a relatively far aft position. Two transsonic airfoils by Grumman are the K-1 and K-2 airfoils, whereas the K-2 airfoil has extended supercritical characteristics. Two more transsonic airfoils that are part of the analysis and trade-off are the NPL 1372 and NPL 1950 airfoils [37], which were developed by the National Physical Laboratory in Great Britain. Another set of British airfoils are the RAE 5212, RAE 5213, RAE 5214, RAE 5215 as well as the RAE 2822 airfoil, whereas the RAE 2822 is a more recent airfoil that has natural laminar flow characteristics due to its small leading edge radius and thickness distribution.

In order to analyse and choose the optimum airfoils for the wing, the candidates given in Table 4.1 are investigated with respect to their position at three different positions in spanwise direction. These include the root and tip section of the wing, as well as the section about half-span where the taper ratio changes. In literature [38] the thickness of the wing sections at these locations for an A320 aircraft is described as 15.2 %, 11.8 % and 10.8 % from root to tip respectively. Assuming that cruise flight was the driving factor with regards to the performance aspect of the wing design, the airfoils given in Table 4.1 are analysed at the Reynolds numbers $9e^6$, $22e^6$ and $36e^6$ of the three wing sections. These correspond to a cruise flight altitude of 39,000 feet and a cruise speed of M equal to 0.82.

Airfoil	Thickness	Camber
NASA HSNLF(1)-0213	13.3% @ 43.3%	1.31% @ 33.3%
NASA SC(2)-0410	10% at 38%	1.1% at 85%
NASA SC(2)-0610	10% at 38%	1.8% at 82%
NASA SC(2)-0710	10% at 37%	2.1% at 81%
NASA SC(2)-0412	12% at 37%	1.3% at 83%
NASA SC(2)-0612	12% at 37%	1.9% at 81%
NASA SC(2)-0712	12% at 37%	2.2% at 81%
NASA SC(2)-0414	14% at 36%	1.5% at 83%
NASA SC(2)-0614	14% at 36%	2.1% at 81%
NASA SC(2)-0714	14% at 37%	2.5% at 81%
Boeing J	10.1% at 40%	1.7% at 78%
Boeing BACXX	11.3% at 35%	1.4% at 15%
Boeing HSNLF	10.1% at 43.7%	1.3% at 76.7%
GRUMMAN K-1	11.6% at 33%	1.9% at 75%
GRUMMAN K-2	10.3% at 38.9%	1.3% at 88.3%
NPL 1372	10.7% at 35.8%	1.1% at 73.7%
NPL 9510	11.1% at 32%	1.6% at 80%
Whitcomb	11% at 35%	2.4% at 82.5%
RAE 2822	12.1% at 37.9%	1.3% at 75.7%
RAE 5212	11.9% at 35.5%	1.8% at 69.1%
RAE 5213	10% at 35.5%	1.4% at 69.1%
RAE 5214	9.7% at 35.5%	1.4% at 69.1%
RAE 5215	9.7% at 35.5%	1.5% at 69.1%

Table 4.1: Airfoil characteristics

While in case of the selection of airfoils for the MLW the mere objective is to determine the highest performing airfoils for their respective locations, for the benchmark model other aspects such as the time period when the airfoils where designed as well as their intended application have to be considered. In order to improve upon the drag characteristics of NACA 6-series airfoils at transonic speeds, NASA developed a family of supercritical airfoils [6] in the 1970's. Ranging from a thickness of 10 % to 14 % and a design C_l of 0.4 to 0.7, these airfoils are suitable for the application on a transport aircraft cruising at transonic speeds. Due to the time-wise proximity of their development to the beginning of the A320 programme and their intended purpose, the SC(2)-0414, SC(2)-0612 and SC(2)-0710 are chosen for the three wing sections from root to tip respectively. In Figure 4.3 the outline of the these airfoils can be found.

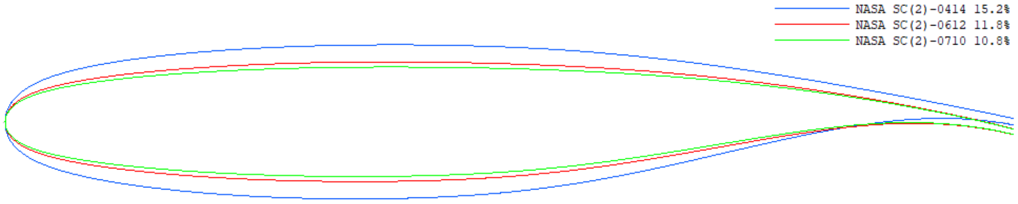

Figure 4.3: NASA SC(2)-0414, SC(2)-0612 and SC(2)-0710 airfoils

While the first two digits of the SC-airfoils relate to the design C_l, the last two digits refer to the thickness in % of the chord. The design C_l's of 0.7 at the tip, 0.6 in the centre and 0.4 at the root of the wing closely relate to the the C_l's at these locations of the wing of the three dimensional model that is discussed later in this section. In order to comply with the actual thickness of the three wing sections, the airfoils were scaled to 15.2 %, 11.8 % and 10.8 % thickness prior to analysis. The C_l/C_d graphs of these airfoils can be found in Figure 4.4 and the $C_l - \alpha$ graphs in Figure 4.5.

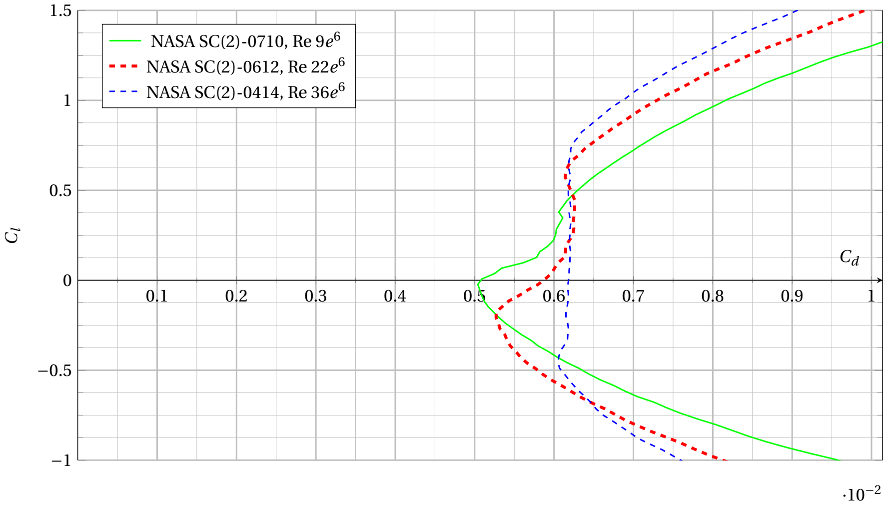

Figure 4.4: C_l/C_d graph of NASA SC(2)-0710, SC(2)-0612 and SC(2)-0414 airfoils

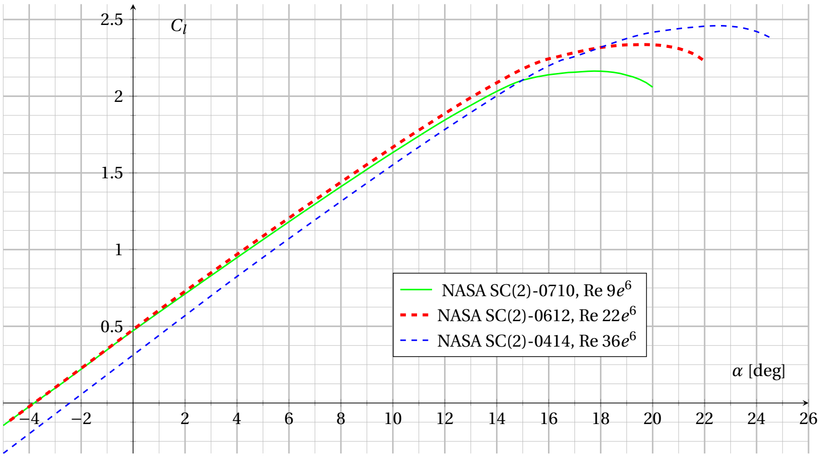

Figure 4.5: $C_l - \alpha$ graph of NASA SC(2)-0710, SC(2)-0612 and SC(2)-0414 airfoils

One of the objectives of the design of the new wing configuration is to obtain a larger region of laminar flow over the wing and by doing so contributing to the decrease in overall drag of the aircraft. While chapter 3 discusses the achievement of this goal by active laminar flow control through suction, an increase in laminar flow can partially be achieved through the selection of the right set of airfoils. Airfoils in Table 4.1 that have natural laminar flow characteristics are the NASA HSNLF(1)-0213, RAE 2822, Grumman K-1, Grumman K-2, Boeing J and Boeing HSNLF airfoils. Similarly to the analyses of the benchmark airfoils, these airfoils are scaled to a thickness of 15.2 %, 11.8 % and 10.8 % that corresponds to the different sections along the span of the wing. Through analysis the Grumman K-1, RAE 2822 and Boeing HSNLF airfoils can be found as optimal for the root, centre and tip section in respective order and can be outlined as found in Figure 4.6.

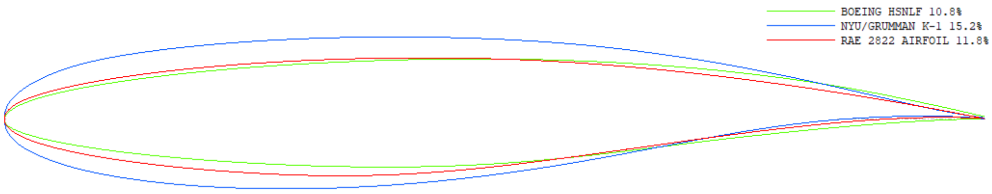

Figure 4.6: Boeing HSNLF, Grumman K-1 and RAE 2822 airfoils

The C_l/C_d and the $C_l-\alpha$ graphs of the Grumman K-1, RAE 2822 and Boeing HSNLF airfoils can be found in Figure 4.7. In case of the Boeing HSNLF airfoil, at a Reynolds number of $9e^6$ a laminar bucket can be found in the C_l/C_d diagram in the close vicinity around the AoA $\alpha = 0$. The RAE 2822 airfoil which is analysed at a Reynolds number of $22e^6$ also has the occurrence of a laminar bucket, however it is less pronounced than in case of the Boeing HSNLF airfoil. While it turns out that at a Reynolds number of $36e^6$ the Grumman K-1 airfoil shows no laminar bucket, it is evident that its performance is far superior to the NASA SC(2)-0414 in Figure 4.4 which is used at the root of the wing of the benchmark model.

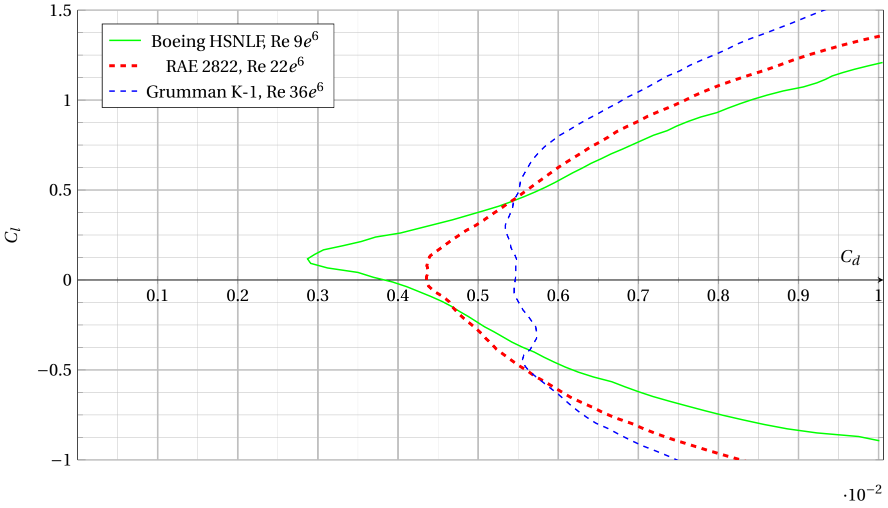

Figure 4.7: C_l/C_d graph of Boeing HSNLF, RAE 2822 and Grumman K-1 airfoils

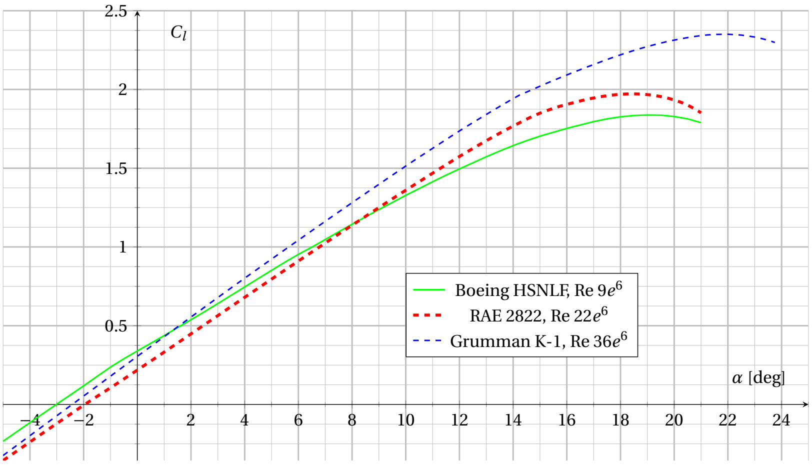

Figure 4.8: $C_l - \alpha$ graph of Boeing HSNLF, RAE 2822 and Grumman K-1 airfoils

4.2.2. Aircraft Model

In order to analyse the modifications made to the benchmark A320 wing as well as the effect of the systems discussed in chapter 3 with respect to the entire aircraft, a complete model of the entire aircraft has to be used. For this purpose a model in XFLR5 is created, which includes the wing, fuselage, horizontal and vertical tail. All these elements are represented in the form of panels, and their effect is taken into account using the vortex lattice method. For the horizontal and the vertical tail the NACA 0012 airfoil is used for the root section and the NACA 0009 airfoil is used for the tip section as suggested in [7]. Elements such as the engines, actuator fairings and gaps in between the wing and retracted flaps or slats cannot be modelled in the program. The effect of these elements on the drag is taken into account by using the exposed areas of these elements and their respective drag coefficients that are elaborated in [7] and [39]. While in case of the benchmark model the effects of all elements have to be considered, for the optimised model only the engines are of importance. Actuator fairings are not existent as discussed in chapter 3 and the use of a continuous morphing trailing edge and a Krueger flap eradicates the drag due to discontinuities on the wing surface. In Figure 4.9 and Figure 4.10 various views of the 3d-model that is used in XFLR5 can be found, while in Figure 4.11 the panels used for the analysis can be seen.

Figure 4.9: XFLR5 Rendering Top view and front view

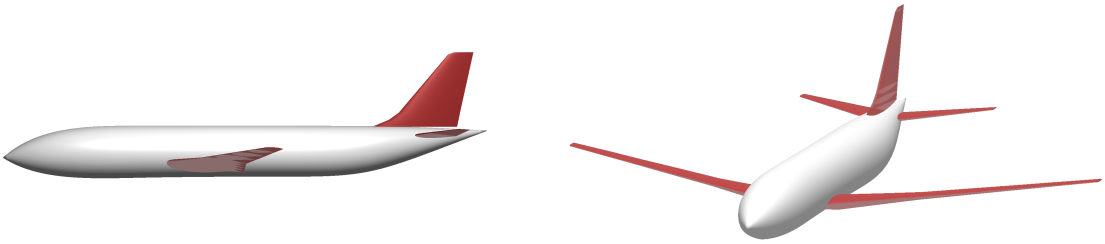

Figure 4.10: XFLR5 Rendering Side view and front view

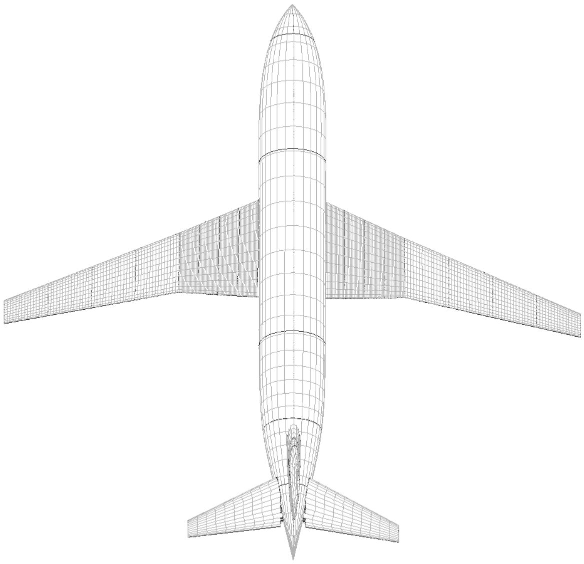

Figure 4.11: VLM Panels Distribution

Using the sets of airfoils that are described in subsection 4.2.1, the twist distribution of the two models can be fine-tuned. This is done using the assumption that the twist is optimised to achieve an elliptical lift distribution at a cruise speed of Mach 0.82 and a cruise altitude of 39,000 ft. An elliptical lift distribution corresponds to a constant downwash over the span of the wing, which is associated with minimum induced drag. The AoA of the aircraft for this cruise configuration is assumed to be zero. In Figure 4.12 the achieved lift distribution can be found in relation to the ideal elliptical case. The drop in lift in the centre of the graph arises due to the fuselage.

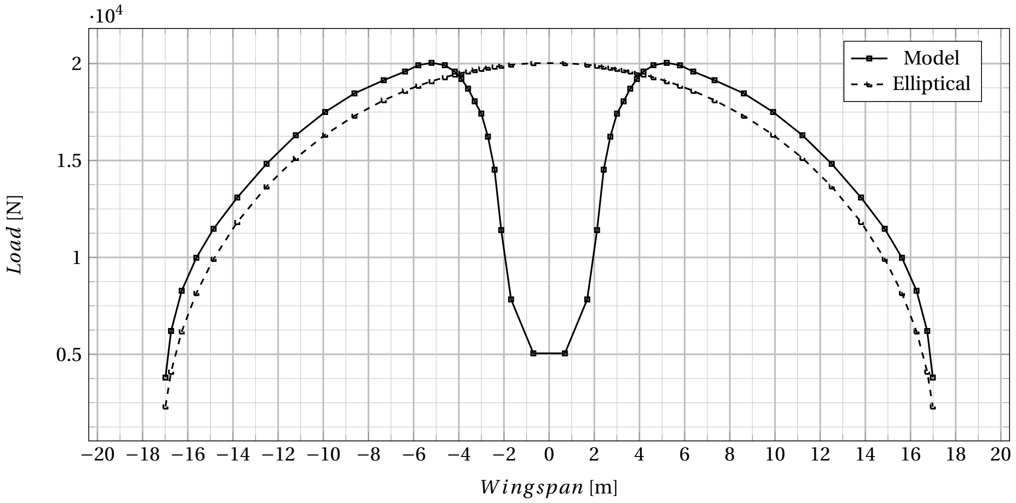

Figure 4.12: Model vs. Elliptical Load Distributions

In case of both models there are a total of nine airfoil sections from the root of the wing to the tip. The airfoils that are located at the sections in between the sections for which the airfoils are selected, as described in the previous paragraphs, are defined using linear interpolation between the selected airfoils. The distribution of the different sections and their respective characteristics can be found in Table 4.2. In [40] the reference value of the centre of gravity within its allowable range is at 33 % of the mean aerodynamic chord. Taking this location of the centre of gravity into account, both aircraft are trimmed such that C_m is equal to zero at $\alpha = 0$, whereas the effect of the tail and the fuselage is taken into account.

Section	**1**	**2**	**3**	**4**	**5**	**6**	**7**	**8**	**9**
Chord [m]	6.070	5.488	4.905	4.322	3.740	3.180	2.620	2.060	1.500
Spanwise Pos. [m]	1.975	3.150	4.325	5.500	6.675	9.269	11.863	14.456	17.050
Reynolds No. x10^6	35.99	23.30	29.08	25.63	22.17	18.85	15.53	12.21	8.89
Thickness [%]	15.20	14.35	13.50	12.65	11.80	11.55	11.30	11.05	10.80
Benchmark Twist [deg]	6.50	5.70	5.03	4.78	4.53	4.20	3.70	3.00	2.40
Optimised Twist [deg]	7.35	7.05	6.75	6.45	6.15	5.65	5.02	4.35	3.55

Table 4.2: Wing Sections

The distribution of the thickness of the wing sections along the span of the wing as presented in Table 4.2 can be visualised as seen in Figure 4.13. While the thickness distributions remain to be the same for both models, the twist distributions vary for the benchmark configuration and the optimised configuration due to the different choice of airfoils. In Figure 4.14 the graphs that correspond to the two distributions can be found.

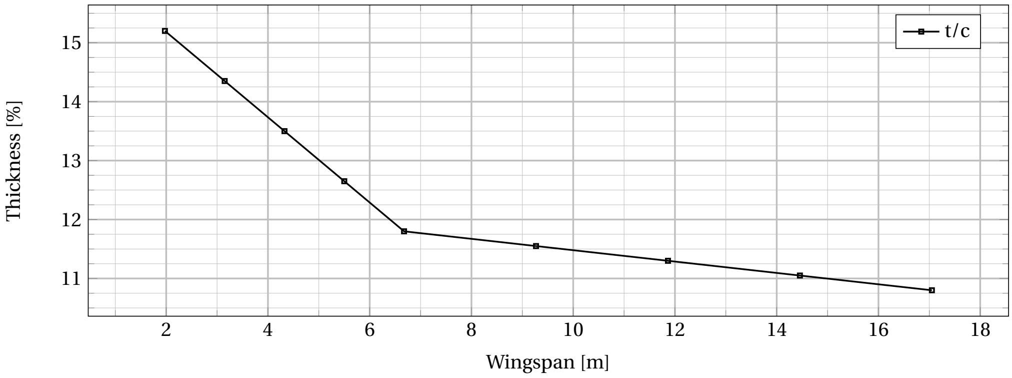

Figure 4.13: Thickness Distribution

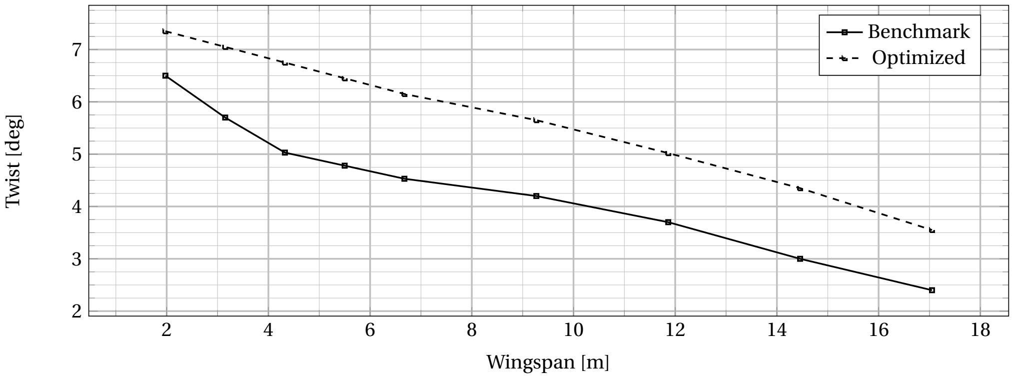

Figure 4.14: Twist Distribution

4.2.3. Verification and Validation of the Aircraft Model

In order to ensure that the configuration of the benchmark aircraft model is in the close proximity to the actual configuration with regards to its geometry it needs to be validated. As the actual airfoils used for the wing of the A320 are intellectual property of Airbus and are not publicly available, they cannot be used for the purpose of validation. While elements such as the shape of the fuselage as well as the horizontal and vertical stabilisers do not have complex shapes that need to be tuned, the twist distribution of the wing is fine-tuned in order to achieve an elliptical lift distribution in mid cruise flight condition and should therefore be validated as it effects the following steps of the analysis significantly. In Figure 4.15 the wist distribution of the actual A320 wing can be found as defined in [38].

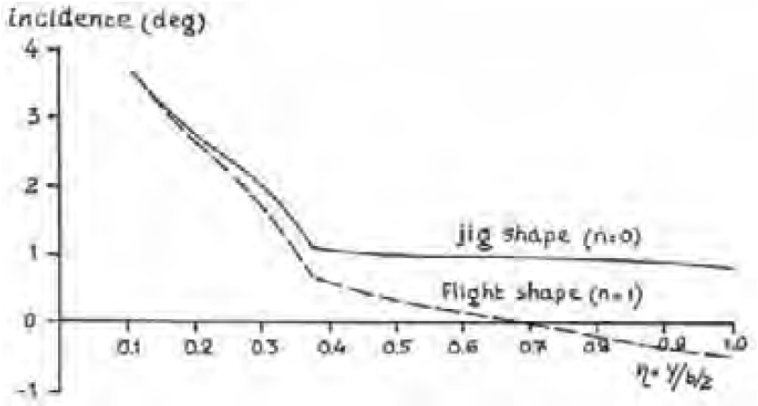

Figure 4.15: A320 twist distribution

Comparing this twist distribution in its flight shape at n=1 to the twist distribution created for the benchmark aircraft in Figure 4.14, it can be found that the overall shape is similar including the kink at around one third of the span, as seen from the root, where the slope of the twist changes. While in case of the actual A320 wing the shape of that kink is rather abrupt at the location where the taper ratio changes, the change in twist of the wing of the benchmark model is more subtle and begins closer to the root. Noticeably is the fact that while in both cases the difference between the incidence angle at the root and the tip of the wing is approximately equal to 3 degrees, the entire twist distribution of the wing of the benchmark aircraft in Figure 4.14 is shifted upwards with respect to the twist of the actual wing in Figure 4.15.

The slightly different shape of the two twist distributions with regards to the location of the kink as well as the kink's peculiarity can be attributed to the fact that the actual airfoils of the A320 most likely differ from the ones that where selected for the benchmark aircraft wing as discussed in section 4.2, but also the flow phenomena and effects of compressibility that cannot be accurately taken into account. The upwards shift of the lift distribution of the benchmark model with respect to the actual wing of the A320 can be explained by a different AoA for which the actual aircraft is most likely tuned in cruise flight condition. While in case of the benchmark model it is assumed that the AoA of the aircraft is equal to zero at amid cruise, it can be reasoned that the twist distribution presented in Figure 4.15 assumes a positive AoA of about three degrees. As the differences between the two twist distributions can be attributed to differences between the airfoils used as well as a different design AoA, it can be concluded that that the twist of the wing of the benchmark model is acceptable and therefore the benchmark model is qualified to serve as the reference for the aerodynamic analysis in the following sections.

4.3. Mission Analysis

In order to draw conclusions on the aerodynamic performance of the benchmark model and the MLW model, it is essential to analyse the whole mission profile of the flight that includes the different climb phases, the cruise flight as well as the different descent phases. The European air traffic control agency [1] has published characteristics of an average mission of an A320 as defined in Table 4.3. As the cruise flight is the major PoF, it is separated into different sub-phases and included in the table. The cruise profile of an A320 as a function of its mass and the cruise speed is given in the A320 Flight Crew Operation Manual [9]. Starting with an altitude of FL 290 at the beginning of the cruise, the cruise altitude gradually rises to FL 390 as the aircraft burns fuel during the cruise. This is due to the aerodynamic layout of the benchmark aircraft which is optimised for a certain lift coefficient C_L for cruise flight. While the mass of the aircraft decreases as described in subsection 4.5.2, the aircraft has to climb to an altitude with a lower air density in order to keep flying at this optimum C_L that corresponds to the maximum C_L/C_D.

Flight Phase	Velocity	Rate of Climb
No.1: Initial Climb 0 to 5000 ft	175 kts	2500 ft/min
No.2: Climb 5000 ft to FL 150	290 kts	2000 ft/min
No.3: Climb FL 150 to FL 240	290 kts	1400 ft/min
No.4: Climb FL 240 to FL 290	M 0.78	1000 ft/min
No.5: Cruise FL 290 to FL 310	M 0.82	35.26 ft/min
No.6: Cruise FL 310 to FL 330	M 0.82	34.95 ft/min
No.7: Cruise FL 330 to FL 350	M 0.82	34.64 ft/min
No.8: Cruise FL 350 to FL 370	M 0.82	34.33 ft/min
No.9: Cruise FL 370 to FL 390	M 0.82	34.32 ft/min
No.10: Descent FL 390 to FL 350	M 0.82	-1000 ft/min
No.11: Descent FL 350 to FL 310	M 0.82	-1000 ft/min
No.12: Descent FL 310 to FL 240	M 0.78	-1000 ft/min
No.13: Descent FL 240 to FL 100)	290 kts	-3500 ft/min
No.14: Approach	250 kts	-1500 ft/min

Table 4.3: Mission Profile of A320 as defined by European air traffic control agency

In case of the MLW model the main feature that affects the cruise performance is the MTE as discussed in chapter 3.

---

[1] Eurocontrol. Aircraft performance database.https://contentzone.eurocontrol.int/aircraftperformance/details.aspx?ICAO=A320

Deflecting the trailing edge up- or downwards allows to shift the C_L/C_D curve of the aircraft resulting in a range of optimum lift coefficients. It is expected that this ability allows to optimise the configuration of MLW continuously to achieve maximum efficiency. While the benchmark aircraft with its fixed trailing edge is constrained to the mission profile presented in Table 4.3, this does not necessarily apply to the new concept with the MTE. While the MLW is likely to show a performance improvement over the benchmark aircraft due to the change in airfoils, removal of actuator fairings, a smoother wing surface as well as boundary layer suction, there is the possibility that the full potential of the MTE design can only be determined when investigating a different cruise profile. A feasibility study is therefore undertaken that has the objective to determine whether a different mission profile may indeed have the potential to lead to a better overall performance. Due to the limited scope of the project only one further mission profile is investigated, with the underlying assumption that a decreased air density will lead to a decrease in drag. In the A320 Flight Crew Operating Manual [9] the maximum cruise altitude is 39,000 ft, which also corresponds to the the final altitude of the specified optimum cruise flight profile. It is therefore assumed that the altitude of 39,000 ft is the maximum altitude at which the aircraft is able to operate, taking aspects such as the pressurisation of the cabin or the engines into account. This altitude is therefore selected to serve as the reference altitude for the feasibility study that considers the case of a constant cruise altitude that does not change. While in case of the benchmark aircraft the climb is finished at an altitude of 29,000 ft from where it proceeds into a cruise phase with a constantly increasing altitude, the alternate climb of the aircraft using the new concept continues all the way to 39,000 ft where it begins it cruise without making further changes in height.

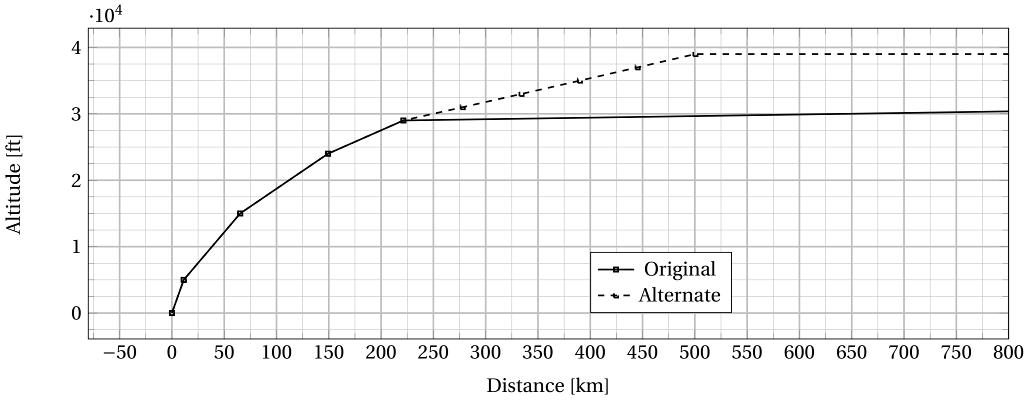

Figure 4.16: Original and alternated profile of the benchmark and optimised model

In order to compare the performance of the MLW model with the one of the benchmark model but also analyse it with respect to its potential at a different cruise layout, it is analysed with regards to the original mission profile as well as one with a constant cruise altitude of 39,000 ft, whereas the benchmark model is only analysed at the original cruise profile. The optimum design range that is used as the foundation for the mission profile is specified as 4,774 km [8]. Combining this range with the information given in Table 4.3, the mission profile in is created. For an enhanced readability of the graph with regards to the climb and descent phases, the mission profile is split into two diagrams in Figure 4.16 and Figure 4.18.

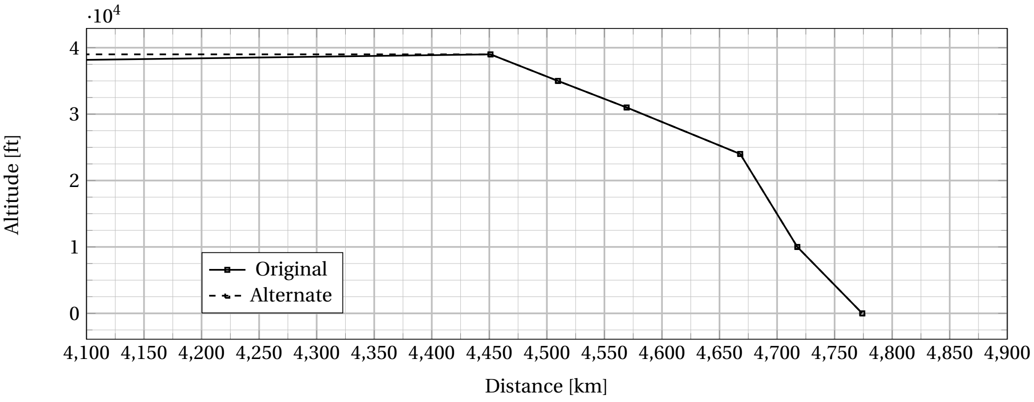

Figure 4.17: Original and alternated profile of the benchmark and optimised model

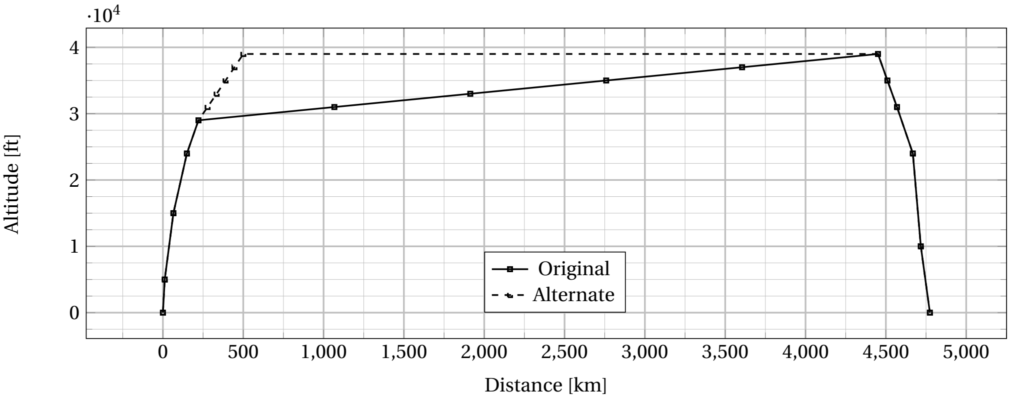

Figure 4.18: Original and alternated profile of the benchmark and optimised model

The mission profile of the flight portrayed in Table 4.3 includes various phases of climb and descent that are of interest when investigating the possibility to decrease drag through the continuous adaption of the MTE. However, in comparison to the different cruise segments of the mission the initial three climb phases as well as the final two descent phases and approach are insignificant with regards to their time fraction. These phases are therefore not subject to the analysis at this stage of the investigation, they should be included though in a subsequent more detailed study on the matter. The phases considered therefore include phase 4 up until including phase 11 as presented in Table 4.3.

4.4. Aerodynamic System Analysis

In order to achieve a significant decrease in the amount of drag that the wing creates, next to the new set of airfoils, the MTE and HLFC are used (as seen in chapter 3). In this section the embedding of these systems into the aerodynamic model is discussed.

4.4.1. HLFC Aerodynamics

Predicting the performance of the suction system is normally a task requiring dedicated software and resources since it is a CFD exercise in any industrial application. There is currently no publicly available tool that would treat the combined suction and transition location problem on high speed aircraft with swept wings. That is mostly because estimating the transition location prior and after suction is a very complex problem, which cannot be solved analytically due to multiple different transition mechanisms that are present. After discussing with *TU Delft* experts of the boundary layer suction on gliders, it was decided that the best results with the existing resource constraints would be achieved by applying friction coefficient estimations based on flat plate theory.

Estimation Method

To begin with, the following assumptions were necessary to establish a drag benefit analysis using flat plate flow theory:

- Wing airfoils are assumed to be thin (required by the approach) [5]
- The mean Reynolds number is assumed to be $Re_c = 30 \cdot 10^6$. Spanwise variations of Re_c are not taken into account because they are in the same order of 10^6 and only cause a minimal effect on the variation of local friction coefficient
- Suction area occupies only the upper wing surface from the leading edge up to the front spar as explained in chapter 3. This is entirely a design option that was chosen for this concept. Lower part of the leading edge could not be equipped with suction due to limitations caused by leading edge high lift devices
- Spanwise natural transition (without suction) locations are obtained from the benchmark aircraft aerodynamic analysis, made on $XFLR5$. On average, this results in transition at about 5% of chord on the top surface and 50% on the bottom surface in cruise conditions. Note that the transition prediction in the tool used only treats one transition trigger - the Tollmien Schlichting waves, which means that estimation has a restricted accuracy[2]. However, a better estimation is unachievable with the current resources
- Transition point on the top surface of the wing is postponed by $2.5 \cdot (x/c)_{suction}$, when HLFC is used. This is a literature-based conservative estimate comprising of B757 and Dassault Falcon 50 wing HLFC tests as well as A320 vertical fin suction system test [10]. All these three examples are comparable to the design conditions for the developed concept in this project, since the operational Mach number is very similar and all of the tested surfaces have a quarter chord sweep of at least 20°. Therefore, this assumption is anticipated to be accurately describing the suction system effects
- Laminar skin friction coefficient does not require a compressibility correction, because the effect of reduced density is simultaneously cancelled out by the increase in viscosity. Compressibility correction to the turbulent skin friction coefficient is done by the factor $(1-0.09M^2)$ [39]

With the assumptions known and stating that transition from laminar to turbulent happens at location x of the chord c, the laminar skin friction drag coefficient can be expressed as follows [5].

$$C_{f,lam,x} = \frac{1.328}{\sqrt{Re_x}} = \frac{1.328}{\sqrt{Re_c}}\sqrt{\frac{x}{c}} \tag{4.2}$$

As for the turbulent skin friction drag coefficient, the following experimental relation was used, which is valid for Reynolds numbers between $10^6 - 10^9$ and includes the compressibility correction factor [39].

$$C_{f,turb,x} = \frac{0.455}{(log_{10}(Re_x))^{2.58}}(1-0.09M^2) = \frac{0.455}{(log_{10}(Re_c\frac{x}{c}))^{2.58}}(1-0.09M^2) \tag{4.3}$$

Taking into account Equation 4.2 and Equation 4.3, a total skin friction coefficient can be calculated for one side of the surface by the following [5]:

$$C_{f,total} = \frac{x}{c}C_{f,lam,x} + C_{f,turb,c} - \frac{x}{c}C_{f,turb,x} \tag{4.4}$$

Using the approach explained above, the C_f coefficient is then calculated for three types of surface definitions: Top wing surface with no suction, bottom wing surface with no suction and top wing surface with suction. These coefficients are then implemented in the friction drag equation $D_f = q_{inf} S_{surface} C_f$ and a comparison is made between the benchmark aircraft values and the developed concept with suction. Results of this analysis indicate, that the HLFC suction system allows the total aircraft drag to be decreased by 3.5%. This quantity will be added to the drag benefits, resulting from other drag decreasing mechanisms of MLW.

Model Verification and Validation

Intermediate steps have been taken, in order to verify and validate whether the performance tool was written correctly. Firstly, verification was performed on the tool segment that calculates the laminar and turbulent skin friction

---

[2] `http://web.mit.edu/aeroutil_v1.0/xfoil_doc.txt`

coefficients. While laminar skin friction coefficient estimation is elementary, turbulent skin friction coefficient has an additional term that corrects for the compressibility effect. In order to investigate, whether this correction is used appropriately, a different source was acquired to compare the turbulent skin friction coefficients for the appropriate Reynolds and Mach number [41]. The comparison concluded no differences in the results, as expected.

A validation step was done on wing area calculations as well. Since the tool created requires to have the ability of calculating chord length at any given spanwise location, the correctness of this interpolation can be checked by calculating the total wing area from a few wing sections, split randomly. For the verification, it was chosen to calculate wing area from four trapezoidal sections - from root to first intermediate location on the inboard part of the wing (before kink), from that intermediate location up to the kink and the same on the outboard side. This area was then compared to real A320 wing area and yielded a difference of 2.7%, which is considered to be sufficiently accurate for the analysis, since wing spanwise chord distribution model was only obtainable through the use of scaled drawings.

Lastly, the tool for suction system performance prediction translates the wing skin friction drag into a percentage of total aircraft drag using a model for a typical transport aircraft, seen in [22]. To validate this translation, the results of HLFC flight experiment for B757 were used, concluding a local drag decrease of 29%, which results in 6% total aircraft drag reduction [10]. The method used in the tool gives a 5.8% total aircraft drag reduction, if the wing skin friction drag due to suction is reduced by 29%. The difference is minimal, thus validation of drag translation is considered successful.

4.4.2. MTE Aerodynamics

In order to be able to implement a significant amount of different deflections of the trailing edge into the aerodynamic model, a MATLAB code is used, which generate airfoils with different hinge deflections automatically, implements these airfoils in aircraft configurations and uses these aircraft configurations in specific free stream VLM analysis files. That way, 450 airfoils are generated and analysed with 2D panel method for the expected local Reynolds number and 50 different MLW aircraft configurations are assembled and simulated for every one-of-the-time intensive flight cases. These 50 different configurations are accounting for MTE deflections of the last hinge for the range of $-2.4° : +1.2°$, combined with deflection of the second hinge for $-1.6° : +1°$. An example with three airfoil deflections and the reference rotational frame can be seen in Figure 4.19.

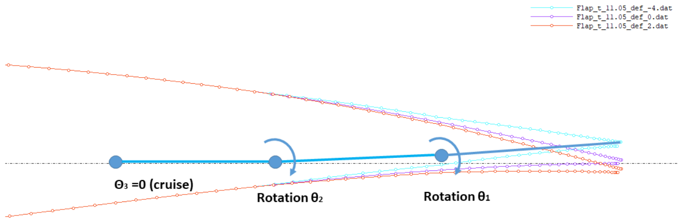

Figure 4.19: MLW airfoils for 11.05% max thickness and deflections of (-2.4,-1.6°), (0°,0°),(+1.2°,+0.8°)

Once both the deflected airfoils and the VLM aircraft configurations are analysed, their performance and aerodynamic parameters are collected and compared with the expected C_L, where the most optimal configuration for C_L/C_D within the predefined limits of AoA is chosen. For exact results of the MTE aerodynamics performance and integration with HLFC, refer to section 4.5.

4.5. Aerodynamics System Integration and Performance Analysis

In this section the performance analysis of the benchmark model and the MLW is discussed with regards to the different mission profiles, as presented in section 4.3.

4.5.1. Performance Analysis

The proposed system architecture of the MLW operates with both HLFC and MTE systems. Both systems were found to improve the aerodynamic performance of the wing when analysed separately. However, to continue with the wing and later on with the aircraft performance, it is necessary to analyse the wing coupling effects of the two systems. Due to resource constraints, coupling analysis will not be performed with the appropriate tools like CFD and Rfoil-Suc. Since the two sub-systems use different physical phenomenons for decreasing the overall drag and since laminar flow is not expected to reach more than 65% of the local chord, it is assumed that the two systems are completely independent. Therefore, only the cruise and high altitude climb/descent will be affected by the HLFC with a decrease of overall aircraft drag of 3.5% (see Equation 4.5). This assumption is not expected to cause high errors in C_L/C_D and C_D directly, but rather on the drag decomposition and the Cp-distribution of the wing.

$$C_{D_{coupled}} = (1 - 0.035) \cdot C_{D_{MTE}} \tag{4.5}$$

The iterative mass-drag estimation of the benchmark model and the MLW model, taking into account the HLFC system, the variable MTE configurations and the laminar airfoils, improve the aerodynamic performance during all PoF. However, this improvement is not uniform through the whole mission profile. Essential for the determination of the aerodynamic performance of the aircraft is the respective configuration of the MTE deflections, the freestream parameters like Re, V_∞, ρ and the required C_L at the local aircraft mass and flight path angle. Since only the free stream values are constant, the other variables require an iterative converging approach, aiming at optimising the local CL/CD (as discussed in section 4.1).

When considering the results of the analysis in terms of the C_L/C_D coefficients, as presented in Table 4.4 as well as in Figure 4.20, the conclusion can be drawn that the MLW model shows a significant performance improvement over the benchmark model when analysed with respect to the original mission profile. Comparing the weighted C_L/C_D coefficients of the two models, a difference of 11.4 % can be found. The results of the separate analysis of the MLW model with respect to the alternate mission profile with a constant cruise altitude at 39,000 ft can be found in Table 4.5 and Figure 4.20. It is apparent that while there is an improvement in the aerodynamic performance over the benchmark model, the difference of its weighted C_L/C_D coefficient with respect to the one of the original model is only 9.79 %. The conclusion can therefore be drawn that in the context of this analysis the MLW model delivers the highest performance improvements when operating at the original mission profile and not at an altered one.

Flight Phase	No.4	No.5	No.6	No.7	No.8	No.9	No.10	No.11	Weighted Mean
Benchmark C_L/C_D	17.69	17.75	17.84	17.86	17.80	17.65	17.82	17.22	17.77
Optimised C_L/C_D	19.91	19.87	19.54	19.24	18.96	18.60	19.53	19.92	20.05

Table 4.4: Weights of the original mission profile

Flight Phase	No.4	No.5	No.6	No.7	No.8	No.9	No.10	No.11	Weighted Mean
Optimised C_L/C_D	17.86	18.85	19.00	19.04	19.17	19.30	19.48	17.22	19.70

Table 4.5: Weights of the alternate mission profile

To investigate the reasons behind the observed differences in performance with respect to the main variable parameters - ρ, V_∞, W_i, the diagram in Figure 4.20 is constructed. It visualises the change in C_L/C_D of the benchmark model and the MLW model with respect to the distance covered in between the beginning of flight phase four and the end of phase eleven. For both the original as well as the alternate mission profile, as presented in Figure 4.16 and Figure 4.18, the MLW concept improves the aerodynamic performance with respect to the benchmark in every PoF as defined in Table 4.3. However, a more significant difference between the benchmark model and the optimised model occurs in the first PoF during the original mission profile, where the wing experiences higher dynamic pressure, which helps to lower the required lift coefficient C_L. On the opposite end, when choosing the alternate mission profile, for which the entire cruise flight takes place at a constant altitude of 39,000 ft, the required C_L in the initial phases of that cruise is higher and the MTE system does not manage to provide it efficiently enough. Therefore the performance gain induced through the MTE deflection cannot overcome the effect of lower altitude and in particular the higher density. This hypothesis is also backed up by the fact that the local performance of the alternative mission profile is slightly higher than the classical mission profile at 39,000 ft. At this point the aircraft flying the alternate mission profile uses negative overall deflection of -3.24°opposite to the +1.2°deflection for the original profile. Based on the difference of the two local weights and the constant free stream parameters, it can be concluded once again that the effect of density and free stream conditions cannot be efficiently compensated by the MTE deflections. Due to the lack of any evidence showing any benefits of implementing the alternate mission profile from this moment on, only the A320 classical mission profile will be used for further analysis will be referred to in the report.

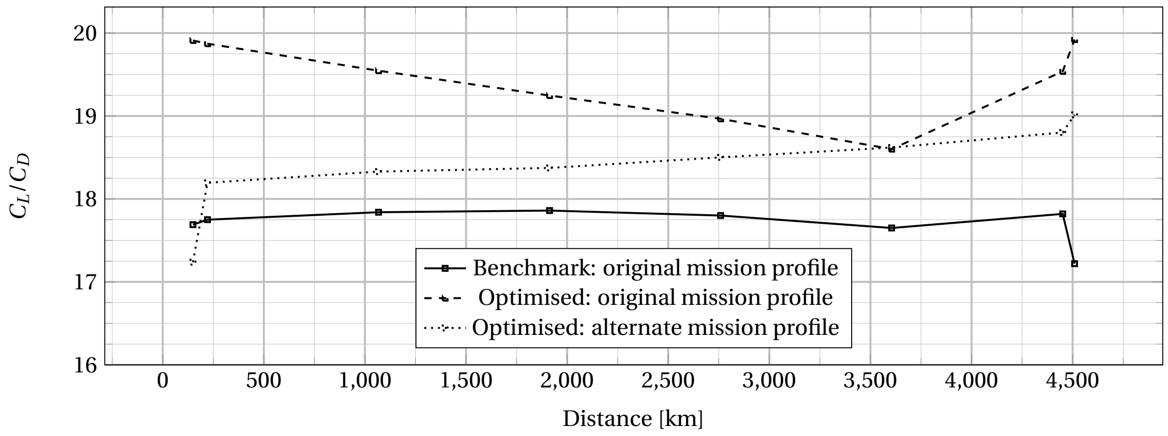

Figure 4.20: C_L/C_D along phases that are investigated

4.5.2. Fuel Mass Savings

The improved aerodynamic drag performance results in a decrease of the fuel burned during the cruise flight and the time intensive PoF of the MLW concept. This benefit can be transformed into an increase of range and the maximum payload mass to satisfy the 7.5 % payload requirement. To estimate the fuel burned with the improved aerodynamic performance, a discretised version of the Breguet Range model is used (see Equation 4.6). This model takes into account the described mission in Table 4.3 and previously explained iterative process for C_L/C_D.

$$R = \sum \frac{V_{TAS}}{gC_t} \frac{C_L}{C_D} \ln\left(\frac{W_{i-1}}{W_i}\right) \tag{4.6}$$

Once the Breguet model is applied for all PoF, the results for the fuel mass fractions M_{ff} can be seen in Table 4.6. This data and the corresponding fuel burned will be used for comparison with the benchmark model to calculate the payload increase, caused by the drag decrease and the corresponding decrease in fuel burn. Note that the mass fractions №0-3 and №12-14 are accounting for taxiing, take-off, initial climb, approach and final descent. They are taken from literature and are possible to cause slight overestimation of the fuel burned.

Phase of Flight	**No.1-3**	**No.4**	**No.5**	**No.6**	**No.7**	**No.8**	**No.9**	**No.10**	**No.11**	**No.12-14**	**Overall**
Mff Benchmark[-]	0.951	0.996	0.952	0.972	0.972	0.719	0.971	0.999	0.997	0.977	0.581
Fuel burned	3678	279	3381	1867	1828	1800	1765	33	139	1380	16150
Mff Optimised[-]	0.951	0.996	0.958	0.975	0.975	0.974	0.974	0.999	0.998	0.977	0.797
Fuel burned	3678	239	2926	1659	1657	1655	1644	30	118	1404	15010

Table 4.6: Mass fractions and the corresponding fuel burned during all PoF

From the table it can be concluded that burned fuel is decreased drastically by 1142kg, which is 5.6% of the total A320 fuel onboard. These fuel savings can be used for increase of the range for this particular mission with 290km or increase the mission payload with 7.7% from 14803kg to 15945kg. The choice at this point is left to the airline and the specific operational limits of the mission.

For model verification purposes of the Breguet and fuel burn mode, two independent models from independent developers are created. The first one in MATLAB and a second one in EXCEL. Both models yield equivalent results, and show a fuel reserve of 21% after the landing. This is within the expected $10-20\%$ for 45-minutes-reserve-fuel for a five hour flight. No accurate and reliable validation is found for fuel burned of the specific mission of 4770km [8]. However, for shorter flights with an average specific fuel consumption of $3.1 l/km$ as found in literature for A320, the mass of $14.72t$ is found. This is a difference of 10% with respect to the benchmark calculations of $16.2t$. This overestimation is expected due to the fuel fractions for final descent, on ground operations and initial climb, which are taken from literature [42]. However, these values are considering the whole PoF, which results in the overestimation found in the validation. All in all, this deviation is not expected to cause significant deviation, except slight increase in the absolute value of save fuel burned.

4.5.3. Payload-Range Diagram

In order analyse effect of the fuel savings discussed in subsection 4.5.2 as well as the change in structural weight as described in chapter 6, the payload-range diagram as seen in Figure 4.21 can be used. It describes the relation between the loading of the aircraft and the corresponding range that can be achieved. While the point of the first change in slope of the graph is associated with the maximum range at maximum payload, the point of the second change in the slope of the graph belongs to the range at maximum fuel. The final point of the graph indicates the maximum ferry range, at maximum fuel and no payload.

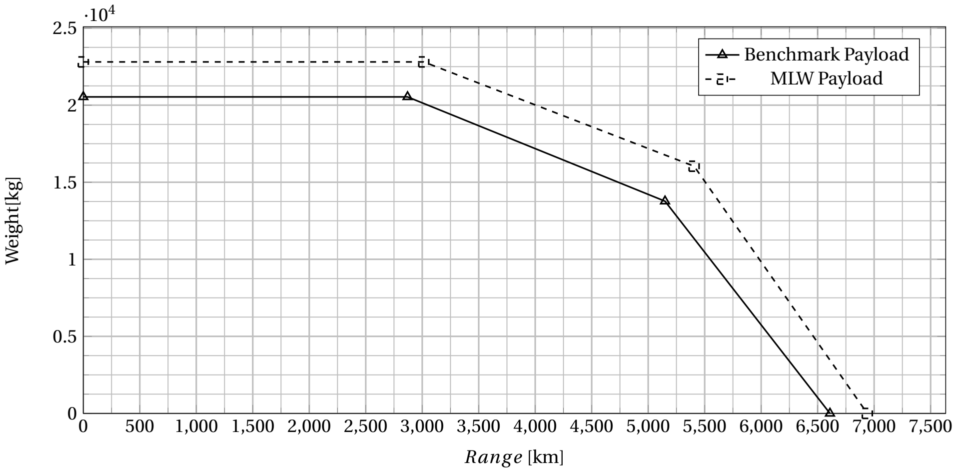

Figure 4.21: Payload-Range Diagram

Analysing the payload graph for the benchmark model as well as the MLW as seen in Figure 4.21, it can be found that there is a shift with regards to the weight as well as the range in case of the MLW. The shift in weight can be be attributed to the overall increase in payload of 2270 kg as discussed in chapter 6, while the increase in range can be traced back to the fuel mass savings discussed in subsection 4.5.2.

4.5.4. Verification and Validation of the Performance Analysis

While the improvement in aerodynamic efficiency, expressed in terms of the C_L/C_D coefficient, appears to be significant for the MLW, it is essential to verify and validate the credibility of these results. This can be achieved by comparing the C_L/C_D values estimated for the benchmark model and the MLW model with the corresponding values determined in prior studies in [33] and [32]. Moreover, it can be achieved by a comparison of the gain in efficiency induced through the MTE with previous studies [43] on the subject.

In a study [32] on aircraft performance parameter estimation of aircraft using ADS-B (Automatic Dependent Surveillance—Broadcast) data, aerodynamic coefficients of various types of aircraft in the different PoF are determined. In case of the A320, the C_L/C_D coefficient is documented as 8.79 in cruise flight and 25.20 during initial descent. As the C_L/C_D is much lower than expected in cruise and much higher that expected during descent, the data from this study cannot be used for the exact verification of calculated C_L/C_D coefficients but rather gives an indication with regards to in which range of values the C_L/C_D should be located. The judgement, that the values given in this study should be treated with caution is the fact that the C_L/C_D coefficient for an Airbus A380 is given as 27.90 in cruise flight, as opposed to 8.79 for the A320. A more reliable study with regards to the consistency of the results is a study on the fuel efficiency characteristics of regional aircraft [33]. The C_L/C_D coefficient for the A320 in cruise flight is here given as 15.88 as opposed to 17.77 found for the benchmark model. This value is 10.63 % lower than than the weighted mean value for the benchmark model in cruise flight, given in Table 4.4. This discrepancy can be explained by the simplified drag model, discussed in section 4.2, which ignores smaller components as well as models the viscous effects in an insufficiently accurate way. Taking these considerations into account, the 10.63 % discrepancy is acceptable at this level of detail and stage in the analysis, and can be expected to become smaller as the level of detail increases and the methodology of analysis improves in subsequent stages of the project. An even closer proximity of the results of the model analysis to verification data with regards to the C_L/C_D coefficient can be found when comparing with a study on historical and future trends in aircraft performance []. Here the C_L/C_D coefficient of an A320 in cruise flight is given as 16.30, which leads to a discrepancy of merely 8.27 % with respect to the C_L/C_D coefficient of 17.77 of the benchmark model.

In a paper [43], the performance gain achieved through the application of MTE in combination with a constant cruise altitude of 37,00ft is investigated for an A320. The study comes to the the conclusion that decrease in fuel burn of 0.4 % is possible, in combination with an increase in range of 20 km. Comparing this with the calculated fuel saving of 5.6 % of the MLW model with regards to the benchmark model, a significant disparity is found. While the different way of analysis may be a contributing factor to this difference, the main reason for this is the fact that while in the paper merely MTE is added to the wing, in case of the MLW an additional change of airfoils as well as HLFC are applied. As the change of airfoils alone leads to a significant decrease in drag, the research paper [43] cannot be used for the direct verification with the model.

4.6. Operational limits

The operational limits of the aircraft address the limitations of the aircraft with regards to the airspeeds, the take-off and landing performance as well as the static stability. These factors combined define the room within which the aircraft can be safely operated.

4.6.1. Stall Compliance

In the sub part 103 of the CS-25 certification specifications [17], the requirements with regards to the stall speed characteristics of the aircraft are described. The reference stall speed V_{SR} is defined by the designer and may not be less that the stall speed at $1g$ as defined in Equation 4.7.

$$V_{SR} \geqslant \frac{V_{CL_{max}}}{\sqrt{n_{nz}}} \tag{4.7}$$

The speed $V_{CL_{max}}$ is the calibrated airspeed obtained when the lift coefficient $\left(\frac{n_{nz}W}{qS}\right)$ is first a maximum during a manoeuvre, where the aircraft decelerates with a rate of no more than 0.5 m/s^2 through the application of the longitudinal control. The Load factor n_{nz} is defined as the load factor normal to the flight path at $V_{CL_{max}}$. As this factor is equal to 1 in the case of the benchmark aircraft and the MLW, $V_{CL_{max}}$ corresponds to the stall speed derived in section 4.6. The reference stall speed V_{SR} can accordingly be chosen to be equal or larger than that speed to fill the certification requirement.

4.6.2. Flight Envelope and Load Distributions

The flight envelope diagram describes the range of velocities and accelerations within which the aircraft is able to operate without being compromised with regards to its structural integrity. While the manoeuvre part of the diagram deals with the velocity limits and load factors within which the aircraft can manoeuvre safely, the gust envelope part considers the effect that vertical gusts in positive and negative direction have on the load acting on the aircraft, starting with a load factor of 1 in level flight condition. In the CS-25 certification specifications [17] for large aircraft by the European Aviation Safety Agency (EASA), the manoeuvre envelope requirements can be found in Table 4.7. The load factors n_1 and n_2 are the maximum positive normal acceleration at minimum and maximum speeds, whereas n_3 and n_4 are the maximum negative normal acceleration at maximum and minimum speed respectively. The minimum dive speed V_{D_min} is defined as 1.25 times the cruise speed V_C, and the manoeuvre speed V_A as $\sqrt{n_1}$ times the stall speed in a clean wing configuration.

$\mathbf{n_1}$	$\mathbf{n_2}$	$\mathbf{n_3}$	$\mathbf{n_4}$	$\mathbf{V_{D_{min}}}$	$\mathbf{V_A}$
2.5	2.5	-1.0	0.0	$1.25V_C$	$V_{S_1}\sqrt{n_1}$

Table 4.7: Manoeuvre envelope requirements for large aircraft as specified by EASA [17]

The two curves that limit the load diagram on the left side result from the maximum positive and negative lift coefficients of the aircraft and indicate the maximum aerodynamic load that the aircraft is able to generate at the corresponding speeds. Using the MTOW for the weight and applying the atmospheric conditions at sea level, the stall curves for the clean wing configuration as well as for the configurations with extended flaps can be found using Equation 4.8. In the CS-25 certification specifications for large aircraft [17], the maximum load factors for extended flaps are defined as 2.0 in the take-off configuration and 1.5 in the landing configuration.

$$n_z = \frac{1}{W}\frac{1}{2}\rho V^2 C_{L_{max}} S \tag{4.8}$$

During operations every aircraft encounters additional aerodynamic loads caused by gusts. These loads cause an increase of the absolute aerodynamic force and consequently increase the structural loads. The gust strengths are defined as 50 ft/s up until the cruise speed V_C and 25 ft/s up until the dive speed V_D. An initial estimation of the increase in lift δL and the normal accelerations that result from these gusts, can be calculated using Equation 4.9, Equation 4.10, Equation 4.11.

$$n_z = 1 + \frac{K g \rho U_{de} V_E a}{2W/S} \tag{4.9}$$

$$K_g = \frac{0.88\mu_g}{5.3+\mu_g} \tag{4.10}$$

$$\mu_g = \frac{2W/S}{\rho_0 MAC \frac{dC_L}{d\alpha}} \tag{4.11}$$

Combining the manoeuvre limitations, the gust loads and the limiting velocities, the flight envelope diagram for the model of the MLW concept can be constructed as seen in Figure 4.22. It can be found that the maximum positive and negative normal load factors are 2.5 and -1 respectively, both induced through the manoeuvre limits defined in the CS-25 specifications [17]. Moreover, the diagram presents the dive speed V_D at 176 m/s and the cruise speed V_C at 141 m/s, as well as the stall speeds V_S at 78.2 m/s for the positive $C_{L_{max}}$ of 1.4 in clean configuration and 95 m/s for the negative $C_{L_{max}}$ of -0.95 in clean configuration.

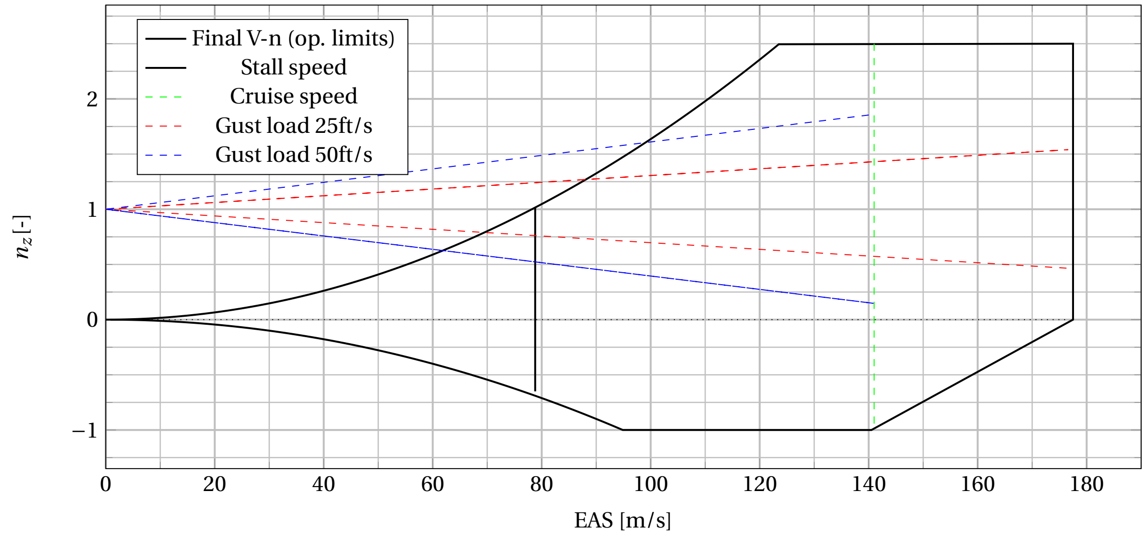

Figure 4.22: V-n -diagram showing the normal loads of the MLW

Using the load limitations as derived from the CS-25 certification specifications [17], and the V-n-diagram is constructed using the characteristics of the the aircraft. In order to perform the structural analysis and mass estimation of the aircraft in chapter 6 as well as the GLA and MLA discussed in chapter 5, it is required to know the load distribution along the span of the wing that correspond to the different load factors. In Figure 4.23 the load distributions that correspond to the benchmark model can be found. As both in the case of the benchmark model as well in the case of the optimised model the twist distribution is tuned for an optimal elliptical lift, the resulting load distributions for both wings turn out to be close to the same. Therefore only the graphs that correspond to the load distributions of the benchmark model are displayed. While in case of the benchmark model the maximum load distributions relate directly to the structural mass determined in chapter 6, an integral component of the concept for the optimised model is the alleviation of gust and manoeuvre loads as discussed in chapter 5 that results in significantly altered load distributions and corresponding structural mass as discussed in chapter 6.

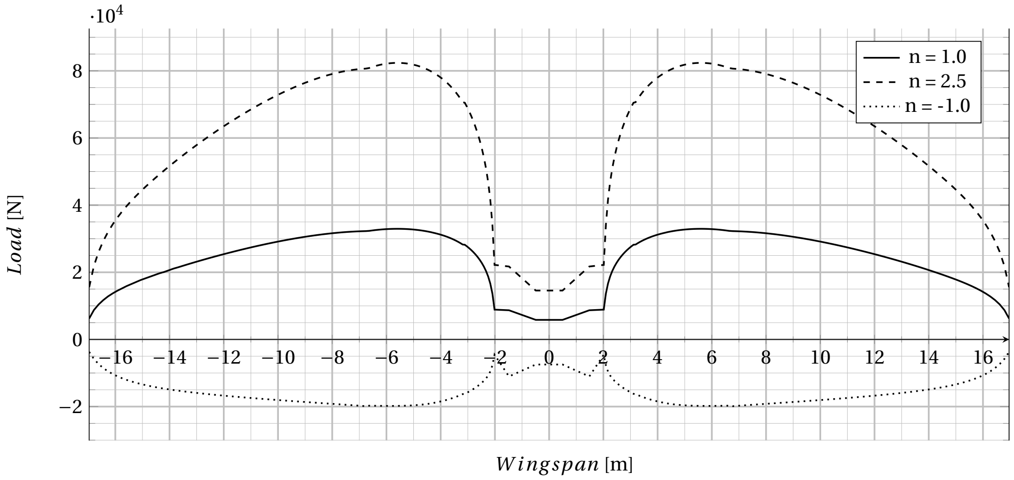

Figure 4.23: Load Distributions

4.6.3. Verification and Validation of the Flight Envelope

In order to determine whether the V-n-diagram in Figure 4.22 is indeed appropriate for the determination of the maximum load cases that are used for the investigation of load distributions and ultimately the structural mass as discussed in chapter 6 it becomes necessary to verifiy and validate the diagram. To verify whether the method used for the creation of the diagram in Figure 4.22 is correctly applied, it can be applied on the model of the benchmark aircraft. The resulting V-n-diagram can be found in Figure 4.24. Comparing the two diagrams it can be found that while the upper and lower manoeuvre load limits as well as the dive speed limit are the same, the load limitations that correspond to the the maximum positive and negative lift coefficients are located at lower airspeeds in case of the V-n-diagram that is associated with the model of the benchmark aircraft in Figure 4.24. This can be related to the maximum lift coefficient $C_{L_{max}}$ of the optimised concept is lower than the one of the benchmark aircraft, both for positive and negative angles of attack.

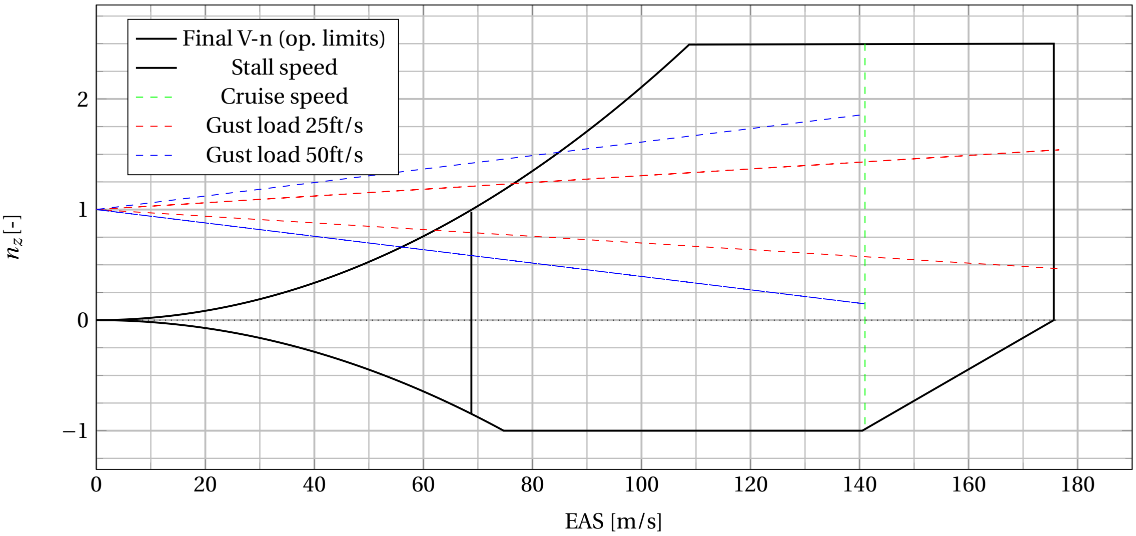

Figure 4.24: V-n -diagram showing the flight envelope of A320 Benchmark

The flight envelope diagram, as portrayed in Figure 4.22, can be validated using statistical load data on the Airbus A320 in commercial operations, as provided by the Federal Aviation Administration [44]. These statistical load data are plotted within the corresponding V-n-diagram of the A320 as seen in Figure 4.25. While the diagram serves only illustrative purposes, the data points correspond to the actual loads that where recorded in flight and should be used for the verification of the diagram in Figure 4.22. When comparing the V-n-diagram constructed in Figure 4.22 with the one of the recorded data in Figure 4.25 it should be noted that the speeds in the former one are indicated in m/s equivalent airspeed, while in the latter one the speeds are described in $knots$ equivalent airspeed.

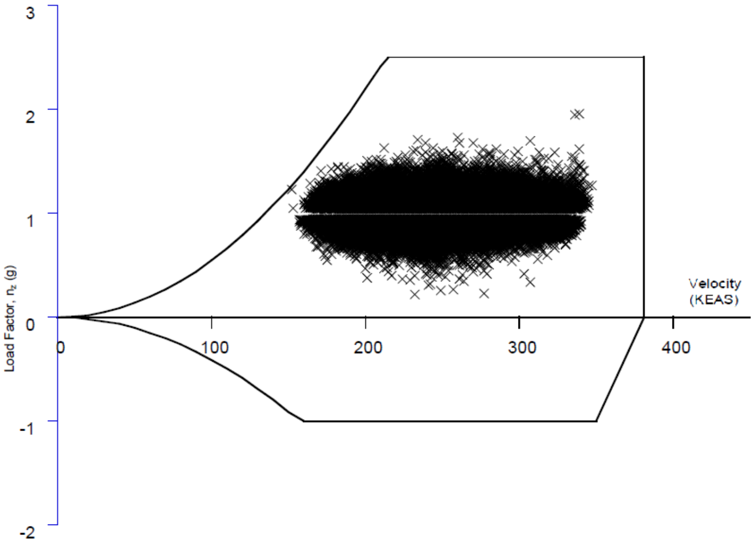

Figure 4.25: A320 statistical load data

It can be found that with regards to the positive and negative load factors, the data points in Figure 4.25 do not exceed the positive load factor of 2.5 or the negative load factor of -1.0, as portrayed in Figure 4.22. The data points on the far right side of Figure 4.25 correspond to a speed of 350 KEAS which is 180 m/s. This speed corresponds to the dive speed limit in the diagram in Figure 4.22. On the opposite side of the spectrum of data points, load factors as high as +1.3 are recorded at airspeeds as low as 80 m/s. This point does not lay within the envelope of the V-n-diagram, as shown in Figure 4.22. However, it can be related to the maximum lift coefficient $C_{L_{max}}$ of the MLW concept that is lower compared to the $C_{L_{max}}$ of the original aircraft.

Considering that for the V-n-diagram presented in Figure 4.22 the discrepancies both in case of the verification and validation can be related to the difference in the maximum lift coefficient $C_{L_{max}}$ of the MLW model in comparison to the benchmark model. Thus, it can be concluded that the diagram is accurate.

4.6.4. Take-Off and Landing

One of the last operational limits in performance is with respect to the take-off distances and landing distance of the new concept. The A320 is a short-medium range aircraft, which lands and takes off in the vast majority of runways. In fact, having 1955m runway length requirement, A320 is believed to able to land on 83% of the international runways, which can be assumed as one of the selling points of Airbus[3]

4.6.5. Maximum Lift Coefficients

At the same time however, the MLW model and in particular the changes of the design from slat to Krueger flap and the substitution of single Fowler flap with the continuous MTE, by definition worsen the landing performance of the aircraft. Therefore, in this chapter initial estimations of the landing and take-off distance are performed. First, one of the most important parameters related to these two critical phases are the corresponding maximum C_L. These maximum lift coefficients of both the classical and the MLW wing can be seen in Table 4.8.

	C_{Lmax} clean	**C_{Lmax} TO**	**C_{Lmax} Landing**
A320-200	1.6	2.3	2.60
Optimised Concept	1.5	2.03	2.21

Table 4.8: Maximum lift coefficient for A320-200 and the optimised concept[38]

Due to the initial state of development of the system and the non-convergence at high angles of MTE deflections for some airfoils, the XFLR5 VLM 3D model is not found suitable for these estimations. Therefore, for initial indication of the C_{Lmax} at take-off and landing configurations, an extrapolation of the 2D C_{lmax} with correction for the sweep and 3D effects is used, see [42]. The airfoil selected for this purpose is located in the middle of the wing and has maximum thickness - t_{max} = 12.65%. At landing configuration of 15/15/15°MTE deflections the airfoil generates C_{lmax} = 2.4 at the reasonable AoA for landing - 7°. By applying the corrections from [42], the estimation for Krueger flap over the whole wing, which provides a $\Delta C_L = 0.24$, it can be estimated a maximum C_{Lmax} of 2.21. [42] A similar analysis for the take-off distance with airfoil deflection of 10/10/10°for the MTE hinges, results in $C_{Lmax} = 2.03$. It should be clear that this C_{Lmax} estimations are extremely inaccurate and could deviate by 20-30%.

4.6.6. Take-off Requirement

The certification take-off distance is based on both ground distance, and airborne one. Using the drag coefficients obtained from XFLR5 for low AoA and the mean aerodynamic coefficients during ground run at $V = V_{LOF}/sqrt(2)$, the ground take-off distance can be found by using Equation 4.12. Additionally the take-off air distance is found by Equation 4.13 for screen altitude at h=50 ft and $V_{scr} = 1.2 * V_{LoF} + 5.1$.[45]. This results in an overall take-off distance of 2.28 km for clear conditions and two operative engines.

$$S_{gr} = \frac{W V_{LOF}^2}{2g(T_m - D_m - D_{gr_{m)}}} \tag{4.12}$$

$$S_a = \frac{1/2gV_{scr}^2 - 1/2gV_{LOF}^2 + h_{scr}}{sin(\gamma)} \tag{4.13}$$

---

[3] `http://aircyber.weebly.com/aircraft-runway-requirements.html`

4.6.7. Landing Requirement

The biggest disadvantage of not being able to deploy a Fowler flap and to increase the surface area of the wing, appears during landing. Firstly, having an AoA 6°and a $C_{Lmax} = 2.21$, which is significantly lower than 2.6 of the original A320, an increase of the approach speed and therefore on the landing air distance is expected. This preliminary air landing distance can be found using Equation 4.14, which results in demonstrated air landing distance of 924m.

$$S_a = \frac{\frac{V_A^2}{2g} - \frac{V_T^2}{2g} + h_{scr}}{1/2(sin(\gamma) + \frac{C_D}{C_L})} \tag{4.14}$$

The ground segment of the runway is characterised with deceleration from V_T to reaching a rest state. This is calculated using the mean values for the reverse maximum thrust with LEAP engine (35% effective thrust reverse). The necessary drag and lift decrease however cannot be delivered due to the lack of devices creating turbulence like holes on flaps, slats,etc. Therefore, a solution to this problem is the quick deflection of the different MTE section in opposite consecutive directions, leaving the last section for aileron control. This will lead to drastic decrease of the lift on the sections with negative 15/15/15°deflection, but also will work as spoilers with deflection on 15°. Last, spoilers taking 19% of the span with maximum deflection of 45°are implemented in the inboard part of the wings. All this contributes to an overall C_{Dg} 0.31 and demonstrated landing ground distance of 457 m with overall deceleration of 1.9g.

$$S_{gr} = \frac{WV_{LOF}^2}{2g(T_m - D_m - D_{gr_{m)}}} \tag{4.15}$$

Last, but not least, this overall demonstrated runway is multiplied by 10/6 as defined in certification documents CS25.[17]. This outcomes a required runway length of 2325 m, which is significantly higher than the one of A320 - 1440 m. [8]

4.6.8. Verification and Validation of Take-off / Landing distance

For verification and validation procedures unit tests for A320 validation data are performed, including take-off, landing distances and unit test for the ΔC_{Lmax} MATLAB function. First unit tests were performed for the scripts estimating Landing and Take-off distances of the A320 using validation data for the aerodynamic coefficients. The achieved landing distances, based on the L/D = 4.55 found in literature [46], is 1.47km, which deviates only 3% from the estimation. Therefore, the landing distance function is assumed to be verified. A similar procedure for unit testing is performed for take-off distance function, which results in a required take-off distance of 1.87km, which is underestimation of 4.4%. Last, the ΔC_{Lmax} code accounting for the HLD is verified. Taking into account the single slotted Fowler flaps and the normal slat over the wing with the DATCOM method [42], a value of $\Delta C_{Lmax} = 1.19$ is estimated. This is 6% higher than validation data, but is still within the predefined allowed error of 10%. Last a validation of $C_{L_{max_{clean}}}$ of the benchmark model was performed. The chosen airfoils showed a $C_{L_{max_{clean}}} = 1.81$, which is 13% higher than the validation data. This error is significant, but is most probably caused by the airfoil selection, which on the other side cannot be validation. Therefore, it is not possible to be concluded if this error will be reproduced for the Morphing Laminar Wing concept. In conclusion it can be said that integrating all models can be used as an initial sizing tool, which has a significant deviation ($10-15\%$) from the real-life ones, estimated by detailed analysis like high fidelity CFD or flight testing.

4.6.9. Conclusions Trade-off Landing Distance

If the whole fuel savings estimated in subsection 4.5.2 are converted to payload, this would mean that the maximum landing mass increases by 1142 kg. This increase even further the landing distance from 2325 m to 2419 m, which may affect the market and the operational capabilities of the final customer - the airlines. Therefore, two different possibilities for landing distances are presented. First, being capable of landing with increased maximum landing mass with 1142k g, which limits to only 69% of the runways. It is expected that most cargo companies may prefer this option for urban agglomerations. Second, limiting the MLW to the original and increasing the payload with only 1128 kg from structural savings will decrease the required landing distance to 2325 m, covering 70% of the worlds international airfields and is similar to the landing requirements of the Boeing 757-200 aircraft. This will be beneficial for both cargo and passenger carriers, since it results in increase of about 10 new seats.

4.6.10. Static Stability

The most fundamental aspect of an aircraft's stability is its static stability. In sub part 173 of the CS-25 certification specifications [17], the requirements for the static longitudinal stability are described. One of the specifications for static longitudinal stability is that a pull of the elevator control must be required to obtain and maintain speeds below the specified trim speed, and that a push must be required to obtain and maintain speeds above the specified trim speed. This behaviour is required to occur at any speeds that are obtainable, with exception of speeds, that are higher than the landing gear or wing flap operating limit speeds, or lower than the minimum non-stalled flight. Furthermore it is specified that the speed of that aircraft must return to within a certain margin from the original trim speed within the range of these speeds, when the control force is released. A different way of describing these requirements is a slope of the moment coefficient C_m, which is smaller than zero due to a change in AoA ($C_{m_\alpha} < 0$). This requirement is fulfilled by the configuration of the benchmark and the MLW model, which are trimmed for a moment coefficient C_m of zero at $\alpha = 0$ as discussed in subsection 4.2.2. In Figure 4.26 the corresponding C_{m_α} can be found which proves that $C_{m_\alpha} < 0$.

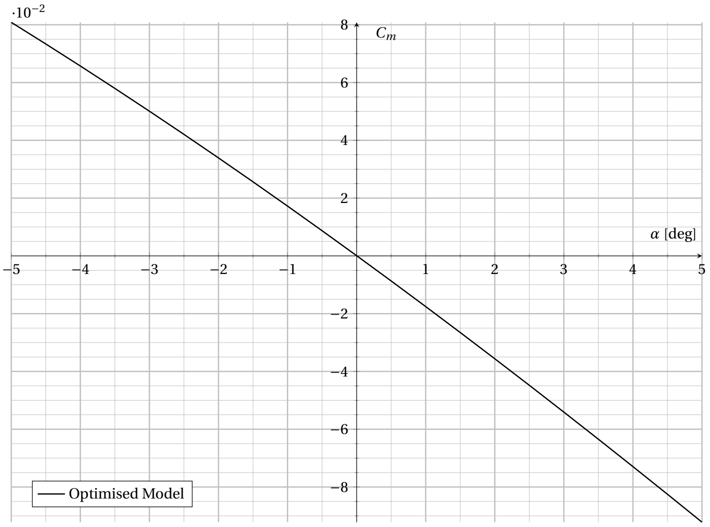

Figure 4.26: $C_m - \alpha$ graph of the optimised model

5

Load Alleviation

During flight an aircraft encounters different types of loading as displayed in Figure 4.22. Depending on the type of aircraft, different flight conditions during flight determine the critical loading cases. The aircraft should be able to cope with these loads by providing an adequately stiffened structure which directly influences the aircraft mass. However in order to minimise structural mass a load alleviation system can be implemented to the wing. In general load alleviation capabilities are split up in two categories: Manoeuvre Load Alleviation (MLA) and Gust Load Alleviation (GLA). In the following section 5.1 the working principles are discussed, followed by the assumptions and simplifications made in section 5.2. Afterwards the MLA (section 5.4) and GLA (section 5.3) system is explained in detail, followed by verification and validation in section 5.5.

5.1. Working Principles

The MLW is equipped with a total of eight flaps, each with three hinge-lines, which provide the possibility to alleviate loads via changing deflection angles of individual flaps, thereby altering the lift-distribution.

From Figure 4.22 it becomes apparent that manoeuvres are responsible for selecting the critical load cases used for structural sizing. The most extreme load cases for which the aircraft has to be certified (CS.25) were considered when making this diagram. The MLA system is designed to alleviate these loads and shall be sized for a 2.5g pull-up manoeuvre and a -1g push-down manoeuvre [17]. The regulations do not allow for changing the total load factor, however the lift distribution may be altered. Which is useful because by moving the centre of pressure inboard the bending stress can be lowered. However, this will induce added torque load due to deflection of the flaps and increase in shear force on the inboard sections of the wing. The absolute effect of MLA on the structural rigidity of the wing is discussed in further detail in section 6.1. For the design of the MLA system it means that the redistribution of the load shall have to be checked with the structural model to ensure that the effect is indeed beneficial.

During flight the MLA system works as follows: Whenever the aircraft performs a pull-up or a push-down manoeuvre, the load factor will change. The load factor change is then measured by an air data inertial reference unit (ADIRU), which is already used in the A320s of today and contains an accelerometer [47]. The change in load factor is checked with a database that contains the appropriate deflections for different load factors. Following the load factor measurement, using this database, the flaps can be deployed accordingly. The MLA system is limited by the maximum flap deflection angle.

Even though in Figure 4.22 the gusts do not have a load factor higher than the manoeuvre loads, it could be that the gusts become the critical sizing case after MLA. This can be resolved since the flaps do not only provide the possibility to redistribute the lift distribution but also to lower the load factor. For structural implications there is an increase in torque load induced by the flap deflection but a decrease in shear and bending load compared to not alleviating the gust. Whether the GLA system actually proves to be beneficial for minimising the structural mass, shall be checked with the structural model section 6.1.

For the GLA to work, the aircraft should know a gust is approaching. Therefore the aircraft is equipped with a Doppler LIDAR sensor placed in the nose of the fuselage. The Doppler LIDAR sensor can detect disturbances based on molecular backscatter, which is better than the normal LIDAR sensor. This is because a normal LIDAR sensor detects disturbances based on aerosol backscatter which was found as not reliable when testing in different atmospheric conditions [11]. The Doppler LIDAR sensor is capable of measuring the gust at a distance of 50 meter, which gives a lead time of 300 ms [11].

Once the GLA controller is warned by an approaching gust it has to calculate the electrical power that the electro-mechanical actuator needs. The actuator shall then deflect the flaps to counteract the increase in lift due to the gust. In an optimal scenario the flaps deflect with a certain speed to a certain angle such that the gust is fully alleviated and the load factor remains one. Some physical limitations might make this impossible, namely: The maximum flap deflection rate, maximum flap deflection angle and the maximum actuator torque. In order to quantify the GLA capabilities a model is build. The model consists of an open-loop controller built in SIMULINK connected to a MATLAB script to run loops, calculate constants and import data. More details of this model are provided in section 5.3.

5.2. Assumptions & Simplifications

Several assumptions & simplifications were made for the creation of both the GLA and MLA model which are listed below:

- Gusts are assumed to not hit during manoeuvres, making both GLA and MLA problems independent from each other
- Gusts are assumed to hit the wing perpendicular to the flight direction from below. Gusts that hit from above are not taken into account since they can only cause sizing load factors during manoeuvre
- Gusts are assumed to hit the wing uniformly in spanwise direction. The 2D-problem of GLA is considered the most interesting and investigating the 3D case becomes feasible with this assumption within the limited time frame
- The extra loads due to gust are superimposed on the 1g flight loads. This assumptions is taken from the CS.25.341 regulations [17]
- The airfoil is assumed to be rigid, see Figure 5.1. The alternative approach would be to go more in depth in the physics of the airfoil, however for this project due to the limited time frame this was infeasible. Making the rigid airfoil assumption simplifies the problem for load alleviation and allows for an investigation of the problem as whole with the resources available
- For load alleviation, quasi-steady conditions are assumed. This means that in the equations used, all terms containing a double derivative are neglected [16]. This assumption is made for similar reasons as the rigid airfoil assumption and the conclusion was drawn from discussion with experts within the field of aeroelasticity. Finally for the equations used from Theodorson this means that only the terms including β and $\dot{\beta}$ remain [12]
- The effect of tip vortices are assumed negligible. Similar to the gust hitting the wing uniform in spanwise direction, this assumption reduces the complexity of the 3D problem. It allows for focusing on the 2D problem
- For the design of the MLA system, only symmetric flight conditions were considered (i.e. wings level). From those symmetric manoeuvres, the pull up and push down manoeuvres are investigated. This is also done to reduce complexity and increase the probability of reaching the deadline

5.3. GLA Model

The GLA model has to quantify the GLA capabilities of the wing and in order to do so it requires several inputs: Gust as specified by CS-25 [17], 1g lift distribution during cruise from chapter 4. Cruise flight parameters: Speed and density as well as dimensional quantities. As an output the GLA model provides: lift distribution due to gust, lift distribution due to gust with GLA and the load factor for both these cases. First the gust model is discussed in subsection 5.3.1.

5.3.1. Gust Model

In order to get results for realistic gust profiles, a gust model was set up according to the specifications in CS25.341 [17]. The design gust is defined as a discrete 1-cosine gust as shown in Equation 5.1.

$$W_g = \begin{cases} \frac{W_{g_{ds}}}{2}\left(1-\cos\frac{\pi \cdot s}{H}\right) & 0 \leq s \leq 2H \\ 0 & s > 2H \end{cases} \tag{5.1}$$

In this equation, H is the distance parallel to the aircraft's flight path for the gust to reach its peak velocity, s is the distance penetrated into the gust and $W_{g_{ds}}$ is the design gust speed. According to the CS25.341 regulations the aircraft should be designed to cope with gusts ranging from H = 30 ft till H = 350 ft [17]. $W_{g_{ds}}$ is calculated using Equation 5.2.

$$W_{g_{ds}} = w_{ref} \cdot F_g \cdot \left(\frac{H}{350}\right)^{(1/6)} \tag{5.2}$$

Values for w_{ref} and H should be entered in ft/s and ft, respectively. The reference gust velocity w_{ref} is obtained from CS25 and is at cruise altitude equal to roughly 33 ft/s as explained in chapter 4. The flight profile alleviation factor (F_g) is calculated using the relations shown in Equation 5.3. [17]

$$F_g = \frac{1}{2}\left(1 - \frac{Z_{MO}}{76200} + \sqrt{\frac{W_{ZF}}{W_{MTO}}\tan\left(\frac{\pi}{4}\frac{W_{MLW}}{W_{MTO}}\right)}\right) \tag{5.3}$$

Values and description of parameters in Equation 5.3 can be found in Table 5.1.

Parameter	Description	Value
Z_{MO}	Maximum operating altitude	12,192 [m]
W_{MTO}	Maximum take-off mass	75,000 [kg]
W_{ZF}	Maximum zero fuel mass	60,500 [kg]
W_{MLW}	Maximum landing mass	64,500 [kg]

Table 5.1: Parameters values for Equation 5.3

5.3.2. Dynamic Gust Response

In order for the model to quantify the GLA capabilities the MLW its response to the gust described in subsection 5.3.1 has to be calculated. The optimal performance of the GLA system would be such that when a gust hits the airfoil the flaps can deflect so that the load factor remains one. Optimally the lift due to gust (L_g) thus equals the lift due to the flap deflection (L_β) making Equation 5.4 valid.

$$L_g - L_\beta = 0 \tag{5.4}$$

For visualisation purposes and to show which deflection directions are defined positive and negative in Figure 5.1 two Free-Body Diagrams (FBDs) are shown. On top is the flat plate taken from Theodorsen and on the bottom the airfoil with a gust approaching from the left taken from Bisplinghoff [12] [13].

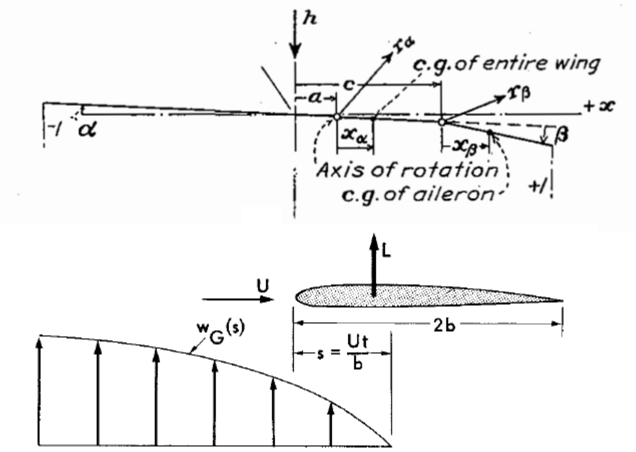

Figure 5.1: Theodorsens flat plate and Bisplinghoffs airfoil with a gust approaching from the left [12] [13]

In order to model the dynamic response, several equations are required. Starting with the increase in lift per unit span due to an arbitrary gust (L_g) as described in Equation 5.5 [13].

$$L_g(s) = 2\cdot\pi\cdot\rho\cdot U\cdot b\int_0^s w_g(\sigma)\cdot\Psi'(s-\sigma)d\sigma \tag{5.5}$$

In this equation, ρ is the air density, U is the flight speed, b is half of the chord length, w_g is the gust and $\Psi(s)$ is the Küssner function. Than there is s which describes the distance travelled measured in half chord lengths b: $U * t/b$. For modelling purposes, a transfer function is useful where the input is the gust and the output is L_g. In order to find the transfer functions the Laplace transform of Equation 5.5 is taken where complications arise with expressing $\Psi(s)$ in simple analytical form [13]. Therefore the satisfactory approximation of $\Psi(s)$ was used, as shown in Equation 5.6 [13].

$$\Psi(s) = 1 - 0.5e^{-0.13s} - 0.5e^{-s} \tag{5.6}$$

With this approximation, the Laplace transform can be taken and the transfer function presented in Equation 5.7 is found.

$$\frac{L_g(p)}{w_g(p)} = 2\cdot\pi\cdot\rho\cdot U\cdot b\cdot\left(\frac{0.565\cdot p+0.130}{p^2+1.130\cdot p+0.130}\right) \tag{5.7}$$

Where the complex Laplace variable used here is the symbol p. The increase in lift caused by deploying the flap is calculated with Equation 5.8 where only the β and $\dot{\beta}$ appear after the assumptions made in section 5.2 [12].

$$L_\beta = \left(b\cdot\frac{T_{11}}{2\cdot\pi} - \rho\cdot b^2\cdot U\cdot T_4\right)\cdot\dot{\beta} + 2\cdot\pi\cdot\rho\cdot b\cdot U^2\cdot\frac{T_{10}}{\pi}\cdot\beta \tag{5.8}$$

Where the T_n constants used in the matrices can be expressed as $T_n = f(x_h, b)$, full equations can be found in [16].From Equation 5.8 another transfer function is made shown in Equation 5.9 in order to model the desired β and $\dot{\beta}$.

$$\frac{\beta(p)}{L_\beta(p)} = \left[\left(b\cdot\frac{T_{11}}{2\cdot\pi} - \rho\cdot b^2\cdot U\cdot T_4\right)\cdot p + 2\cdot\pi\cdot\rho\cdot b\cdot U^2\cdot\frac{T_{10}}{\pi}\right]^{-1} \tag{5.9}$$

With Equation 5.7 and Equation 5.9 it is possible to, given a arbitrary gust input, calculate the desired flap deflection β_d and the deflection speed $\dot{\beta}_d$ for optimal GLA.

Then there are some physical limitations namely: $\beta_{max} = 15\,°$, $\dot{\beta}_{max} = 30\,°/s$ and the required moment of the actuator (M_a) which is calculated in subsection 5.3.3. Since the actuators are a design choice, actuators that can provide this moment at a rate of $30\,°/s$ shall be chosen. Due to these physical limitations, it could be the case that the aircraft is not able to deploy the flaps far and/or fast enough to fully alleviate the load increase due to the gust. In that case, Equation 5.4 will not add up to zero. The lift that remains can be calculated using Equation 5.8 and is an indication of the aircraft's ability to alleviate gust loads.

A SIMULINK model open loop controller was built using: Equation 5.7, Equation 5.8, Equation 5.9, several constants, the physical limitations and the gust model. Then a MATLAB script was written to calculate the constants, be able to run the SIMULINK model in a loop and make plots of the lift distribution. Since one has to design for the ultimate loading case and the gusts as described in subsection 5.3.1 are a function of H, one has to check which gust causes the critical loading case. The GLA capabilities for different gusts are presented as load factor and shown in Table 5.2, where the load factor is calculated with respect to the MTOW.

H (ft)	**30**	**100**	**200**	**300**	**350**
n_{gust}	1.07	1.27	1.55	1.82	1.94
$n_{gust+GLA}$	1.01	1.04	1.11	1.16	1.26

Table 5.2: Load factor of the gust with and without GLA as a function of H

From Table 5.2 it becomes clear that H = 350 ft gives the critical loading case and is thus the sizing case for GLA. The GLA capabilities of the wing reduce the loading factor n by approximately 0.65 during the critical loading case. In Figure 5.2 the 1g lift distribution discretised in 50 span wise steps obtained from chapter 4 is shown together with the lift distribution due to the gust and the lift distribution with GLA.

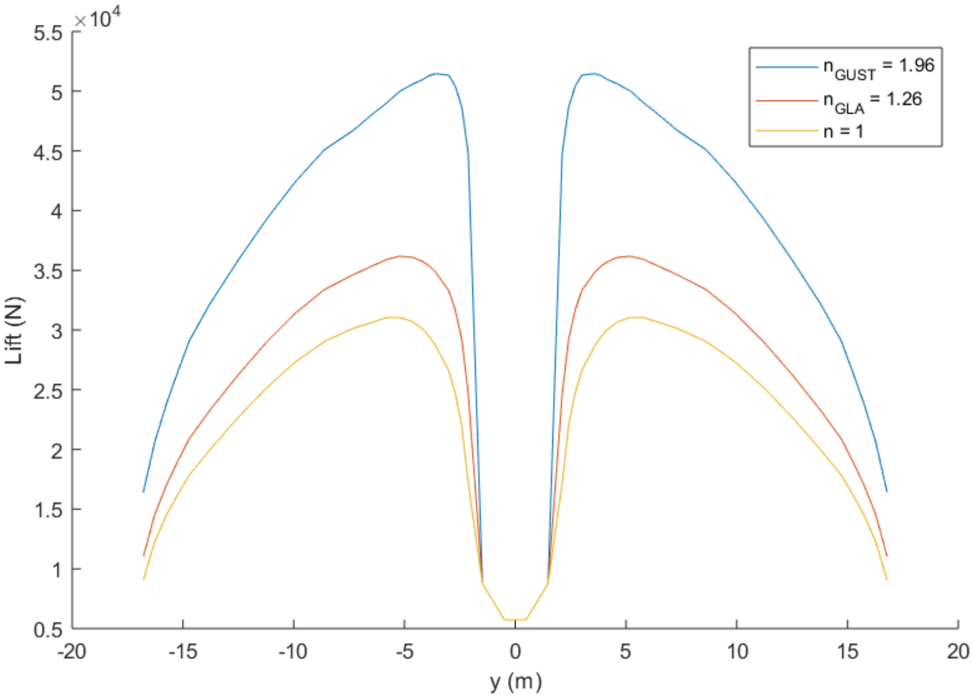

Figure 5.2: Lift distributions for n = 1, 1.94, 1.26

Besides lowering the load factor, extra torque load is induced by the gust and the flaps. Per unit span, the moment around the shear centre due to the gust (M_{sc}^{g}) is calculated using Equation 5.10.

$$M_{sc}^{g} = L_g b \cdot (a - 0.5) \tag{5.10}$$

Where the lift due to gust is calculated using Equation 5.5. Constant a is can calculated using $x_f/b-1$, where x_h refers to the location of the hinge measured from the leading edge. The moment around the shear centre due to flap deflection (M_{sc}^{β}) is calculated using Equation 5.12.

As explained in section 5.1 after MLA, the gust might be the sizing loading case which is the reason for the GLA system to be implemented. To check if the wing its structural strength is sufficient to be able to cope with the strongest gusts reduced by GLA, Figure 5.2 and the added torque load are used as an input into the structural model which is described in chapter 6.

5.3.3. Hinge Moment

The actuator moment is calculated by setting the magnitude equal to the moment due to the flap deflection (M_{β}), which is calculated using Equation 5.11 [12]. Similarly to Equation 5.8 only the β and $\dot{\beta}$ terms are taken into account.

$$M_a = M_{\beta} = \rho b^3 U \frac{1}{2\pi}\left[-T_4 T_{11} + T_{11} T_{12}\right]\cdot\dot{\beta} + \rho b^2 U^2 \frac{1}{\pi}\left[(T_5 - T_4 T_{10}) + T_{10} T_{12}\right]\cdot\beta \tag{5.11}$$

By discretising halve of the wing into the eight flap sections, each with their own chord length and span distance, the required actuators moments were calculated for each flap using Equation 5.11. Since the inner hinges have to be able to deflect the flap even when the outer flaps have already been deflected, for M_a of the inner hinges the moments of the actuators of the outer hinges are taken into account. Table 5.3 shows the results with the respective hinge-line location.

Hinge (x/chord)	**0.704**	**0.805**	**0.899**
Section 1	6.2	2.8	0.9
Section 2	5.1	2.3	0.8
Section 3	4.1	1.8	0.6
Section 4	3.3	1.5	0.5
Section 5	5.1	2.3	0.8
Section 6	3.9	1.7	0.6
Section 7	2.8	1.2	0.4
Section 8	1.9	0.8	0.3

Table 5.3: M_{β} max in $kN\cdot m$ for each flap

5.4. MLA Model

The goal of MLA is to move the centre of pressure inboard, thus relieving the stress induced to the wing structure due to bending. In order to not compromise the manoeuvre capabilities of the aircraft and to still comply with regulations, the total lift force should remain the same compared to before alleviating the load [17]. The principle of MLA is visualised in Figure 5.3.

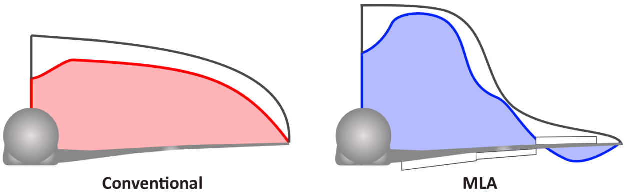

Figure 5.3: Principle of MLA [48]

Moving the centre of pressure inboard is achieved by deflecting the most outboard section of the flaps upwards. To make sure the load factor remains constant the most inboard flap section must deflected downwards. Different studies have been performed on MLA, in which the outboard control surface deflections are usually limited to ± 10°-13° [49][50][51]. Furthermore, a reference Airbus aircraft use a maximum control surface deflection of -11°[49].

Therefore, a setting a maximum flap deflection of -11°is set for the MLA design. This maximum setting will be used for the three most outboard flaps with the 2.5g load case. When the load factor is 1.0, the flaps do not deflect. In between, the deflection scales linearly with the load factor. By using Equation 5.8 one can calculate the required deflection and the number of inboard flaps that need to deflect to still end up with a load factor of 2.5. The results are shown in Table 5.4. These deflections, but also deflections for all the other load factors, shall be used by the MLA system its open loop controller during flight.

Segment	**1**	**2**	**3**	**4**	**5**	**6**	**7**	**8**
β	-10.5	-10.5	-10.5	0	0	11	11	11

Table 5.4: MLA β deflections for a load factor of 2.5

The resulting lift distribution with MLA applied, the manoeuvre lift distribution and the 1g lift distribution are shown in Figure 5.4.

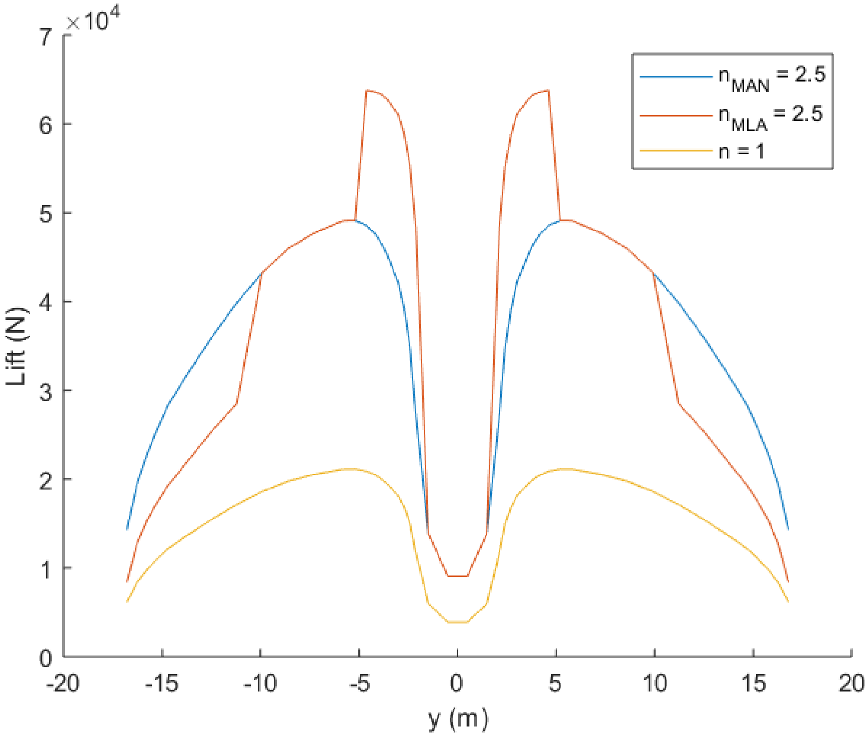

Figure 5.4: Lift distributions for 1g, manoeuvre and MLA

Deflecting the flaps has an effect on the torque load on the wing which is calculated first per unit length of the span and than expanded span wise. The moment around the shear centre due to flap deflection (M_{sc}^{β}) is calculated using Equation 5.12, where only the β and $\dot{\beta}$ are considered after the assumptions made in section 5.2 [12].

$$M_{sc}^{\beta} = \rho b^3 V(-T_1 + T_8 + (c-a)T_4 + aT_{11}) \cdot \dot{\beta} + \rho b^2 V^2 \big(-T4 + T_{10} 2a \big) \cdot \beta \tag{5.12}$$

This addition in torque load together with Figure 5.4 is used as input for the structures model. As described in chapter 6 it calculates the structural strength required to cope with the new loads after being alleviated by the MLA system.

5.5. Verification & Validation

Unit code testing was performed on all the calculations, which showed a calculations error since between the input and output one has to transform the units from ft to m which was forgotten.

The filters chosen in the SIMULINK, to make sure the β signal response would not go over the physical limitations, were first constructed in the following fashion. By using using Equation 5.4 to set L_g equal to L_β one has an input for the transfer function described in Equation 5.9 and out comes the desired deflection angle (β_d). This β_d was split up into two signals, both were passed through a filter and the filtered signal was merged together again using Equation 5.8 to find the L_β that the flaps are able to provide. This method is incorrect, since whenever the $\dot{\beta}$ max has been reached the β would still keep increasing with the same rate. In order to fix this first the β_d was passed through a rate filter and then through a saturation filter which would make sure the signal response would not surpass the physical limitations of the GLA system. For visualisation purposes Figure 5.5 shows on top the incorrect version and on the bottom the correct version of the β - filter setup.

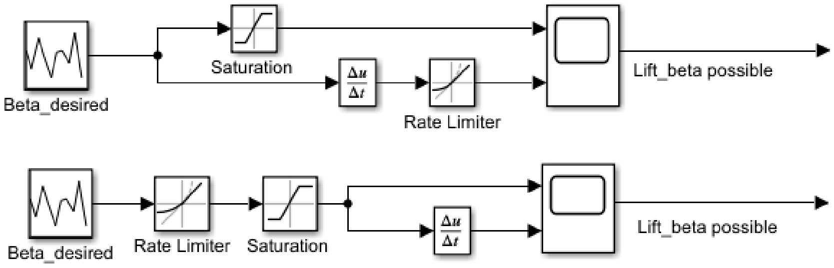

Figure 5.5: Part of the SIMULINK controller, with the incorrect β filter setup on top and the corrected version on the bottom

For validation of the gust model, a thesis work done by D. Westerveld was consulted [52]. The equations used were also taken from CS.25 and perfectly match the equation described in subsection 5.3.1. A similar version of Table 5.1 is made and an A320-200 like aircraft is studied as well. The values correspond almost one-to-one, with the maximum deviation being 2% for the values of the W_{MTO}.

About the quantification of the GLA capabilities, where a final value of approximately 0.65 reduction in load factor was found. For a lower flight speed of 150 m/s an A320-200 type of aircraft is capable of lowering the load factor from approximately 1.8 to 1.3 using a quasi-steady rigid airfoil model according to D. Westerveld [52]. Taking the difference in flight speed into account the result serve as an indication that the GLA capabilities are in roughly the same order of magnitude as calculated by D. Westerveld.

In chapter 4 an gust model was build independently of the gust model presented in this chapter. The final value of the load factor increase due to gust calculated in chapter 4 is equal to 1.86. Which compared to the value calculated in this chapter deviates by 5 % and is a means of verifying the accuracy of the model its calculations.

The calculations of the hinge moments of the flaps have also been preformed during the preliminary design phase. The moments were calculated for three hinge lines using the average chord length. The results are not accurate and several assumptions were taken. The assumptions that dynamic loads, arising from the moving of the flap, can be neglected were now taken into account. With the added quasi-steady dynamic loads the hinge line moment values increases as expected. For the first hinge-line the increase in moment is roughly a factor of three, which just for including the dynamic load is a bit off [53]. Therefore most likely other factors are in play here: the use of different equations and assumptions are expected to cause the biggest part of the deviation in outcome.

6

MLW Mass Analysis

Implementation of MLW on the legacy A320 has a number of implications on the aircraft wing mass which are discussed in this chapter. Firstly, the effect of active load alleviation, as discussed in chapter 5, on wing structural mass is presented in section 6.1. Then, mass estimations for both MTE (section 6.2) and HLFC (section 6.3) are discussed. Finally the overall effect of MLW on aircraft mass is summarised in section 6.4.

6.1. Wingbox Structural Analysis

In order to asses the structural implication of the active load alleviation and to ensure structural integrity of the system, a structural model has been created in MATLAB which sizes the structural parameters of the wingbox based upon a lift distribution input from the aerodynamic model. The structural model relies on first estimation dimensions for the wingbox structural parameters which are then optimised for the input loading case.The criteria for updating the structural parameters comes from a comparison of experienced local Von Mises stress and a failure criterion of the material. These optimised values are then converted to a mass estimation for the wing structural mass of the MLW. The model has been validated using legacy A320 wing structural mass. From this mass estimation, the relative difference as a result of implementation of active load alleviation is used in order to find the structural mass savings. Here, the working mechanism of the model is described and its results are discussed. Verification and validation procedures on the model are presented as well as a sensitivity analysis. The governing equations in this section are obtained from [54].

6.1.1. Assumptions and Simplifications

During the creation of the model, a number of simplifying assumptions have been made. These are listed below and their effect is discussed.

- The wing structural mass is estimated using an estimation of wingbox structural parameters (skin thickness, spar thickness and number of stringers) subjected to a load case of n = 2.5 with respect to MTOW of the benchmark A320. The model is not expected to provide 100% accurate results so a factor will be applied to all outcomes of the model. This factor comes from the initial comparison between results of the model, using as input the loading case 2.5g with no load alleviation, and legacy A320 wing structural mass.
- All forces acting on the wing are assumed to be transferred through the wingbox. Structural components from leading edge and trailing edge are ignored. This implies that the wingbox is sized to withstand all forces the wing is subjected to. This is considered a valid assumption and the effect is considered negligible as other systems on the wing have small load carrying capabilities.
- The only external force assumed to act on the structure is lift force. Drag is neglected as the contribution of the drag force is considered negligible when compared to lift force. This will lead to an undersized wingbox.
- The wingbox is idealised as a tapered box with rectangular and symmetric cross section. The curvature of the top and bottom panel has not been taken into account, leading to an underestimation of moment of inertia about the bending axis. Due to the symmetric nature of the structural idealisation, I_{xy} is equal to zero and

the shear centre is located in the centre of the wingbox. Since the offset due to the curvature of the wingbox is small when compared to its outer dimensions, this is considered a valid assumption.

- Fuel mass and fuel system mass are not considered in the calculation of internal force and moment distributions. The contribution due to the fuel mass components in the wing are considered negligible with respect to lift force. Since the design load factor is determined to be 2.5 with respect to MTOW, this assumption will lead to a conservative estimation of structural mass and thus an overestimation of wingbox parameters.
- The mass of leading and trailing edge systems have not been taken into a count in the internal force and moment calculations, leading to an overestimation of structural parameters.
- The wingbox is split into 24 sections over the span on which different constant distributed lift loads are available. This lift force is assumed to act on quarter chord of the local airfoil.
- The analysis is limited to normal stress, shear stress and internal torque analysis. As no major differences are expected in the skin buckling analysis of the MLW with respect to benchmark A320, the same rib mass fraction of structural mass is assumed.

6.1.2. Internal Force and Moment Distributions

As a first step in the structural analysis of the wingbox, all external forces are identified and displayed in a FBD as shown in Figure 6.1. The coordinate system assumes positive x perpendicular to the fuselage, positive z along the fuselage (toward nose) and positive y up.

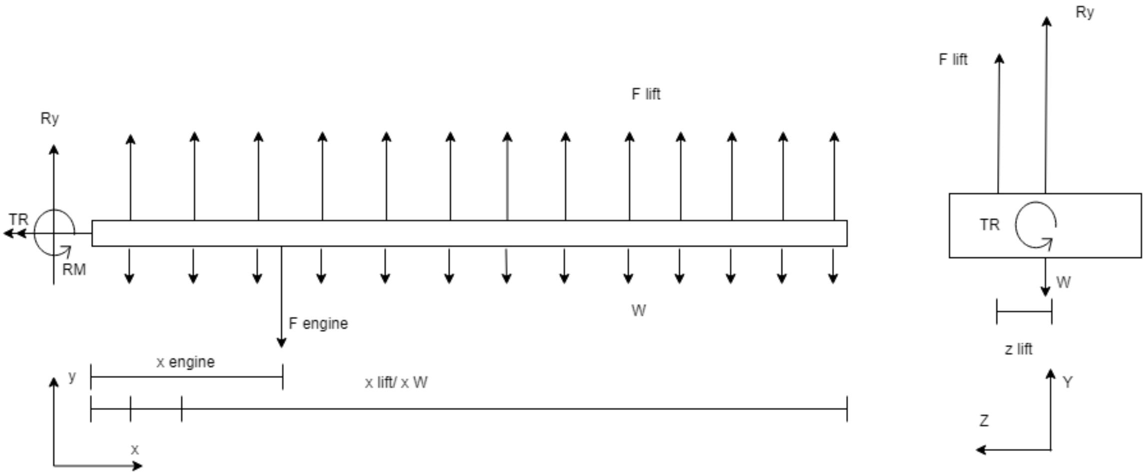

Figure 6.1: Free Body Diagram consisting of wing front view (left) and sectional view along wing (right)

From this FBD, three equilibrium equations can be set up: force equilibrium in the y direction (Equation 6.1), moment equilibrium about the z axis (Equation 6.2) and moment equilibrium about the x-axis (Equation 6.3) (Equation 6.1). These are solved for reaction moment about the x and z-axis (TR, RM respectively) as well as the reaction force in y direction (Ry). Furthermore F_{lift} represents the lift force in 24 distributed loads along the span, F_{engine} represents the weight of the engine and W represents the wing structural weight.

$$\sum Fy = 0 : R_y + F_{lift} - W - F_{engine} \tag{6.1}$$

$$\sum M_z = 0 : -M_R - F_{lift} \cdot x_{lift} + W \cdot x_W + F_{engine} \cdot x_{engine} \tag{6.2}$$

$$\sum M_x = 0 : -T_R + F_{lift} \cdot z_{lift} \tag{6.3}$$

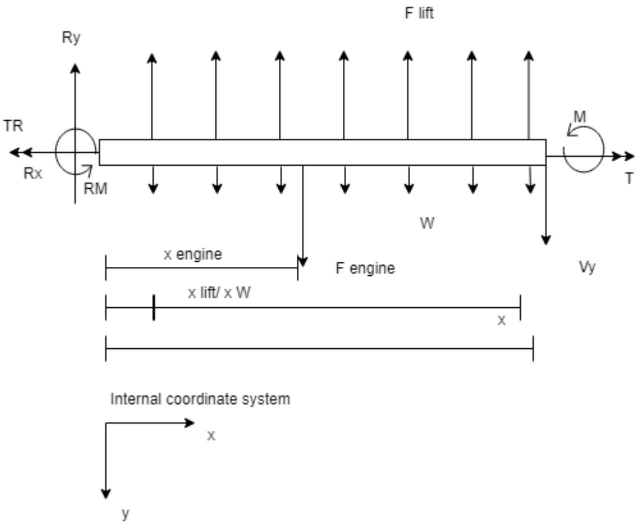

Figure 6.2: Internal FBD wing side view

From the internal free body diagram as depicted in Figure 6.2, the equations as function of location along the span for internal moment, shear and torque can be set up. These equations are depicted in Equation 6.4, Equation 6.6 and Equation 6.5, respectively.

$$M = -R_M - F_{engine} \cdot (x - x_{lift}) + F_{lift} \cdot (x - x_{lift}) - W \cdot (x - x_W) + Ry \cdot x \tag{6.4}$$

$$V_y = R_y + F_{lift} - W - F_{engine} \tag{6.5}$$

$$T = -T_R + F_{lift} \cdot z_{lift} \tag{6.6}$$

6.1.3. Structural Idealisation

In order to analyse the wingbox, a structural idealisation is created. This idealisation places 32 booms along each cross-section along the span. This idealisation is visualised in Figure 6.3.

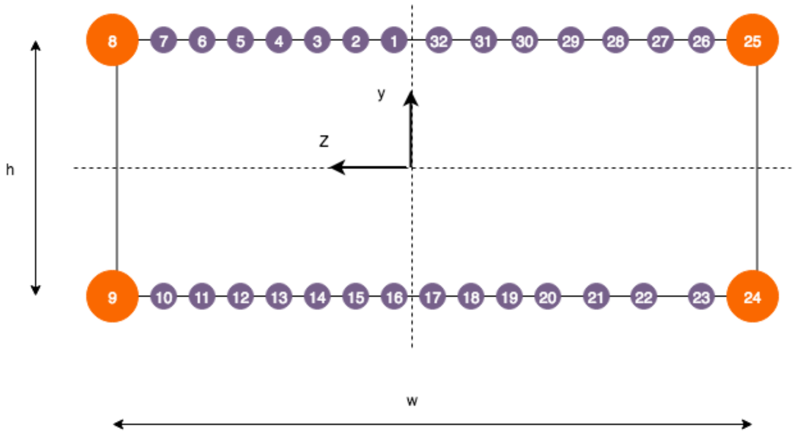

Figure 6.3: Structural idealisation with spar cap booms in orange and stringer booms in blue

The corner booms are placed on the location of the spar caps of the wingbox and its area is calculated using Equation 6.8. All other booms equally spaced over the top and bottom Panel and have both a stringer and skin contribution. When a stringer is placed on the boom, its area is calculated using Equation 6.7. If there is no stringer on the boom location, the area of the stringer drops out of this equation so the boom area is only dependent on skin contribution. In these equations, $A_{stringer}$ represent the stringer area which is found to be 328 mm^2, a value that is the result of an estimation using stringer mass and dimensional information from benchmark A320 [9]. t_{skin} is the skin thickness of the top or bottom panel, t_{spar} represents the thickness of the spar while w_{box} and h_{box} represent the width and height of the wingbox respectively. The booms are then connected by skin of the top and bottom panel. The corner booms are connected via the spars.

$$B_{stringer} = A_{stringer} + 2\frac{t_{skin} w_{box}}{6}(2+(1)) \tag{6.7}$$

$$B_{spar} = \frac{t_{spar} h_{box}}{6}(2+(-1)) + \frac{t_{skin}\frac{w_{box}}{16}}{6}(2+(1)) \tag{6.8}$$

6.1.4. Stress Analysis

Based on the structural idealisation created and the internal force and moment distribution, a stress analysis is performed on the wingbox. This analysis is split up into a normal and shear stress analysis which are then converted to a Von Mises stress at 32 different locations along the cross section for 24 locations across the span. The values for the Von Mises stress are used as failure criteria of the wingbox elements.

The normal stress due to bending experienced by the booms for each cross section is calculated using Equation 6.9. In this equation, the moment is obtained from the internal moment analysis for the specific section, the offset of the booms is calculated from wingbox geometry and the moment of inertia is calculated using Equation 6.10.

$$\sigma = \frac{M \cdot y_{boom}}{I_{zz}} \tag{6.9}$$

$$I_{zz} = (28 \cdot B_{stringer} + 4 \cdot B_{spar}) \cdot y_{boom}^2 \tag{6.10}$$

The shear stress analysis of a cross section is split into two parts: Shear stress due to shear force itself and due to torque generated by the distance between the point of application of the shear force and the shear centre. The difference in shear flow across a boom is calculated using Equation 6.11. Here, V_y is the shear force as experienced by the section, I_{xx} is the corresponding moment of inertia while B_i and y_i are the respective boom areas and corresponding vertical offset to the center line of the section. These values are then converted to shear flow as experienced by the skin segments connecting the respective booms.

$$q_b = \frac{V_y}{I_{zz}} \cdot \sum_{i=1}^{32} B_i \cdot y_{boom_i} \tag{6.11}$$

This value is then superimposed with shear flow due to torque calculated using Equation 6.12, with T being the torque as experienced by the section with A_m equal to the enclosed area of the section.

$$q_0 = \frac{T}{2 \cdot A_m} \tag{6.12}$$

The value for shear flow between all booms is then converted to shear stress by dividing it with the corresponding value for skin thickness. Having obtained both normal (σ_n) and shear stress (τ) values across the different cross sections along the span, the corresponding Von Mises stress can be calculated using Equation 6.13. This value is compared to the failure criteria of the material defined as yield stress of the material over 1.5 as specified by CS-25 [17]. The material used for all components of the wingbox is aluminium 6062. For this material, the yield stress is equal to 300 MPa [1] making the failure criteria equal to 200 MPa. The dynamic structural analysis of the structure is performed in chapter 7.

---

[1] `http://asm.matweb.com/search/SpecificMaterial.asp?bassnum=ma6061t6`

$$\sigma_v = \sqrt{\sigma_n^2 + \tau^2} \tag{6.13}$$

Dividing the maximum Von Mises stress, as experienced by a section, by the failure criteria of the material, gives a dimensionless factor which is used to update the dimensions of the local structural parameters. When this factor is lower than one, the structure is under-designed which is corrected by increasing skin and spar thickness and adding four stringers equally distributed around the centre of the wingbox. When this factor is higher than one, four stringers are removed and the skin and spar thickness is lowered accordingly. This adjustment is made across the span until the difference between the maximum sectional Von Mises stress and yield criteria of aluminium 6062 is smaller than 5%.

6.1.5. Mass Comparison to Benchmark A320

Having sized the wingbox parameters for all sections, a mass estimation of the structural mass can be performed. A mass breakdown of the benchmark A320 is analysed and presented in Table 6.1 [55]. In this table the mass of structural components is compared to the results of the model when the critical loading case is used as input. The critical loading case is defined as load factor 2.5 due to manoeuvre with respect to MTOW, without implementation of a load alleviation system.

Type	Mass A320 [kg]	Mass model [kg]
Wing structure mass	9045.8	11996
- spars	1161	1540
- stringers	419	455
- rib	6225	8254
- skin	1241	1645

Table 6.1: Mass of various structural components of A320 wing

These results reveal a discrepancy between benchmark A320 wing structural mass and calculated wing structural mass of 24.6%. Therefore a correction factor of 0.754 is applied to all mass estimations for wing structural mass. This offset can be explained by the effect the assumptions and simplifications the structural model is subjected to as described above. Seeing the amount of simplifications and their implications on the stress analysis, this correction factor is seen as realistic.

6.1.6. Results and Discussion

Having finalised the static structural model, the critical loading cases as experienced by the MLW over the entire flight envelope can be used as input in order to size wingbox parameters and generate structural mass estimations. The basis for this analysis will be critical lift distributions due to gust and manoeuvre after implementation of MLA and GLA as described in chapter 5. MLA will move the lift over the span more inboard, alleviating bending moment as experienced by the wingbox, however the overall load factor of the wing will not change. For GLA, the absolute value of load factor is decreased over the entire span, thus decreasing overall loads the wing is subjected to. The torque induced by flap deflection for both forms of load alleviation have been superimposed on the torque analysis. The values for the induced torque are imported from the respective load alleviation models.

Table 6.2 displays the structural mass of benchmark A320 as well as the structural mass obtained from analysis with MLA and GLA implemented, respectively. The loading case as experienced during manoeuvre is revealed to be critical and thus is leading in sizing of the structural parameters of the wingbox. This analysis reveals a decrease in 18.3% with respect to Benchmark A320, which is 1655.4 kg.

Type	**Mass A320 [kg]**	**Mass MLA [kg]**	**Mass GLA [kg]**
- spars	1161.4	948.9	653.8
- stringers	418.8	342.1	234.5
- rib	6224.7	5085.3	3504.4
- skin	1240.9	1013.8	698.6
Total	9045.8	7390.1	5092
% A320	**100**	**81.7**	**56.3**

Table 6.2: Structural mass comparison Benchmark A320 to MLW

The final wingbox for the MLW is sized for the critical manoeuvre loading with active MLA implemented. This final wingbox is subjected to A. critical manoeuvre loading without MLA, B. critical manoeuvre loading with MLA and C. critical gust loading with GLA. The Von Mises stress distribution of the wingbox for all three loading cases is visualised in Figure 6.4. This visualisation reveals the effect of active MLA and proves structural integrity of the wing structure for the critical loading cases due to gust and manoeuvre.

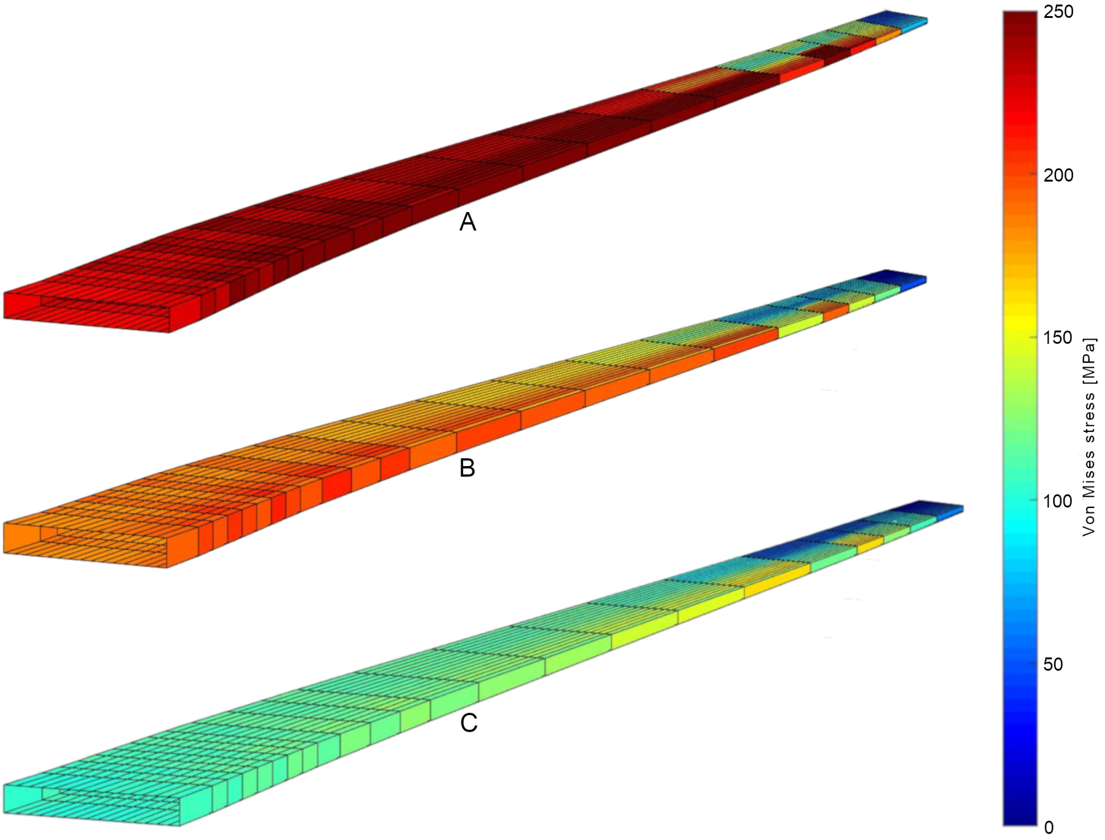

Figure 6.4: MATLAB visualisation of results showing Von Mises stresses for the various wingbox load cases. A) critical manoeuvre loading without MLA, B) critical manoeuvre loading with MLA, C) critical gust loading with GLA.

6.1.7. Verification and Validation

In order for the model to be used to generate meaningful results, it has to be verified and validated. Firstly, verification procedures have been presented in order to prove the model generates results in line with the assumptions and simplification it has been subjected to. Then validation procedures are presented which prove real world accuracy of the model.

- Verification on internal force and moment diagrams have been performed by visual inspection of the relation between internal shear and moment diagrams as well as analytically calculating maximum values at the root.

The internal diagrams are presented in Figure 6.5. The verification of these diagrams reveal no discrepancies with expectations as explained above, verifying the internal force and moment distributions.

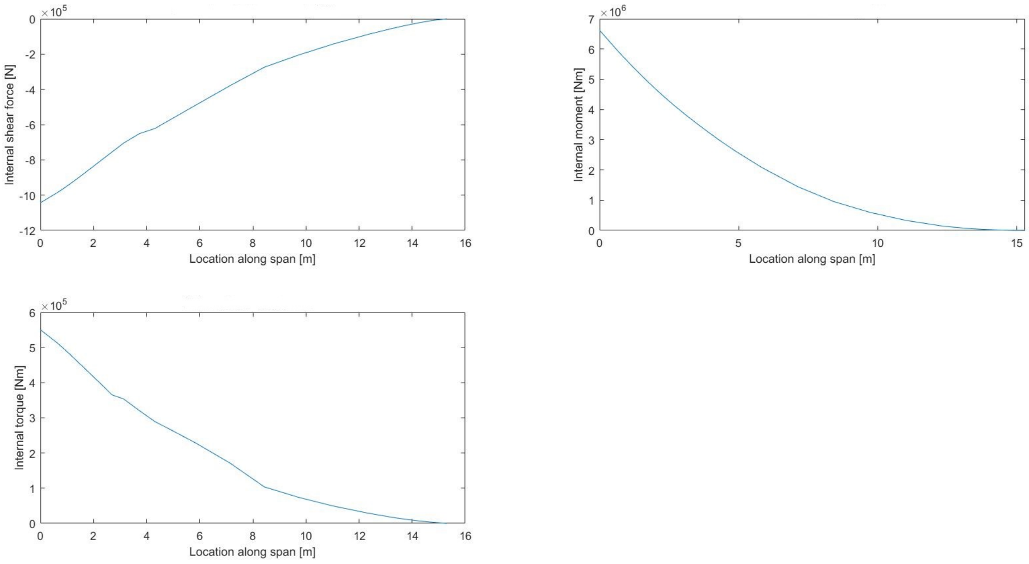

Figure 6.5: Internal shear diagram (top-left), internal moment diagram (top-right) and internal torque diagram (bottom-left)

- The structural idealisation and booms areas have been verified using visual inspection and hand calculation of boom areas for different cross sections along the span. The number of stringers as obtained from the wingbox geometry determine the amount of stringer boom area's which only rely on skin contribution or on stringer area as well. The placement of the booms have been inspected for any discrepancy's.
- From the structural idealisation results and wingbox parameters, a simple hand calculations for moment of inertia can be performed using Equation 6.10. This calculation is compared to results for moment of inertia at arbitrary locations along the span, revealing no discrepancy between hand calculations and outputs from the structural model.
- Finally, the model output wingbox geometry has been built in CATIA which is imported into ABAQUS. Most and foremost CATIA allows a visual inspection and for example rejects any discontinuous skin thickness distribution. From this geometry a finite element analysis (FEM), can be performed on the obtained geometry by imposing a simplified lift distribution on the geometry. From this analysis, deflection and Von Mises stresses over the span are obtained and compared to results as obtained from the model. The deflection and Von Mises stress results of this analysis are visualised in Figure 6.6. In the structural model, the equation used for obtaining the deflection due to bending of the wingbox for a specific section is shown in Equation 6.14. The values obtained for each section is summed in order to obtain total deflection at the tip which is compared to the result from the FEM analysis.

$$v(x) = \frac{1}{E} \cdot \frac{M(x) \cdot x}{I_{zz}(x)} \tag{6.14}$$

The comparison of both deflection and Von Mises is summarised in Table 6.3. The discrepancies between the two models are considered sufficiently small for verification of the model. Also, visual inspection of the Von Mises stress plot as obtained from the FEM model as shown in Figure 6.6, shows similar results for Von Mises stress for different locations along the span.

Parameter	**MATLAB model**	**FEM model**	**Discrepancy**
Maximum deflection due to bending [m]	0.94	0.95	1.4%
Von Mises stress top skin root [MPa]	187	196	4.8%
Von Mises stress top skin half-span [MPa]	180	190	5.6%

Table 6.3: Mass of various structural components of A320 wing

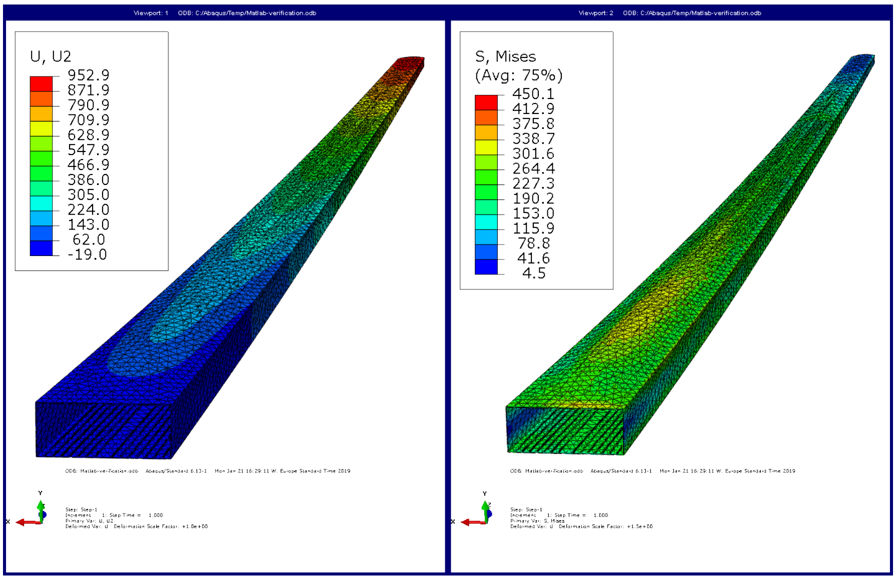

Figure 6.6: Vertical deflection [mm] of wingbox next to Van Mises stresses [MPa] as obtained by the ABAQUS model

After having subjected the model to a number of unit and system verification test, the model is considered verified. Now the model is subjected to a number of validation procedures as listed below.

- The mass estimation as obtained from the model using the critical loading case for legacy A320 (2.5g with respect to MTOW, no load alleviation) is compared to the structural mass breakdown of the benchmark wing. This comparison as described above, revealed a discrepancy of 24.6%. This is accepted to be valid due to the high number and impact of the assumptions the model is subjected to. The overestimation in structural mass is in line with the expectation of impact of the assumptions and simplifications.
- In order to validate the effect of MLA implementation obtained by the model, a comparison is made to a study by NASA in 1993 [56]. This study provides comparison of wing root bending moment experienced by lift load for a F-111A with mission adaptive wing. This study revealed a alleviation of wing bending root moment of approximately 30%. The structural model revealed a decrease in bending root moment as experienced by the wingbox of 14.9% with the implementation of MLA. In the study, as performed by NASA, the load factor was not kept as constant. Due to the difference in nature of the aircraft studied as well as the difference in approach, the difference in result is accepted as validation for the model. The absolute values for relative differences are non-comparable however comparison increases confidence the model does not overestimate the effect of MLA on the structure.
- A number of validation test are displayed in Table 6.4. These rely on validation methods beyond the scope of this report and will thus be mentioned as recommendations. The results of this validation analysis will provide confidence in the validation of the model.

Validation Method	Description	Validation Success criteria
Analysis	Perform a detailed FEM to analyse stresses in the wingbox under various conditions.	Validation test will be considered passed if FEM model predicts the same stresses, with 5% accuracy, as preliminary structural model
Demonstration	Building a full scale model of the wingbox and applying tip limit load.	Validation test will be considered passed if the model manages to withstand limit load predicted by structural model.
Test	Testing full scale wingbox by applying varying load and measuring strains, then comparing them with results predicted by structural model.	Validation test will be considered passed if structural model predicts measured stress and strain values with 5% accuracy.

Table 6.4: Structural model validation overview

6.1.8. Sensitivity Analysis

Following the verification and validation of the model, two separate sensitivity analyses are performed. The effect of both GLA and MLA on wing structural mass are analysed. The input for the model is a lift distribution, dependent on load factor, for which the structural parameters have been optimised so that the yield criteria ($\frac{\sigma_{yield}}{1.5}$) is not exceeded over the span. The GLA model decreases the absolute value of critical load factor. The effect of adjusting this value on wing structural mass is analysed by adjusting input load factor and comparing wing structural mass output. This analysis is visualised in Figure 6.7. The analysis reveals a near-linear relation between gust load factor and wing structural mass. As the structural parameters are optimised for a predefined stress criteria, this is in line with the expectations. The non-linear kink near the origin is the result of build in constraints on minimal thickness for structural parameters. It can be concluded from the analysis, a decrease in critical load factor of one, leads to a decrease in required wing structural mass of approximately 2900 kg which is deemed acceptable.

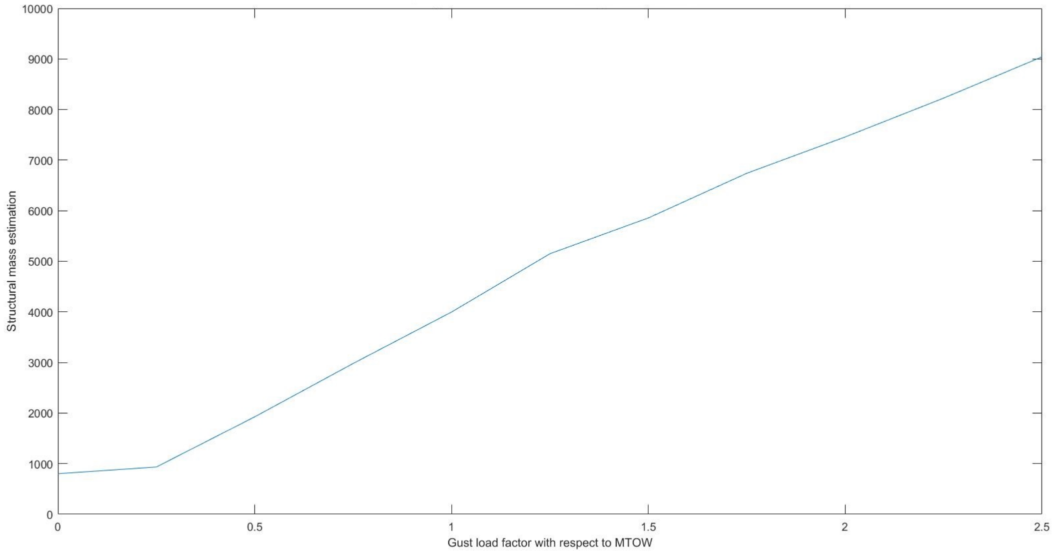

Figure 6.7: Sensitivity analysis effect of gust load alleviation on wing structural mass

Finally the effect of MLA on wing structural mass is analysed by using three different loading cases as input and analysing the output wing structural mass. All different loading cases analysed are generated for load factor 2.5 with respect to MTOW. Loading case A moves the lift force more outboard, by means of negative deflection of the outboard flaps of five degrees, and is therefore expected to shown an increase in required wing structural mass. Loading case B alleviates loads by alleviating the middle wing sections via a positive deflection of eleven degrees for the middle flaps and is thus expected to show a decrease in required wing structural mass. The third loading case C, describes the optimal MLA distribution for which the final wingbox parameters have been determined as described in section 5.4, alleviating the outboard sections of the wing. This loading case is expected to show the largest decrease in required wing structural mass. The result of the analysis is summarised in Table 6.5. The results of the sensitivity analysis are in line with the expectations.

Loading case	**Required wing structural mass[kg]**	**Relative with respect to benchmark A320[%]**
A	9724	107.5
B	8205	90.7
C	7390	81.7

Table 6.5: Results sensitivity analysis on MLA effect on wing structural mass

6.2. MTE Mass Estimation

The system mass estimation for MTE is based mass estimation of the MTE structural components and actuation system. The mass estimation of the structural component is based on the geometrical layout of the system as explained in section 3.1. The dimensional constraints are used to build up CATIA models of the different structural components of MTE, which are imported into ABAQUS. A FEM stress analysis is performed on the critical sections of the wing providing thickness estimations for the different components. These values are then extrapolated over the span. In combination with the geometrical data of the MTE, a complete mass estimation of the MTE is made. For the MTE actuation system mass estimation, required actuation force as obtained in chapter 5 is used as a basis for analysis.

Components of the MTE subjected to analysis are: aluminium alloy stringers, aluminium alloy ribs, and skin consisting out of Hyperflex-02 foam inserts, skin coating and aluminium skin reinforcement. Finally, connecting sections of the different flap segments are sized for both length and thickness. Sheet metal parts like ribs, stringers and skin are modelled as shell structure for which sections are assigned that contain the shell thickness as a parameter, which can be quickly adjusted for each iteration. The rear spar of the wingbox was used as a boundary condition due to its high structural stiffness with respect to the MTE components.

6.2.1. Sizing Stringers

The stringers of the MTE structure (located in pairs next to the blue Hyperflex-02 pads, see Figure 3.1) are responsible for transferring spanwise forces. From deflection of the wing (obtained in section 6.1) the stringers can be sized, thus sizing the stringers so they are able to cope with the normal stresses generated due to bending of the wing.

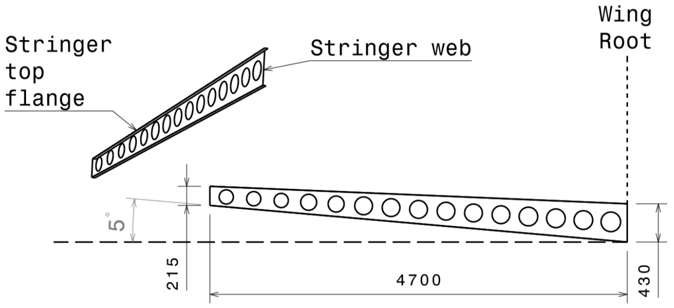

Figure 6.8: Drawing of the inboard stringer showing the 5 degree dihedral and taper of the stringer itself. The pinned boundary condition is applied on the root and the deflection is applied on the MAC spanwise position.

The stringer webs are limited by the TE skin, therefore they follow the dihedral of the wing as well as the sweep. However for this analysis it is assumed that the thickness of web or width of flange of an individual stringers doesn't change along the spanwise location. Each section consists of six stringers for which three categories have been defined: two large stringers connected to the most forward rib, two medium sized stringers connected to the centre rib and two small sized stringers connected to the most aft rib. This leads to a total amount of stringers of 96 (4 sections per wing inboard, 4 sections per wing outboard) for both wings. The stringers consist two flanges connected by a web. Both thicknesses are estimated for all stringers.

One end of the stringers is pinned whereas the other side is deflected in the vertical direction according to the deflection dictated by the wingbox. Figure 6.9 shows that the stresses are concentrated on the flanges as one would expect from structural component subjected to bending moments. Even at a web thickness of 1mm the Von Mises stresses stay far below the critical value of 200 MPa, determined in section 6.1. Further mass reduction of 24 percent is achieved by adding holes aligned on the centre line of the stringers. This web thickness along the span is constant for the stringers.

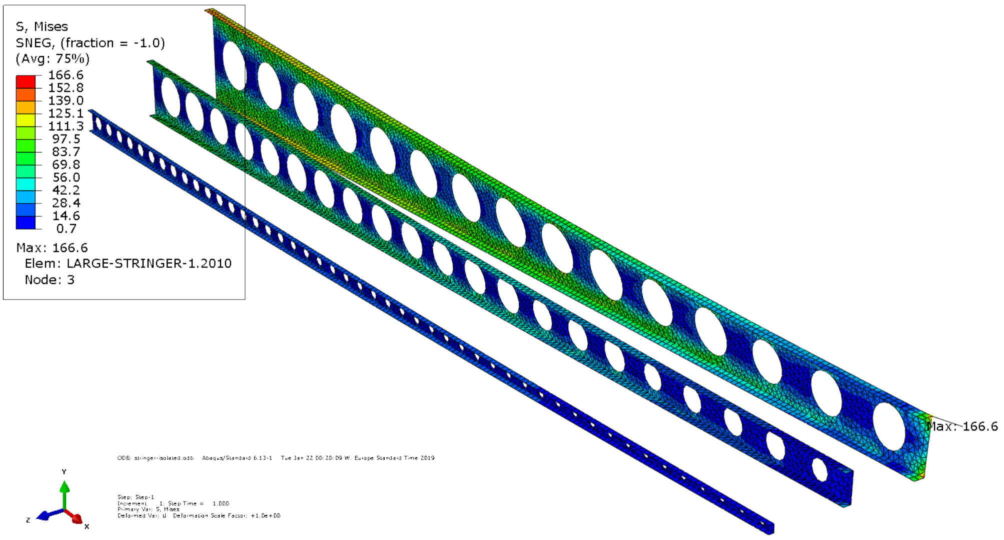

Figure 6.9: Optimised stringers of the inboard section at a vertical deflection of 90mm with minimised web thickness

For the flange thickness, more variation is possible. Large sized stringers have been sized with 2 mm flange thickness whereas the medium and small stringers are sized to 1 mm flange thickness. The stresses acting on these stringers can be reviewed in Figure 6.9. Using these thickness estimations, the total stringer mass can be calculated within ABAQUS to be 63 kg for all stringers.

6.2.2. Sizing Chordwise Ribs

The active chordwise ribs encapsulate each flap section, leading to a total amount of 32 active chordwise ribs for the whole MTE system. The ribs are threefold, interlinked via hinges with the most forward hinge connected to the MTE mount which is attached to the rear spar. The ribs main structural load are the aerodynamics forces on the MTE. To avoid complications of interactions between assembly parts in ABAQUS it was chosen to model the active rib segment as an integral part. This approach mimics a situation when the actuators are locked and the ribs have to sustain the lift load which introduces a bending moment to the ribs. Boundary conditions are applied on the trailing edge mount at the edges that are connected to the rear spar. The lift force is modelled as a constant distributed force as a shell edge load on the top edge.

Only the most critical rib segment, the one closest to the wing root at the fuselage, is analysed and the results are extrapolated upon all other segments proportional to the MTE chord length. This is a conservative estimation of the structure as the lift force decreases towards the tip, lowering the force due to lift as experienced by the MTE. The thicknesses of web and flange are held constant. The final stress analysis for the rib segment at the root is shown in Figure 6.10. The section parameters of the individual shell partitions are listed in Table 6.6.

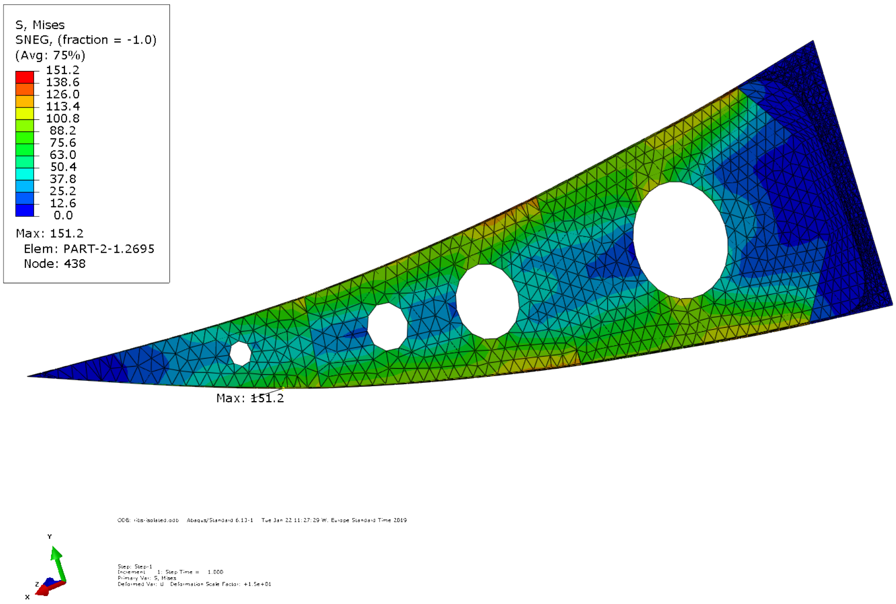

Figure 6.10: Optimised root rib at maximum lift force with reduced web thickness with deformation scale factor 500

Rib component	web thickness [mm]	flange width [mm]
Rib mount	3	15
Large rib partition	2	15
Medium rib partition	1	12.5
Small rib partition	1	10

Table 6.6: Thickness estimations root rib components

Extrapolating the mass as obtained from the root segment via chordwise regression towards the tip for the other rib segments leads to a total rib mass 115 kg per wing.

6.2.3. Sizing Skin Components

For the skin components, and estimation for aluminium alloy skin reinforcement and Hyperflex-02 foam is performed by looking at the maximum deflection of the root section. The root section is chosen due to the longest MTE chord which results in the highest deflection for the given maximum deflection angle leading to a maximum vertical deflection of 103.8 cm

The morphing skin, is tested and compared to a conventional aluminium skin subjected to maximum deflections. The skin is modelled as a planar shell for which a boundary condition applied at one edge. The results of the stress analysis is presented in Figure 6.11. During this analysis a 2 mm thick aluminium skin is compared to a segmented 1 mm coating material with Hyperflex-02 inserts (80 x 20 mm) and 1 mm skin reinforcements. Even though the stresses acting on the skin are small it has to be noted that a reduction of the Hyperflex-02 material below 20 mm thickness leads to a loss of smoothness of the skin surface. These thickness estimations are constant over the span leading to a mass estimation of 186 kg per wing.

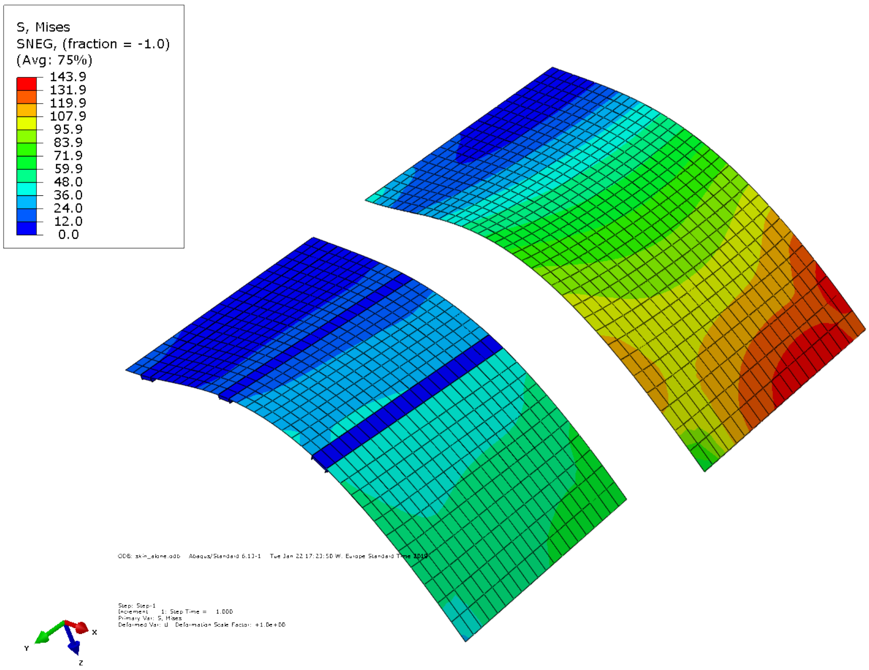

Figure 6.11: Comparison of morphing skin (bottom left) versus a conventional aluminium skin. The skin itself follows the taper and therefore isn't symmetric

6.2.4. Sizing Connection Flap Segment

The connection material allows continuous surfaces for MTE deflection differences between flap segments. For the connection, polydimethylsiloxane (PDMS) is used. PDMS is a high strain material that can be enhanced to work at low temperatures [21]. The maximum deflection difference on the MTE is provided by load alleviation requirements as described in chapter 5. So the connection length is sized for a deflection angle difference of eleven degrees. This difference in deflection leads to a vertical deviation on the chordwise edges of the trailing edge section which is proportional to the local MTE chord and calculated using the tangent function. With eight MTE sections it is required to have seven junctions with each having a unique gap width. In reality the gap material is subject to a distributed shear force but it has been assumed that the loading acting on the gap material is treated as a pure tensile elongation. Given the E-modulus for polydimethylsiloxane of 0.615 GPa together with a yield stress of 2.24 leads to a maximum elongation of 360 percent. Since polydimethylsiloxane is a hyper-elastic material which hasn't been widely applied in the aerospace industry so far, a safety factor of 2.0 is used. This safety factor compensates for the inability to analyse PDMS as a hyperelastic material in detail. However the flap segment connection also is not a critical part of the wing. In case it rips, the flight can still continue with less efficiency. Since the gap width is obtained from the tensile limits of the material, the only unknown is the thickness of the layer. It has been decided to size the thickness so that the gap material can sustain the trailing edge lift loads which are present on the ribs segments. The result of the analysis reveals a thickness of 2 mm for all sections and a total mass for all connections of 12 kg per wing.

6.2.5. Sizing of Actuation System

To size the actuation system it is necessary to look at the force required to deflect the morphing surfaces under different conditions. These hinge moments were calculated for each of the three hinge of eight different span-wise sections, this was done in subsection 5.3.3. When looking at the hinge moments presented in Table 5.3 it can be noticed that the first and second hinge line require quite high moments. To be able to create enough torque to actuate these hinges it has been decided to use a gearbox system, this will increase the mass of the system and decrease the achievable deflection rates. As the first and second hinge lines are only used for high lift purposes, and therefore do not require high deflection rates this will not cause too much problems.

To design this system it was necessary to look at different manufacturers of actuators to get familiar with different types of actuators on the market, in the end the specifications from [2] were used. From this research it was decided to use the strongest actuator available for the first and second hinge line with an extra mass factor added for the gearbox system, for the third hinge line the actuators are sized using the actual required hinge moments, the final actuation system mass is estimated to be 824 kg.

6.2.6. Structural Mass MTE Summary

Now all MTE structural components and actuation system mass estimations have been performed, all results can be summarised as shown in Table 6.7. The final MTE system mass is determined to be 1200.2 kg. Since the MTE system completely replaces all legacy A320 trailing edge systems, which has a mass of 960 kg [4], the net mass increase of implementation of MTE on legacy A320 is determined to be 240 kg.

Subsystem	Component	Quantity	Total mass (kg)
MTE structural components	Ribs	32	115
	Stringers	96	63
	Flap skin	16	186
	Connection flaps	14	12
SUBTOTAL			**376**
MTE actuation system	Actuator hinge-line 1	16	308
	Actuator hinge-line 2	16	308
	Actuator hinge-line 3	18	208
SUBTOTAL			**824**
TOTAL			**+1200**

Table 6.7: A summary of MTE system masses

6.3. HLFC Mass Estimation

The mass estimation for the HLFC system is done by splitting it into three segments: (1) Suction surface, ducts and valves; (2) Control & Monitoring system; (3) Pump system & Power supply. Suction surface, duct and valve mass estimate is done using a bottom-up approach, whereas the other two segments were sized using a reference design study on a B757 HLFC system [14].

Mass estimation of the suction surfaces, ducts and valves was done by calculating mass of each component that was included in the detailed system design. That includes a perforated sheet, stringers, inner sheet, connecting ducts and shut-off/control valves. The ducting was chosen to be made from anodised aluminium but the outer suction surface is chosen to be made of titanium due to its evidently better durability properties when compared to other materials applied in a suction surface design [24]. Since flutes and pressure chambers need to be airtight, stringers and inner surface also need to be made out of titanium, because otherwise it would be very difficult to ensure structural durability together with airtightness [14]. Unfortunately, titanium also suffers from a number of severe disadvantages, mainly, it is very difficult to machine, and titanium based structures are difficult to produce [57]. The results can be seen in the system mass summary in Table 6.9.

Due to human resource constraints of the project, the mass of air pumping and HLFC control subsystems had to be estimated by analysing the mass division of a suction system applied on a B757-200 class aircraft's horizontal tailplane and not by a self-conducted research. This reference study involved a suction system applied to 20% of the horizontal tailplane's chord which is very comparable to this project's HLFC system extent and the conditions in which it operates (most importantly - altitude, velocity and sweep) [14]. The output of this reference study is mass of air pumping and HLFC control subsystems per kilowatt of pump power. Therefore, in order to obtain an estimate for these masses, required pump power has to be calculated for the HLFC applied to the concept of this project. Equation 6.15 calculates the power assuming an adiabatic pumping process [58].

$$P_{pump} = \frac{\dot{m}}{\eta_{pump}} \left(\frac{\gamma}{\gamma - 1}\right) R T_{in} \left\{ \left(\frac{p_{in}}{p_{out}}\right)^{\frac{\gamma-1}{\gamma}} - 1 \right\} \tag{6.15}$$

---

[2] `http://www.moog.com/literature/MCG/actprodguide.pdf`

In this equation further calculations are required for $\dot{m}$ (mass flow rate through the suction surfaces) and $T_i n$ (stagnation temperature inside the suction chambers). These are expressed by the succeeding Equation 6.16 and Equation 6.17.

$$\dot{m} = \rho V_w S_{panel} \tag{6.16}$$

$$T_{in} = \left(1 + \frac{\gamma - 1}{2} M^2\right) T \tag{6.17}$$

The values in the three previous equations for the design of HLFC system for this project are generated by estimations made in the detailed design sizing procedures as well as some assumptions based on previous research. Table 6.8 summarises these values.

Parameter	**Meaning**	**Value**	**Source of acquisition**
ρ	Air density	$0.348 kg/m^3$	Reference cruise conditions
V_w	Mean velocity of air going through the suction surface	$0.124 m/s$	From the suction coefficients, as used in Boeing 757 HLFC experiment, which were chosen to be pursued in this project [3]
S_{panel}	Wetted area of suction panels	$12 m^2$	From calculating the available suction area on the outboard part of the wing, as described in section 3.5
T	Static temperature	$216K$	Reference cruise conditions
M	Pump exit flow Mach number	0.2	This value is suggested in [14] p.322 to limit pressure losses in the system
γ	Ratio of specific heats	1.4	Extracted for approx. $216K$ temperature
η_{pump}	Suction pump efficiency	0.81	Multiplication of assumed compressor efficiency of (0.9) and motor efficiency (0.9)
p_{in}/p_{out}	Total pressure ratio across the pump	2.3	Value calculated in the detailed design of the suction system (see section 3.7)

Table 6.8: Values for pump power calculation and the explanation of their acquisition

The result yields that a power requirement for the suction pump is 37.2 kW. The reference sizing method used indicates that Control & Monitoring system has a mass 'density' of 1.07 kg/kW and the Pump system & Power supply has it at 2.86 kg/kW [14]. The breakdown of these masses is given in summarised Table 6.9.

Subsystem	Component	Quantity	Mass (kg)
Suction surface, ducts and valves	Aluminium leading edge sheets	2	-194
	Perforated titanium sheet	2	+205
	Titanium stringers	40	+31
	Inner titanium sheet	2	+54
	Main transfer duct	2	+30
	Manifold ducts	18	+6
	Bleed air ducts	2	+4
	Shut-off valves	2	+5
SUBTOTAL			**+141**
Control & Monitoring system	HLFC computer	1	+12
	Control valves	6	+10
	Static pressure sensors	8	+8
	Wiring harness	-	+12
SUBTOTAL			**+41**
Pump system & Power supply	Compressor	1	+25
	Electric motor	1	+32
	Starter turbine	1	+11
	Wiring harness	-	+15
	Additional power generation	2	+22
SUBTOTAL			**+105**
TOTAL			**+287**

Table 6.9: A summary of HLFC suction system masses

This concludes, that the added mass to the wing due to HLFC suction system is approximately 285 kg.

6.3.1. Sensitivity Study

A small sensitivity study was conducted to see how the drag benefit of HLFC changes with the system mass of HLFC (Figure 6.12). As expected, the methods to estimate system mass have a linear relationship with drag of the aircraft. Note, that it only makes sense to look at HLFC mass above approximately $100kg$ because installation factors of HLFC diminish this linear relationship.

This linear relationship indicates, that there is no optimal extent, to which the HLFC system must be applied. It was chosen to design the HLFC system for the maximum possible implementation (full outboard wing), because the increase in system mass is lower than the benefits of fuel reduction. Using Breguet analysis (see subsection 4.5.2), it can be shown that implementing HLFC to get 3.5% reduction will lead to $410kg$ lower fuel consumption over a mission whereas drag savings of 1% only achieve $120kg$. This becomes clear that for economical reasons it is more worthy to apply the highest possible extent of HLFC on the wings, because it leads to more significant fuel savings.

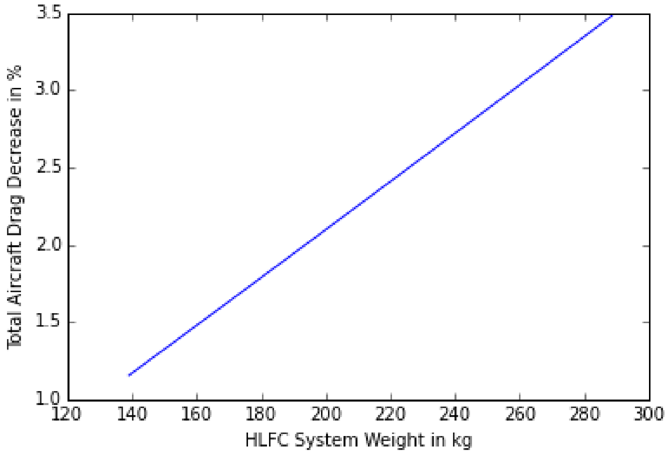

Figure 6.12: Sensitivity of HLFC system mass on aircraft drag decrease

6.4. MLW Payload Implication

Implementation of the MLW to a legacy A320 has a number of implications on total aircraft mass. Firstly, the implementation of MTE and HLFC has an effect due to the mass of the two systems. Besides this, the significant drag reduction of MLW compared to legacy A320 wing leads to an increase in efficiency and thus a decrease in fuel required as explained in subsection 4.5.2. Finally the load alleviation system of the MLW has an positive effect on wing structural mass as described in section 6.1. These implications are summarised in Table 6.10. Implementation of MLW on legacy A320 thus leads to a decrease in aircraft mass of 2270 kg. This reduction can be used for an increase in payload of 11.35% with respect to maximum legacy A320 payload (20767 kg) [8] without exceeding MTOW.

Table 6.10: Aircraft mass implications MLW

Source	**Effect on aircraft mass [kg]**
Implementation MTE	+240
Implementation HLFC	+285
Fuel mass savings	-1142
Wing structural mass	-1655
Total	**- 2270**

7

Wing Stability Analysis

Since aeroelasticity as a phenomenon is the main source of instability of an aircraft, it is crucial to consider aeroelastic characteristics in aircraft structure design. According to aeroelastic stability requirements of CS-25.629, the freestream velocity in flight where the aeroelastic instabilities occurs should be higher than the defined V-n range by a factor of 1.15 [17]. These aeroelastic instabilities include flutter, divergence, control reversal and any undue loss of stability and control as a result of structural deformation. From various types of instabilities, self-excitation vibration of wing or coupled bending-torsional vibration of wing and aileron called flutter is a very important phenomenon [59]. Therefore, in this chapter, analysis is mainly focused on flutter of the wing.

Analysis begins by setting up the suitable discretised wing model in section 7.1. The governing differential equations used for the analysis and the derived state matrix are presented in section 7.2. In section 7.3, modal analysis is performed for coupled Multiple Degree-Of-Freedom (MDOF) system wing model. Then, the aeroelastic instabilities are identified in section 7.4. In section 7.5, validation method and the results are presented. Finally, all the results are summarised and discussed in section 7.6.

7.1. Wing Modelling

In order to analyse aeroelastic behaviour of the wing, it has been modelled as 24 discretised lumped masses and spring system over the span, each section having three Degrees of Freedom (DOF), which means that it is elastically restrained by linear springs in pitch α, heave h and the rotation of morphing trailing edge β. The number of discretised sections is chosen to be 24, as data received from the static structural analysis used 24 sections, which makes it consistent and convenient. Figure 7.1 shows the description of the lumped mass-spring model with its sign convention.

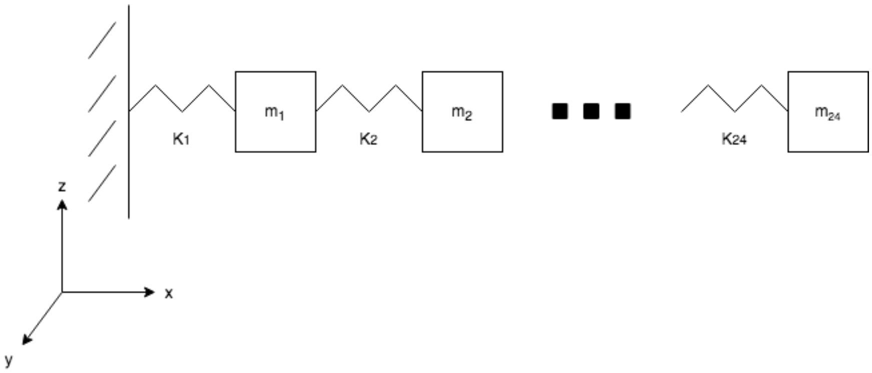

Figure 7.1: Lumped model of the wing

Figure 7.2 shows the sign convention for the DOFs in 2D section where upward pitch, downward heave and downward rotation of MTE are defined as positive. Here, it shows that the airfoil section is suspended by an extension spring of stiffness K_h and a torsional spring of stiffness K_α. Moreover, the MTE is attached with a stiffness K_β. The complete system is then immersed in incompressible flow with density ρ and a horizontal freestream velocity of V_∞.

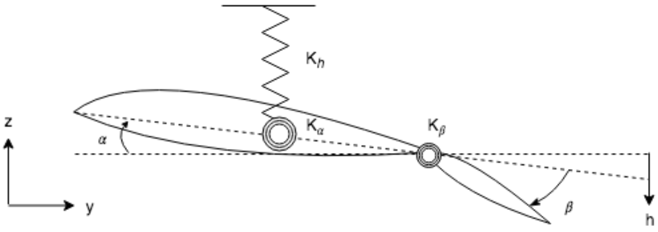

Figure 7.2: 2D wing section with deflected MTE

Some of the important geometric parameters of this model include x_f, the location of the elastic axis relative to the chord as well as x_h, the location of the MTE hinge.

Based on the static structural analysis, it turned out that the location of the shear centre of the wingbox is in the range of 0.35 - 0.42 of the chord. Although wingbox is the major part that contributes to the location of elastic axis, it has been decided to add a correction to take the entire cross section into account, which includes leading edge as well as the trailing edge. In [15], location of the elastic axis of the experimental wing model is obtained from static as well as vibration tests. Thus, for the following wing stability analysis, the averaged value from the static structural analysis and the experimental wing model of the literature is considered for the x_f. For x_h, the first hinge location is used, as defined in section 3.1.

The local stiffness K_h and K_α are computed using the material and structural properties from the structural analysis. For K_β, these properties are approximated by scaling with respect to the other stiffness terms based on the experimental wing model [15].

7.2. Governing Equations

In this section, governing equations of the wing model are presented. For this analysis, aeroelastic equations of motion for pitch-plunge-aileron model with quasi-steady aerodynamics are used. This model is developed by Theodorsen in order to develop his theory of unsteady aerodynamics and is also known as the typical aeroelastic section [16].

The governing differential equation is presented in a matrix form in Equation 7.1. The matrices **A** and **B** are the structural and aerodynamic inertial terms, while matrices **C** and **D** are structural and aerodynamic damping terms. Lastly, matrices **E** and **F** refer to the structural and aerodynamic stiffness terms.

$$(\mathbf{A}+\rho\mathbf{B})\frac{\partial^2\mathbf{x}}{\partial t^2}+(\mathbf{C}+\rho V_\infty\mathbf{D})\frac{\partial\mathbf{x}}{\partial t}+(\mathbf{E}+\rho V_\infty^2\mathbf{F})\mathbf{x}=0 \tag{7.1}$$

The matrix **A** in Equation 7.1 is the local structural mass matrix for the n^{th} section, with coupled inertial terms. Similarly, Equation 7.3 represents the aerodynamic inertial matrix.

$$\mathbf{A}_\mathrm{n}=\begin{bmatrix} M & S & S_\beta \\ S & I_\alpha & I_{\alpha\beta} \\ S_\alpha & I_{\alpha\beta} & I_\beta \end{bmatrix} \tag{7.2}$$

$$\mathbf{B}_\mathrm{n}=b^2\begin{bmatrix} \pi & -\pi ab & -T_1 b \\ -\pi ab & \pi b^2(1/8+a^2) & -(T_7+(c-a)T_1)b^2 \\ -T_1 b & 2T_{13}b^2 & -T_3 b^2/\pi \end{bmatrix} \tag{7.3}$$

The structural damping matrix **C** is set to zero as damping force is often negligible in aeroelastic problems, while the aerodynamic damping matrix **D** is shown in Equation 7.4 [60]. $\Phi(0)$ is the exponential approximation of the Wagner function evaluated at t=0.

$$\mathbf{D}_{\mathrm{n}} = \mathbf{D}_{\mathrm{n}_1} + \Phi(t=0)\mathbf{D}_{\mathrm{n}_2} \tag{7.4}$$

$$\mathbf{D}_{\mathrm{n}_1} = b^2 \begin{bmatrix} 0 & \pi & -T_4 \\ 0 & \pi(1/2-a)b & (T_1 - T_8 - (c_h - a)T_4 + T_{11}/2)b \\ 0 & (-2T_9 - T_1 + T_4(a-1/2)b & -T_4 T_{11} b/2\pi \end{bmatrix} \tag{7.5}$$

$$\mathbf{D}_{\mathrm{n}_2} = \begin{bmatrix} 2\pi b & 2\pi b^2(1/2-a) & b^2 T_{11} \\ -2\pi b^2(a+1/2) & -2\pi b^3(a+1/2)(1/2-a) & -b^3(a+1/2)T_{11} \\ b^2 T_{12} & b^3 T_{12}(1/2-a) & b^3 T_{12} T_{11}/2\pi \end{bmatrix} \tag{7.6}$$

For each n$^{\text{th}}$ section, the structural stiffness matrix is coupled as in Equation 7.7. Notice that wing sections along the span are coupled through these stiffness terms. Lastly, the aerodynamic stiffness matrix is shown in Equation 7.8.

$$\mathbf{E}_{\mathrm{n}} = \begin{bmatrix} K_h & 0 & 0 \\ 0 & K_\alpha & 0 \\ 0 & 0 & K_\beta \end{bmatrix} \tag{7.7}$$

$$\mathbf{F}_{\mathrm{n}} = \mathbf{F}_{\mathrm{n}_1} + \Phi(0)\mathbf{F}_{\mathrm{n}_2} + \Xi\mathbf{F}_{\mathrm{n}_3} \tag{7.8}$$

$$\mathbf{F}_{\mathrm{n}_1} = b^2 \begin{bmatrix} 0 & 0 & 0 \\ 0 & 0 & T_4 + T_{10} \\ 0 & 0 & (T_5 - T_4 T_{10})/\pi \end{bmatrix} \tag{7.9}$$

$$\mathbf{F}_{\mathrm{n}_2} = \begin{bmatrix} 0 & 2\pi b & 2bT_{10} \\ 0 & -2\pi b^2 & T_4 + T_{10} \\ 0 & 0 & (T_5 - T_4 T_{10})/\pi \end{bmatrix} \tag{7.10}$$

Furthermore, in Equation 7.11, the local state vector for the n$^{\text{th}}$ element is defined for three DOFs.

$$\mathbf{x}_{\mathrm{n}} = \begin{Bmatrix} h_{\mathrm{n}} \\ \alpha_{\mathrm{n}} \\ \beta_{\mathrm{n}} \end{Bmatrix} \tag{7.11}$$

While the T_n constants used in the matrices can be expressed as $T_n = f(x_h, b)$, full equations can be found in [16]. In addition, constant a can be expressed as $a = f(x_f, b)$. x_h and x_f refer to the location of the hinge and the elastic axis respectively, while b refers to the half length of the chord. Similarly, the inertial terms, except for the lumped masses, are evaluated as a function of b, x_f and x_h.

Lastly, all the matrices are coupled along the span of N = 24 sections. Resulting state matrix of a coupled system is derived as in Equation 7.12.

$$\mathbf{A}_{\mathrm{s}} = \begin{bmatrix} \mathbf{0}_{3\mathrm{N}x3\mathrm{N}} & \mathbf{I}_{3\mathrm{N}x3\mathrm{N}} \\ -(\mathbf{A}+\rho\mathbf{B})^{-1}(\mathbf{E}+\rho V_\infty^2\mathbf{F}) & -(\mathbf{A}+\rho\mathbf{B})^{-1}(\mathbf{C}+\rho V_\infty\mathbf{D}) \end{bmatrix} \tag{7.12}$$

Then, Equation 7.13 is the corresponding global state vector.

$$\mathbf{x} = \begin{bmatrix} h_1 & \alpha_1 & \beta_1 & \cdots & \frac{\partial h_{\mathrm{N}}}{\partial t} & \frac{\partial \alpha_{\mathrm{N}}}{\partial t} & \frac{\partial \beta_{\mathrm{N}}}{\partial t} \end{bmatrix}^T \tag{7.13}$$

For better understanding, first few columns and rows of the global stiffness matrix is shown in Figure 7.3.

```
K =

   1.0e+11 *

  Columns 1 through 5

    0.870649077921048                    0                    0   -0.782975429329429                    0
                    0    0.038511137135197                    0                    0   -0.025576189680190
                    0                    0    0.015580829847958                    0                    0
   -0.782975429329429                    0                    0    1.527622866601969                    0
                    0   -0.025576189680190                    0                    0    0.049974076607314
                    0                    0   -0.010347610826633                    0                    0
                    0                    0                    0   -0.744647437272539                    0
                    0                    0                    0                    0   -0.024397886927125
                    0                    0                    0                    0                    0
```

Figure 7.3: First few lines of the global stiffness matrix

7.3. Modal Analysis

Through modal analysis, self-excitation vibration of a wing is analysed to ensure that no piece of structure with lightly damped resonant characteristics has the ability to be excited by a forcing resonance at the same frequency. This analysis is important as vortex shedding is not the only source of forcing resonance in aerodynamically loaded systems [61]. To achieve this, natural excitation frequencies of the wing, in bending and torsion, as well as the natural excitation frequency of the MTE deflection are analysed using a coupled MDOF system aeroelastic model introduced in the previous section.

The results of vibration analysis of a numerical wing model are shown in Table 7.1. This table shows the natural frequencies of free vibration for the lowest four modes in wing bending, torsion as well as the MTE deflection. From these results it is clear that the natural frequencies of bending and torsion are different from each other. In addition, it is shown that the frequency of the MTE deflection and the natural frequency of the wing are also different from each other. These results imply that in normal cruise flight condition, a structure of one mode shape is not expected to be excited by a forcing resonance at the same frequency of another mode shape that could lead to catastrophic failure.

Mode number	Frequency [Hz]	Mode shape
1	23.0	Bending
2	33.6	MTE Deflection
3	48.5	Bending
4	62.8	Torsion

Table 7.1: Results of vibration analysis of a numerical wing model

Each eigenvalue has a mode shape which represents relative amplitude in all three DOFs. These mode shapes show the relative mass/stiffness to the aerodynamic loads, which means they will change with the dynamic pressure, similarly to the eigenvalues. Figure 7.4 shows the first three mode shapes of bending in MDOF in the cruise condition.

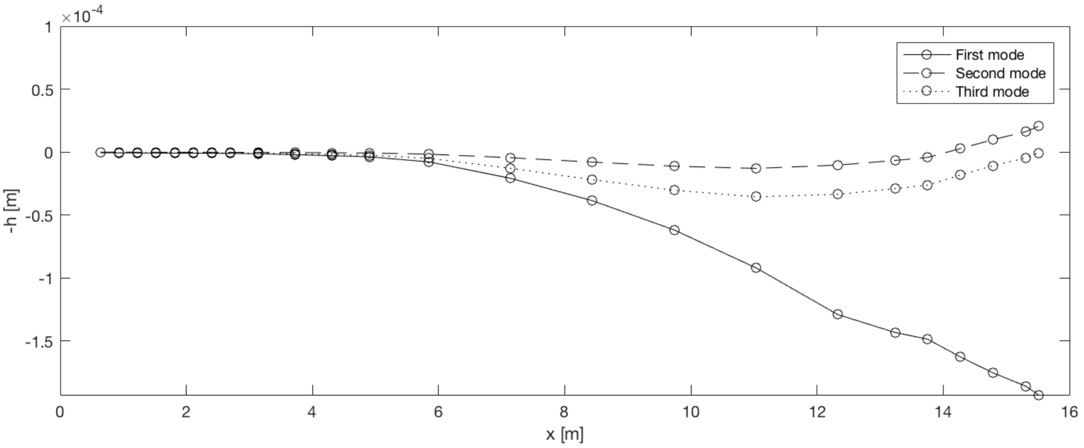

Figure 7.4: First three modes of bending in coupled system at cruise condition

It has been realised that the mass data received only includes mass of the wingbox. Therefore, in the revised computation, mass of the MTE, HLFC as well as the engine were added. In addition, the correction factor that was taken into account for the moment of inertia during the weight estimation has been removed. Lastly, the MATLAB code for frequency is revised. As a result, first four modes are found to be as follow.

Mode number	Frequency [Hz]	Mode shape
1	3.91	Torsion
2	4.29	Bending
3	5.34	Torsion
4	6.0	MTE deflection

Table 7.2: Updated Results of vibration analysis of a numerical wing model

7.4. Aeroelastic Analysis

In this section, analysis on aeroelastic stability is performed by identifying any diverging mode occurring in the range of the flight velocities. Ensuring the aeroelastic stability is essential in the aircraft design process as aeroelastic instabilities could lead to a catastrophic failure of structure. According to the aeroelastic stability requirement of CS-25.629, if there is any aeroelastic instabilities, the freestream velocity in flight where these instabilities occur should be higher than the defined V-n range by 15% [17]. While examples of aeroelastic instability involves divergence, control reversal and any undue loss of stability/control as a result of structural deformation, self-excitation vibration of wing or coupled bending-torsional vibration of wing and aileron, also known as flutter, is the most critical phenomenon [59]. Therefore, in this section analysis is mainly focused on flutter and divergence of the wing. The cruise flight flow conditions are used for the analysis.

Figure 7.5 show the plots of the eigenvalues of the system for different freestream flight velocities. The plot on the left shows the real component of the eigenvalues. While all the frequencies damp out until the velocity reaches about $V_\infty = 1000$ m/s, it can be noticed that there are several diverging modes growing from around $V_\infty = 1000$ m/s. The first diverging mode occurring at $V_\infty = 756$ m/s, marked as the first cyan square, is the oscillatory mode that represents flutter. Although there are several modes diverging after this flutter point, the divergence does not occur until the velocity reach $V_\infty = 1915$ m/s, marked as the second cyan square. This can be confirmed by the plot on the right side of Figure 7.5 that shows the imaginary component of the divergence mode.

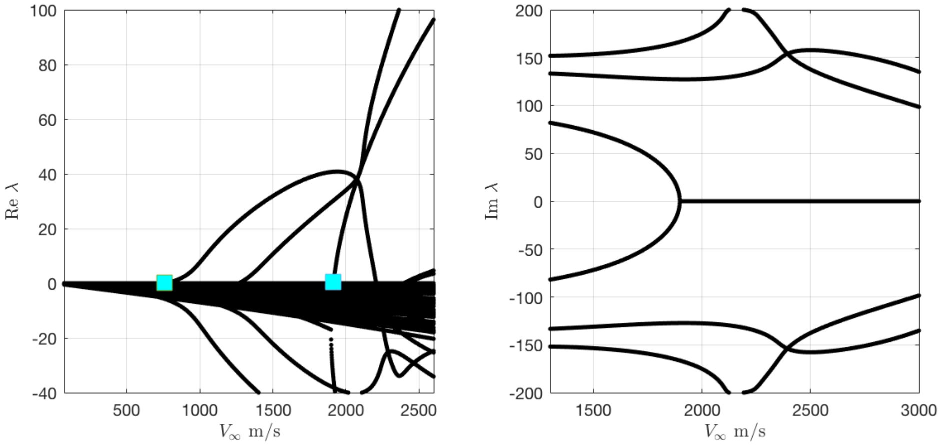

Figure 7.5: Results of aeroelastic analysis (left) Plot of real part of the eigenvalues of all modes (right) Plot of the imaginary part of the divergence mode

7.4.1. Flutter

Flutter refers to dynamic instability where a self-sustained oscillation can grow in time under certain conditions, and the flutter point is defined as the point where the self-sustained oscillation transitions from convergent to divergent motion [62]. From these flutter points with flutter speed V_f, boundary can be formed between the region where one can expect to operate the vehicle without any structural failure and the region where structural failure is likely. As discussed, from Figure 7.5, the first oscillation transition occurs at $V_\infty = 756$ m/s, which defines flutter speed of $V_f = 756$ m/s

According to the CS-25.625, [17], aeroelastic stability should be ensured by a factor of 1.15 of the maximum flight velocity defined in V-n diagram. According to the aerodynamic analysis in chapter 4, the maximum flight velocity defined is the dive speed of $V_D = 309$ m/s. Based on the identified flutter velocity from the analysis, it is clear that the MLW is free from flutter based on the given requirement of aeroelastic stability.

7.4.2. Divergence

Divergence of a wing refers to the static instability where α tends to infinity theoretically. More specifically, when there is a significant increase in the dynamic pressure such that the perturbation, that increases α, cannot be resistant by the spring stiffness, the aerodynamic moment balances the spring moment. This point is defined as divergence point at divergence speed V_d. [62]

As discussed from the results of Figure 7.5, the divergence speed of MLW is shown to be much higher than the flutter speed as $V_d = 1915$ m/s. Although divergence occurring after flutter may preferable, this is not relevant for the MLW as it is much higher than the dive speed as well as the flutter speed. In theory, α increases without a bound in response to a perturbation if the aircraft flies beyond this divergence speed.

The results of aeroelastic analysis are summarised in Table 7.3.

Instability type	Velocity [m/s]
Flutter (V_f)	756
Divergence (V_d)	1915

Table 7.3: Results of aeroelastic analysis

7.5. Verification & Validation

In order to validate the numerical model used for the analysis, current model is compared to the experimental aeroelastic model developed by Duke University aeroelastic group [15]. This experimental model has been developed to evaluate new aeroelastic computational models and theories, which suits well as a validation model. Figure 7.6 shows overview of this experimental model in the wind tunnel test setting. This model has the same DOFs in 2D as the model used in this analysis. Detailed input model parameters are shown in Table 7.4. For the density, standard sea level density is assumed.

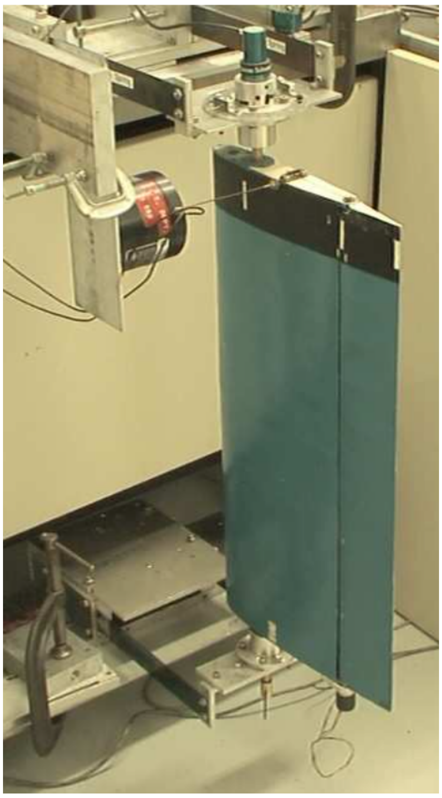

Figure 7.6: Experimental model test set-up

Model Parameters	
Chord	0.254 m
Span	0.52 m
Elastic axis w.r.t semi chord	-0.5
Hinge line w.r.t semi chord	0.5
Mass parameters	
Mass/length of wing-aileron	1.73 kg/m
Mass of wing	0.713 kg
Mass of aileron	0.18597 kg
Inertial parameters	
S_α	0.0726 kg
S_β	0.00393 kg
I_α	0.0185 kgm
I_β	0.00025 kgm
Stiffness parameters	
K_α	46.88 kgm/s^2
K_β	2.586 kgm/s^2
K_h	2755.4 kg/ms^2
Damping parameters	
ζ_α	0.0175
ζ_β	0.032
ζ_h	0.0033

Table 7.4: Input parameters used for validation

Figure 7.7 shows the eigenvalues of the numerical model as a function of the freestream velocity V_∞. From the real component of the eigenvalue, it is clear that there is a diverging mode starting to grow at $V_\infty = 26 m/s$. The exact type of the instability is identified by the imaginary component of the eigenvalue of the same mode. From the figure, it is clear that the diverging mode is dynamic instability, which confirms the $V_f = 26 m/s$

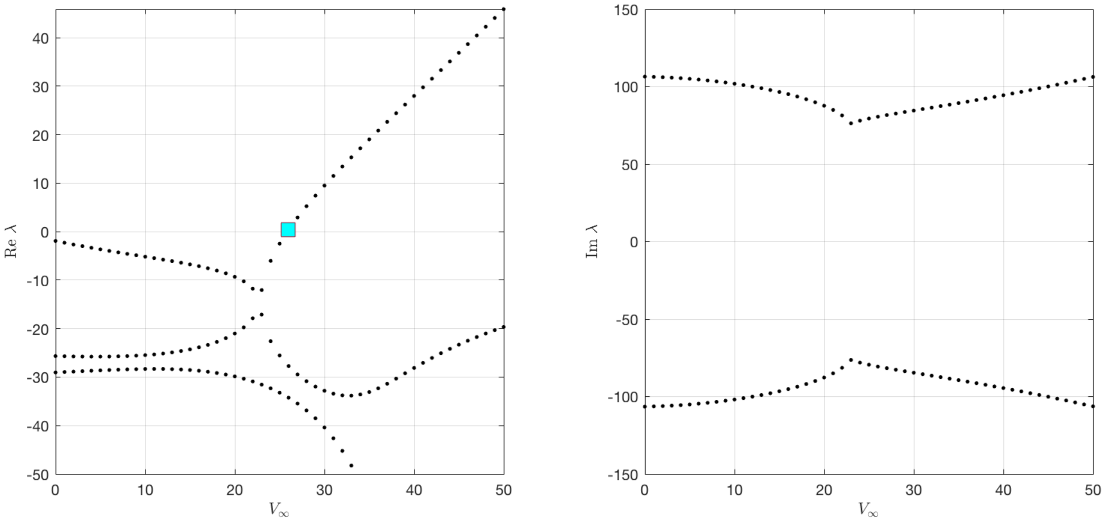

Figure 7.7: Plot of eigenvalues of the numerical model

The validation results are summarised in Table 7.5.

	Numerical model	**Experimental model**	ΔV_{abs}	ΔV_{rel} [%]
V_f	26	26.5	0.5	1.9

Table 7.5: Results of validation

7.6. Conclusion

The main objective of this analysis is to prove that the MLW is free from flutter and divergence based on CS25 standard using a numerical model. Throughout the analysis, it is shown that the natural frequencies of bending and torsion are different from each other. In addition, it is shown that the frequency of rotation of MTE and natural frequencies of the wing are different from each other. Moreover, it is shown that the flutter as well as divergence modes do not occur until the flight velocity reaches over 952 m/s in cruise flight conditions. The numerical model is validated for the flutter speed computation by comparing it to the experimental aeroelastic model developed by Duke University aeroelastic group, which results in the discrepancy of approximately 1.9%. Finally, based on CS-25 and the results obtained from analysis it is concluded that the aircraft, in the range of design speeds of V-n diagram, is free from divergence as well as flutter.

It has been realised that the mass data received only includes mass of the wingbox. Therefore, in the revised computation, mass of the MTE, HLFC as well as the engine were added. In addition, the correction factor that was taken into account for the moment of inertia during the weight estimation has been removed. Lastly, the MATLAB code for frequency is revised. As a result, flutter speed of 756 m/s and the divergence speed of 1915 m/s were obtained.

In order to improve the analysis, error analysis can be performed for uncertainties and errors involved in the numerical model. The main sources of errors are from the model errors and discretisation errors. Although, quasi-steady flow model is known to be sufficiently accurate for many cases, ignoring the wake vortices can be quite significant, as it reduces the magnitude of the aerodynamic load acting on the airfoil. Since this reduction can have a quite significant effect on flutter estimation, model could be further improved by using quasi-unsteady or unsteady aerodynamic models, which could reduce the errors that arise from the governing equations of the system [63]. Furthermore, discretisation errors could be controlled by increasing number of sections.

8

Financial Analysis

This chapter contains the financial analysis for the MLW. First a market analysis was performed, which can be found in section 8.1. In section 8.2 the cost for the different subsystems as well as the complete wing are determined. Finally the Return on Investment (ROI) for the different business cases is calculated in section 8.3.

8.1. Market Analysis

To determine the volume of the market for the MLW and to establish a competitive cost price, a market analysis is performed. This analysis is based on two business cases, the first is the retrofitting of the MLW to existing A320 aircraft and the second one is selling a new A320 aircraft with the MLW implemented right away.

To perform a good market analysis the following aspects are examined: The customers, market size, market trends, competitors and potential barriers for market entry, SWOT (Strengths, Weaknesses, Opportunities and Threats) analysis and the foreseen market share. The whole market analysis is done from the point of view of Airbus who is developing the wing and after that selling the MLW.

In 2016 Airbus delivered the first A320neo and at this moment there is still a big backlog of orders for this aircraft. Therefore it has been decided to first start with retrofitting the current A320 CEO, before starting to produce a new A320 with the MLW. By doing this the potential market is increased, and beside that it is possible to setup a new production line for the MLW to be able to meet the future orders in time.

8.1.1. Customers

The customers of the MLW can be identified by looking at the current users of the A320, these are airlines that are operating mid-range flights with single-aisle aircraft. A distinction can be made between the existing and potential customers: The existing customers are airlines who own an A320 aircraft, these are the customers that might be interested in retrofitting the A320 with the MLW. The potential customers are airlines who are interested in buying a new aircraft for these types of operation, to these customers the first business case can be applied.

Although both business cases are applied to different customers the key factors for the purchase decision are quite similar for both types of customers and can be identified as the following:

- Expected operating costs: These costs depend highly on the expected maintenance for the MLW and its performance during flight. High maintenance will drive up the cost and good performance will decrease it
- Aircraft characteristics: Each aircraft has different flight characteristics of which range and payload are the most important. These characteristics should match to the types of flights the airline is operating
- Purchase price: The purchase price should be competing with similar type of aircraft from different companies
- ROI: This factor is critical for the retrofitting business case, depending on the amount of time it takes earn back the money it takes to retrofit an A320, it can be determined if it is worth retrofitting certain aircraft in the fleet or not. For the retrofitting business case the ROI should be lower than the remaining operating years of the aircraft

To convince a customer to buy the product the MLW should score well for all these factors.

8.1.2. Market Volume

The market size for the A320 with the MLW is based on the number of airliners wanting to buy single-aisle medium range aircraft, this will be discussed first. Both Airbus[1] and Boeing[2] perform an extensive global market analysis every year, in this analysis short-term (two years) and long-term (20 years) forecast are made for the aircraft industry. For this market analysis both forecasts are used, to be on the conservative side the lowest values of either are used.

Looking at the aircraft industry an annual increase of 7% in Revenue Passenger Kilometres (RPK) can be noted for the last two years. RPK is a key indicator of airline economic growth and the same amount of growth is expected for the coming few years. This growth is mainly focused in North America, Europe and some emerging markets. Reasons are the low airfares, growth of tourism/travel and new airline business models which make flying accessible to a larger number of people. The long-term growth is expected to be 4.4% RPK per year. The most important growth market will be the Asia-Pacific region, in 20 years this region will account for 42% of the new deliveries compared to a total of 35% for North America and Europe. The main reasons for this growth is the growing middle class in Asian countries and therefore the increase of living standards which will lead to an increase in number of air passengers.

Single-aisle market

Of all the different aircraft types the single-aisle aircraft make up the majority of the market (currently 69% of all deliveries) as these aircraft are the backbone for the business models of the low cost carriers. In the coming 20 years this share will increase to 75% as there is a strong need for replacement of old aircraft, and most of the emerging markets have a high number of low cost carriers. The largest market regions will be North America, Europe and the Asia-Pacific as these account for 90% of the global low cost carriers capacity. Therefore these regions make up around 80% of the total number of deliveries for single-aisle aircraft.

Selling new A320

In the global market analysis of Airbus and Boeing, forecasts are presented for the expected number of deliveries of single-aisle aircraft over the next 20 years. Airbus expects to receive a total of 28,552 deliveries for single-aisle aircraft while Boeing expects to have 31,360 deliveries over this period. Currently the A320 and Boeing 737-800 account for 57% of the single-aisle market[3] and if this percentage remains the same this will lead to around 34,000 deliveries for these type of aircraft over the coming 20 years. Taking into account an annual growth of 4% of the market, the number of total deliveries will range from 1,000 in 2019 to 2,700 in 2037. Combining these values with the current sales prices of the A320 of 101 million USD gives a total market value of 3,434 billion USD.

Retrofitting A320

For the retrofit the market volume is based on the total number of A320 that are being operated by airliners at this moment for which it is profitable to upgrade the wing with the MLW. To determine this number it is important to look at the economic life of an aircraft which lasts up until the point in time where the cost to operate the aircraft exceed the profits generated. If this point is reached the relevant aircraft is removed from operation and is retired. Indicators for this economic life point are age of the aircraft, the number of flight hours and pressurisation cycles the aircraft has undergone, and increased maintenance requirements. The typical service time of an aircraft is between 20 and 30 years [64], for this analysis the economic life is set to 25 years.

Every year Airbus publishes the total number of orders, deliveries and aircraft in operation for each aircraft type[4]. From this data it is known that there are currently 4,383 A320 CEO aircraft in operation, with an average age of ten years. With the use of historical data of A320 deliveries it is possible to estimate the number of years in economic life left for each of these aircraft. This in combination with the ROI calculated in section 8.3, which is seven years, makes it possible to estimate the total volume of the retrofit market. Taking into account five years of development the first retrofit could take place earliest in February 2024, at this time there are still 3,000 A320 CEO left with an economic lifetime of more than 8 years. With the sales price that is determined in section 8.2 it can be determined that the market value will be 52.6 billion USD.

---

[1] https://www.airbus.com/content/dam/corporate-topics/publications/media-day/GMF-2018-2037.pdf

[2] https://www.boeing.com/resources/boeingdotcom/commercial/market/commercial-market-outlook/assets/downloads/2018-cmo-09-11.pdf

[3] http://www.alafco-kw.com/upload/Media_Library__March_2016____Aircraft_Market_Report__March_2016__921.pdf

[4] https://www.airbus.com/aircraft/market/orders-deliveries.html

8.1.3. Market Trends

Nowadays sustainability is a big thing within society and the same is true for the aircraft industry, to ensure the sustainable future of aviation three goals were set among different industry leaders. These goals are: A 1.5% average annual fleet fuel efficiency improvement from 2009 to 2020, the stabilisation of net aviation CO_2 emissions at 2020 levels through carbon neutral growth and by 2050, the reduction of net aviation CO_2 emissions to 50% of what they were in 2005. Different ways to reach these goals are breakthroughs in aircraft design and propulsion technologies, advancement in airspace management and airline operational efficiencies, and the development and commercialisation of sustainable alternative fuels.

When looking solely at the single-aisle market it can be noted that most of the airlines operate the aircraft on short-haul flights. However due to the improvement of aircraft technology leading to more efficient and capable singe-aisle aircraft it is possible to connect cities that have not been considered profitable in the past. Due to this fact a trend can be seen that of new single-aisle aircraft which are more frequently used on longer-haul routers today. For example last year almost 40 new single-aisle routes with distances over 5,500 km have been introduced and it is expected that this trend will continue to carry through for the coming years. Next to this airlines have been increasing the number of seats for single-aisle aircraft over the last 20 years. The average number of seats offered went from 140 in 1998 to 169 seats in 2017. However it is difficult to predict how this trend will continue in the coming years. To conclude two trends are found in the single-aisle market: Increase of range and increase of payload, of which the first one is the most promising.

8.1.4. Competition & Barriers

The main (and only) competitor for Airbus is Boeing, and this competition has even been characterised as a duopoly. At this moment Airbus is leading the single-aisle market in number of deliveries. Airbus has outsold Boeing in the single-aisle aircraft market in seven out of the past ten years, capturing 54% of net sales. In order to stay competitive with respect to Boeing it is important to exploit the possibilities of new wing designs. Recently Boeing made an announcement about the new transonic truss-braced wing on which the company has been working on[5]. This wing is designed to be more aerodynamic and fuel efficient, due to the presence of a truss it possible to design a ultra-thin wing with a high aspect ratio which is favourable for the aerodynamic performance. Next to that the new Boeing 777X features folding wingtips, these make it possible to increase the span of the aircraft, and thus the aerodynamic performance, whilst still being able to operate at most airports.

The barriers to enter the market are estimated to be low, Airbus has a lot of experience with building wings and already owns manufacturing lines for different types of aircraft. This means that the development cost will be lower compared to a company that is entering the aircraft market for the fist time. Next to that Airbus is a well established company within the aircraft industry, therefore airlines already have confidence the company and will buy aircraft quicker.

8.1.5. SWOT Analysis

In Figure 8.1 the SWOT analysis of the MLW is shown.

---

[5] `https://www.boeing.com/features/2019/01/spreading-our-wings-01-19.page`

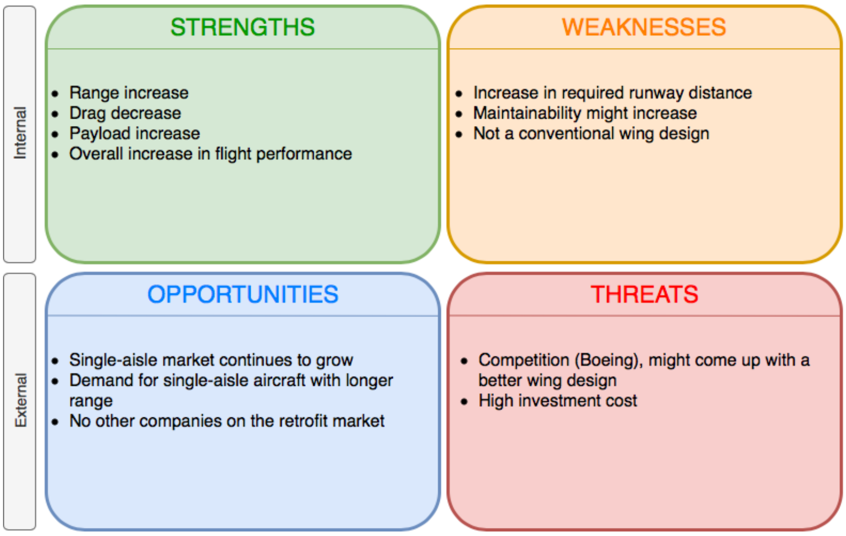

Figure 8.1: SWOT analysis of the Morphing Laminar Wing

From this analysis two main conclusions can be drawn. First, many of the strengths of the MLW overlap with the current trends within the single-aisle aircraft market and secondly the main disadvantage of the wing is the increase in runway length which will limit the number of airport the A320 can land.

8.1.6. Foreseen Market Share

Current market share of the A320 is 54%, in the future it is expected that 45% of the deliveries will be for the A320 with the MLW while the remaining 9% will be for the A320neo. The main reason for this is the increased landing distance due to the MLW, therefore the aircraft will only be able to land at 70% of the airports in the world, compared to 83% for the conventional A320, as stated in subsection 4.6.9. It has been decided that after the development phase the first two and a half years of production will be solely for the retrofit market, so the earliest delivery date will be September 2026 for an A320 with the MLW. It is expected that it it takes five years to get the production to full capacity, this will lead a total of 10,000 deliveries and a market value of 996.97 billion USD up until 2037. The breakdown of these numbers per year can be found in Table 8.1, these values will be used in section 8.3 to calculate the ROI and PBP for this case.

Year	Deliveries	Market value
2026	146	14.75
2027	307	31.04
2028	479	48.43
2029	671	67.80
2030	881	88.98
2031	925	93.43
2032	971	98.10
2033	1020	100.30
2034	1071	108.16
2035	1124	113.57
2036	1181	119.25
2037	1240	125.21

Table 8.1: Expected deliveries and market value [billion USD] for A320 with MLW for different years

8.2. Cost Analysis

The production cost of both systems is determined by analysing both manufacturing cost and material cost. For the manufacturing cost the estimation technique from [18] is used. With this technique it is possible to make an estimation for both the recurring and non-recurring cost of producing an aircraft structure. This is done by looking at the type and mass of the materials used. Next to the manufacturing cost, the material cost were analysed. This is done by looking at the amount of material used and the average prices for these materials.

8.2.1. HLFC Cost

In order to estimate the production cost of the HLFC system, it was broken down into following components:

1. **Material costs**: suction surface, ducts, valves; pump, power supply, electric harness; control system, monitoring, sensors
2. **Human and tooling costs**: manufacturing, quality Assurance, (non)recurring tooling and engineering

For the suction surface material, Grade 2 titanium sheets are going to be used, whereas ducts are made of 6065-T6 aluminium. Due to little cost-related information available, Pump & Power subsystem cost estimates are made by estimating a compressor cost per kilogram and then translating the cost to other components by means of their mass, as defined in section 6.3. It was estimated that some additional costs are also expected from the slat replacement by Krueger flaps, for more information see section 3.8. Total material resource cost of the system is estimated to be 142,000 USD. The cost breakdown is summarised in Table 8.2.

Out of human and tooling resources, the manufacturing cost is the largest component, estimated to be slightly less than 270,000 USD. This estimation, as well as all other labour estimations, are made on statistical data provided in [18]. The second biggest cost component is tooling, estimated to be 124,000 USD. Titanium alloys are very difficult to machine [57], and titanium based structures are very difficult to produce, which results in high manufacturing and tooling costs. Nevertheless, titanium sheets must be micro-perforated, and though Young proposed to use Nd:Yag Lasers for micro-drilling [18], Nd:Yag lasers are becoming obsolete due to their low reliability and high maintenance costs[6]. Instead, it is proposed to use Pulsed Fiber Lasers, which are currently considered to be state-off-art [65]. This allows saving up to 50,000 USD per year on tooling costs[7].

As seen in Table 8.2, the final HLFC related production cost is expected to be approximately 0.66 million USD. 15% of these are dedicated to non-recurring expenses, which do not repeat with each aircraft produced. However it has to be noted that non-recurring costs are bound to increase with increasing production of HLFC-equipped aircraft due to tooling wear for instance.

Table 8.2: Overview of recurring and non-recurring manufacturing cost for the HLFC

Cost type	Components	Recurring [USD]	Non-recurring [USD]	Total Cost [USD]
Material Resources	Suction Surface, Ducts, Valves	10,000	Not applicable	10,000
	Pump, Power supply, Electric harness	40,000	Not applicable	40,000
	Control, Sensors, Monitoring	12,000	Not applicable	12,000
	Additional Krueger flap cost	80,000	Not applicable	80,000
Human and Tooling Resources	Engineering	21,000	17,000	38,000
	Tooling	48,000	76,000	124,000
	Manufacturing	269,000	Not applicable	269,000
	Quality assurance	86,000	Not applicable	86,000
Total Production Cost		566,000	93,000	**659,000**

---

[6] `https://www.permanentmarking.com/yag-lasers/`

[7] `http://www.laserphotonics.com/docs/Fiber_v_YAG[1].pdf`

8.2.2. MTE Cost

In order to estimate the production cost of MTE system, it was broken down into following components:

1. **Material costs**: ribs, mini-spars and skin all made of aluminium, elastomer materials, actuation system
2. **Human and tooling costs**: manufacturing, quality assurance, (non-)recurring tooling and engineering

From the sizing of the actuation system the cost of this system can be determined by looking at the price per actuator and the total number of actuators used. There is not a lot of information about component prices of actuation systems for aerospace applications, that is why the cost price of standard EMA's is used from Bimba presentation[8]. The price of aerospace actuators is a lot higher because of reliability level required, thus a scaling factor of ten is used. The final results of the cost estimation, containing manufacturing, material and actuator costs, can be found in Table 8.3.

Cost type	**Components**	**Recurring [USD]**	**Non-recurring [USD]**	**Total Cost [USD]**
Material Resources	Aluminium	4600	Not applicable	4600
	Elastomer materials	77,000	Not applicable	77,000
	Actuation system	1,600,000	Not applicable	1,600,000
Human and tooling Resources	Engineering	271,000	297,000	567,000
	Tooling	522,000	323,000	845,000
	Manufacturing	3,005,000	Not applicable	3,005,000
	Quality control	475,000	Not applicable	475,000
Total production cost		5,573,000	619,000	**6,574,000**

Table 8.3: Overview of recurring and non-recurring manufacturing cost for MTE

Now that the total cost for the MTE are known, it is possible to compare these to the cost of the current TE of the A320 wing. The production cost for this part was estimated with the use of the cost model mentioned in [4] and is based on a purchase cost of 101 million USD [9]. From this breakdown the total production cost are estimated at 5.555 million USD. When comparing the cost of the MTE with the current TE it is possible to see that the MTE will increase the total wing cost by 1.019 million USD.

8.2.3. System Purchase Cost

Based on the cost model presented in [4]the sales price of the A320 can be broken down into different parts, this breakdown can then be used to find the production cost of the current A320 wing. From the cost analysis of the MTE and HLFC systems it is clear that these systems will add 1,521,000 USD to the wing production cost. With this increase a new sales price for the aircraft has been determined, the results of this method are shown in Table 8.4

	A320	**A320 with MLW**	**Increase in %**
Production cost	55,550,000	57,071,000	2.7
Wing (part of production cost)	11,110,000	12,631,000	13.7
Engines	25,250,000	25,250,000	0
Spares and training	10,100,000	10,290,000	1.9
Profit	10,100,000	10,290,000	1.9
Sales price	**101,000,000**	**102,901,000**	**1.9**

Table 8.4: Cost comparison with and MLW

When comparing the new sales price to that of the current A320 it can be concluded that the final concept will lead to an increase of 1.9% percent for the sales price, which is well below requirement MLW-Sys-019 that states that a

---

[8] `http://fluidpowerjournal.com/wp-content/uploads/2012/12/08_guajardo-electric-vs.-pneumatic.pdf`

[9] `https://www.airbus.com/newsroom/press-releases/en/2018/01/airbus-2018-price-list-press-release.html`

maximum increase of 3% is allowed.

8.2.4. Lifetime Cost

When comparing the lifetime cost of the MLW to the one of the conventional A320 the main difference will occur due to the change in operating cost of the aircraft. As explained in section 10.2 the initial maintenance cost of are expected to be higher than the benchmark A320, but will overtime go down to the original levels. On the other hand the operating cost will go down because of the increased performance due to flight. Overall it is expected that this effect will outweigh the increase of maintenance cost and therefore it is likely that the requirement MLW-Sys-021 is going to be met.

8.3. Return on Investment

To see if the MLW project is a good investment for Airbus, and to determine the potential market, two different cases are analysed. For each of these cases the ROI and Payback period (PBP) will be calculated, ROI is measure that is used to determine the efficiency of an investment and to compare it with different investments, it can be calculated with Equation 8.1.

$$ROI = \frac{Gain of Investment - Cost of Investment}{Cost of Investment} \tag{8.1}$$

Besides the ROI it is also important to now the time it takes to earn back the cost of the investment, this value is the PBP and can be calculated with Equation 8.2.

$$PBP = \frac{Cost of Investment}{Annual Gain of Investment} \tag{8.2}$$

To establish the size of the retrofitting market it is necessary to calculate the payback period of the investment that airlines have to make to retrofit an A320. This investment consist of the production price of the MLW plus the cost for removing the old wing and attaching the MLW, in this price is estimated to be 17,2 million USD and is based on the cost price calculated in section 8.2. With the MLW attached the operational cost of the aircraft will go down and due to the increase of payload the profits per flight will go up. For this analysis it is assumed that an A320 makes four flights a day, of each two hours. During each flight 400 kg of kerosene will be saved, which amounts to 250 USD, and the profits due to payload increase are determined to be 1,500 USD. Thus the total gains per day will be about 8,000 USD, so 2.45 million USD per year. With the investment cost and the gains per year known it is possible to determine that the PBP will be seven years, this means that it is only profitable to retrofit aircraft with a minimum of eight years of economic life left. In Figure 8.2 the values for ROI are shown for different years of economic lifetime left.

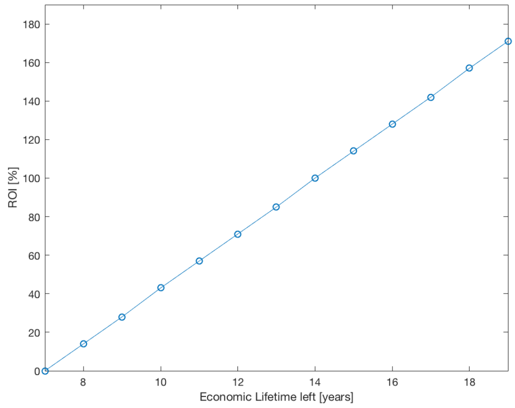

Figure 8.2: ROI for different time of economic life left

It is important to note that in this analysis it is not taken into account that retrofitting a conventional A320 will increase the economic life of this aircraft, therefore in reality the ROI will be higher. Next to that the price of kerosene is expect to increase in the coming years, this will lead to that the fuel saving will become more effective money-wise.

To calculate the ROI and PBP out of the perspective of Airbus the total investment cost are needed. The development phase of the MLW is expected to take five years, as can be found in section 13.5, in which 2,000 engineers will be working full-time to complete the design for production. The total cost of this period are estimated to be 11.75 billion USD. After this phase the current A320 aircraft in operation can be retrofitted with the MLW, two and a half years later the first new A320 with the MLW is expected to be delivered. With help of the forecasted market share it is possible to estimate the profits that will be made with retrofitting and selling the new aircraft, this will lead to a PBP of 13 years with a ROI of 8.6% in 2037.

9

Budget Breakdown and Resource Allocation

To ensure that the MLW design satisfies its specified requirements, a technique called Technical Performance Measurement (TPM) is applied. First, technical resources and major system parameters in design project are identified based on the requirements analysis and general development constraints in section 9.1. Secondly, contingency policy for the identified budgets and parameters are defined, and corresponding management strategy is presented in section 9.2.

9.1. TPM Strategy and Parameters

In this section, strategies for the TPM procedure for the technical resource budgets are discussed. In addition, TPM parameters for the product development project are identified based on the requirements analysis and general development constraints. Finally, the total system cost breakdown structure is presented.

In order to process the design project that leads to the successful development efficiently, it is important to track and manage the available technical resources that could directly have an effect on the success or failure of the project. For this, the following TPM procedure is defined.

1. Define and set up TPM strategy and procedures
2. Identify TPM parameters
3. Analyse TPM parameters
4. Set up a budget breakdown structure for the total system cost
5. Define and set up contingency management strategy
6. Perform the contingency allowance estimation for TPM parameters

The first step is to define and set up an appropriate TPM strategy and procedures for the specific design project, which is the design of the autonomous wing. Secondly, the corresponding TPM parameters are identified based on the requirement analysis, general development constraints as well as the technical overview. Thirdly, these identified TPM parameters are decomposed and analysed by describing its significance as a technical resource based on the requirements. Then for the total system cost, the budget breakdown structure involving purchase costs as well as the ownership costs that consist the total system cost or the Life Cycle Cost (LCC) is set up. Then, in the following section, a strategy specifically for the contingency management is defined and discussed. Finally, based on the TPM analysis, contingency allowance estimation is performed for the TPM parameters.

Before presenting and discussing the identified TPM parameters, criteria for the TPM parameters identification are briefly described as follows.

- Parameters that describe how well the system functions
- Parameters that are most important to the ultimate customer

9.1.1. Mass

Mass of an aircraft is identified as one of the most critical TPM parameters in this project as there is a specific requirement (**MLW-CuSh-012**) that the MTOW of the aircraft equipped with the MLW design should not exceed the MTOW of the A320. To ensure that this requirement is satisfied, MTOW is kept constant from the preliminary budget estimation throughout the detailed design phase.

In addition, the requirement states that the mass distribution can be changed as long as stability margins are preserved. Throughout the detailed design phase, it has shown that the mass distribution of a wing is changed as a result of load alleviation. However, in chapter 4, it has been shown that the static longitudinal stability is conserved.

9.1.2. Drag

Drag of an aircraft is identified as one of the TPM parameters of the project based on the identified stakeholder requirement (**MLW-CuSh-006**), which requires 7.5% of drag reduction throughout the entire flight with respect to the A320. In order to be safe from this limit of the drag, different drag components need to be identified and closely analysed in chapter 4.

Based on the analysis, it has been shown that the there is drag reduction of 3.5% by implementing HLFC system, a result that is derived from increasing flow laminarity and reducing the skin friction. Moreover, there is additional drag reduction resulting from implementing the MTE system and the airfoil selection, which makes the total drag reduction of 11.34%.

9.1.3. Payload

Payload is identified as one of the TPM parameters based on the requirement (**MLW-CuSh-007**), which states that the wing shall result in payload increase of 7.5% with respect to the A320. Although payload increase as a technical resource is dependent on the mass of the aircraft, it is closely analysed throughout chapter 4 and chapter 6. As a result, there is total 11.35% increase in the payload with respect to the A320.

9.1.4. Cost

Cost is also one of the major TPM parameters as this can be a limiting factor in available technical resource budget. According to the requirement (**MLW-CuSh-013**), only 3% purchase cost increase as compared to the current A320 is allowed. In addition, the requirement (**MLW-CuSh-014**) states that the overall lifetime cost of the A320 should not be exceeded.

Purchase cost of the A320 with MLW include the costs resulting from R& D as well as investment. While the main cost change with MLW comes from the investment cost that includes manufacturing, construction and initial logistic support, Table 8.4 shows the breakdown of the purchase cost of A320 with MLW. According to the financial analysis in chapter 8, it shows that increase in the sales price is approximately 1.9% meaning that it will not exceed the available resource budget. This slight increase in the purchase cost mainly comes from adding HLFC system as well as the MTE system.

Implementing the HLFC system increases the total production cost of the system by approximately 659,000 USD compared to the current A320 wing cost. The manufacturing cost of 269,000 USD is the largest portion of this production cost of the system. This is mainly due to the fact that Titanium alloys as well as titanium based structures used for the HLFC system are very difficult to produce. The second largest portion of the production cost is tooling, which costs approximately 124,000 USD. In addition, implementation the MTE adds additional production cost of 6,574,000 USD, which is mainly from the additional material costs as well as the human and tooling resources cost.

The cost breakdown structure of the total system cost is shown in Figure 9.1. This diagram briefly shows the allocation of the cost budget in different levels. Although cost analysis is mainly focused on the production cost, it is important to set up the cost breakdown of the entire total system cost that does not only include the production costs, but also the ownership costs. Having a breakdown structure of the complete system cost will allow to solve any cost budget related issues that arise during the later stages of the project more efficiently and strategically.

Figure 9.1 shows that the overall LCC is decomposed as purchase cost and the ownership cost. Then, the purchase cost is broken down again for the R&D and production cost. In the R&D cost, there are cost resulting from technical analysis at the current level (DSE) and more advanced technical analysis and testing which will then be performed in the future (Post DSE). In production cost, there are costs resulting from materials and manufacturing of the wingbox, MTE structure and the HLFC subsystems. The remaining parts of the production cost are allocated to the wing assembly, aircraft integration, tooling, quality assurance, fabrication and tools & test equipment. Finally, the ownership cost mainly consist of the cost resulting from operations and maintenance. Also a small fraction of the operations & maintenance cost is allocated to the disposal.

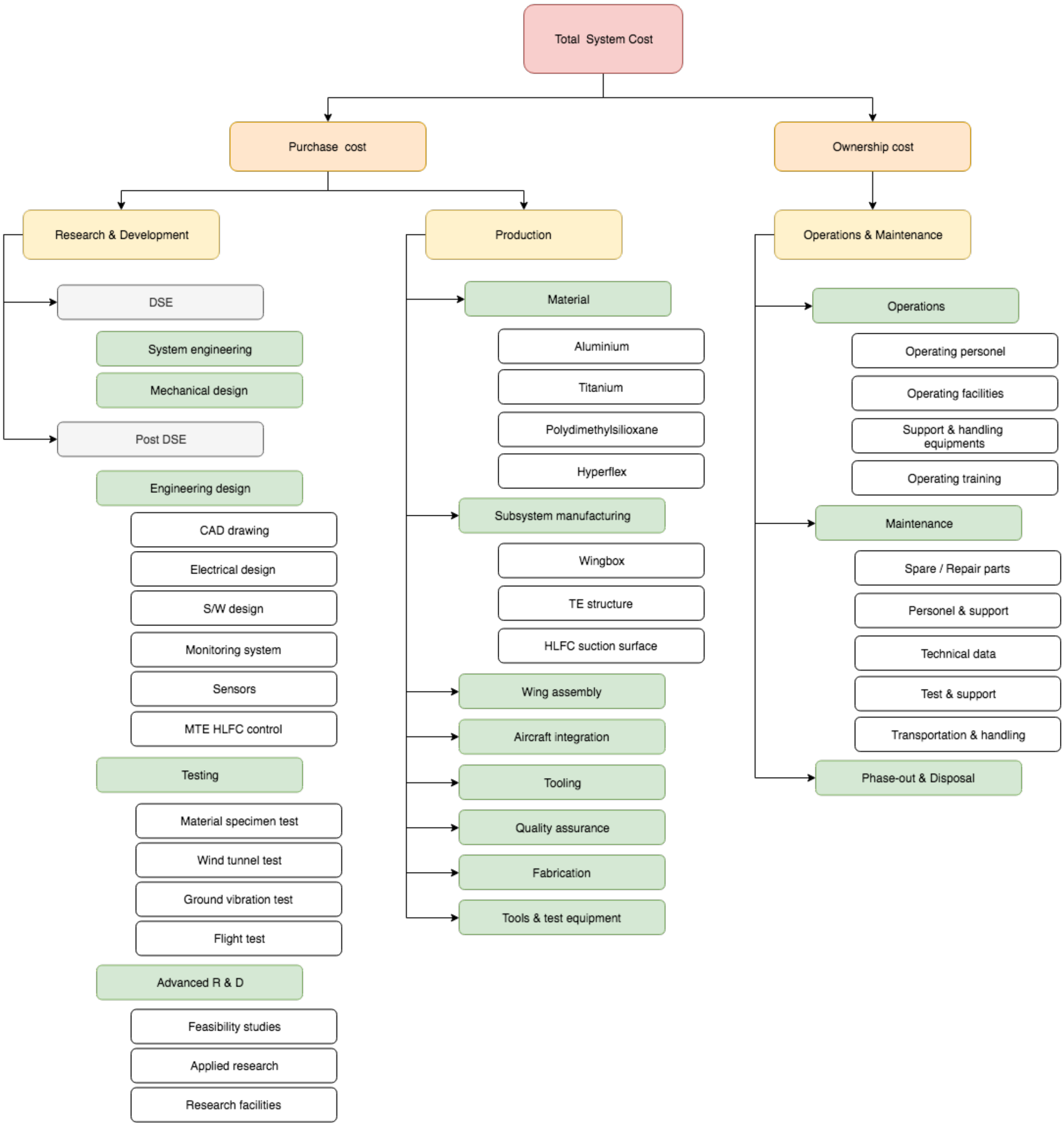

Figure 9.1: Cost Breakdown Structure

9.2. Contingency Management

Contingency management of the resource allocation plays an important role in covering of unexpected costs during the execution of the project. This has been set up based on the TPM strategy discussed in the previous section.

The contingency management plan is presented in Table 9.1. In this table, the development of the selected critical budget resource allowance is given in percentages for each of the design and development phase. From this table, it is obvious that the contingency percentage decreases as the design maturity increases throughout the project. Then, during the actual hardware and flight measurements, the contingency is reduced considerably.

	Contingency (%)					
Design Maturity	MTOW	OEW	Drag	Payload	Fuel	Cost
Conceptual phase	30	25	35	25	25	30
Preliminary phase	20	15	15	15	15	25
Detailed phase	10	5	5	5	10	15
Hardware measurement	1	1	1	1	1	1
Flight measurement	0	0	0	0	0	0

Table 9.1: Contingency allowance

10

Risk Assessment

In order to ensure the success of the design a technical risk plan is set up and applied throughout all phases of the project, as discussed in section 10.1. Besides this risk plan, a RAMS analysis of the MLW is presented in section 10.2 which serves as a high level assessment of the risk as a result of the implementation of MLW on legacy A320.

10.1. Risk analysis

The risk analysis plan first strives to identify any and all risk the design is subjected to which are ranked in both impact on the system and likelihood of occurrence. The impact of any risk event runs from marginal impact, the system can perform the mission as planned, to catastrophic, the mission cannot be executed by the system. This ranking reveals critical risk events for which mitigation techniques are presented which decrease either impact, probability of occurrence or both. The risk events identified can be placed in two main categories: organisational risk and technical risk. Organisational risk has been extensively analysed in an earlier stage and its mitigation techniques have been implemented during the course of the project as described in [66]. An initial technical risk analysis has been done in the preliminary design phase of the project, as described in [53]. Here, this plan is extended whenever new risk events presented itself and mitigation techniques have been improved upon whenever relevant. The risk events are further split into categories: general risk, design and production risk and operational risk.

10.1.1. General Risk

A risk event is categorised as general risk when it endangered meeting requirements to which the design is subjected to.

Risk ID	Risk	Risk mitigation
G01	Final design fails to perform in practice.	The final design will be verified, validated and tested before it is used, which will then decrease the level of probability of occurrence.
G02	Final design fails to reduce the drag of 7.5% throughout the entire flight with respect to the A320 legacy aircraft.	Through extensive drag estimation, design parameters will be further modified in case the drag estimation is not satisfied. Other systems of the aircraft can be modified and optimised so the drag requirement is met.
G03	Final design fails to increase a payload by 7.5% with respect to the A320.	Since this is closely related to improvement in aerodynamic performance, related design parameters should be modified. Then, both the severity and the likelihood of the risk are expected to be decreased.
G04	Final design fails to increase the flow laminarity over the wing.	Hybrid laminar flow control technique will be revised and improved to ensure the flow laminarity, which could reduce the likelihood of the risk.

G05	Purchase cost exceeds 3% compared to the A320.	Alternative design options can be chosen for the minor subsystems that could lead to lower purchase cost.
G06	The overall lifetime cost exceeds that of the A320.	Subsystem could be altered to which it requires lower cost per subsystem, which will reduce the severity as well as the likelihood of the risk.
G07	Stability margins are too low to ensure longitudinal stability.	Resizing of the subsystem is required to ensure the stability margins. Stability margins are investigated throughout the design and taken into a count when major design choices are made.
G08	Numerical errors and uncertainties involved.	Possible sources of errors and uncertainties shall be identified first, and if necessary, finer grids or higher order methods could be used, this will reduce the likelihood of risk.
G09	Failure to satisfy the required roll rate.	Control mechanism of the roll with the continuous trailing edge could be revised. This will reduce the likelihood of the risk.

10.1.2. Design and Production Risk

The risk events placed in this category capture all risk associated with the design and production of the two main subsystem of the MLW: MTE and HLFC. Besides this, all risk due to the redesign of any subsystems of the legacy A320 wing caused by the implementation of HLFC and MTE is also placed in this category.

Risk ID	Risk	Risk mitigation
D01	Difference in deflection of different flap segment's of MTE required exceeds physical constraint due to elastomer connection.	Elastic connection is sized for the most critical case so it is able to withstand all deflection settings.
D02	Warping of the skin of different flap segments of MTE due to non-continuous deflection over a flap section decreases continuity trailing edge flap.	Build in constraint in control system which minimises this effect to an acceptable level. The addition of stringer minimises the probability of this phenomena.
D03	Ribs of MTE are not able to transfer actuation loads to the required deflection after a large number of cycles due to fatigue.	The fatigue capabilities are maximised by material selection and safety factors. Regular inspections of the flap will decrease the probability of occurrence.
D04	Optimisation method of control system of MTE reveals to be non feasible for the physical constraints.	Revise the optimiser so that it complies with the physical constraints, which will lessen the likelihood of the risk.
D05	Actuation system of MTE fails to withstand the aerodynamic load it is subjected to while holding a flap in place.	Different type or number of the actuator could used, which will reduce the likelihood of the risk. A safety factor will be build in the actuation system selection.
D06	Elastomer of MTE fails to withstand and transfer the aerodynamic loads to underlying structure.	In the final design phase the geometrical properties will be sized to minimise to probability of occurrence by implementing sufficient safety factors. Regular maintenance shall be conducted to prevent unexpected failure of elastomer which will reduce severity as well as likelihood of the risk.
D07	Elastomer of MTE is not resistant enough for extreme weather conditions.	In the material choice, the most resistant material is chosen. Elastomer will be inspected on the regular basis.
D08	Production of the structural components of MTE with optimised geometrical parameters is not possible.	Set constraints on structural dimensions which might to be optimal but allow for easier production.

D09	The actuation systems of MTE do not have sufficient bandwidth for fast response for active GLA.	The GLA focuses on actuation of the most aft actuation mechanism. This system is chosen with as main focus a high bandwidth of which the physical constraint is build into the control system.
D10	Insect residue striking the leading edge can cause transition to turbulent flow.	Make an adjustment to the design so a Krueger flap is implemented which shall protect perforated surface of HLFC as a shield. This will decrease likelihood of impact.
D11	Insect swarm could create sufficient surface roughness to cause transition.	Krueger flap shall protect perforated surface of HLFC as a shield. Flaps shall decrease probability of insect contamination.
D12	Pressure sensor failure in HLFC could cause inability of control system to receive information.	Individual pressure sensors are not critical HLFC components, but for better control and reliability flow sensors in pipes shall be included. This will decrease likelihood of failure as well as impact severity.
D13	Suction system HLFC incompatible with the current A320 leading edge high-lift devices.	Redesign the slats into a Krueger flap system, which allows the flap to be stored under the wing, rather than on top of the leading edge segment. This will diminish the likelihood of the risk.
D14	Krueger flap does not deliver the required take-off/landing performance.	In the design phase determine which geometrical properties of a Krueger flap influence the effectiveness of it the most and ensure that these quantities are optimised in the design. This reduces both the severity and likelihood of this risk.
D15	Combination of suction system HLFC and Krueger flap does not fit in the leading edge compartment of the wing.	The likelihood can be decreased by ensuring that all means are taken to minimise the space that the ducting of suction system occupies. Moreover, the Krueger flap has to be designed with a folding nose, which would further save space.
D16	Suction system HLFC is consistently unable to achieve the required performance in every flight.	The likelihood can be decreased by increasing the extent of the system on the wing, to provide some redundancy in case the system systematically underperforms. The aircraft is still able to perform the mission, however with a decrease in efficiency.
D17	The smallest achievable hole diameter in the perforated surface of HLFC is larger than the designed value.	Decreasing the severity is done by means of increasing the spacing of the perforations accordingly, so that the producible hole diameter is in sync with the spacing requirements.
D18	Final design of a subsystem fails to be integrated to the aircraft.	Integrated model can be simulated, which will decrease the likelihood of the risk.
D19	Final design fails to accommodate aircraft fuel system.	The design of the final configuration uses the existing fuel system as constraint. If integration of the existing fuel system is not possible, a redesign of the fuel system will be performed.
D20	Final design fails to accommodate aircraft landing gear system.	The final design is sized to accommodate the landing gear system. If this is not possible, a redesign of the landing gear system is required to a fuselage mounted landing gear system.
D21	Requirements constrain detailed design development.	Design development procedure that opposes to the requirements should be avoided. This will reduce the likelihood of the risk.
D22	Occurrence of wing divergence or flutter.	Aeroelastic analysis will be conducted under expected flight conditions, which will reveal any problems in an early stage allowing for resign of the structural parameters of the wing.

D23	Final design fails to fulfil the fuel-volume requirement.	Supplementary or the back up fuel tank could be planned in case main fuel tank on the wings turn out to be not sufficient, this will reduce the severity of the risk.

10.1.3. Operational Risk

Operational risk analysis covers all risk associated with the operations of the final product MLW.

Risk ID	Risk	Risk mitigation
OP01	MTE actuation failure.	Regular inspection on the actuators will be performed. Besides this, the number of actuators decreases the effect of single actuation failure. Other two actuation systems of a flap can still perform their function which leads to a decrease in impact of the event.
OP02	MTE control system failure.	Control system redundancy or the back up control system can be implemented for critical flight stages so MTE can still be used to finalise the mission albeit less efficient. This will reduce severity of the risk.
OP03	MTE gust sensing system failure.	Implementation of a secondary sensing system able to take on the function of the primary system in case of failure.
OP04	The implementation of MTE to legacy A320 leads to revision of take-off and landing capabilities.	The effect on take-off and landing performance is investigated and analysed. The design is adjusted until this effect is deemed acceptable. Take-off and landing distances can be increased, which decreases the impact on the system.
OP05	HLFC suction device failure, which makes system inoperative.	A Top Level Requirement (TLR) shall be added, which would require wing to function with HLFC inoperative.
OP06	HLFC valve state sensor failure could cause control systems internal errors.	Individual Valve state sensors are not critical system components. Likelihood of several of them failing simultaneously is small.
OP07	HLFC failure due to ice formation on the suction surface on the leading edge.	Activating de-contamination mode of the system, which blows hot air out of the micro-holes on the perforated leading edge surface. This will clean pores and decrease level of severity. The aircraft is able to fulfil the mission however at lower efficiency.
OP08	HLFC failure due to insect residue blocking holes in the leading edge sheet, preventing suction.	Blow air out of holes on the perforated leading edge surface. This will decrease impact severity. The aircraft is able to fulfil the mission however at lower efficiency.
OP09	HLFC failure due to ice crystal formation from cirrus clouds, causing laminar-turbulent transition.	Careful planning, with cirrus clouds forecasting taken into account. This will decrease likelihood of the cirrus clouds interference. Moreover, the de-contamination mode could be activated to significantly decrease the severity of this risk. The aircraft is able to fulfil the mission however at lower efficiency.

OP10	HLFC failure due to rain droplets and humidity collecting inside suction system.	Likelihood is decreased by ensuring, that decontamination mode is activated at any point of flight, where the cloud layer is not yet escaped. Severity is decreased by enabling de-contamination mode, where hot air is purged out of the system and thus cleaning it. The aircraft is able to fulfil the mission however at lower efficiency.
OP11	HLFC failure due to airborne particles blocking holes in the leading edge sheet, preventing suction	Blow air out. of holes on the perforated leading edge surface. This will decrease level of impact severity. The aircraft is able to fulfil the mission however at lower efficiency.
OP12	Failure leading edge temperature failure leads to failing to recognise ice contamination.	Failure of all sensors simultaneously is unlikely, but just in case, blowing of hot air shall be routine procedure before every take-off. This will decrease severity as well as probability of ice contamination, therefore temperature sensors failure's impact.
OP13	The reliability of critical components of the MLW is not sufficient so that it is able to last the lifetime of legacy A320.	A RAMS analysis is performed on the MLW. Any discrepancies found by this analysis will lead to suitable design changes to that the reliability of the system increases. Fatigue life of all materials is analysed as well which decreases the probability of the risk event.

10.1.4. Risk Map

Now all risk of the different categories are identified and their mitigation techniques are discussed, the different risk events identified are displayed in a risk map as shown in Figure 10.1.

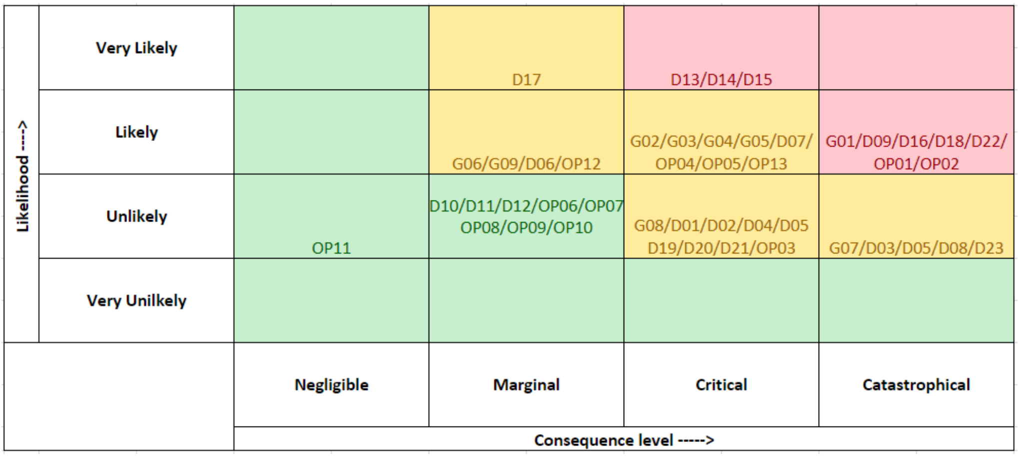

Likelihood ---->	Very Likely		D17	D13/D14/D15	
	Likely		G06/G09/D06/OP12	G02/G03/G04/G05/D07/ OP04/OP05/OP13	G01/D09/D16/D18/D22/ OP01/OP02
	Unlikely	OP11	D10/D11/D12/OP06/OP07 OP08/OP09/OP10	G08/D01/D02/D04/D05 D19/D20/D21/OP03	G07/D03/D05/D08/D23
	Very Unilkely				
		Negligible	Marginal	Critical	Catastrophical
		Consequence level ----->			

Figure 10.1: Risk map prior to risk mitigation

In order to minimise both probability and severity of impact of all risk events risk mitigation techniques as described above are applied to all risk events leading to an updated risk map for which the mitigation techniques have been implemented, displayed in Figure 10.2.

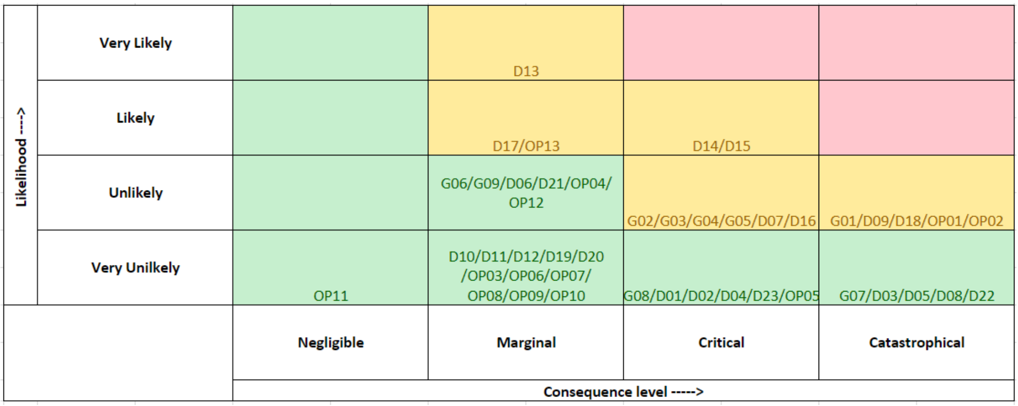

Likelihood ---->	Negligible	Marginal	Critical	Catastrophical
Very Likely		D13		
Likely		D17/OP13	D14/D15	
Unlikely		G06/G09/D06/D21/OP04/OP12	G02/G03/G04/G05/D07/D16	G01/D09/D18/OP01/OP02
Very Unilkely	OP11	D10/D11/D12/D19/D20/OP03/OP06/OP07/OP08/OP09/OP10	G08/D01/D02/D04/D23/OP05	G07/D03/D05/D08/D22

Consequence level ----->

Figure 10.2: Risk map following risk mitigation

10.2. RAMS

The RAMS evaluation deals with the consideration of the concept regarding reliability, availability, maintainability and safety concerns, and can be seen as a high level assessment of the risk associated with the project as a whole. As at the present stage of the development of the concept the level of technical detail is rather scarce, RAMS related aspects are still hardly quantifiable. The discussion about the RAMS of the concept is therefore intentionally held qualitative, considering aspects of the various systems that are applied.

The reliability is the ability of a system to perform a specific function and can be measured by the probability or rate of success, hence the rate of non-occurrence of failure. In case of the MLW systems such as the MTE as well as the Krueger slat and the HLFC system as described in chapter 3 are decisive. While the Kruger slat is a well-established system that has been applied on a multitude of aircraft, both the MTE and the HLFC are novel technologies that have been scarcely applied and tested [3]. Regarding the reliability of the MLW, the an important factor is the fact both HLFC and MTE have to be continuously operated throughout the entire flight as outlined in chapter 4. This is in contrast with legacy A320 systems. From this, it can be concluded that the reliability of the MLW will be less than the one of the original wing.

Linked to the reliability of the concept is its availability. The availability can be defined as the ability of a system to be kept in a functioning state. In aviation operations it is usually expressed in terms operational available versus operational planned or scheduled. As discussed with regards to the reliability, an increased number of systems running that are essential for the full operation of the wing, leads to an increased probability for the failing of one of these systems. The resulting operational availability of the MLW can therefore be expected to be lower than the one of the original design.

The maintainability of a system is defined as the ease at which it can be repaired and maintained, both in terms of time and cost. Comparing the MLW with the original design of the A320 wing, it is apparent that there is a higher number of systems and with an increase in complexity, when compared to legacy A320 systems. As an example, the MTE is considered more complex then the conventional Fowler flap. The overall effort to maintain these systems is therefore likely to be higher. In addition to the increased system complexity, there is no experience or established procedures that are tailored to the maintenance of novel systems such as the HLFC system. Materials like the polydimethylsiloxane, which is applied on the MTE, have previously not been applied on the outer skin of commercial aircraft and at the current state there is no knowledge base available with respect to aspects such as the degradation of the material and change of its elastic properties when exposed to the cruise flight environment of a commercial aircraft. While final quantitative conclusions on the expected maintainability of the optimised wing can only be drawn once the design of the various systems has evolved to a higher level of detail, the qualitative statement can be made that effort required for the maintenance of the MLW design is higher than for the one of the original design both in terms of time and cost. While initially high, both time and cost can be expected to decrease over time as the design is in service.

As the consequences from failure are potentially disastrous, safety is the paramount aspect among the RAMS considerations. It can be defined as the ability of a system within its life cycle, to not harm the environment, assets or people through its operation. While the overall reliability of the new wing concept is not on the same level as the one of the original design, the effect of the failure or partial failure of different systems or components is varying and should be discussed case by case. In case of the HLFC system a partial or complete failure leads to a reduction in aerodynamic efficiency, however the manoeuvrability and operational safety of the aircraft is not affected. While the failure of the MTE has similar effects on the aerodynamic performance when occurring in cruise flight, the failing of the system has potentially catastrophic effects when required for take-off or landing. Similar effects can be expected with regards to the failing of the Kruger slat, which is, just like the MTE, essential for the slow flight performance of the aircraft. While as elaborated in the discussion on the reliability the Kruger slat is not expected to fail more frequently than the conventional slat, the MTE is likely to have a higher failure rate than the original Fowler flap due to the novelty of the system. The MLW design can therefore be considered as less safe in its operation compared to the original design.

Considering the RAMS analysis with respect to its different aspects, it is apparent that the MLW design is seemingly performing worse than the original design. This can be partially attributed to the novelty of the systems that are applied and partially to the overall increased complexity. While aspects such as the availability and maintainability concern the operations and ultimately the cost of the MLW design, there is a very small margin of tolerance with regards to the safety. With regards to the increased complexity of the MLW design it should be emphasised that its further development has a major influence on how the various RAMS turn out to manifest themselves and the downsides with regards to safety of for instance the MTE are likely to dissolve over time with a growing experience and routine.

11

Sustainable Development Strategy

In this chapter, the MLW design will be analysed from a sustainability point of view. As defined in previous reports, a sustainable development strategy aims to reduce the negative impact upon the environment and combines social, environmental and economic factors. The sustainable development strategy is based on life cycle thinking. A description of the life cycle phases of interest is given in section 11.1. Next, in section 11.2, a comparison from a sustainability point of view of the MLW and the benchmark aircraft is presented.

11.1. Life Cycle Phases

The product life cycle is visualised in Figure 11.1. It starts with the extraction of raw materials and ends with some type of waste management, through which the product or a part of the product gets a second life. In the following subsections, the life cycle phases of interest for the design are discussed.

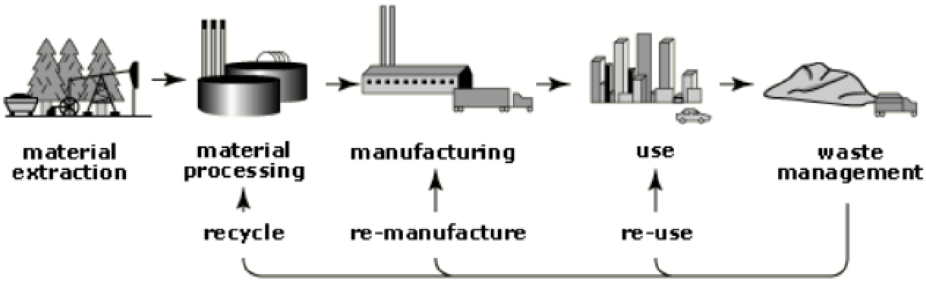

Figure 11.1: Life cycle of a product

11.1.1. Production Phase

Some requirements relate to sustainability of the design in the production phase. The requirement MLW-HuSh-002 states that no toxic materials shall be used for the production of the wing and requirement MLW-HuSh-009 states that the wing shall be lead free. Furthermore, requirement MLW-HuSh-001 states that the wing shall contain no more than 5% mass non-recyclable materials.

11.1.2. Operations Phase

The MLW design provides a drag reduction of 11.4%. This drag reduction means that the design will result in a more efficient flight, which means less fuel burn and therefore less emission of greenhouse gasses. Clearly, sustainability in the operations phase is inherent to the design.

11.1.3. End-of-Life

To make sure that, in the end-of-life phase, as many parts as possible of the aircraft are re-used and recycled, Airbus has, together with other companies developed a process: Process for Advanced Management of End-of-Life Aircraft (PAMELA), visualised in Figure 11.2 [19]. Applying this process reduces the life cycle footprint of the aircraft.

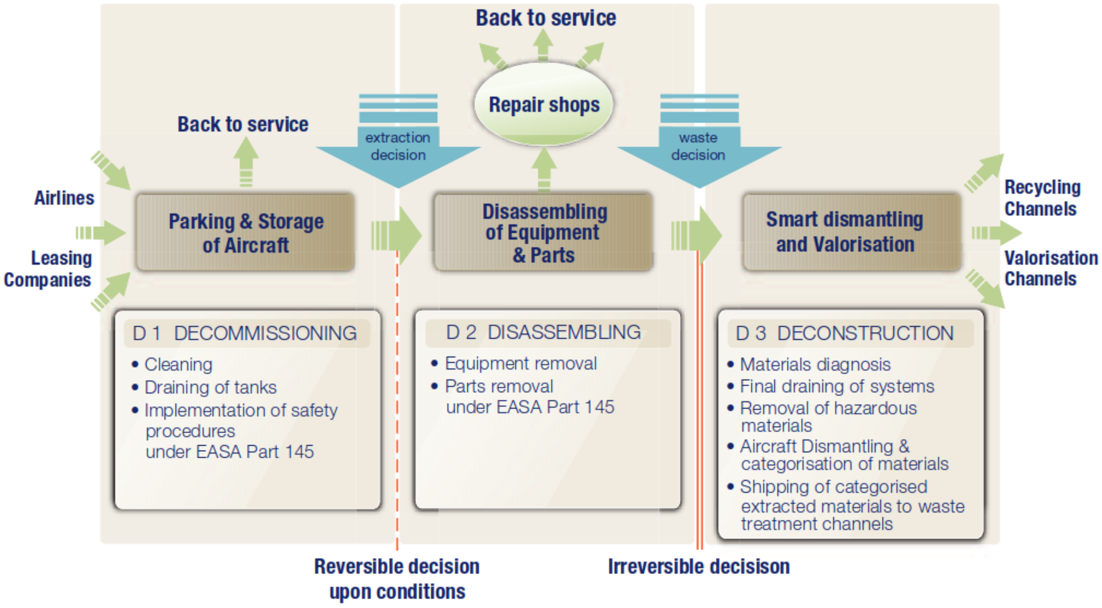

Figure 11.2: PAMELA overview

PAMELA consists of three phases. In the first phase, all necessary steps to make the aircraft ready for storage are carried out. At this stage, it is still possible to take the aircraft back into service, which is the 're-use' loop in Figure 11.1. In the next phase the disassembly of the aircraft is started. Some parts can be re-used, so they will be brought to the second hand market, from where the parts enter a second life. During this second phase, it is still possible to take the aircraft back into service, provided that the level of disassembly is acceptable. Finally, in the third phase, deconstruction of the aircraft will take place. As much material as possible should be recycled, which is the 'recycle' loop in Figure 11.1.

11.2. Sustainability Comparison

In order to analyse the performance of the MLW design compared to the benchmark aircraft from a sustainability point of view, the CES EduPack Eco Audit tool is used. This tool contains databases on material properties, manufacturing processes and more. A high-level assessment of the CO_2-footprint has been performed.

In the tool, for both the MLW design and the benchmark, the components that make up the wing have been defined. Components that were taken into account are the structural components and the systems, being the flaps, slats, HLFC, etc. For every component, parameters were defined: quantity, material, mass, primary production process and end-of-life use. The type of material is still top-level, so for example, the skin is made of an aluminium alloy, without specifying the exact alloy. Furthermore, the way the product is used had to be specified, in terms of product life time and product use per day. The product use is defined the same for the MLW design and the benchmark.

After specifying the use case and all the components and their parameters, the tool calculates the energy consumption and CO_2-footprint for every phase of the product life cycle. The results are presented in Table 11.1.

Phase	**Benchmark CO_2-footprint [kg]**	**MLW CO_2-footprint [kg]**	**ΔCO_2-footprint**
Material	$2.02 \cdot 10^5$	$2.19 \cdot 10^5$	+8%
Manufacture	$3.90 \cdot 10^3$	$4.34 \cdot 10^3$	+11%
Use	$6.90 \cdot 10^8$	$5.83 \cdot 10^8$	-16%
Disposal	$546 \cdot 10^0$	$394 \cdot 10^0$	-28%
Total	$6.90 \cdot 10^8$	$5.83 \cdot 10^8$	-16%
End-of-life potential	$-1.13 \cdot 10^5$	$-7.53 \cdot 10^4$	-33%

Table 11.1: CO_2-footprint comparison

From this analysis it can be concluded that the MLW design has a CO_2-footprint which is 16% lower compared to the benchmark aircraft. Another conclusion that can be drawn is that the 'use' phase of the MLW has by far the most impact on the CO_2-footprint. This means that assumptions made on the type of production process or the type of material used have little impact on the overall CO_2-footprint. Finally, it should be mentioned that the Eco Audit tool does not take into account the drag reduction of 11.4%. Using the fuel savings due to the drag reduction and the CO_2 emission factor of jet kerosene provided by the EPA[1], it is calculated that the drag reduction leads to another saving of $1.27 \cdot 10^5$ tonnes of CO_2 in the aircraft's lifetime.

In the remainder of the design process, the Eco Audit tool aids in making sure a sustainable design is made. When selecting for example the production process, the Eco Audit tool shows the effect of the production process on the energy consumption and the CO_2-footprint. This way, the production process with the lowest impact on these factors can be selected, provided the required material properties can be achieved.

---

[1] Emission Factors for Greenhouse Gas Inventories. `https://www.epa.gov/sites/production/files/2015-07/documents/emission-factors_2014.pdf` (accessed on 18 January, 2019)

12

Requirement Compliance Summary

This chapter presents compliance matrix, where each requirement presented in Table 2.1 is verified using information provided by the rest of the report. Each requirement was checked against available analysis and design layout. For those requirements, which could not be verified due to constrained time and resources available, a verification method was described. Some of them require prototype building or flight test. In either case, it is recommended to continue research in a prescribed direction. For a quick view, Table 12.1 provides the top-level requirement summary. All of these requirements were met, except the sensor/actuator reliability requirement, due to an increased number of actuators and their low technology readiness level.

Top-Level Requirements	Achieved?
7.5% drag reduction	✓
7.5% payload increase	✓
Lead-free smart materials	✓
Increased laminar flow region	✓
Current A320 MTOW not exceeded	✓
Purchase increase not more than 3%	✓
Overall lifetime cost not exceeded	✓
Sensor/actuator reliability maintained at A320 level	X

Table 12.1: Top-Level requirement compliance summary

12.1. Requirement Compliance Matrix

Table 12.2: System Level Requirement Compliance Matrix

ID	Requirement Specification	Verification method	Verified?
MLW-Sys-000	The wing shall reduce drag with 7.5% throughout the entire flight with respect to Airbus A320 legacy wing.	Analysis: chapter 4	Yes, total drag reduction is shown to be 11.4%
MLW-Sys-001	The wing shall provide sufficient lift during each flight phase, as defined in "A320 Flight Envelope" document.	Analysis: chapter 4	Yes, it’s shown in chapter 4

MLW-Sys-003	The wing shall continuously sense approaching gusts at least 300ms before they hit the leading edge of the wing	Design Review: section 5.1 demonstrates design of a sensor layout which enables to sense upcoming gusts.	Yes, section 5.1 describes how sensor layout was designed
MLW-Sys-004	(GLA) The wing shall autonomously alleviate loads due to gusts, described by model in subsection 5.3.1, and gust induced load factors shall not exceed 1.3	Analysis: chapter 5	Yes, Table 5.2 in chapter 5 shows resultant critical load factor to be 1.26
MLW-Sys-005	(MLA) The wing shall autonomously update lift distribution during symmetric manoeuvres to decrease bending moment at the root by at least 14.5%	Analysis: chapter 5 and chapter 6	Yes, chapter 5 describes how lift distribution is changed, and chapter 6 shows that MLA decreases root bending moment by 14.9%
MLW-Sys-008	The wing shall generate sufficient roll moment to perform 45° in 1.4s	Analysis	No, shall be verified by more in depth aerodynamic analysis
MLW-Sys-009	The wing shall autonomously optimise its shape during flight for minimal drag	Design Review: chapter 3	Yes, design implementation is described in chapter 3
MLW-Sys-010	The wing shall perform asymmetric required manoeuvres.	Analysis: chapter 4.	No, demands additional resources for analysis of asymmetric manoeuvres
MLW-Sys-011	The wing shall withstand limit loads, as defined in chapter 6, without permanent deformation.	Analysis: chapter 6	Yes, verified in chapter 6
MLW-Sys-012	The wing shall withstand limit loads without local stresses exceeding yield stress as defined in chapter 6 to be $200 MPa$	Analysis: chapter 6	Yes, verified in chapter 6
MLW-Sys-013	The Wing shall withstand ultimate loads without failure for 3 seconds, as defined in "Operational loads" document	Test	No, will be verified through prototype testing
MLW-Sys-014	The Wing shall withstand birdstrike of 4lb bird at a sea level V_c or $0.85 V_c$ at 2438 m.	Test	No, this is certification requirement, which will be verified through a testing
MLW-Sys-015	The wing shall function with HLFC inoperative	Demonstration: chapter 4	Yes, chapter 4 shows, that even without HLFC drag benefits, wing delivers sufficient, albeit sub-optimal, performance
MLW-Sys-016	The wing shall be free from these aeroelastic instabilities: flutter and divergence. - below the 1.15% of the maximum flight envelope velocity.	Analysis: section 7.4	Yes, analysis in section 7.4 shows compliance with this requirement
MLW-Sys-017	The wing shall result in payload increase of 7.5% with respect to A320	Analysis: section 6.4	Yes, payload is increased by 11.35%, as shown in section 6.4

MLW-Sys-018	The cost of the wing shall not exceed 103% of the A320 wing cost	Analysis: section 8.2	Yes, cost breakdown is shown in Table 8.4
MLW-Sys-019	The mass of MLW shall not exceed the mass of the A320 benchmark wing	Analysis: section 6.4	Yes, final mass estimation is presented in Table 6.10
MLW-Sys-020	The wing shall perform required symmetric manoeuvres	Analysis: chapter 4	Yes, verified in chapter 4
MLW-Sys-021	The LCC of the wing shall not exceed A320 benchmark wing LCC	Analysis: section 11.1	Yes, verified in section 11.1

13

Project Development Logic

This chapter contains the process and steps that will be undertaken after this project is complete. It was decided to give this chapter an approach that would be as realistic as possible and that additional resources are provided, which include a large engineering team, access to CFD/FEM software, testing facilities and budget for test aircraft setup. The first step after this project would include an additional design stage (see section 13.1). Moreover, before the MLW equipped A320 aircraft are ready to enter the market, they need to be wind-tunnel tested and produced, once the approval is issued. These two phases are addressed in section 13.2 and section 13.4 respectively. After the first aircraft is produced, it will continue with a series of in-flight tests, as explained in section 13.3. A timeline for these stages is given in section 13.5. Finally, aspects considering the operations & logistics of the MLW aircraft are discussed in section 13.6.

13.1. Succeeding Design Phase

Once this project is complete, it is expected that a larger group of engineers would take over the development of this project and, firstly, would make a transition to more sophisticated design tools such as CFD for aerodynamic analysis or FEM tools for structural analysis. This would help in achieving more accurate results for the investigations conducted throughout this design project. Another large block of work would be dedicated to designing computer algorithms and flight control tools for the HLFC/MTE control units, sensor data extraction, actuation input generation and monitoring of the subsystems.

After the final verified design is achieved, the next phase would include virtual wing testing and simulations. Moreover, specimen testing would be incorporated for better understanding of the materials, used in the MLW. Subsequently, detailed computer aided design drawings would be made for the real wing as well as the model for wind tunnel tests, as described in the following section.

13.2. Wind Tunnel Testing Phase

The testing phase is an essential part of this project due to two main reasons. Firstly, it generates validation data which is very important in making sure that all the analysis is done accurately and that there is no unforeseen behaviour. The second reason is that it enables further optimisation of Morphing Laminar Wing systems.

Undoubtedly, the first reason requires a model to be tested in a wind-tunnel rather than performing in-flight experiments. That is because the real state of wing behaviour is still only known in theoretical terms and needs to be investigated much further before human pilots can take it in their hands. The goal of wing model testing is to establish validation for the aerodynamic analysis and ensure that the MLW can indeed deliver the expected aerodynamic characteristics, such as $C_L - alpha$ and pitching and rolling moment coefficients. Once the wind tunnel tests are performed and it is certified that the wing is ready to move to the next phase, production of the first MLW-incorporated aircraft for testing purposes is done, using the production plan defined in section 13.4.

13.3. In-Flight Testing Phase

The first MLW A320 aircraft will be modified to perform a variety of tests in-flight, which are needed to validate the predicted HLFC performance, cruise optimisation and the effectiveness of MTE in the sense of load alleviation.

The primary objective of in-flight HLFC tests is to determine the transition location on the wing as a function of suction distribution. That is because uncertainty in the required suction remains rather significant due to the complexity of flow transition mechanisms on high-mach backwards swept wings. For instance, Boeing 757 wing HLFC flight tests concluded that the transition is delayed the most with one-third of the suction, calculated in the design phase [67]. This testing phase will require a variety of sensors to be added in flight. Transition over the wing top surface will be captured with infrared cameras, mounted on top of the fuselage as well as flush-mounted pressure taps to determine the external pressure distribution over the top surface. The registered data will be monitored real time by the flight test crew. By varying the suction pressure distribution, it is expected to determine the suction that results in the best aerodynamic results.

Besides HLFC, tests will be conducted to determine how well the in-flight shape optimisation of the wing achieves the designed performance. The shape of the wing will be adjusted, as described in chapter 4, and by means of a pressure sensor array, the effect will be derived. It is expected that these tests will determine the exact shapes of the aircraft wing as a function of aircraft mass in order to achieve the lowest drag.

Furthermore, MLA techniques will be analysed and fine-tuned regarding the pitch motions of the aircraft and the most optimal MTE deflections to achieve effective MLA will be determined. To achieve this, the test pilot will induce pitch manoeuvres of different rates and the morphing structure angle deflections will be closely monitored. The structural implications will be registered by an array of high accuracy strain sensors, distributed over the wingbox spars and ribs as well as structural elements of the MTE. Since gust load testing cannot be simulated and is merely opportunity-based, most of the gust load testing will be done while the test aircraft is flying through a cloud layer, which will induce random levels of gust load and the response of morphing surfaces will be investigated.

13.4. Production Phase

The complete wing production phase is split into three stages - component acquisition or production, wing assembly and aircraft integration. A detailed description and flow of these stages is given in Figure 13.1. The first phase is where all the required components and materials are obtained and the first sub-assemblies are made. This phase is broken down further into four production lines, which are wingbox, MTE, HLFC production lines and the production line of other wing components. In the production flow diagram, blue boxes define the initial assemblies, whereas the orange boxes indicate the materials or system hardware that is delivered from external entities. Note that some of these orange boxes are not linked to the rest of the flow in this phase. That is because these parts can only be implemented at a certain phase of the wing assembly.

The second phase is where the wing build-up starts. The starting point is the assembled wingbox, to which the other components are connected. That starts with internal wing subsystems such as hydraulics, pressure sensors for HLFC, pneumatics, electronics and winglets. After that the MTE, HLFC and Krueger flap sub-assembly are added.

The last production phase regarding the wing starts with connecting the wing to the fuselage sub-assembly that contains the centre wingbox. After that is complete, the remainder of the wing subsystems, that are stored inside the fuselage, are stored in place. Once everything is completed and approved, the aircraft continues to further assembly lines.

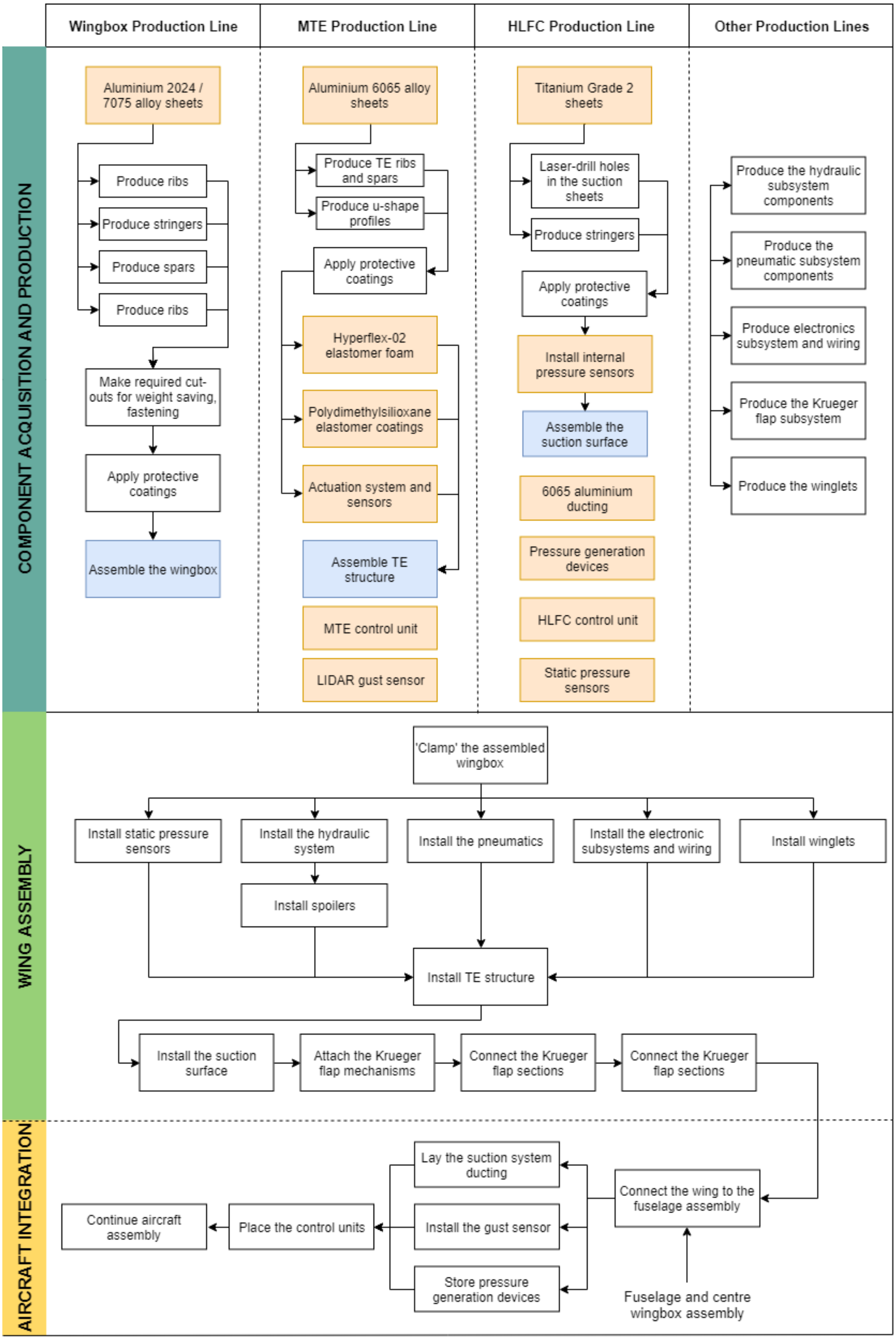

Figure 13.1: Production plan of the MLW, including three phases - component acquisition and first sub-assemblies, wing assembly and aircraft integration. The orange blocks indicate components, that will be delivered from external providers. Blue blocks indicate sub-assemblies that are required before the complete wing assembly line

13.5. Development Chart

The project development logic can be summarised and put to a time scale using a project development logic Gantt chart as shown in Figure 13.2. The total project development time is determined to be five years.

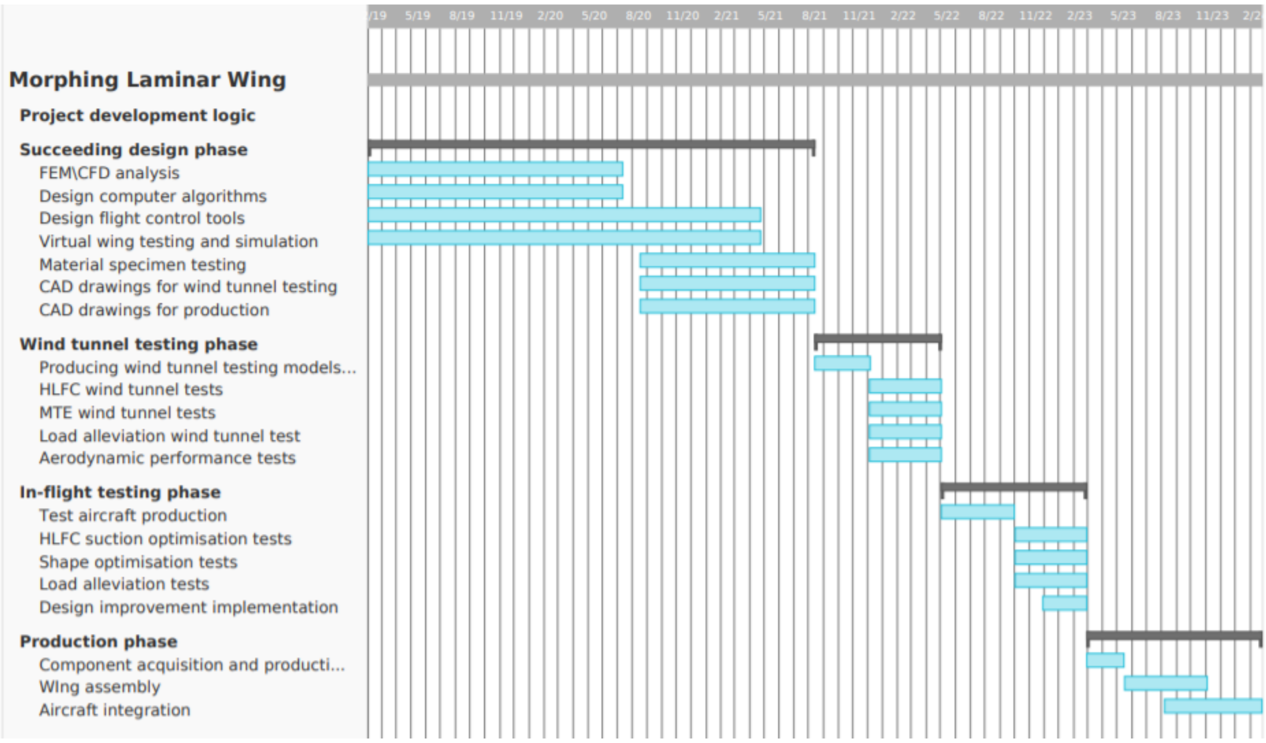

Figure 13.2: Project development logic gantt chart

13.6. Operations and Logistics

The Operations and Logistics of the MLW is a part of the design which was already briefly touched upon during the preliminary design phase. Aircraft have the highest accident rate on the ground. Research states that 61% of accidents are not airborne caused when establishing an interface between the aircraft and ground handling equipment [68]. This means that especially aircraft standing operations should be carefully executed and well planned for. The MLW shall change several operations and some of those changes focusing on the standing operations are discussed here.

A rough sketch of the operations during the standing phase are presented in Figure 13.3. As can be seen in Figure 13.3 several operations happen simultaneously, since a MLW is designed and not a new aircraft the wing operations are of interest here. The MLW is retro-fitted to an A320 aircraft which leaves operations like check-in, boarding, cleaning, catering and cargo loading unchanged.

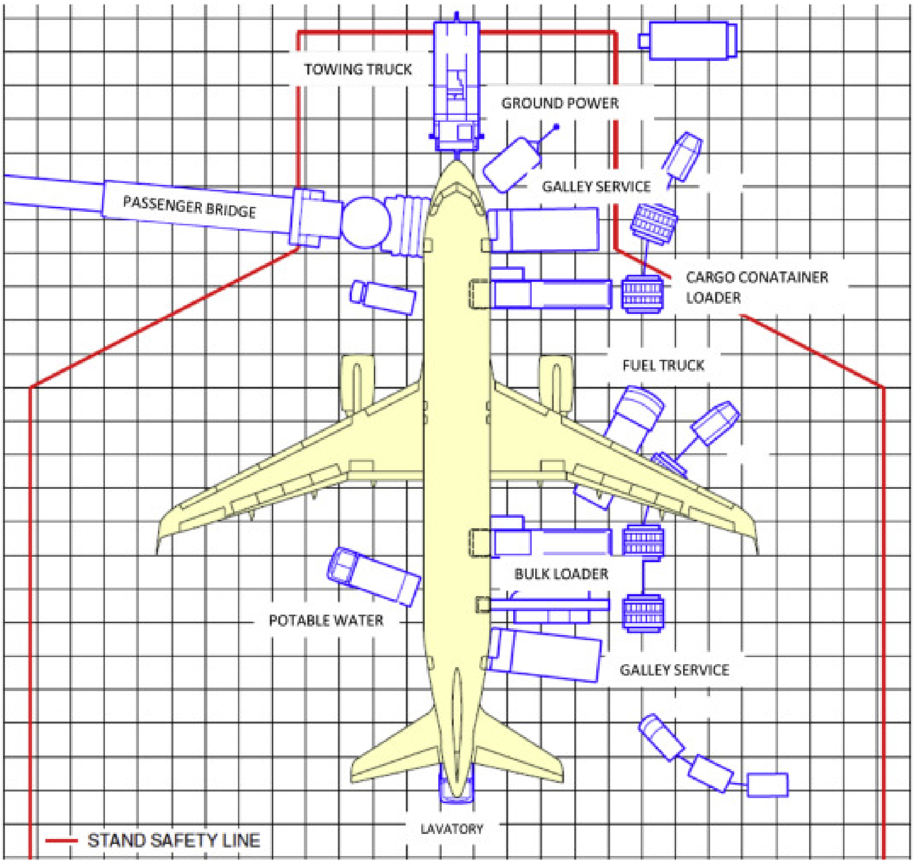

Figure 13.3: Ground operations of an A320 [69]

Operations like fuelling, maintenance and ground support will most likely change due to the implementation of the MLW. Since the wingbox is resized and the design is not further adapted, the fuel tanks remain on the same location. With the bottom part of the wing also barely altered, the fuelling operation of the MLW remains similar to that of an A320 wing.

For maintenance and ground support however, the new systems introduce new challenges. For the HLFC one issue was already identified during the preliminary design phase. During de-icing, the de-icing fluid that is sprayed on top of the wing could enter into the wing through the holes in the leading edge of the wing [53]. In order to still be able to de-ice the wing, without damaging the internal system with the de-icing fluid, the HLFC system shall blow air out of the holes throughout the de-icing process. In the event of precipitation, a similar approach shall be used. It should be noted that in some scenarios, some fluid shall inevitably enter through the holes, which is not directly harmful, since this can be simply blown out by the HLFC system. In order to clean the internal system, a similar approach is used as during flight. When the engine is running, pressurised dry hot air from the high pressure compressor of the engine is blown through the pipes, which cleans the pipes. For visual checks on the leading edge, the Krueger flap shall be deployed such that the perforated leading edge plate becomes visible.

For the MTE its maintenance and ground support, the visual inspection is not very different compared to a normal A320 wing. There are more flaps and there is more surface area to be checked but everything is just as visible as with regular flaps. What changes is the time it takes to check and what is being focused on. Especially the elastomer requires checking. In order to make sure the wing is still fully functional a maximum deflection test could be done before each flight both upwards and downwards. With this test, damaged material or actuator flaws shall be easier detected.

If the maintenance shows that parts of the wing need repairing operations, the repair of the MLW will take longer than a regular A320 wing due to the increase in complexity. The HLFC and MTE elements are also less accessible than the normal leading and trailing edge structures.

14

Conclusions and Recommendations

Over the last decades, the aviation industry has been experiencing a stagnation of performance increase with the existing technology. In an effort to bypass this stagnation, a new and innovative design has been created showing great potential in both aerodynamic performance increase as well as load alleviation capabilities. This design is the Morphing Laminar Wing (MLW) and utilises a combination of Hybrid Laminar Flow Control (HLFC) and a Morphing Trailing Edge (MTE). A list of customer and functional requirements the design has to meet was presented. All key and driving requirements are met by the MLW design. For some requirements, it was not yet possible to verify whether or not the MLW design meets them, due to time and resource constraints.

In the preliminary design phase, a number of design concepts were created, from which the HLFC and MTE systems were selected for detailed analysis. HLFC shows great potential in drag reduction, by means of postponing transition of laminar to turbulent flow. This is achieved via selecting a laminar airfoil whose effect is enhanced by a suction system implemented on the leading edge, eliminating the slowest part of the boundary layer. The increase in laminar flow region leads to a decrease in skin friction drag. The HLFC system provides a total drag reduction of 3.5%. This value is further increased by airfoil shape optimisation in all flight phases, as a result of the morphing capabilities of the MTE. This leads to a total aircraft drag reduction of 11.4% with respect to the benchmark A320. This increase in aerodynamic performance has a positive effect on the efficiency of the MLW compared to the benchmark A320, decreasing fuel consumption by 1142 kg per flight.

The second big advantage of the MLW design with respect to the benchmark A320 is captured in the high load alleviation capabilities of the MTE. The load alleviation systems created alleviate critical gust and manoeuvre loads experienced by the MLW aircraft. Analysis of the mission profile V-n diagram revealed that the critical load case is due to manoeuvres, which is therefore leading in sizing of structural components of the MLW. Implementation of MLA shows a decrease in wing structural mass of 18.3% or 1655.4 kg. A study of the dynamic stability has been performed on the resulting MLW structure. This showed that the MLW design does not experience flutter or divergence within the MLW operational profile.

Analysis of system mass for both HLFC and MTE allow for a final structural mass reduction of MLW with respect to benchmark A320 of 1415 kg. Adding the reduction in fuel mass allows for a payload increase of 2270 kg, without exceeding the benchmark A320 MTOW. Furthermore, the reduction in wing mass and fuel burn leads to a decrease in CO_2-footprint of 16%.

Financial analysis of the MLW design showed that the market has a potential for 10,000 MLW deliveries with a total market value of almost 1,000 billion USD up until 2037. Retrofitting aircraft with the MLW design has a payback period of seven years. After this period, the MLW design will generate extra profit for the customer.

Furthermore, a RAMS analysis of the MLW design has been performed. Since the MLW design adds new subsystems to an existing design, the overall complexity increases. With this increased complexity, the RAMS characteristics are expected to decrease. However, this decrease is not expected to be as significant as to the extend that it would drive the design unfeasible. Where applicable, appropriate risk mitigation techniques have been implemented. Also, after gaining real world experience with the MLW design, the RAMS characteristics are expected to improve.

Recommendations

This section contains all recommendations found during the analysis of MLW in an effort to improve the analysis and performance of the MLW in future development. The recommendations are split according to type of analysis performed on the MLW and the design of its subsystems.

14.0.1. Aerodynamics

The aerodynamic analysis of the benchmark model and the optimised model of the aircraft as presented in chapter 4 deals with the methodology with regards to the workflow and the software used, as well as the creation of the aerodynamic model and the performance analysis. Recommendations regarding the aerodynamic analysis address both the methodological approach as well as the strategy chosen for the performance assessment.

For the aerodynamic analysis of the different models the software XFLR5 is used, which combines the 2D airfoil analysis capabilities of XFOIL with a vortex lattice method solver for 3D analysis. While it is great tool for the preliminary analysis of aircraft at sub-sonic speeds, it lacks the ability to simulate the effects of compressibility in an accurate way and does not take effects such as wave drag at transsonic speeds into account. In order to perform analysis on an aircraft in the class of an A320 appropriately, XFLR5 or a similar program using the vortex lattice method would have to be expanded to take these effects sufficiently into account. Another approach to dealing with the issue would be to use professional CFD software, however this has the potential to limit the iterative nature of the design process significantly. Next to the effects of compressibility and pressure waves during transsonic flight, the analysis of the effect of high lift devices such as slats or flaps poses a challenge with the current set of tools. Detailed CFD analysis could here be useful alternative to the application of correction factors in an analytical fashion, and thereby increases the overall accuracy of the simulation.

Next to the tools available for simulation, the approach used for the tuning and optimisation of the aircraft model has potential to be refined. This concerns the the selection of airfoils, as well as the changes in geometry both locally and globally. While in chapter 4 only a limited amount of airfoils was analysed, the number could increase greatly and even extend to airfoils that are specifically designed for the purpose of implementing systems such as the morphing trailing edge. In addition to that the deflection of the morphing trailing edge should be investigated in a numerical fashion that includes a vast amount of possible combinations of deflections. In addition to a more sophisticated approach for the analysis and optimisation of the wing geometry, the process of analysing the performance with regards to the mission requires to be refined. In chapter 4 a mere feasibility study on one alternate mission profile that deviates from the original A320 mission profile was investigated. While it did not prove to be advantageous for the overall drag performance when compared to the original profile, this does not necessarily apply to all mission profiles that deviate from the original one. In order to determine whether the performance advantage of using a morphing trailing edge, new airfoils and a boundary layer suction system fully manifests itself when flying at a different mission profile, a wide variety of various profiles should be included in the investigation.

Besides the methodology of aerodynamic analysis and the approach to optimisation, the take-off and landing performance of the aircraft using the morphing laminar wing should be be improved. This can be achieved by either reconsidering the use of high lift devices, such as the application of a Fowler flap in combination with a morphing trailing edge, or a modification of the wing planform. As a planfrom change has far reaching implications, the use of additional high lift devices should be prioritised though.

14.0.2. Load Alleviation

To improve the GLA model described in section 5.3 the lead time of the LIDAR sensor could be incorporated, this will give more insight into the requirements for the sensing system. Besides that the implications of the computational time of the required deflections could be analysed. Researching these two aspects will give a clearer overview of the limitations for GLA. For the MLA it is necessary to look at non-symmetric manoeuvres and it might be beneficial to look at the consequences of increasing the number of sections and the deflection limits, this could lead to to a lighter design. After these improvements both models could be integrated to be able to find the optimum combination of GLA and MLA, which leads to the lightest design.

14.0.3. Wingbox Structural Model

In order to quantitatively asses the effect of active load alleviation on wing structural mass as well as to confirm structural integrity of the MLW, a structural model was created as described in section 6.1. This model has been subjected to extensive verification and validation procedures as well as a sensitivity analysis. Despite this a number of recommendations can be made which will have positive effect on the validity of the model. Firstly, the model should be validated using the critical loading case to which legacy A320 has been structurally sized. The model now relies on validation using an assumed critical lift distribution which is expected to generate bias results. Secondly, a skin buckling analysis could be implemented in order to asses the effect of active load alleviation on skin buckling. This effect is not taken into a count in estimation wing structural mass. Finally, extensive FEM analysis can generate more accurate verification of the model, while producing and testing the generated structural layout for the wingbox to the critical loading case can further validate the results of the model.

14.0.4. Wing Stability Analysis

In order to improve the analysis, error analysis can be performed for uncertainties and errors involved in the numerical model. The main sources of errors are from the model errors and discretisation errors. Although, quasi-steady flow model is known to be sufficiently accurate for many cases, ignoring the wake vortices can be quite significant, as it reduces the magnitude of the aerodynamic load acting on the airfoil. Since this reduction can have a quite significant effect on flutter estimation, model could be further improved by using quasi-unsteady or unsteady aerodynamic models, which could reduce the errors that arise from the governing equations of the system [63]. Furthermore, discretisation errors could be reduced by increasing the number of sections. Controlling the uncertainties can be more challenging, which can still be done through sophisticated uncertainty quantification techniques.

14.0.5. HLFC system development

The main recommendation for the suction subsystem is to switch to more sophisticated design and analysis tools. That would involve computational fluid dynamics flow solutions, incorporated with a boundary layer suction option. By doing so, it is expected to benefit in two fields - flow transition estimations and drag reduction values. Moreover, in terms of hardware it is recommended to investigate an option of replacing the pump system by a passive suction mechanism, which would be very beneficial in reducing system mass. Such mechanism has already been investigated by Boeing, however, the performance results of it remains unavailable to the public [70]. Lastly, the system analysis would be greatly improved if the RAMS of the system was analysed in more detailed and quantified in terms of resource budgeting and how it affects the operations of MLW equipped aircraft.

14.0.6. MTE structural sizing

For the MTE mass estimation initial sizing techniques have been used that allow a quick, conservative sizing of the structure. The limitations of the analysis are mainly due to fact that dynamic/advanced aircraft structures as well as hyper-elastic materials (Hyperflex-02, Polydimethylsiloxane) are involved which require structural analysis methods that are not available during the DSE. Still even with the local knowledge it would be possible to improve the model if the FEM is performed for each component individually. Especially if more detailed aerodynamics data is available, namely the pressure distribution on the MTE, this method would give optimised structures. Another approach would require to model all the components in an assembly and then perform the FEM stress analysis which eventually allows to study the interactions of components. Interaction properties are especially important for the linkage of active ribs and skin. Also hyper-elastic material properties could be studied by ordering sample material on which tensile tests can be performed in the Delft Aerospace Structures and Materials laboratory.

Bibliography

[1] John D Anderson Jr. *A history of aerodynamics: and its impact on flying machines*, volume 8. Cambridge University Press, 1999.

[2] Matthias Horn, Arne Seitz, and Marvin Schneider. Novel tailored skin single duct concept for hlfc fin application. In *7th European Conference for Aeronautics and Space Sciences (EUCASS)*, 2015.

[3] Boeing Commercial Airplane Group. High reynolds number hybrid laminar flow control (hlfc) flight experiment ii. aerodynamic design. Technical report, NASA, 1999.

[4] Peter K. C. Rudolph. High-lift systems on commercial subsonic airliners. Technical report, NASA, 1996.

[5] John David Anderson Jr. *Fundamentals of aerodynamics*. Tata McGraw-Hill Education, 2010.

[6] Charles D. Harris. Nasa supercritical airfoils; a matrix of family-related airfoils. *NASA Technical Paper 2969*, 1990.

[7] Egbert Torenbeek. *Advanced Aircraft Design: conceptual design, analysis and optimization of subsonic civil airplanes*. Wiley, 2013.

[8] Élodie Roux. *Avions civils à réaction : plan 3 vues et données caractéristiques*, volume 3. Éditions Élodie Roux, 2007.

[9] Airbus. *A318/A319/A320/A321 Flight Crew Operating Manual*, flight operations edition.

[10] Jr. F. S. Collier. An overview of recent subsonic laminar flow control flight experiments. *Fluid Dynamics Conference*, February 1993.

[11] Christopher D Regan and Christine V Jutte. Survey of applications of active control technology for gust alleviation and new challenges for lighter-weight aircraft. Technical report, NASA, 2012.

[12] T. Theodorsen, W.H. Mutchler, and United States. National Advisory Committee for Aeronautics. *General Theory of Aerodynamic Instability and the Mechanism of Flutter*. National Advisory Committee for Aeronautics: Report. National Advisory Committee for Aeronautics, 1935.

[13] R.L. Bisplinghoff, H. Ashley, and R.L. Halfman. *Aeroelasticity*. Dover Books on Aeronautical Engineering Series. Dover Publications, 1996.

[14] T.M. Young. Investigations into the operational effectiveness of hybrid laminar flow control aircraft. appendix j.6. Master's thesis, Cranfield University, October 2002.

[15] Deman Tang and Earl H. Dowell. Experimental aeroelastic models design and wind tunnel testing for correlation with new theory. *Aerospace MDPI*, April 2016.

[16] G. Dimitriadis. *Introduction to nonlinear aeroelasticity*. John Wiley & Sons, Incorporated, 2017.

[17] European Aviation Safety Agency. *Certification Specifications for Large Aeroplanes CS-25*. European Aviation Safety Agency, September 2007.

[18] Susan A Resetar, James Curt Rogers, and Ronald W Hess. Advanced airframe structural materials: A primer and cost estimating methodology. Technical report, RAND CORP SANTA MONICA CA, 1991.

[19] Airbus. Process for advanced management of end-of-life of aircraft. 2008.

[20] Upender Kaul Sonia Lebofsky Eric Ting Daniel Chaparro James Urnes Nguyen, Nhan. Development of varialble camber continious trailing edge flap for performance adaptive aeroelastic wing. Technical report, NASA Ames Research Centre, Stinger Ghaffarian Technologies, Boeing Research Centre, 2015.

[21] Ignazio; Lecce Leonardo; Pecora Rosario Concilio, Antonio; Dimino. *Morphing Wing Technologies - Large Commercial Aircraft and Civil Helicopters.* Elsevier, January 2018.

[22] G. Schrauf. Status and perspectives of laminar flow. *The Aeronautical Journal*, page 639, 2005.

[23] Max Kingsley-Jones. Aero secrets of boeing's new dreamliner. *FlightGlobal*, July 2014.

[24] B. Humphreys T. Young, B. Mahony. Durability of hybrid laminar flow control (hlfc) surfaces. *Aerospace Science and Technology*, page 190, 2002.

[25] MAB Van den Berg. Internal systems design for smart fixed wing technologies using knowledge based engineering. 2010.

[26] B.R. Munson, A.P. Rothmayer, and T.H. Okiishi. *Fundamentals of Fluid Mechanics, 7th Edition.* Wiley, 2012.

[27] MD Bassett, DE Winterbone, and RJ Pearson. Calculation of steady flow pressure loss coefficients for pipe junctions. *Proceedings of the institution of mechanical engineers, part C: Journal of Mechanical Engineering Science*, 215(8):861–881, 2001.

[28] Boeing Commercial Airplane Group. High reynolds number hybrid laminar flow control (hlfc) flight experiment iv. suction system design and manufacture. Technical report, NASA, 1999.

[29] Jr. R.D. Wagner M.C. Fischer, A.S. Wright. A flight test of laminar flow control leading-edge systems. *NASA Technical Memorandum*, page 10, December 1983.

[30] Peter K. C. Rudolph. Mechanical design of high lift systems for high aspect ratio swept wings. Technical report, NASA Ames Research Center, 1998.

[31] Christopher J. Bahr H. Dogus Akaydin, Jeffrey A. Housman. Computational design of a krueger flap targeting conventional slat aerodynamics. *American Institute of Aeronautics and Astronautics*, pages 7–9, 2017.

[32] Thijs W. Gloudemans. Aircraft performance parameter estimation using global ads-b and open data.

[33] Stephen P. Lukachko Raffi Babikian. The historical fuel efficiency characteristics of regional aircraft from technological,operational,and cost perspectives. *Journal of Air Transport Management*, 2002.

[34] David E. Hahne Frank L. Jordan William G. Sewall, Robert J. McIhee. Wind tunnel results of the high-speed nlf(1) 0213 airfoil. *NASA Report N90-12542.*

[35] Ray V. Hood David B. Middleton, Dennis W. Bartlett. Energy efficient transport technology. *NASA Reference Publication 1135*, September 1985.

[36] The Boeing Company. European patent application 0 111 785 a1. *European Patent Office*, 1984.

[37] R.C.Pankhurst. N.p.l. aerofoil catalogue and bibliography. *A.R.C. Technical Report*, 1972.

[38] Ed Obert. *Aerodynamic Design of Transport Aircraft.* IOS Press BV, 2009.

[39] S.F.Hoerner. *Fluid-Dynamic Drag.* Hoerner Fluid Dynamics, 1965.

[40] Airbus SAS. A318/a319/a320/a321 performance training manual. *Performance Part of Transition Course with Airbus Documentation*, 2005.

[41] E.R. van Driest. Turbulent boundary layer in compressible fluids. *Journal of the Aeronautical Sciences*, page 1024, March 1951.

[42] Daniel Raymer. Aircraft design: A conceptual approach, 1992. AIAA.

[43] Roelof Vos Martin Orlita. Cruise performance optimization of the airbus a320 through flap morphing. *17th AIAA Aviation Technology, Integration and Operations Conference*, 2017.

[44] Statistical loads data for the airbus a-320 aircraft in commercial operations. Technical report, U.S. Department of Transportation, Federal Aviation Administration, 2002.

[45] Gerrit J.J. Ruijgrok. Elements of airplane performance, 1990. VSSD.

[46] Robert E. Hage Courtland D. Perkins. *Airplane Performance Stability and Control.* 149.

[47] B. Dominique and T. Pascal. Airbus a320/a330/a340 electrical flight controls-a family of fault-tolerant systems. In *FTCS-23 The Twenty-Third International Symposium on Fault-Tolerant Computing*, pages 616–623, 1993. IEEE.

[48] Jia Xu and Ilan Kroo. Aircraft design with maneuver and gust load alleviation. In *29th AIAA Applied Aerodynamics Conference*, page 3180, 2011.

[49] Jia Xu and Ilan Kroo. Aircraft design with active load alleviation and natural laminar flow. *Journal of Aircraft*, 51(5):1532–1545, 2014.

[50] J.C. Lewolt H.D. Ramsey. Design maneuver loads for an airplane with an active control system. *AIAA*, 1979.

[51] Roeland De Breuker Vega Handojo, Paul Lancelot. Implementation of active and passive loads alleviation methods on a generic mid-range aircraft configuration. *AIAA*, 2018.

[52] D Westerveld. Unsteady aerodynamics in the gust and manoeuvre response of flexible aircraft. Master's thesis, TU Delft, 2016.

[53] Group 2. Midterm report smart autonomous wing. Technical report, Delft University of Technology, 2018.

[54] T.H.G. Megson. *Aircraft Structures for Engineering Students.* Butterworth-Heinemann, 4 edition, March 2007.

[55] Chen Bai, Luo Mingqiang, Shen Zhong, Wu Zhe, Man Yiming, and Fang Lei. Wing weight estimation considering constraints of structural strength and stiffness in aircraft conceptual design. *International Journal of Aeronautical and Space Sciences*, 15(4):383–395, 2014.

[56] Stephen V. Thornton. Reduction of structural loads using maneuver load control on the advanced fighter technology integration (afti)/f-111 mission adaptive wing. Technical report, NASA Ames Research Center, 1993.

[57] EO Ezugwu and ZM Wang. Titanium alloys and their machinability—a review. *Journal of materials processing technology*, 68(3):262–274, 1997.

[58] O.Bertram K.S.G. Krishnan. Assessment of a chamberless active hlfc system for the vertical tail plane of a mid-range transport aircraft. *Deutscher Luft- und Raumfahrtkongress*, page 3, 2017.

[59] F.T. Behrooz M.M. Shokrieh. Wing instability of a full composite aircraft. *Composite Structures*, 54:335–340, 2001.

[60] S. Gutschmidt A. Pons. Multiparameter spectral analysis for aeroelastic instability problems. *J. Appl. Mech*, Apr 2018.

[61] G. Gratton. *Initial Airworthiness: Determining the Acceptability of New Airborne Systems.* Springer, 2 edition, 2018.

[62] S.J. Hulshoff. *AE4930 Aeroelasticity.* TU Delft, November 2011.

[63] C. W. Rowley S. L. Brunton. Modeling the unsteady aerodynamic forces on small-scale wings. *AIAA*, January 2009.

[64] Helen Jiang. Key findings on airplane economic life. *Aviation Systems Analysis, Boeing Commercial Airplanes*, 3, 2013.

[65] Carlo Alberto Biffi, Nora Lecis, Barbara Previtali, Maurizio Vedani, and Gian Marco Vimercati. Fiber laser microdrilling of titanium and its effect on material microstructure. *The International Journal of Advanced Manufacturing Technology*, 54(1-4):149–160, 2011.

[66] Group 2. Project plan smart autonomous wing. Technical report, Delft University of Technology, 2018.

[67] Ronald D Joslin. Aircraft laminar flow control. *Annual review of fluid mechanics*, 30(1):51, 1998.

[68] A.D. Balk. Safety of ground handling. *NLR-CR-2007-961*, page 44, January 2008. National Aerospace Laboratory NLR.

[69] Michael Schmidt, Annika Paul, Mara Cole, and Kay Olaf Ploetner. Challenges for ground operations arising from aircraft concepts using alternative energy. *Journal of Air Transport Management*, 56:107–117, 2016.

[70] Pradip G. Parikh. Passive removal of suction air for laminar flow control, and associated systems and methods. *United States Patent*, June 2007.

A

Appendix

Application of Project Management and System Engineering

At the beginning of this project, several project management and system engineering ideas and tools were explained by the supporting parties. In this chapter, the usage of this knowledge during the detailed design phase is briefly touched upon.

Organogram

All organisational and technical roles were identified and presented in an organogram in the mid-term report [53]. These proved to be useful during the detailed design phase, for all contact regarding external parties was done by the external communication manager. The result was that if any of the team members had questions regarding external parties all information was at one place, readily available. Similarly for the other tasks like quality control, for all questions related to quality control the team members could ask the quality manager. Who would not only answer all questions, but also actively take his responsibility to ensure quality control.

Planning

At the beginning of the detailed design phase an initial planning was made with estimations for the tasks to perform at hand and the time it would take to complete those tasks. The plannings were made using a Gantt-chart, where the work break down structures made during the mid-term phase where used to plan up to such detail that individuals could be assigned to each assignment. Some buffers were build into the planning, in the case that an intern deadline would not be met. The resource allocation also had several buffers included for later stages during the detailed design phase, this in order to be able to give attention to areas that would only be discovered later. The planning was made by the project manager and planning manager. The planning manager was in charge of updating the project manager on potential delays. The risk manager also played an important role here by being responsible for identifying risks as early as possible and communicating with other team members to incorporate a buffer or mitigation strategy to deal with the risk.

Project control was used continuously to switch between checking status and taking adaptive action. This proved necessary because the initial planning made underestimated several of the tasks up-hand. It became evident that internal deadlines had to be moved and re-scheduling activities were required. By sticking to earlier on agreed daily meetings with status updates of each department or individual, the team was able to identify the planning issues early on.

Concurrent engineering and inter-task relationship management

The importance of the project management, showed since concurrent engineering was applied in the planning. Multiple teams working on multiple different aspects which required multiple inputs. This required a strict planning and good communication to ensure efficiency. Identifying the inter-task relationship up front showed useful since the groups within the team knew what outputs the other groups needed to further progress.

One example of the inter-task relationship is the lift distribution which was made by the aerodynamics department which was than handed over to the control group. The control department altered them by applying load alleviation and provided the structures group with the altered lift distribution and the added torque loads. The structures department than used these to calculated structural mass based on the stresses that these loads induce. This was identified up front and lead to that all departments build parameterised models, which were able to import and output an upfront agreed on date type file.

Team rules, SWOT and requirement analysis

Earlier in the project during the project planning phase team rules were set up. The rule was agreed upon that every time a team member came late by more than 5 minutes, they had to supply the rest of the group with a cake. Where once again the project management showed very beneficial for the work ethic and social environment of the team. Also during the project plan phase a SWOT analysis was also performed, which showed useful during the detailed design phase. Certain team members are more experiences with certain things, like one of our team members is an expert in numerical solutions. During the detailed design phase, multiple team members have consulted the expert which increased the overall efficiency and kept the work flow high. The requirement analysis process that was gone through from the beginning of the project lead from a need statement all the way to the subsystem requirements. During the detailed design phase the last step (of this project) from system requirements to subsystem requirements was made.